# Wetland Characterization through Multi-Sensor Satellite Data and Advanced AI Models

by

© **Hamid Jafarzadeh**

A dissertation submitted to the School of Graduate Studies in partial fulfillment of the requirements for the degree of
**Doctor of Philosophy**.

Faculty of Engineering and Applied Science
Memorial University of Newfoundland

May 2025

St. John's, Newfoundland and Labrador, Canada

# Abstract

Wetlands are generally defined as areas that are inundated or saturated with water for at least part of the year, though definitions can vary significantly across different scientific disciplines. Recognized as some of Earth's most valuable and productive ecosystems, wetlands provide a range of essential ecological services. These include regulating global climate through carbon storage, naturally purifying water by filtering pollutants, mitigating flood and drought impacts, protecting shorelines from erosion, conserving soil, and supporting biodiversity by serving as critical habitats for diverse wildlife species. Wetlands also offer spaces for recreation, cultural appreciation, and aesthetic enjoyment, underscoring their multifunctional importance for environmental health and human well-being. They are dynamic ecosystems characterized by complex and fluctuating vegetation, water, and soil interactions. Traditional monitoring methods rely on in-situ sampling of vegetation, hydrology, and soil, which are labor-intensive, time-consuming, and challenging to scale across vast or inaccessible regions. In contrast, remote sensing (RS) technology, coupled with advanced artificial intelligence (AI) techniques, offers an efficient, scalable, and non-intrusive approach for assessing wetland health, spatial extent, and ecological status. Through the integration of multisource - multispectral, Synthetic Aperture Radar (SAR), and Light Detection and Ranging (LiDAR) data - RS enables high-resolution monitoring across long-term periods and expansive spatial scales, allowing for efficient mapping and characterization of different wetland classes. These tools are crucial in quantifying wetland changes, identifying anthropogenic impacts, and understanding seasonal ecological variations in wetlands, thereby facilitating data-driven conservation and sustainable management efforts.

This thesis focuses on improving wetland mapping and characterization by introducing novel methodologies that utilize advanced RS technologies and multisource

satellite data. First, it presents a comprehensive literature review on wetland monitoring, focusing on the integration of RS and machine learning (ML) techniques. In the context of rapidly changing wetland landscapes, the synergy between multisource RS data and ML algorithms offers an opportunity to enhance decision-making support for wetland management. The review provides guidance on selecting suitable ML algorithms and RS data types for detailed wetland monitoring. A second key contribution of this work is the development of a novel deep learning (DL) framework to address the challenge of limited sample data, advancing the potential of RS techniques for wetland mapping. Emphasizing the integration of SAR and optical data, the framework utilizes multimodal data sources and applies Graph Convolutional Networks (GCN) and Convolutional Neural Networks (CNN). The experimental results demonstrate significantly improved classification accuracy, particularly in mapping complex ecosystems, compared to single-stream approaches. Thirdly, this research highlights the importance of RADARSAT Constellation Mission (RCM) compact polarimetric SAR (CP-SAR) data in wetland studies. A novel framework is developed to extract robust features for wetland mapping, showcasing notable improvements in wetland classification performance compared to existing models. Fourthly, a new SAR decomposition technique is introduced, designed specifically for CP-SAR data from RCM imagery. This technique refines the analysis of wetland structures and compositions. Additionally, a unique descriptor termed compact polarimetry signature (CPS) is proposed based on time-series RCM data, enabling a detailed investigation of wetland phenological cycles and associated SAR backscatter variations during active growing seasons. The results demonstrate the superior effectiveness of these techniques in characterizing complex wetland landscapes, surpassing the accuracy and detail of traditional single-date approaches. Finally, this work evaluates the added value of incorporating diverse data sources, including optical, SAR, and LiDAR data, into wetland mapping. Using the Google Earth Engine (GEE) platform, two main objectives are pursued: (1) integrating Global Ecosystem Dynamics Investigation (GEDI) LiDAR footprint heights with multisource datasets to generate vegetation canopy height (VCH) maps, and (2) enhancing wetland mapping by using VCH as a predictive input. Results highlight the critical role of VCH derived from GEDI samples in improving wetland classification accuracy, offering a vertical vegetation profile that enriches understanding of wetland ecosystems. This thesis introduces innovative

methodologies that pave the way for practical and scalable solutions in wetland mapping. The approaches outlined not only enhance our ability to map complex wetland systems in Canada but also provide adaptable strategies applicable to ecologically similar wetlands around the world.

**Keywords:** Wetland, Remote Sensing (RS), Synthetic Aperture Radar (SAR), Compact Polarimetry (CP), RADARSAT Constellation Mission (RCM), Artificial Intelligence (AI), Convolutional Neural Network (CNN), Google Earth Engine (GEE), Earth Observation (EO), Sentinel missions

*Dedicated to my family*

# Acknowledgements

I would like to express my gratitude and appreciation to my supervisor, Dr. Masoud Mahdianpari, and co-supervisor, Prof. Eric W. Gill, for their invaluable guidance, encouragement, and insights throughout this research. I also thank Dr. Fariba Mohammadimanesh for her valuable suggestions and feedback. Their expert advice and thoughtful contributions have been instrumental in shaping the direction and depth of this thesis.

Financial support from the Government of Canada, through the Natural Sciences and Engineering Research Council of Canada (NSERC) under Grant Nos. RGPIN-2022-04766 and RGPIN-2020-05003, is acknowledged. The funding provided made the pursuit of this research possible.

Special thanks to the Canadian Space Agency (CSA) for supplying RADARSAT Constellation Mission (RCM) data, which was critical in advancing this study. I would like to extend my sincere thanks to the European Space Agency for providing open-access Sentinel-1 and Sentinel-2 data, as well as to NASA for the GEDI LiDAR data, all of which significantly contributed to the data analysis conducted in this research.

Field data collected and provided by Ducks Unlimited Canada, the Government of Newfoundland and Labrador's Department of Environment and Conservation, Nature Conservancy Canada, and the Canadian Department of Environment and Local Government were essential in validating and enriching the findings of this work. I sincerely thank them for their valuable contributions.

Finally, I deeply appreciate my parents for their constant support and encouragement, which have been a steady source of strength and motivation throughout this journey. Their belief in me has been invaluable.

# Table of contents

**Title page** i

**Abstract** ii

**Acknowledgements** vi

**Table of contents** vii

**List of tables** xiii

**List of figures** xv

**List of symbols** xxi

**List of abbreviations** xxiii

**1 Introduction** 1

1.1 Overview . . . . . 1

1.2 Background . . . . . 2

1.3 Research Motivations . . . . . 6

1.4 Scope and Objectives . . . . . 7

1.5 Contributions and Novelty . . . . . 8

1.5.1 Remote Sensing and AI for Wetland Studies . . . . . 9

1.5.2 A Novel Multimodel Framework for Wetland Classification . . . 9
1.5.3 Wetland Mapping Using RCM CP-SAR Data and DL . . . . . 10
1.5.4 Wetland Characterization Using RCM CP-SAR Data . . . . . 10
1.5.5 Advancing Wetland Mapping with Multi-Source Data Integration 11
1.6 Organization of this Doctoral Dissertation . . . . . 11
1.7 Other Publications . . . . . 12
1.8 References . . . . . 13

**2 Remote Sensing and Artificial Intelligence for Wetland Studies 22**
2.1 Preface . . . . . 22
2.2 Abstract . . . . . 22
2.3 Introduction . . . . . 23
2.4 Methods . . . . . 28
2.4.1 Bibliographic Base and Search Query Definition . . . . . 28
2.4.2 Extracted Attributes from the Screened Records . . . . . 29
2.5 Results and Discussion . . . . . 30
2.5.1 General Characteristics of Wetland Publications . . . . . 31
2.5.2 Study Focus and Applications . . . . . 36
2.5.3 Case Study Analysis . . . . . 40
2.5.4 RS Data Used in Wetland Studies . . . . . 41
2.5.5 Methodology Analysis . . . . . 47
2.5.6 Feature Selection and Derivation . . . . . 54
2.5.7 Accuracy Assessment . . . . . 54
2.5.8 Preprocessing and Processing Tools . . . . . 57
2.6 Future Perspective . . . . . 57
2.7 Conclusions . . . . . 61

2.8 Future Directions & Recommendations . . . 63
2.9 References . . . 65

**3 A Novel Multimodel Framework for Wetland Classification 88**
3.1 Preface . . . 88
3.2 Abstract . . . 88
3.3 Introduction . . . 89
3.4 Related Work . . . 94
3.5 Proposed Methodology . . . 97
3.5.1 Mini-GCN-Based Branch . . . 97
3.5.2 CNN-Based Branch . . . 98
3.5.3 Feature Fusion . . . 99
3.6 Results . . . 101
3.6.1 Study Site . . . 101
3.6.2 Datasets . . . 101
3.6.3 Experimental Setup . . . 104
3.6.4 Classification Maps . . . 105
3.6.5 Accuracy Assessment . . . 107
3.6.6 Computation Run-Time . . . 109
3.7 Discussion . . . 110
3.8 Conclusion . . . 111
3.9 Future Directions & Recommendations . . . 112
3.10 References . . . 113

**4 Wetland Classification Using CP-SAR & DL 121**
4.1 Preface . . . 121
4.2 Abstract . . . 121

4.3 Introduction . . . 122
4.4 The $m$-$\delta$ and $m$-$\chi$ Decompositions Review . . . 124
4.5 Study Area and Dataset . . . 126
4.5.1 Study Area . . . 126
4.5.2 Satellite Imagery and Pre-processing . . . 126
4.5.3 Reference Data and Sample Patches Partitioning . . . 128
4.6 Methodology and Experimental Design . . . 129
4.6.1 Proposed Method . . . 129
4.6.2 Classification and Output . . . 134
4.7 Conclusion . . . 136
4.8 Future Directions & Recommendations . . . 137
4.9 References . . . 138

**5 Wetland Characterization Using Compact Polarimetric SAR Data 141**

5.1 Preface . . . 141
5.2 Abstract . . . 142
5.3 Introduction . . . 142
5.4 Methodology . . . 147
5.4.1 Compact-polarimetric Signature (CPS) . . . 148
5.4.2 Three Scattering Power Components . . . 151
5.5 Study Area and Dataset . . . 155
5.5.1 Study Site . . . 155
5.5.2 RCM Time-series Data Acquisition . . . 156
5.5.3 Pre-processing of RCM Data . . . 156
5.5.4 Reference Data . . . 157
5.6 Results and Discussion . . . 159

5.6.1 Ecological Characteristics and Dynamics of Wetlands . . . . . 159
5.6.2 Analysis of CPS over Wetlands . . . . . 163
5.6.3 Analysis of the Scattering Power Components over Wetlands . . 166
5.6.4 Classification of Wetlands . . . . . 169
5.7 Conclusion . . . . . 171
5.8 Future Directions & Recommendations . . . . . 173
5.9 References . . . . . 174

**6 Advancing Wetland Mapping with Multi-Source Data Integration 180**
6.1 Preface . . . . . 180
6.2 Abstract . . . . . 180
6.3 Introduction . . . . . 182
6.4 Study Sites and Datasets . . . . . 185
6.4.1 Study Sites . . . . . 185
6.4.2 Reference Data Repository . . . . . 187
6.4.3 Multi-Source/Multi-Sensor Data Collection on GEE and Pre-Processing . . . . . 188
6.5 Methods . . . . . 192
6.5.1 Methodology Overview . . . . . 192
6.5.2 Vegetation Canopy Height (VCH) Model . . . . . 194
6.5.3 Wetland Cover Classification . . . . . 196
6.5.4 Accuracy Assessment . . . . . 196
6.6 Experimental Results . . . . . 197
6.6.1 VCH Maps and Validation . . . . . 197
6.6.2 Wetland Classification Map and Validation . . . . . 201
6.7 Discussion . . . . . 205
6.7.1 Leveraging GEDI Data for Large-Scale VCH Mapping . . . . . 205

6.7.2 Leveraging VCH Data Across Environmental Domains . . . . . 206
6.8 Conclusions . . . . . 207
6.9 References . . . . . 207

**7 Summary, Conclusions, and Future Outlook** **215**

7.1 Summary . . . . . 215
7.2 Conclusions . . . . . 217
7.3 Future Outlook . . . . . 218
7.3.1 Wetland Mapping Benchmark Dataset . . . . . 218
7.3.2 Wetlands in Tidal Zones . . . . . 219
7.3.3 Toward Physics-Informed AI for Wetland Mapping . . . . . 219

# List of tables

1.1 Organization of the thesis. . . . . 12

2.1 List and a brief summary of previous reviews related to the topic. The list was sorted by publication date (the number of citations is reported by 30 June 2022 on the WoS database). . . . . 26

2.2 A listing of extracted sub-fields/attributes considered for the content analysis of included papers. . . . . 31

2.3 List of highly cited papers in the database, ranked by the total number of citations (as of 30 June 2022). . . . . 36

2.4 Overview of study site locations grouped by countries coupled with various scales of the study site's extent. Sites with four or more studies were included. . . . . 40

2.5 List of the commonly used optical satellites in wetland studies ranked by the number of times they have been utilized in the papers. . . . . 46

2.6 List of the commonly used SAR satellites in wetland studies, ranked by the number of times they have been utilized in the papers. . . . . 46

2.7 List of included papers in the meta-analysis that applied GEE in wetland studies sorted by publication date. . . . . 53

2.8 Common features extracted from Optical and SAR imagery in wetland studies. . . . . 55

3.1 The mini-GCN configuration of the proposed Wet-GC framework. . . . 98

3.2 CNN configuration of the proposed Wet-GC framework. . . . . 99

3.3 The bands/features extracted from S1 & S2 imagery in this study. . . . 102
3.4 The number of selected training, validation, and testing pixels of wetland classes in the study area. . . . . 104
3.5 Implementation details for RF, SVM, and XGB classifiers. . . . . 105
3.6 Implementation details for the Wet-GC model. . . . . 105
3.7 Accuracy assessment metrics. . . . . 108
3.8 The accuracy assessment indices of employed approaches in this study. 108
3.9 Approximate execution time of the classification models. . . . . 110

4.1 The characteristics of RCM images utilized in this study. . . . . 128

5.1 Characteristics OF RCM Time-series images used in this study . . . . . 156
5.2 Number of Reference Wetland and Non-Wetland Ground-Truth Polygons. 159
5.3 CPS Responses of Bog, Fen, And Marsh Wetlands for Some Specific Ellipticity ($\chi$) and Orientation ($\psi$) Angles. . . . . 161

6.1 Study sites and the geological characteristics. . . . . 187
6.2 Number of reference ground-truth polygons for each land cover class. . 188
6.3 Partitioning of GEDI Waveforms (N) into training and validation sets. 190
6.4 List of predictors used for VCH prediction and wetland cover classification in this study. . . . . 193
6.5 Validation results for RF and CART models. . . . . 204

# List of figures

1.1 Wetland classification system used in this study. Class definitions and pictures are derived from the Canadian Wetland Classification System [23]. . . . . 3

2.1 A conceptual overview of the use of ML and RS tools to derive productions. . . . . 27

2.2 The predefined search query and list of keywords to prepare the procurements of this meta-analysis. . . . . 29

2.3 Paper selection and the review process flow diagram. A total of 528 papers were found in our primary search in the WoS database. . . . . 30

2.4 Temporal distribution and the total number of reviewed papers per year, and publication trends from three top publishing countries. . . . . 32

2.5 Word cloud shows the most frequent terms in wetland studies. The larger the text, the more frequently the word appeared in considered papers. . . . . 33

2.6 The number of journal and conference publications included in the meta-analysis. . . . . 33

2.7 An overview of (a) the journals included in this meta-analysis and the number of papers per journal. (b) A listing of the leading publishers and the number of papers per publisher. . . . . 34

2.8 Country and continent-based overview of first author affiliations. Among the continents, Asia (with 42%), America (with 40%), and Europe (with 13%) hold the largest shares, and among countries, China (with 35%), the USA (with 21%), and Canada (with 17%) hold the largest shares. . . . . 35

2.9 Overview of the diversity of application domains of RS Earth observations in wetland areas. . . . . 37

2.10 Frequency of short-term and long-term CD. . . . . 39

2.11 Distribution of employed data types and their combinations with the largest shares for multispectral and hyperspectral (46%), SAR (20%), and LiDAR/DEM (10%) data types. . . . . 41

2.12 Frequency of single- and multi-source RS data usage in wetland studies. 44

2.13 Frequency of high-resolution, medium-resolution, and coarse-resolution images used in wetland studies. . . . . 47

2.14 Frequency of single- and multi-date RS data usage in wetland studies. . 48

2.15 (a) Frequency of ML algorithms in wetland studies with (b) percentage of supervised and unsupervised approaches. . . . . 49

2.16 Number of studies employed different ML models in wetland studies. . 51

2.17 (a) Frequency of each type of wetland study using GEE. (b) Frequency of GEE-based wetland studies per year. . . . . 52

2.18 Percentage of studies that use each type of feature category. Note that as almost all studies have used either optical or SAR imagery features, the category of imagery features was excluded here. . . . . 56

2.19 (a) The histogram of the overall accuracies reported in wetland classification papers. Box-and-whisker plots displaying the overall accuracies reported in RS-based wetland classification studies according to the (b) study extent, (c) utilized data type, (d) type of employed ML algorithm, (e) supervised or unsupervised models, (f) pixel-based or object-based methods, and (g) selected image resolution. . . . . 58

2.20 The main tools used for data preprocessing and processing in wetland studies. The larger the text, the more frequently the tool used in papers. 59

2.21 General overview of key recommendations for future studies to combat the challenges of wetland monitoring. . . . . 60

3.1 General flowchart of the proposed Wet-GC model. The feature extraction module extracts different features by using both CNNs and GCNs. The feature fusion module concatenates the resulting features as the final classification input. . . . . 97

3.2 (a) Location of the study site in Newfoundland province, Canada. (b) Grayscale VH band illustration of S1 imagery. (c) RGB illustration of S2 imagery. . . . . 101

3.3 Snapshot of (a) a portion of the study area in which the reference training samples were selected. (b) Reference wetland and non-wetland data collected in the study area . . . . . 103

3.4 Resulting classification maps for different methods. (a) RF. (b) SVM. (c) XGB. (d) ResNet50. (e) GCN-branch. (f) CNN-branch. (g) Wet-GC. 106

3.5 Zoomed-in representation of a small portion of the classification maps obtained by (a) RF, (b) SVM, (c) XGB, (d) ResNet50, (e) GCN-branch, (f) CNN-branch, and (g) Wet-GC. . . . . 107

3.6 Confusion matrices summarizing the accuracy of results based on the evaluation of different algorithms. (a) RF. (b) SVM. (c) XGB. (d) ResNet50. (e) GCN-branch. (f) CNN-branch. (g) Wet-GC. Each entry of the confusion matrices is shown as a percentage calculated from the total number of entries in each column. . . . . 109

4.1 Study area with coverage of a portion of two RCM images. . . . . 127

4.2 Preparation of training sample patches used in this study. . . . . 128

4.3 Evaluating the effect of different image patch sizes on the accuracy of DL models. . . . . 130

4.4 Illustration of the proposed model architecture. . . . . 131

4.5 Comparative analysis of classification accuracy across employed DL models. . . . . 136

4.6 Classification results for Location 1: (a) ResNet50, (b) DenseNet121, (c) InceptionResNetV2, and (d) Ours. Classification results for Location 2: (e) ResNet50, (f) DenseNet121, (g) InceptionResNetV2, and (h) Ours. . . . . 137

5.1 Flow diagram depicting the processing steps for analyzing wetland signatures based on RCM datasets. The process involves three major steps: (1) pre-processing of SAR datasets, (2) the proposed method, which explores wetlands CPS through multi-date basis analyses, along with introducing $\mu - \chi$ decomposition power, and (3) wetland classification. . . . . 147

5.2 A representation of decomposition of the total power ($g_0$) using the Raney decomposition and the proposed method. . . . . 152

5.3 The values of $m$ and $\mu$ for a mixture of pure target and random volume (ideal depolarizer) target. $q$ represents the mixture proportion. The target is pure for $q = 0$, while for $q = 1$, it becomes a complete depolarizer. 152

5.4 A close-up view of the study area located within the province of New Brunswick, Canada. . . . . 155

5.5 The ground-truth data for three wetland classes in the study area, including fen, bog, and marsh. . . . . 158

5.6 Temporal variation of CPS for the bog class, showing changes in received power over time: (a) 26 May, (b) 07 June, (c) 17 July, (d) 14 August, and (e) 23 September. Contours represent the received power, with brighter (yellow) colors indicating higher received power levels. . . 164

5.7 Temporal variation of CPS for the fen class, showing changes in received power over time: (a) 26 May, (b) 07 June, (c) 17 July, (d) 14 August, and (e) 23 September. Contours represent the received power, with brighter (yellow) colors indicating higher received power levels. . . . . 165

5.8 Temporal variation of CPS for the marsh class, showing changes in received power over time: (a) 26 May, (b) 07 June, (c) 17 July, (d) 14 August, and (e) 23 September. Contours represent the received power, with brighter (yellow) colors indicating higher received power levels. . . 165

5.9 Values of $\mu$ for three wetland classes (bog, fen, and marsh) in CP mode. 166

5.10 Scattering powers (%) computed over wetlands using (a) $\mu - \chi$ and (b) $m - \chi$ decomposition technique. . . . . 167

5.11 (a) The RGB representation of scattering power components extracted from $\mu - \chi$ technique in the vegetation peak using RCM image acquired on 14 August. (b) The zoomed-in areas highlight the variations in scattering powers among different wetland types. . . . . 169

5.12 The classification maps obtained via time-series of scattering power components extracted using (a) the proposed $\mu - \chi$ decomposition and (c) the $m - \chi$ decomposition along with the corresponding confusion matrices (b) and (d), respectively. . . . . 171

6.1 (**a**) An overview of the Island of Newfoundland and pilot sites; (**b**) a representation of collected field data in St. John's area. . . . . 186

6.2 A visual example of the distribution of GEDI RH95 points on GEE in the St. John's site. . . . . 190

6.3 A representation of the approach developed for VCH and wetland mapping utilizing multi-source and multi-sensor remote sensing data. . . . . 194

6.4 VCH maps for the year 2021 were produced through the integration of GEDI data (June–September 2021) and multi-source EO datasets for (**a**) St. John's, (**b**) Grand Falls-Windsor, (**c**) Deer Lake, and (**d**) Gros Morne. . . . . 199

6.5 The correlation between the generated VCH and GEDI validation data for the four pilot sites in the study area: (**a**) St. John's, (**b**) Grand Falls-Windsor, (**c**) Deer Lake, and (**d**) Gros Morne. The figures show the scatter plots of the generated VCH data against the GEDI validation data for each of the four pilot sites. Each plot includes individual data points (dots) and a best-fit line (solid red line) between the two datasets. 200

6.6 The correlation between the GEDI RH95 observations and GEDI-V27 in wetland areas using the same validation samples of our methodology: (**a**) St. John's, (**b**) Grand Falls-Windsor, (**c**) Deer Lake, and (**d**) Gros Morne. The figures show the scatter plots of the GEDI-V27 canopy height data against the GEDI validation data for each of the four pilot sites. Each plot includes individual data points (dots) and a best-fit line (solid red line) between the two datasets. . . . . 202

6.7 Wetland classification maps for the year 2021 were produced through the integration of VCH and metrics/features derived from multi-source EO datasets for (**a**) St. John's, (**b**) Grand Falls-Windsor, (**c**) Deer Lake, and (**d**) Gros Morne. . . . . 203

6.8 (**a**) The normalized importance of factors used in the wetland classification process of pilot sites, (**b**) the average value of the variables' importance. . . . . 204

# List of symbols

| | | |
|---|---|---|
| $\mathcal{V}$ | Vertices | 95 |
| $\mathcal{E}$ | Edges | 95 |
| $\mathcal{G} = (\mathcal{V}, \mathcal{E})$ | Graph | 95 |
| $A_{ij}$ | Adjacency matrix | 95 |
| $L$ | Laplacian matrix | 95 |
| $L_{\text{sym}}$ | Symmetric normalized Laplacian matrix | 95 |
| $\Lambda$ | Diagonal matrix of $L$'s eigenvalues | 96 |
| $\mathcal{F}$ | Fourier transform | 96 |
| $\mathcal{S}$ | $S$-th subgraph | 98 |
| $g_t$ | Polarization state of transmitting antenna | 148 |
| $g_r$ | Polarization state of receiving antenna | 148 |
| $K$ | Kennaugh matrix | 148 |
| $P$ | Received power | 148 |
| $\chi$ | Ellipticity angle | 148 |
| $\psi$ | Orientation angle | 148 |
| $E$ | Jones vector | 149 |
| $\mathbf{S}$ | Complex scattering matrix | 149 |
| $C_2$ | Covariance matrix | 150 |
| $P_{\text{max}}$ | Maximum received power | 151 |
| $P_{\text{min}}$ | Minimum received power | 151 |
| $m$ | Degree of polarization | 151 |
| $g_0$ | Total power | 152 |
| $P_v$ | Random Scattering (unmatched power) | 142 |
| $P_s$ | Odd-bounce Scattering (matched power) | 142 |
| $P_d$ | Even-bounce Scattering (matched power) | 142 |
| $\mu$ | Purity parameter | 142 |
| $L$ | Left-handed circular polarization | 149 |
| $R$ | Right-handed circular polarization | 149 |
| $H$ | Linear horizontal polarized component | 149 |
| $V$ | Linear vertical polarized component | 149 |
| DoC | Degree of Circularity | 153 |

| | | |
|---|---|---|
| $\sigma^0$ | Backscattering coefficient | 156 |
| dB | Decibels | 156 |

# List of abbreviations

| | | |
|---|---|---|
| AI | Artificial Intelligence | 7 |
| BP | Backpropagation | 48 |
| CNN | Convolutional Neural Network | 9 |
| CD | Change Detection | 28 |
| CP | Compact Polarimetry | 10 |
| CPS | Compact Polarimetric Signature | 10 |
| CSA | Canadian Space Agency | 61 |
| CWCS | Canadian Wetland Classification System | 2 |
| DEM | Digital Elevation Model | 191 |
| DL | Deep Learning | 8 |
| DT | Decision Tree | 48 |
| EBV | Essential Biodiversity Variable | 182 |
| EO | Earth Observation | 3 |
| ERA5 | European ReAnalysis | 181 |
| ESA | European Space Agency | 3 |
| FC | Fully Connected | 98 |
| FP | Full Polarimetry | 144 |
| FP | False Positive | 108 |
| FN | False Negative | 108 |
| FPS | Full-polarimetric Signature | 150 |
| GEDI | Global Ecosystem Dynamics Investigation | 11 |
| GEE | Google Earth Engine | 11 |
| GRD | Ground Range Detected | 101 |
| GT | Ground Truth | 101 |
| HH | Horizontal transmit and Horizontal receive | 55 |
| HV | Horizontal transmit and Vertical receive | 55 |
| KNN | K-Nearest Neighbors | 48 |
| LiDAR | Light Detection and Ranging | 7 |
| MAE | Mean Absolute Error | 181 |
| MERIT | Multi-Error-Removed Improved-Terrain | 181 |
| ML | Machine Learning | 6 |

| | | |
|---|---|---|
| NIR | Near-Infrared | 102 |
| OA | Overall Accuracy | 89 |
| PS | Polarimetric Signature | 146 |
| RCM | RADARSAT Constellation Mission | 5 |
| RELU | Rectified Linear Unit | 98 |
| RBF | Radial Basis Function | 95 |
| RF | Random Forest | 48 |
| RH | Relative Height | 189 |
| RMSE | Root Mean Squared Error | 181 |
| RS | Remote Sensing | 3 |
| S1 | Sentinel-1 | 89 |
| S2 | Sentinel-2 | 89 |
| SAR | Synthetic Aperture Radar | 5 |
| SLC | Single Look Complex | 156 |
| SNR | Signal-to-Noise Ratio | 189 |
| SRTM | Shuttle Radar Topography Mission | 192 |
| SVM | Support Vector Machine | 48 |
| TN | True Negative | 108 |
| TP | True Positive | 108 |
| VCH | Vegetation Canopy Height | 181 |
| VH | Vertical transmit and Horizontal receive | 55 |
| VV | Vertical transmit and Vertical receive | 55 |
| WoS | Web of Science | 28 |
| XGBoost | Extreme Gradient Boosting | 48 |

# Chapter 1

# Introduction

## 1.1 Overview

Wetlands can be defined simply as areas inundated or saturated by water for at least part of the year [1, 2], although this definition will vary widely depending on the field of study. They occupy transition zones between aquatic and terrestrial environments and share the characteristics of both zones [3, 4]. Wetlands are amongst the most valuable and productive resources on Earth and are critically linked to many ecological services, including global climate regulation, carbon sequestration [5], natural water purification [6], flood and drought amelioration [7], shoreline erosion protection, soil conservation [2], space for recreation and aesthetic appreciation, and habitat for wildlife [8, 9], and other critical services. Playing an important role in providing essential ecosystem services, wetlands are among the ecosystems most sensitive to environmental changes.

Wetlands and the services they provide are under the direct and indirect influences of anthropogenic activity [10, 11], which can and do result in increased rates of wetland change and loss [12]. Since the beginning of the 20th century, about two-thirds of the world's wetlands have been lost or severely altered [13]. This loss has not only resulted in a decrease in total global wetland coverage but has influenced the provision of valuable wetland services to humans and non-humans alike [14]. In Canada, historical causes of wetland loss included land-use change due to European settlement, development and agriculture, and associated bi-products such as re-direction

of run-off and pollution [15].

In recent times, climate change has emerged as a major environmental challenge with the potential to amplify ongoing wetland loss and change [16, 17]. The current and predicted impacts of a warming climate on wetlands have been extensively reported, including in Canada. These reports demonstrate the potential of climate change to increase fire incidents and impact the ability of wetlands and surrounding habitats to recover from natural disasters [18] and permafrost melt, and shifts in vegetation composition [19, 20], among others. In turn, these impacts will alter the ability of wetlands to provide ecosystem services. Such impacts highlight the need for efficient and timely adaptation to climate change. This need may be addressed in part through the implementation of accurate methods for the estimation of past and future changes to wetlands [21, 9]. Given these challenges, there is a pressing need for advanced methodologies that can accurately characterize wetland dynamics and inform adaptive management strategies. As such, understanding the distribution of wetland-cover types and sites is crucial to ensuring sustainable management and assessment of resource use [22].

The Canadian Wetland Classification System (CWCS) categorizes wetlands into five distinct classes within the vegetated wetland category: bog, fen, marsh, swamp, and shallow open water. Each class is defined based on specific hydrological, ecological, and vegetative characteristics, reflecting the diversity of wetland ecosystems. These classifications provide a foundational framework for understanding the structure and function of wetlands, as well as their ecological significance. Figure 1.1 illustrates the definitions and distinguishing features of each wetland class. This classification serves as a critical tool for researchers, policymakers, and conservationists aiming to manage and protect wetland habitats effectively.

## 1.2 Background

As a prelude to targeting wetland conservation efforts, the thematic information on land-use and land-cover (LULC) of wetlands and regional-scale inventories needs to be obtained and updated. Given the vast extent and diverse nature of wetlands, conventional field surveys and aerial photographs for mapping and monitoring wetlands are laborious, time- and cost-intensive, and are limited by either spatial or temporal

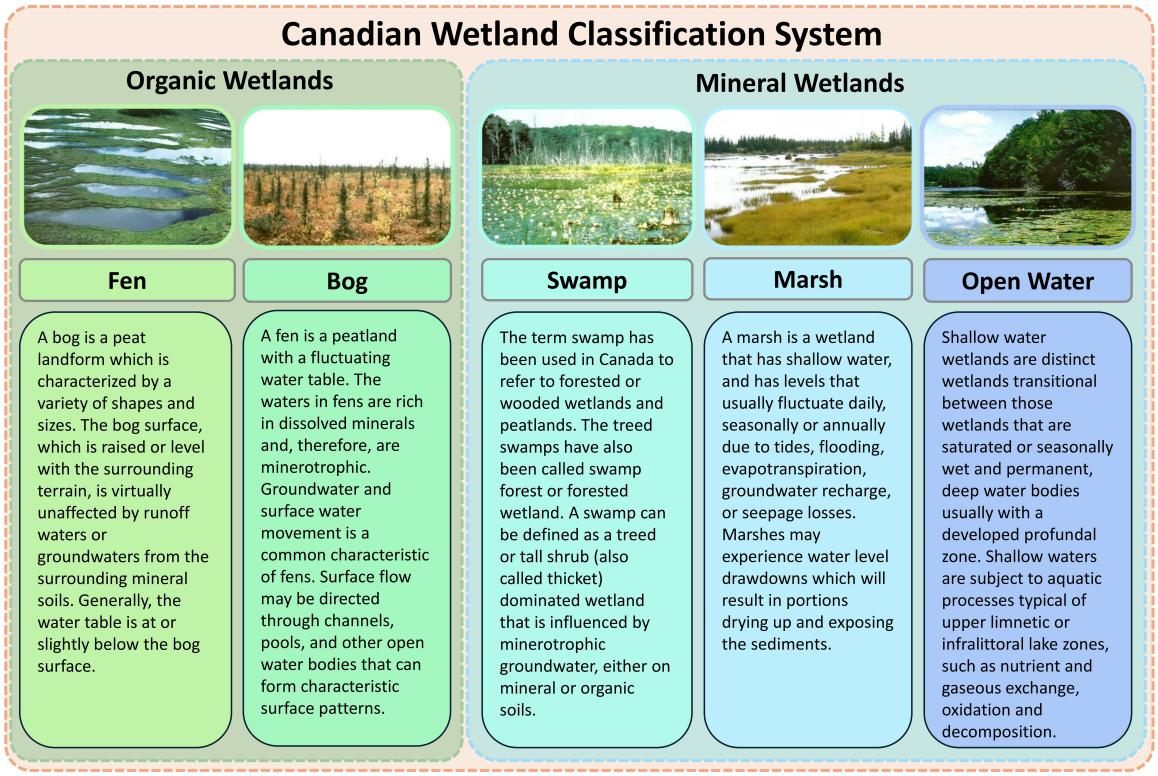



Figure 1.1: Wetland classification system used in this study. Class definitions and pictures are derived from the Canadian Wetland Classification System [23].

coverage, specifically for large-scale applications [24]. Moreover, these methods can be error-prone, especially when dealing with inaccessible wetland areas [25]. Remote sensing (RS) technology, which is large-scale, integrated, and rapid, is available for timely investigations of wetlands [26]. Although RS may have limitations, it also possesses several features that make it suitable for wetland mapping and monitoring. For example, RS is both cost and time effective because it minimizes the need for site visits, covers large geographical areas, and is capable of collecting data from inaccessible locations. Moreover, wetland maps resulting from RS imagery can be regularly updated based on the temporal frequency of the images used for classification.

The increasing availability of satellite imagery for Earth Observation (EO) has significantly advanced environmental monitoring and research. Government initiatives, such as the European Space Agency's (ESA) Copernicus program and NASA's EO missions, have been instrumental in providing free and continuous access to EO data. This accessibility enables researchers, scientists, and technology experts to address critical environmental challenges, including wetland mapping and monitoring, with

greater precision and scale.

Despite these advancements, challenges remain in utilizing specific RS data. The high discrimination capabilities demonstrated through the usage of high spatial and spectral resolution satellite imagery, such as Quickbird, Worldview, GeoEye, and GF-5, and unmanned aerial vehicles (UAVs), are balanced in turn by their limitation of time, scale, cost, and availability; thus, their widespread use is not practical in wetland monitoring applications [27, 28, 29]. Additionally, the professional wetland data are either not freely shared, or the accuracy is uncertain at the local scale. In contrast, open-access multispectral and long time-series RS imagery at medium spatial resolution, such as the Landsat series and Sentinel-2, are powerful alternatives [30]. These sensors have recently been widely used in the characterization of wetland ecosystems since they have a high temporal depth of the archive with different spatial and spectral resolutions according to different requirements and are freely available [30]. However, high similarity in the spectral signatures of various vegetation species leads to low accuracy for vegetation classification based on a single image, even at the community level.

To address these limitations, the field of RS image scene classification has emerged as a pivotal research area. With its ability to interpret remotely sensed images effectively, scene classification aims to assign predefined semantic labels to image scenes based on their content [31]. Given its potential to enhance land cover mapping and tackle complex challenges in wetland monitoring, this capability has drawn significant attention in recent years, [32]. Building on this foundation, extensive research over the past decades has been conducted on developing various RS image scene classification methods. This has been motivated by its large real-world application domain: urban planning [33], agriculture, natural hazards detection [34, 35], climate change, LULC determination, geospatial object detection [36], vegetation mapping [37], environmental monitoring [2, 38, 39], among others. To begin with, the processing and transformation of satellite images into structured semantics are essential to fully utilizing the data for these practical domains [40].

Wetlands are the most challenging natural landscape features to map and monitor due to their complicated morphology, i.e., heterogeneous and fragmented landscapes ranging from sparse vegetation to thickly wooded areas [41]. For a long time, wetland mapping has been carried out with optical RS data, but the level of accuracy varies

over time and space based on the complexity of wetlands. The process of wetland classification is complicated by the rapid and frequent changes in plant coverage type, distribution, and density caused by vegetation cover dynamics with water fluctuation [42, 43]. The complexity of this process is further increased by the need for frequent data collection, as well as high spectral and spatial resolution imagery.

The variability within wetlands further complicates the classification process. On the one hand, the spectral characteristics of some wetland covers, such as bog and fen, differ slightly. So, in some cases, it is difficult to discern the differences between these similar wetland-cover types. On the other hand, there is great spectral heterogeneity between wetlands of the same type due to variations in water volume, salt content, vegetation density, and illumination conditions [44, 45]. Thus, wetlands present some of the most challenging classification problems because of their high within-class variability and low between-class disparity. While the current ML-based classification models in literature have been shown to be somewhat effective in classifying wetlands, they still tend to misjudge similar wetland surfaces.

Owing to its weather-, illumination-, and time-independent characteristics, Synthetic Aperture Radar (SAR) data has been extensively used in the context of wetland type identification, yield estimation [46, 47], and biophysical parameter calculation [48, 49], as well as vegetation indices formulation [50]. SAR components, particularly the acquisition wavelength, polarization, and incidence angle, strongly affect the reflected signals from the target [51, 52]. As a result, the collected backscattering SAR signals influenced by vegetation and soil properties carry information related to wetlands and the soil's geometric structure and dielectric properties.

With respect to SAR imagery, the RADARSAT Constellation Mission (RCM) imagery offers great wetland characterization and mapping opportunities. The RCM was designed as the next generation of the Canadian RADARSAT program, following the highly successful RADARSAT-1 and RADARSAT-2 missions. This constellation configuration comprised three identical C-band SAR satellites launched in the summer of 2019 into closely coordinated orbits, providing a four-day repeat cycle [53, 54]. With RCM datasets, the potential of CP emerged as a viable mode to address the needs of users seeking wide swath coverage while preserving polarization richness [55]. In addition to its technical capabilities, the RCM offers a more cost-effective approach to satellite deployment compared to its predecessors, thanks to its advanced yet more

affordable architecture and components. This makes it an attractive option for large-scale, repeated RS applications such as wetland monitoring and classification.

The integration of SAR data, particularly from the RCM, with machine learning (ML) and advanced classification techniques, offers a promising pathway for more accurate and scalable wetland mapping and characterization. This integration can overcome the limitations of traditional optical methods, addressing the challenges posed by complex wetland dynamics and spectral variability. As we continue to refine these technologies and approaches, the potential to monitor wetlands with high accuracy and at larger scales becomes increasingly feasible, offering useful information into the state of these critical ecosystems.

## 1.3 Research Motivations

Canada, the United States, and Mexico collectively host the majority of wetland areas on the North American continent [56]. Canada is rich in biological resources and contains about 1.29 million $km^2$ of wetlands, covering 13% of Canada's terrestrial area [57]. This is close to one-quarter of the world's remaining wetlands. A wide variety of wetland habitats exist in Canada, from permanently inundated to seasonally flooded wetlands, and from coastal saline water to freshwater wetlands [56]. The temperate regions of North America, including southern Canada and most of the United States, contain many types of wetlands, such as bogs, fens, marshes, and forested swamps [58]. Nevertheless, wetlands are among the most threatened ecosystems on Earth, experiencing declines in the area or even disappearance [59, 60, 61]. Even though natural phenomena such as tides and storms threaten the wetlands, continuous human interference in wetland regimes, resulting in their conversion into agricultural fields or built-up lands, poses a most significant threat to wetland ecology and habitat [62, 63]. Indeed, the rapid pace of economic development and population growth have led to significant loss of wetlands in many countries worldwide over the past decades [64]. Therefore, wetlands must be protected, and accurate characterization and land cover mapping are essential to scientific management and sustainable development [65, 66]. Advancements in RS technologies and access to multi-source data have made it possible to monitor these ecosystems with unprecedented detail.

Fortunately, wetland monitoring and studies have garnered great interest among researchers, and significant progress has been achieved in this area recently.

## 1.4 Scope and Objectives

The motivation for conducting this research is to enhance wetland characterization and mapping methodologies in Canada by using multi-source and advanced RS data, in combination with cutting-edge artificial intelligence (AI) models. The focus is on improving the accuracy and efficiency of wetland mapping methodologies to better monitor and analyze these ecosystems. By integrating multiple data sources, such as optical & SAR imagery, Light Detection and Ranging (LiDAR) data, and other EO datasets, this work addresses key limitations in wetland classification, particularly for wetland classes with similar backscattering or spectral signatures.

A core aspect of this research is its pioneering use of RCM imagery and exploiting the advantages offered by compact polarimetry (CP). In line with this, an innovative component of this thesis is the development and application of a novel decomposition technique and SAR signature descriptor, aimed at enhancing wetland class differentiation using CP-SAR data. What makes these CP-SAR-based novel approaches more interesting is their ability to capture and analyze multi-date RCM data sequentially. This allows for a more thorough investigation of the backscattering characteristics of different wetland classes, enabling a deeper assessment of wetland phenology and dynamics. In contrast to conventional methods that typically analyze single-date datasets independently, this time-series approach captures temporal variations in backscatter and reflectance, leading to more accurate and reliable wetland class discrimination.

The research contribution of this thesis is comprised of five chapters, with the main objectives being:

i) **Review of RS and AI Techniques for Wetland Studies:** To present an extensive literature review on the application of RS, machine learning, and AI in wetland monitoring and mapping, providing a foundation for understanding current methodologies and identifying gaps (Chapter 1).

ii) **Developing a Multimodel AI Framework for Classification with Limited Training Samples:** To propose a new deep learning (DL) based multimodel classification approach that can operate effectively with limited ground-truth data, addressing challenges in data scarcity for wetland mapping (Chapter 2).

iii) **Exploring Wetland Mapping using DL and CP-SAR Features:** To design a DL model utilizing CP-SAR-derived features for wetland class mapping (Chapter 3).

iv) **Advancing Wetland Characterization with CP-SAR Data:** To investigate the role of CP-SAR data in wetland classification, specifically from the RCM imagery, by exploring and implementing a novel SAR decomposition technique and time-series signature analysis (Chapter 4).

v) **Assessing Wetland Canopy Height Using Multi-source Data Integration :** To create a multisource data framework that incorporates EO datasets to accurately estimate wetland canopy height, which is essential for ecosystem assessment and monitoring (Chapter 5).

Together, the approaches developed and introduced in this study form a cohesive framework for wetland mapping and characterization, applicable across all Canadian provinces. Moreover, these approaches have the potential to be extended to other wetland-rich regions with similar ecological characteristics globally, enabling broader applications in ecologically comparable areas.

## 1.5 Contributions and Novelty

This section outlines the original contributions and unique aspects of this doctoral dissertation, highlighting its impact on advancing methodologies for accurate mapping and characterizing complex wetland ecosystems. Below is a summary of the primary methodological advancements and innovations introduced in this PhD thesis, with comprehensive details provided in the respective chapters of this study.

### 1.5.1 Remote Sensing and AI for Wetland Studies

As a foundation for this thesis, an extensive literature review was conducted on wetland mapping using RS data intergrated with AI techniques. This review spans over three decades of published studies, offering a systematic analysis of the types of RS data, ML & DL frameworks, case studies, accuracy assessment methods, and other essential parameters relevant to RS-based wetland research. This review identifies key methodologies and computational tools, presenting a comprehensive survey that highlights trends, gaps, and emerging techniques in the field.

### 1.5.2 A Novel Multimodel Framework for Wetland Classification

Propelled by the fast development of computational technologies and powerful feature learning capabilities of DL models, DL-based wetland classification and mapping achieved significant breakthroughs [30]. The Convolutional Neural Network (CNN) stands as a successful DL adept at analyzing discriminative information hidden in RS images [67].

In light of the recent success of deep CNNs, a significant amount of training data is essential to train such networks [40]. In general, the most significant obstacle hindering the development of ML-based wetland mapping is the lack of suitable training samples, particularly across broad scales [68]. As is often the case in supervised ML, the performance of classification models significantly depends on the availability of high-quality samples with a suitable set of classes [69]. Regardless of the algorithm used, errors can occur due to inappropriate or unrepresentative training samples in the classification process [70, 71]. In parallel, this research introduces a Graph Convolution Network (GCN) based framework to overcome issues related to limited training data - a common constraint in RS applications - and achieve high classification accuracies, which is essential for distinguishing between various wetland types.

### 1.5.3 Wetland Mapping Using RCM CP-SAR Data and DL

The RCM CP-SAR architecture utilizes a circularly polarized signal and coherently records both the horizontal and vertical components (H + V) of the backscattered signal in a circular-transmit and linear-receive (CL) configuration [54]. This is achieved by driving the H and V feeds simultaneously with a 90-degree phase difference [55]. By employing a single transmit polarization, this configuration significantly reduces power requirements compared to Full Polarimetric (FP) modes [72].

Polarimetric decomposition is a critical technique for extracting meaningful parameters from SAR data. It involves separating the received signal into different scattering components, such as surface scattering, double-bounce scattering, and volume scattering. Each component reveals specific physical and structural properties of the target, enabling better characterization of land surfaces. This decomposition is particularly useful to successfully distinguishing between various land cover types, including complex ecosystems like wetlands. It allows researchers to analyze complex scattering behaviors and improve the accuracy of land cover classification. This research specifically focuses on assessing the utility of RCM CP-SAR data for wetland mapping through the application of DL techniques. The integration of CP decomposition with the DL models enhances wetland class discrimination compared to traditional methods.

### 1.5.4 Wetland Characterization Using RCM CP-SAR Data

As a key data source for this research, the RCM and compact polarimetric (CP) data play a crucial role in advancing wetland monitoring. With the continuous advancements in SAR technology, particularly through the regional coverage and high-resolution data provided by RCM, innovative decomposition methodologies and signature analysis techniques are becoming increasingly vital for effective wetland monitoring.

The primary objective of this study is to introduce and explore the compact polarimetric signature (CPS) and assess its potential in enhancing wetland monitoring and characterization using time-series RCM data. Additionally, a secondary scientific objective is to propose a new decomposition technique based on CP-SAR data.

### 1.5.5 Advancing Wetland Mapping with Multi-Source Data Integration

Google Earth Engine (GEE) enables the efficient handling of massive datasets, eliminating the computational challenges often faced in traditional wetland mapping workflows. The platform's extensive data archives and built-in processing capabilities streamline multi-sensor data integration, making the proposed framework scalable and applicable across large geographical regions. This work demonstrates how the unique advantages of GEE, combined with advanced multi-sensor data fusion, can significantly improve the accuracy, efficiency, and accessibility of wetland mapping methodologies.

This study introduces a novel framework for wetland mapping by integrating data from multiple RS platforms, including Sentinel-1, Sentinel-2, and Global Ecosystem Dynamics Investigation (GEDI), within the GEE environment. This multi-sensor approach enables a more comprehensive understanding of wetland ecosystems by incorporating various types of data, such as radar and optical imagery, as well as LiDAR-based vegetation structure information, addressing key limitations in single-sensor approaches. Sentinel-1's radar data offers sensitivity to wetland hydrology and vegetation structure, Sentinel-2's optical imagery captures detailed spectral signatures, and GEDI contributes valuable information on vertical vegetation profiles. By synergizing these datasets, the study enhances the ability to delineate wetlands with greater precision and reliability across diverse landscapes.

## 1.6 Organization of this Doctoral Dissertation

This PhD thesis follows a manuscript-based format, consisting of a series of research studies, as outlined in Table 1.1.

Table 1.1: Organization of the thesis.

| **Chapter Title** | **Paper Title** |
|---|---|
| Chapter 1: Introduction | N/A |
| Chapter 2: Remote Sensing & Artificial Intelligence | *Remote sensing and Machine Learning tools to support wetland monitoring: a meta-analysis of three decades of research.* Remote Sensing, 14(23), p.6104, (2022) |
| Chapter 3: Multi-branch DL Framework for Wetland Classification | *Wet-GC: a novel multimodel graph convolutional approach for wetland classification using Sentinel-1 and 2 imagery with limited training samples.* IEEE Journal of Selected Topics in Applied Earth Observations and Remote Sensing, 15, pp.5303-5316, (2022). |
| Chapter 4: DL & CP-SAR for Wetland Classification | *A compact polarimetry-aware wetland classifier using RCM imagery.* |
| Chapter 5: Wetland Characterization using RCM CP-SAR Data | *Compact-polarimetric SAR signature analysis for wetland characterization using RADARSAT constellation mission.* IEEE Transactions on Geoscience and Remote Sensing, 62, pp. 1-16, (2024). |
| Chapter 6: Multi-source Data for Wetland Classification | *Enhancing Wetland Mapping: Integrating Sentinel-1/2, GEDI Data, and Google Earth Engine.* Sensors, 24(5), p.1651, (2024). |
| Chapter 7: Summary, Conclusions, and Future Outlook | N/A |

## 1.7 Other Publications

In addition to the journal papers mentioned above, the candidate also contributed to the following published peer-reviewed journal articles as the first author during his PhD program.

- **Jafarzadeh, H.**, Verma, A., Mahdianpari, M., Bhattacharya, A. and Homayouni, S., 2024. Enhanced Crop Discrimination and Monitoring Using Compact-Polarimetric SAR Signature Analysis From RADARSAT Constellation Mission. IEEE Journal of Selected Topics in Applied Earth Observations and Remote Sensing, 17, pp.6308-6327.

- **Jafarzadeh, H.**, Mahdianpari, M., Gill, E., Mohammadimanesh, F. and Homayouni, S., 2021. Bagging and boosting ensemble classifiers for classification of multispectral, hyperspectral and PolSAR data: a comparative evaluation. Remote Sensing, 13(21), p.4405.

- **Jafarzadeh, H.**, Mahdianpari, M., Homayouni, S., Mohammadimanesh, F. and Dabboor, M., 2021. Oil spill detection from Synthetic Aperture Radar Earth observations: A meta-analysis and comprehensive review. GIScience & Remote Sensing, 58(7), pp.1022-1051.

## 1.8 References

[1] R. W. Tiner, *Wetland indicators: A guide to wetland formation, identification, delineation, classification, and mapping*. CRC press, 2016.

[2] M. Mahdianpari, H. Jafarzadeh, J. E. Granger, F. Mohammadimanesh, B. Brisco, B. Salehi, S. Homayouni, and Q. Weng, "A large-scale change monitoring of wetlands using time series landsat imagery on google earth engine: a case study in newfoundland," *GIScience & Remote Sensing*, vol. 57, no. 8, pp. 1102–1124, 2020.

[3] S. Gxokwe, T. Dube, and D. Mazvimavi, "Multispectral remote sensing of wetlands in semi-arid and arid areas: a review on applications, challenges and possible future research directions," *Remote Sensing*, vol. 12, no. 24, p. 4190, 2020.

[4] B. Chen, L. Chen, B. Huang, R. Michishita, and B. Xu, "Dynamic monitoring of the poyang lake wetland by integrating landsat and modis observations," *ISPRS Journal of Photogrammetry and Remote Sensing*, vol. 139, pp. 75–87, 2018.

[5] M. Grenier, S. Labrecque, M. Garneau, and A. Tremblay, "Object-based classification of a spot-4 image for mapping wetlands in the context of greenhouse gases emissions: The case of the eastmain region, québec, canada," *Canadian Journal of Remote Sensing*, vol. 34, no. sup2, pp. S398–S413, 2008.

[6] M. Trepel, "Assessing the cost-effectiveness of the water purification function of wetlands for environmental planning," *Ecological Complexity*, vol. 7, no. 3, pp. 320–326, 2010.

[7] R. Touzi, A. Deschamps, and G. Rother, "Wetland characterization using polarimetric radarsat-2 capability," *Canadian Journal of Remote Sensing*, vol. 33, no. sup1, pp. S56–S67, 2007.

[8] R. W. Tiner, M. W. Lang, and V. V. Klemas, "Remote sensing of wetlands: applications and advances," 2015.

[9] T. Xu, B. Weng, D. Yan, K. Wang, X. Li, W. Bi, M. Li, X. Cheng, and Y. Liu, "Wetlands of international importance: Status, threats, and future protection," *International journal of environmental research and public health*, vol. 16, no. 10, p. 1818, 2019.

[10] C. Gibbes, J. Southworth, and E. Keys, "Wetland conservation: change and fragmentation in trinidad's protected areas," *Geoforum*, vol. 40, no. 1, pp. 91–104, 2009.

[11] W. J. Mitsch and J. G. Gosselink, "The value of wetlands: importance of scale and landscape setting," *Ecological economics*, vol. 35, no. 1, pp. 25–33, 2000.

[12] A. D. Syphard and M. W. Garcia, "Human-and beaver-induced wetland changes in the chickahominy river watershed from 1953 to 1994," *Wetlands*, vol. 21, no. 3, pp. 342–353, 2001.

[13] R. Connor, *The United Nations world water development report 2015: water for a sustainable world*, vol. 1. UNESCO publishing, 2015.

[14] R. C. Gardner, S. Barchiesi, C. Beltrame, C. Finlayson, T. Galewski, I. Harrison, M. Paganini, C. Perennou, D. Pritchard, A. Rosenqvist, *et al.*, "State of the world's wetlands and their services to people: a compilation of recent analyses," 2015.

[15] E. Byun, S. A. Finkelstein, S. A. Cowling, and P. Badiou, "Potential carbon loss associated with post-settlement wetland conversion in southern ontario, canada," *Carbon balance and management*, vol. 13, pp. 1–12, 2018.

[16] A. Breeuwer, B. J. Robroek, J. Limpens, M. M. Heijmans, M. G. Schouten, and F. Berendse, "Decreased summer water table depth affects peatland vegetation," *Basic and Applied Ecology*, vol. 10, no. 4, pp. 330–339, 2009.

[17] J. Edvardsson, R. Šimanauskienė, J. Taminskas, I. Baužienė, and M. Stoffel, "Increased tree establishment in lithuanian peat bogs—insights from field and remotely sensed approaches," *Science of the Total Environment*, vol. 505, pp. 113–120, 2015.

[18] D. Boucher, S. Gauthier, N. Thiffault, W. Marchand, M. Girardin, and M. Urli, "How climate change might affect tree regeneration following fire at northern latitudes: a review," *New Forests*, vol. 51, no. 4, pp. 543–571, 2020.

[19] L. R. Potvin, E. S. Kane, R. A. Chimner, R. K. Kolka, and E. A. Lilleskov, "Effects of water table position and plant functional group on plant community, aboveground production, and peat properties in a peatland mesocosm experiment (peatcosm)," *Plant and soil*, vol. 387, pp. 277–294, 2015.

[20] K. C. Sulphur, S. A. Goldsmith, J. M. Galloway, A. Macumber, F. Griffith, G. T. Swindles, R. T. Patterson, H. Falck, and I. D. Clark, "Holocene fire regimes and treeline migration rates in sub-arctic canada," *Global and Planetary Change*, vol. 145, pp. 42–56, 2016.

[21] A. Ayanlade and U. Proske, "Assessing wetland degradation and loss of ecosystem services in the niger delta, nigeria," *Marine and Freshwater Research*, vol. 67, no. 6, pp. 828–836, 2015.

[22] F. Mohammadimanesh, B. Salehi, M. Mahdianpari, M. Motagh, and B. Brisco, "An efficient feature optimization for wetland mapping by synergistic use of sar intensity, interferometry, and polarimetry data," *International journal of applied earth observation and geoinformation*, vol. 73, pp. 450–462, 2018.

[23] B. G. Warner and C. D. Rubec, *The Canadian wetland classification system*. Wetlands Research Centre, University of Waterloo, 1997.

[24] C. Zhu, X. Zhang, and Q. Huang, "Four decades of estuarine wetland changes in the yellow river delta based on landsat observations between 1973 and 2013," *Water*, vol. 10, no. 7, p. 933, 2018.

[25] Y. Lin, J. Yu, J. Cai, N. Sneeuw, and F. Li, "Spatio-temporal analysis of wetland changes using a kernel extreme learning machine approach," *Remote Sensing*, vol. 10, no. 7, p. 1129, 2018.

[26] K. B. Byrd, J. L. O'Connell, S. Di Tommaso, and M. Kelly, "Evaluation of sensor types and environmental controls on mapping biomass of coastal marsh emergent vegetation," *Remote Sensing of Environment*, vol. 149, pp. 166–180, 2014.

[27] H. Su, W. Yao, Z. Wu, P. Zheng, and Q. Du, "Kernel low-rank representation with elastic net for china coastal wetland land cover classification using gf-5 hyperspectral imagery," *ISPRS Journal of Photogrammetry and Remote Sensing*, vol. 171, pp. 238–252, 2021.

[28] C. Sun, S. Fagherazzi, and Y. Liu, "Classification mapping of salt marsh vegetation by flexible monthly ndvi time-series using landsat imagery," *Estuarine, Coastal and Shelf Science*, vol. 213, pp. 61–80, 2018.

[29] L. Wang, M. Jia, D. Yin, and J. Tian, "A review of remote sensing for mangrove forests: 1956–2018," *Remote Sensing of Environment*, vol. 231, p. 111223, 2019.

[30] H. Jafarzadeh, M. Mahdianpari, and E. W. Gill, "Wet-gc: A novel multimodel graph convolutional approach for wetland classification using sentinel-1 and 2 imagery with limited training samples," *IEEE Journal of Selected Topics in Applied Earth Observations and Remote Sensing*, vol. 15, pp. 5303–5316, 2022.

[31] G. Cheng, X. Xie, J. Han, L. Guo, and G.-S. Xia, "Remote sensing image scene classification meets deep learning: Challenges, methods, benchmarks, and opportunities," *IEEE Journal of Selected Topics in Applied Earth Observations and Remote Sensing*, vol. 13, pp. 3735–3756, 2020.

[32] H. Jafarzadeh, M. Mahdianpari, E. Gill, F. Mohammadimanesh, and S. Homayouni, "Bagging and boosting ensemble classifiers for classification of multispectral, hyperspectral and polsar data: a comparative evaluation," *Remote Sensing*, vol. 13, no. 21, p. 4405, 2021.

[33] N. Longbotham, C. Chaapel, L. Bleiler, C. Padwick, W. J. Emery, and F. Pacifici, "Very high resolution multiangle urban classification analysis," *IEEE Transactions on Geoscience and Remote Sensing*, vol. 50, no. 4, pp. 1155–1170, 2011.

[34] G. Cheng, L. Guo, T. Zhao, J. Han, H. Li, and J. Fang, "Automatic landslide detection from remote-sensing imagery using a scene classification method based on bovw and plsa," *International Journal of Remote Sensing*, vol. 34, no. 1, pp. 45–59, 2013.

[35] Z. Y. Lv, W. Shi, X. Zhang, and J. A. Benediktsson, "Landslide inventory mapping from bitemporal high-resolution remote sensing images using change detection and multiscale segmentation," *IEEE journal of selected topics in applied earth observations and remote sensing*, vol. 11, no. 5, pp. 1520–1532, 2018.

[36] G. Cheng and J. Han, "A survey on object detection in optical remote sensing images," *ISPRS journal of photogrammetry and remote sensing*, vol. 117, pp. 11–28, 2016.

[37] J. Verrelst, G. Camps-Valls, J. Muñoz-Marí, J. P. Rivera, F. Veroustraete, J. G. Clevers, and J. Moreno, "Optical remote sensing and the retrieval of terrestrial vegetation bio-geophysical properties–a review," *ISPRS Journal of Photogrammetry and Remote Sensing*, vol. 108, pp. 273–290, 2015.

[38] M. Mahdianpari, H. Jafarzadeh, J. Granger, F. Mohammadimanesh, B. Brisco, B. Salehi, S. Homayouni, and Q. Weng, "Monitoring of 30 years wetland changes in newfoundland, canada," in *2021 IEEE International Geoscience and Remote Sensing Symposium IGARSS*, pp. 88–91, IEEE, 2021.

[39] T. Zhang and X. Huang, "Monitoring of urban impervious surfaces using time series of high-resolution remote sensing images in rapidly urbanized areas: A case study of shenzhen," *IEEE Journal of Selected Topics in Applied Earth Observations and Remote Sensing*, vol. 11, no. 8, pp. 2692–2708, 2018.

[40] P. Helber, B. Bischke, A. Dengel, and D. Borth, "Introducing eurosat: A novel dataset and deep learning benchmark for land use and land cover classification," in *IGARSS 2018-2018 IEEE international geoscience and remote sensing symposium*, pp. 204–207, IEEE, 2018.

[41] J. Mallick, S. Talukdar, S. Pal, A. Rahman, *et al.*, "A novel classifier for improving wetland mapping by integrating image fusion techniques and ensemble machine learning classifiers," *Ecological Informatics*, vol. 65, p. 101426, 2021.

[42] E. Belluco, M. Camuffo, S. Ferrari, L. Modenese, S. Silvestri, A. Marani, and M. Marani, "Mapping salt-marsh vegetation by multispectral and hyperspectral remote sensing," *Remote sensing of environment*, vol. 105, no. 1, pp. 54–67, 2006.

[43] R. Pande-Chhetri, A. Abd-Elrahman, T. Liu, J. Morton, and V. L. Wilhelm, "Object-based classification of wetland vegetation using very high-resolution unmanned air system imagery," *European Journal of Remote Sensing*, vol. 50, no. 1, pp. 564–576, 2017.

[44] L. Demarchi, F. Canters, C. Cariou, G. Licciardi, and J. C.-W. Chan, "Assessing the performance of two unsupervised dimensionality reduction techniques on hyperspectral apex data for high resolution urban land-cover mapping," *ISPRS Journal of Photogrammetry and Remote Sensing*, vol. 87, pp. 166–179, 2014.

[45] K. Rogers, N. Saintilan, and C. D. Woodroffe, "Surface elevation change and vegetation distribution dynamics in a subtropical coastal wetland: implications for coastal wetland response to climate change," *Estuarine, Coastal and Shelf Science*, vol. 149, pp. 46–56, 2014.

[46] P. Ghosh, D. Mandal, S. Wilfling, J. Hollberg, D. Bargiel, and A. Bhattacharya, "Synergy of optical and synthetic aperture radar data for early-stage crop yield estimation: a case study over a state of Germany," *Geocarto International*, vol. 37, no. 25, pp. 10743–10766, 2022.

[47] D. Mandal and Y. Rao, "SASYA: An integrated framework for crop biophysical parameter retrieval and within-season crop yield prediction with SAR remote sensing data," *Remote Sensing Applications: Society and Environment*, vol. 20, p. 100366, 2020.

[48] D. Mandal, V. Kumar, H. McNairn, A. Bhattacharya, and Y. Rao, "Joint estimation of Plant Area Index (PAI) and wet biomass in wheat and soybean from C-band polarimetric SAR data," *International Journal of Applied Earth Observation and Geoinformation*, vol. 79, pp. 24–34, 2019.

[49] D. Mandal, V. Kumar, J. M. Lopez-Sanchez, A. Bhattacharya, H. McNairn, and Y. S. Rao, "Crop biophysical parameter retrieval from Sentinel-1 SAR data with a multi-target inversion of Water Cloud Model," *International Journal of Remote Sensing*, vol. 41, no. 14, pp. 5503–5524, 2020.

[50] D. Mandal, V. Kumar, D. Ratha, J. M. Lopez-Sanchez, A. Bhattacharya, H. McNairn, Y. S. Rao, and K. Ramana, "Assessment of rice growth conditions in a semi-arid region of india using the Generalized Radar Vegetation Index derived from RADARSAT-2 polarimetric SAR data," *Remote Sensing of Environment*, vol. 237, p. 111561, 2020.

[51] S. Dey, N. Bhogapurapu, S. Homayouni, A. Bhattacharya, and H. McNairn, "Unsupervised classification of crop growth stages with scattering parameters from dual-pol Sentinel-1 SAR data," *Remote Sensing*, vol. 13, no. 21, p. 4412, 2021.

[52] P. Ferrazzoli, S. Paloscia, P. Pampaloni, G. Schiavon, D. Solimini, and P. Coppo, "Sensitivity of microwave measurements to vegetation biomass and soil moisture content: A case study," *IEEE Transactions on Geoscience and Remote Sensing*, vol. 30, no. 4, pp. 750–756, 1992.

[53] M. Mahdianpari, F. Mohammadimanesh, H. McNairn, A. Davidson, M. Rezaee, B. Salehi, and S. Homayouni, "Mid-season crop classification using dual-, compact-, and full-polarization in preparation for the Radarsat Constellation Mission (RCM)," *Remote Sensing*, vol. 11, no. 13, p. 1582, 2019.

[54] M. Dabboor, I. Olthof, M. Mahdianpari, F. Mohammadimanesh, M. Shokr, B. Brisco, and S. Homayouni, "The RADARSAT Constellation Mission core applications: First results," *Remote Sensing*, vol. 14, no. 2, p. 301, 2022.

[55] R. K. Raney, "Hybrid-polarity SAR architecture," *IEEE Transactions on Geoscience and Remote Sensing*, vol. 45, no. 11, pp. 3397–3404, 2007.

[56] G. Tana, H. Letu, Z. Cheng, and R. Tateishi, "Wetlands mapping in north america by decision rule classification using modis and ancillary data," *IEEE Journal of Selected Topics in Applied Earth Observations and Remote Sensing*, vol. 6, no. 6, pp. 2391–2401, 2013.

[57] M. A. Wulder, Z. Li, E. M. Campbell, J. C. White, G. Hobart, T. Hermosilla, and N. C. Coops, "A national assessment of wetland status and trends for canada's forested ecosystems using 33 years of earth observation satellite data," *Remote Sensing*, vol. 10, no. 10, p. 1623, 2018.

[58] M. M. Brinson and A. I. Malvárez, "Temperate freshwater wetlands: types, status, and threats," *Environmental conservation*, vol. 29, no. 2, pp. 115–133, 2002.

[59] S. v. Asselen, P. H. Verburg, J. E. Vermaat, and J. H. Janse, "Drivers of wetland conversion: a global meta-analysis," *PloS one*, vol. 8, no. 11, p. e81292, 2013.

[60] M. Dixon, J. Loh, N. Davidson, C. Beltrame, R. Freeman, and M. Walpole, "Tracking global change in ecosystem area: The wetland extent trends index," *Biological Conservation*, vol. 193, pp. 27–35, 2016.

[61] R. T. Kingsford, A. Basset, and L. Jackson, "Wetlands: conservation's poor cousins," *Aquatic Conservation: Marine and Freshwater Ecosystems*, vol. 26, no. 5, pp. 892–916, 2016.

[62] C. Fang, Z. Wen, L. Li, J. Du, G. Liu, X. Wang, and K. Song, "Agricultural development and implication for wetlands sustainability: a case from baoqing county, northeast china," *Chinese Geographical Science*, vol. 29, pp. 231–244, 2019.

[63] M. Mahdianpari, J. E. Granger, F. Mohammadimanesh, S. Warren, T. Puestow, B. Salehi, and B. Brisco, "Smart solutions for smart cities: Urban wetland mapping using very-high resolution satellite imagery and airborne lidar data in the city of st. john's, nl, canada," *Journal of environmental management*, vol. 280, p. 111676, 2021.

[64] S. L. Ozesmi and M. E. Bauer, "Satellite remote sensing of wetlands," *Wetlands ecology and management*, vol. 10, pp. 381–402, 2002.

[65] S. Mahdavi, B. Salehi, J. Granger, M. Amani, B. Brisco, and W. Huang, "Remote sensing for wetland classification: A comprehensive review," *GIScience & Remote Sensing*, vol. 55, no. 5, pp. 623–658, 2018.

[66] A. Zhang, G. Sun, P. Ma, X. Jia, J. Ren, H. Huang, and X. Zhang, "Coastal wetland mapping with sentinel-2 msi imagery based on gravitational optimized

multilayer perceptron and morphological attribute profiles," *Remote Sensing*, vol. 11, no. 8, p. 952, 2019.

[67] X. Hu, P. Zhang, Q. Zhang, and J. Wang, "Improving wetland cover classification using artificial neural networks with ensemble techniques," *GIScience & Remote Sensing*, vol. 58, no. 4, pp. 603–623, 2021.

[68] H. Huang, J. Wang, C. Liu, L. Liang, C. Li, and P. Gong, "The migration of training samples towards dynamic global land cover mapping," *ISPRS Journal of Photogrammetry and Remote Sensing*, vol. 161, pp. 27–36, 2020.

[69] O. Russakovsky, J. Deng, H. Su, J. Krause, S. Satheesh, S. Ma, Z. Huang, A. Karpathy, A. Khosla, M. Bernstein, *et al.*, "Imagenet large scale visual recognition challenge," *International journal of computer vision*, vol. 115, pp. 211–252, 2015.

[70] G. Foody and M. Arora, "An evaluation of some factors affecting the accuracy of classification by an artificial neural network," *International Journal of Remote Sensing*, vol. 18, no. 4, pp. 799–810, 1997.

[71] C. Li, J. Wang, L. Wang, L. Hu, and P. Gong, "Comparison of classification algorithms and training sample sizes in urban land classification with landsat thematic mapper imagery," *Remote sensing*, vol. 6, no. 2, pp. 964–983, 2014.

[72] L. Dingle Robertson, H. McNairn, X. Jiao, C. McNairn, and S. O. Ihuoma, "Monitoring crops using compact polarimetry and the RADARSAT constellation mission," *Canadian Journal of Remote Sensing*, vol. 48, no. 6, pp. 793–813, 2022.

# Chapter 2

# Remote Sensing and Artificial Intelligence for Wetland Studies [1]

## 2.1 Preface

This manuscript has been published in the MDPI Remote Sensing journal. I am the primary author with co-authors Masoud Mahdianpari, Eric W. Gill, Brian Brisco, and Fariba Mohammadimanesh. The paper is a comprehensive literature review in which I conducted an extensive review of the relevant literature, synthesizing and comparing findings from all investigated studies.

I presented the literature review to my co-authors, incorporating their feedback throughout the process. I was responsible for drafting the initial manuscript and subsequently revised it multiple times, incorporating editorial suggestions, scientific insights from my co-authors, and feedback from the journal's reviewers.

## 2.2 Abstract

Despite their importance to ecosystem services, wetlands are threatened by pollution and development. Over the last few decades, a growing number of wetland studies

[1] Jafarzadeh, H., Mahdianpari, M., Gill, E.W., Brisco, B. and Mohammadimanesh, F., 2022. Remote sensing and machine learning tools to support wetland monitoring: a meta-analysis of three decades of research. Remote Sensing, 14(23), p.6104.

employed remote sensing (RS) to scientifically monitor the status of wetlands and support their sustainability. Considering the rapid evolution of wetland studies and significant progress that has been made in the field, this paper constitutes an overview of studies utilizing RS methods in wetland monitoring. It investigates publications from 1990 up to the middle of 2022, providing a systematic survey on RS data type, machine learning (ML) tools, publication details (e.g., authors, affiliations, citations, and publications date), case studies, accuracy metrics, and other parameters of interest for RS-based wetland studies by covering 344 papers. The RS data and ML combination is deemed helpful for wetland monitoring and multi-proxy studies, and it may open up new perspectives for research studies. In a rapidly changing wetlands landscape, integrating multiple RS data types and ML algorithms is an opportunity to advance science support for management decisions. This paper provides insight into the selection of suitable ML and RS data types for the detailed monitoring of wetland-associated systems. The synthesized findings of this paper are essential to determining best practices for environmental management, restoration, and conservation of wetlands. This meta-analysis establishes avenues for future research and outlines a baseline framework to facilitate further scientific research using the latest state-of-art ML tools for processing RS data. Overall, the present work recommends that wetland sustainability requires a special land-use policy and relevant protocols, regulation, and/or legislation.

## 2.3 Introduction

Wetlands are the most valuable dynamic biophysical resources [1] existing at the terrestrial-aquatic interface [2] and the hub of a great variety of flora and fauna species [3]. Wetlands, which are landscape features that exist all over the world, in every kind of climate zone from the tropics to the tundra [4], provide an appropriate living environment for aquatic vegetation and various biological activities and play an irreplaceable role in improving the environment and mediating the ecological balance [5].

They serve multiple ecological functions and values [6, 7]. Erosion prevention, flood control, pollution alleviation, climate regulation, sewage purification, biodiversity maintenance, water storage and groundwater recharge, and wildlife support are

just a few of the functions that wetlands perform [7, 8, 9, 10]. Wetlands also contribute to tourism facilities, bio-energy production, and social benefits [8]. As such, understanding the distribution of wetland types and sites is crucial to ensure sustainable management and assessment of resource use [3]. As such, wetlands have been referred to as the "kidneys" of nature [11] because of the many environmental services and ecological benefits they provide.

In terms of levels and purposes, more than 50 definitions of wetlands throughout the world have been presented [12, 13]. The varying definitions come from the characteristics of the wetlands and how they are managed in different countries. However, in most definitions, wetlands are regarded as a unique ecosystem formed by interactions between the local area's geomorphology, hydrology, soil, and ecology. As defined explicitly in the Ramsar Convention, wetlands are distinct ecosystems that can be detected and monitored on a variety of scales using satellite remote sensing (RS) imagery and machine learning (ML) algorithms [14]. The combination of RS and ML can greatly relieve the heavy burden of manual work for wetland-related studies and offer huge potential and a wide scope of application space in these areas.

Even though there is a lack of reliable data, it is a concern to stakeholders that wetlands continue to be lost and degraded, as no science-based protocols are available in the most wetland regions to guide the monitoring of wetlands [6, 7]. Under the joint influence of natural accumulation, artificial reclamation, and urbanization, wetlands are constantly changing over time. Moreover, several factors influence wetland changes, including the local terrain, hydrology, soil, economy, population, and policy. As such, wetland sustainability requires special land-use policy and relevant regulation and/or legislation to monitor and assess the status of these crucial habitats locally, regionally, and globally. Furthermore, the rapid expansion of agricultural areas and urbanization are important factors in wetland areas having decreased significantly over the past three decades. Wetland resources can be effectively preserved by having up-to-date information on the status and extent of land cover within the ecosystem [15].

Monitoring and assessing wetlands by RS is an advanced analytical approach [16, 17] that allows for faster, less destructive, and more geographically expansive observation of the spatiotemporal changes in wetlands, as well as changes in the surrounding land use and land cover (LULC). Currently, Satellite RS technology is acknowledged

as the most powerful source of data for wetland identification by the U.S. Army Corps of Engineers (USACE) [18], and it has been extensively and successfully employed to monitor, assess, and preserve wetland areas in the past 50 years [18, 12]. As a complement to conventional approaches in wetland monitoring, RS has the potential to deepen our understanding of both local and global patterns of landscape and biodiversity. Through the development of satellite and sensor technology as well as ML algorithms, human involvement in wetland delineation has gradually decreased, leading to progress in techniques and algorithms for mapping these natural resources with RS tools [19, 20]. Using various satellite datasets (e.g., Landsat, Sentinel, MODIS, ...), researchers have produced land cover maps that include wetlands at national, provincial, regional, and local scales.

With the increased development of optical and radar sensor platforms, spaceborne sensors are becoming more accurate and useful in characterizing wetland extent and discriminating LULC types [21]. A broad range of users, organizations, and researchers can now benefit from technological advances in open-access satellite data streams, cloud computing, and data science to perform fast, accurate, large-scale, and high-resolution land cover classifications [22, 23, 24]. Recently, the advent of the Google Earth Engine (GEE, https://earthengine.google.com (accessed on 20 August 2022)) has provided a professional platform to assist geoscientists interested in geo-big data analysis [7, 25]. This cloud-based platform has revolutionized the processing and analysis of open-source earth observation data, introduced automatic training sample migration possibilities, and supports some ML methods [7, 26]. The most impressive feature of GEE is its ability for large spatial and temporal scale environmental (e.g., wetland) monitoring through parallel computation service.

Meanwhile, the development of data science algorithms and the open-source Python language environment and its packages (such as TensorFlow and Keras) have resulted in detailed modeling and analysis of a wide variety of open-source satellite data sets. Therefore, coupling easy access RS satellite data with data analysis, visualization, geo-computation, modeling, and ML tools/packages has dramatically enabled scientists to map and monitor land cover within larger regions more accurately and in an automated and repeatable way. Currently, the combined use of GEE with state-of-the-art deep learning (DL) models in wetland studies is absent from the literature and has not yet been well documented.

As listed in Table 2.1, several review papers have summarized the studies conducted on wetlands from different perspectives. Given its importance, a meta-analysis of studies on the capabilities of RS sensors, features, and ML models for monitoring and characterizing worldwide wetlands is overdue. Thus, we reviewed the literature related to RS data and the methods of producing spatial information on wetlands.

Table 2.1: List and a brief summary of previous reviews related to the topic. The list was sorted by publication date (the number of citations is reported by 30 June 2022 on the WoS database).

| # | Reference | First Author | Year | #Citation | Publication Journal | Review Type | | Reviewing Period |
|---|---|---|---|---|---|---|---|---|
| | | | | | | DR* | QR* | |
| 1 | [This Paper] | Jafarzadeh, H. | 2022 | 0 | Remote Sensing | ✓ | ✓ | 1990–2022 |
| 2 | [27] | Czapiewski, S. | 2021 | 0 | Land | ✓ | ✓ | 2010–2021 |
| 3 | [28] | Mirmazloumi, S.M. | 2021 | 0 | Remote Sensing | ✗ | ✓ | 1976–2020 |
| 4 | [29] | Montgomery, J. | 2021 | 1 | Remote Sensing | ✓ | ✗ | N/A |
| 5 | [30] | Gxokwe, S. | 2020 | 9 | Remote Sensing | ✓ | ✗ | 2000–2020 |
| 6 | [31] | Adeli, S. | 2020 | 31 | Remote Sensing | ✗ | ✓ | 1991–2019 |
| 7 | [13] | Mahdianpari, M. | 2020 | 21 | Remote Sensing | ✗ | ✓ | 1980–2019 |
| 8 | [32] | Chasmer, L. | 2020 | 14 | Remote Sensing | ✓ | ✗ | 1973–2018 |
| 9 | [33] | Chasmer, L. | 2020 | 6 | Remote Sensing | ✓ | ✗ | 1973–2018 |
| 10 | [34] | Minasny, B. | 2019 | 34 | Earth-Science Reviews | ✓ | ✓ | N/A |
| 11 | [11] | Mahdavi, S. | 2018 | 79 | GIScience & Remote Sensing | ✓ | ✗ | N/A |
| 12 | [12] | Guo, M. | 2017 | 154 | Sensors | ✓ | ✗ | 1964–2015 |

**Note:** * DR and QR stand for descriptive review and quantitative review, respectively.

The findings of the available review studies indicate that a further review paper should be carried out to compare the different techniques and concepts. Moreover, to the best of our knowledge, a comprehensive review of recent achievements regarding ML and DL for global wetland studies using RS data is still lacking. In order to reach this objective, the following lead questions are considered, and the current meta-analysis sought to address them:

- Which ML method is best suited to monitor wetlands surface cover and adjacent areas and provide the best result from RS imagery? To what extent are the commonly applied ML approaches valid?
- How have the ML models varied over the last decades?
- What are the key factors in ML model selection for wetland studies? Are there any specific problems that are being solved preferentially by a specific algorithm?
- How important is optical imagery compared to SAR (synthetic aperture radar)

data? What is the contribution of clear-sky observations from SAR imagery relative to optical imagery?

- Is multi-sensor (multi-source dataset) integration more accurate for wetland area delineation than a single sensor?
- What are the individual and combined contributions of SAR and optical data to wetland monitoring?
- What are the common satellite sensor types utilized for wetland studies?
- What are the common RS image features utilized for wetland studies?
- What are recommended steps for future wetland studies and management?

Toward responding to these important questions and describing future needs, empirical evidence is needed to protect natural resources, resolving conflicts, and appropriately managing common pool resources of wetland areas among stakeholders. As a step in reacting to these calls, this paper's main objective is to help find the best combination of data sources and methods to successfully follow the needs of wetland studies, as pictured in Figure 2.1.

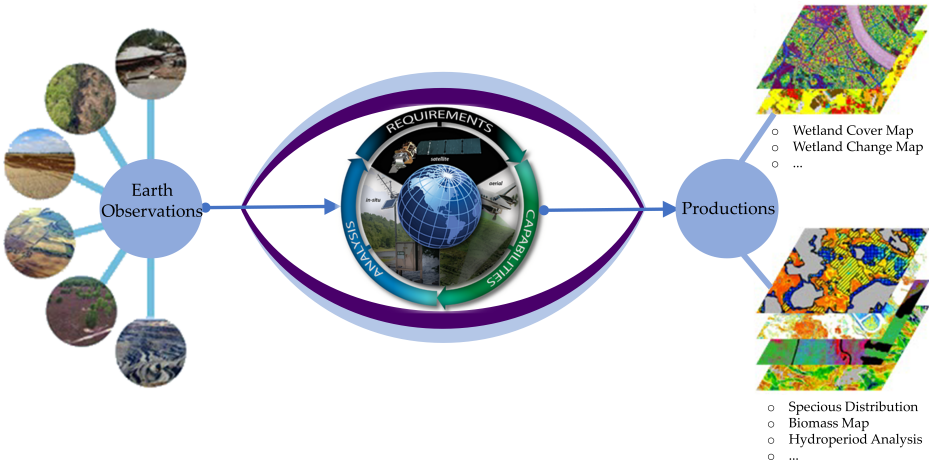



Figure 2.1: A conceptual overview of the use of ML and RS tools to derive productions.

The paper is structured as follows. A search procedure will be defined as the first step in finding and evaluating the candidate studies in consideration of this paper's objectives. Our next step is presenting a typology of the main wetland-based practices with their definitions. We identified the following main categories of practices:

classification, change detection (CD), vegetation mapping, biomass estimation, wetland area delineation, hydrological characterization, soil, and carbon estimation. We reviewed RS-based studies used to address each practice. In turn, the most critical features of the studies are highlighted and discussed, as are the research requirements for producing accurate and robust information on the wetlands. Finally, we present recommendations for future research in this field. In the conclusion section, the findings of this meta-analysis are summarized with respect to the questions mentioned earlier.

## 2.4 Methods

### 2.4.1 Bibliographic Base and Search Query Definition

In preparation for this meta-analysis and systematic review, the Science Citation Index (Web of Science (WoS) Core Collection) bibliographic database was used on and up to 30 June 2022 to retrieve scientific documents, including papers published in journals and conference proceedings constrained to the time span from 1990 to 2022. For this purpose, three sets of keywords were systematically defined, providing a logical literature search query to locate highly relevant references in the database (see Figure 2.2). To retrieve papers that incorporated RS data and ML tools to address a wetland application, the search was conducted in the topic field (i.e., title/abstract/keyword) using the keywords listed in the second and third columns. However, to narrow down the search results and make them more specific, the first column keywords were only searched in the title field. Consequently, the predefined search query retrieved 528 journal and conference papers in the primary search in the WoS database. Afterward, the PRISMA checklist, known as the methodology of Preferred Reporting Items for Systematic Reviews and Meta-Analyses, was followed [35, 36] to delineate the papers that fit within the scope of the topic and are eligible to be included in this meta-analysis. An overview of the paper selection methodology as per the PRISMA statement and review process is outlined in Figure 2.3.

The screening of the resulted 528 potential papers was then started to filter them by title and abstract, providing 404 candidates. The meta-analysis did not consider

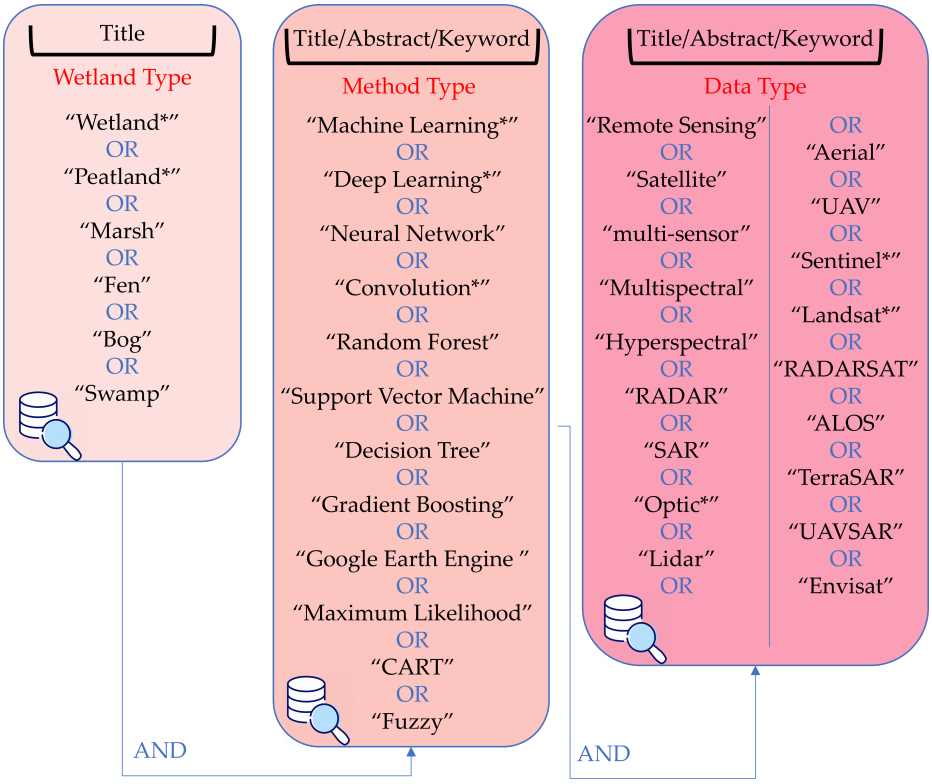



Figure 2.2: The predefined search query and list of keywords to prepare the procurements of this meta-analysis.

documents categorized as review studies, book chapters, reports, and non-English papers. In the next stage, by assessing the full texts of those candidates, only publications utilizing RS and ML techniques in wetland monitoring were selected as the final items for review to comply with the predefined inclusion criteria and maintain a controllable workload while focusing on the lead questions and objectives of the current study. Finally, a total of 344 papers were included in our meta-analysis procedure (see Figure 2.3).

### 2.4.2 Extracted Attributes from the Screened Records

The review process was conducted based on the 344 selected papers by full-text reads while looking for and focusing on a set of primary attributes. Looking at the previous review papers in the field of wetland studies, several study characteristics (presented in Table 2.2) were identified for the analysis of the final set of included papers in the context of our systematic review using a custom-made data extraction worksheet. In

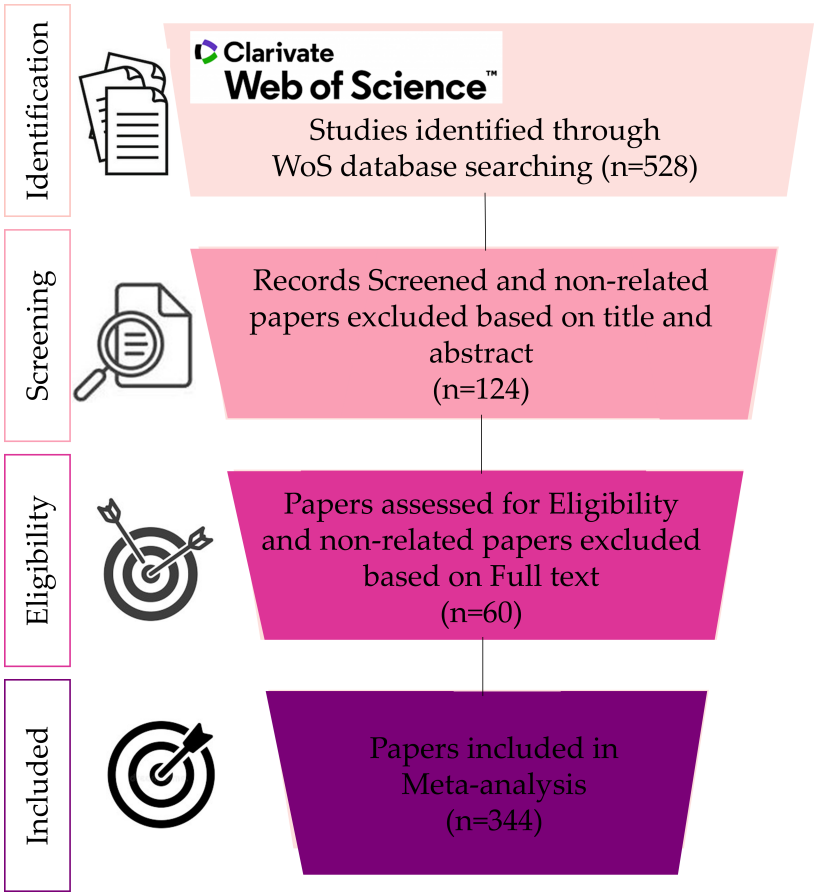



Figure 2.3: Paper selection and the review process flow diagram. A total of 528 papers were found in our primary search in the WoS database.

the current meta-analysis, these attributes are summarized to attain an overview of how RS imagery and ML techniques have been used to support wetland studies.

## 2.5 Results and Discussion

A detailed report of the systematic review will be provided in this section. We will begin by giving an overview of the general characteristics of wetland publications, including the author affiliations, journals, and the number of publications per year/journal/publisher. Afterward, study objectives and applications, study regions, data and sensor type, and ML algorithms utilized in the literature will be discussed.

Table 2.2: A listing of extracted sub-fields/attributes considered for the content analysis of included papers.

| # | Attribute | Type | Categories |
|---|---|---|---|
| 1 | Publication Title | Free-text | - |
| 2 | Keywords | Free-text | - |
| 3 | Authors | Free-text | First Author Name |
| 4 | First Author Affiliation | Free-text | University/Organization Country |
| 5 | Publication Year | Free-text | Published Year |
| 6 | Document Type | Classes | Journal; Conference |
| 7 | Source | Free-text | Published Journal or Conference |
| 8 | Publisher | Classes | MDPI, IEEE, Elsevier, etc. |
| 9 | Citation | Numeric | - |
| 10 | Study Focus/Objective | Classes | classification, change detection, vegetation mapping, etc. |
| 11 | Study Area Country | Free-text | Countries all around the world |
| 12 | Study Area Extent | Classes | Very small, Local, Regional, Provincial, National |
| 13 | Data Type | Classes | Multispectral, Hyperspectral, SAR, etc. |
| 14 | Sensor Type | Classes | Landsat, Sentinel, RADARSAT, etc. |
| 15 | Feature Type | Classes | Imagery Features, Spectral Indices, Textural metrics, etc. |
| 16 | Methodology | Classes | ensemble learning, decision tree, DL-based, etc. |
| 17 | Accuracy Assessment | Numeric | Overall Accuracies analysis based on seven factors |
| 18 | Processing Tools | Classes | ArcGIS, ENVI, Python, SNAP, etc. |

### 2.5.1 General Characteristics of Wetland Publications

#### Scientific Productions Trend

Figure 2.4 reflects the temporal distribution of the total number of reviewed papers along with the publication trends from three top publishing countries among 344 papers reviewed using PRISMA from 1997 to 2022. As shown, there is an increasing trend of scientific publications highlighting the importance of wetlands to the scientific community. The apparently drastic reduction from 2021 to 2022 can be attributed to the fact that the query results are until the middle of 2022. Considering the growing number of RS sensors and their promising performances in environmental monitoring tasks, about 67% (n = 232 out of 344) of the papers were published in the last five years (2018–2022).

#### Keyword Frequency Analysis

A word cloud based on keyword frequencies is shown in Figure 2.5. Keyword size is calculated by the frequency of occurrence of each keyword in all included papers. The

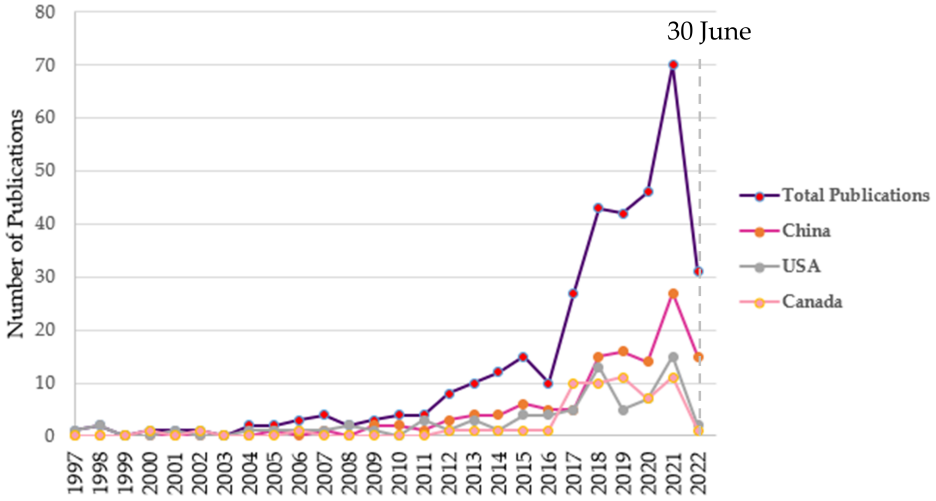



Figure 2.4: Temporal distribution and the total number of reviewed papers per year, and publication trends from three top publishing countries.

size of each particular keyword corresponds to how frequently it appears throughout all papers in the review. Considering the combination for the literature search, "Wetland" and "Remote Sensing" were the most frequently mentioned keywords in the reviewed literature. Note that there was a lack of consistency in the keywords because the reviewed papers came from a wide variety of journals in different formats. Therefore, some simplifications were made before feeding the keywords into the word-cloud generator. Our approach was to convert plural keywords into singular forms, capitalize all the keywords, and exclude those rarely appearing in the reviewed papers.

### Journal and Conference Analysis

The eligible publications in our systematic review appeared in 88 different journals and conferences, illustrating the diversity of disciplines interested in wetland studies. Among the selected papers, 307 and 37 were journal and conference papers, respectively (see Figure 2.6).

Among peer-reviewed publishing journals, 51 have published one or two papers on the topic. The majority of reviewed sources come from 8 peer-reviewed journals (with a share of 52%); see Figure 2.7a. Only journals with at least three publications are




Figure 2.5: Word cloud shows the most frequent terms in wetland studies. The larger the text, the more frequently the word appeared in considered papers.

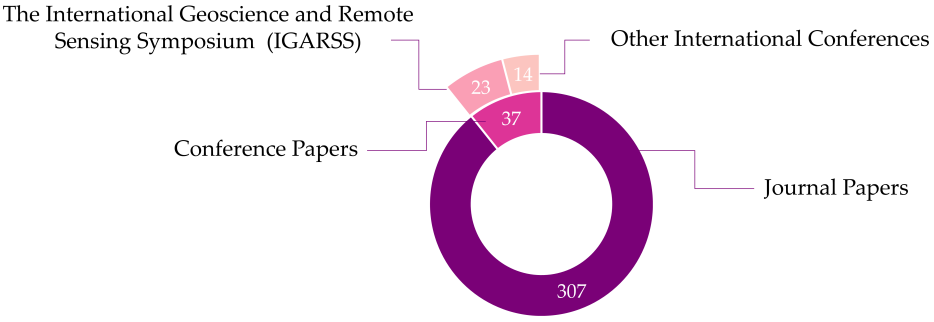


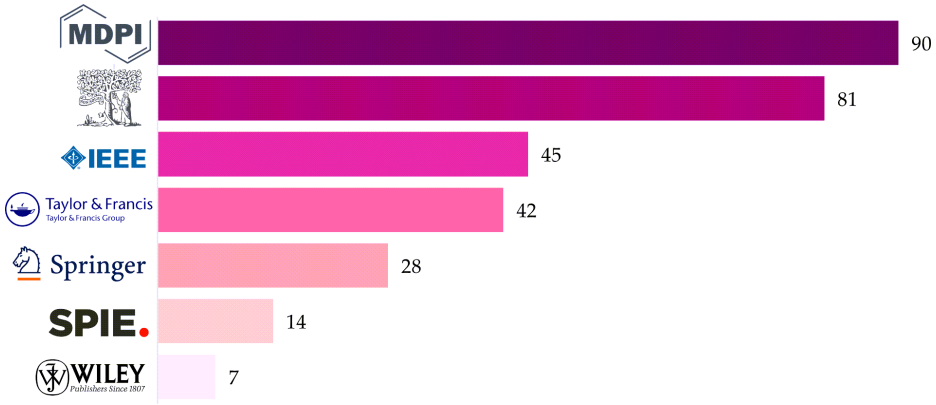

Figure 2.6: The number of journal and conference publications included in the meta-analysis.

included in this figure. As shown, the highest number (top five) of publications associated with wetland studies occurs in the Remote Sensing (MDPI), Remote Sensing of Environment (RSE), International Journal of Applied Earth Observation and Geoinformation, IEEE Journal Selected Topics in Applied Earth Observation and Remote

Sensing (IEEE-JSTARS), and Canadian Journal of Remote Sensing (CJRS) journals.




(a)




(b)

Figure 2.7: An overview of (a) the journals included in this meta-analysis and the number of papers per journal. (b) A listing of the leading publishers and the number of papers per publisher.

As shown in Figure 2.7b, the order of the publisher centers, whose journals account for the majority of the published papers is as follows: MDPI, followed by Elsevier, and IEEE (with an overall share of 70%). Moreover, 14% of the journal papers were published by Taylor & Francis, 9% by Springer, 5% by SPIE, and only 2% by WILEY. Among the conference proceedings, the IEEE International Geoscience and Remote Sensing Symposium (IGARSS), with 63% of papers (n = 23 out of 37), is the first ranked conference for publishing papers with the focus on wetland studies.

### First Author Affiliation Analysis

The spatial distribution of the first author's affiliations illustrated in Figure 2.8 clearly indicates the dominant share has Asian affiliations (with 42%), with 35% having Chinese affiliations alone. Furthermore, North American affiliations (with 40%) ranked second in this review, with 21% coming from the USA and 17% from Canada. Around 13% of publications are attributed to European affiliations. The high percentage of publications from Chinese, USA, and Canadian affiliations can be associated with the extensive wetland coverage in these countries, which needs to be studied, as well as a significant contribution of papers with strong methodological backgrounds. Researchers conducted such studies to develop ML algorithms and evaluate RS datasets, considering field data collection for wetland studies.

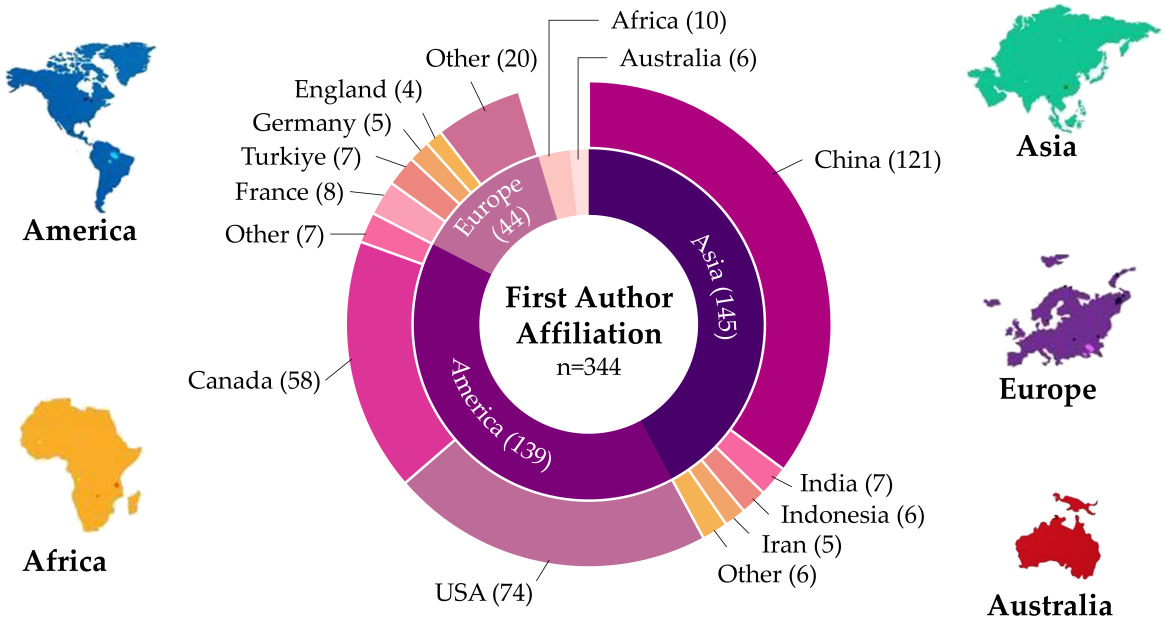



Figure 2.8: Country and continent-based overview of first author affiliations. Among the continents, Asia (with 42%), America (with 40%), and Europe (with 13%) hold the largest shares, and among countries, China (with 35%), the USA (with 21%), and Canada (with 17%) hold the largest shares.

### Citation Analysis

Analysis of citations provides a way to identify papers that have a significant impact on the field. Citation analysis also indicates the quality and objectivity of a paper by

demonstrating the number of researchers or scholars who are attracted to cite that paper. As a result, the citation numbers of all considered papers until 30 June 2022 were extracted from the WoS database in order to identify those that contributed the most. In Table 2.3, papers were ranked based on the number of citations; however, we also calculated the average citation per year to lessen the effect of elapsed time since the publication of the cited documents.

Table 2.3: List of highly cited papers in the database, ranked by the total number of citations (as of 30 June 2022).

| Rank | Ref. | First Author | Total Citations | Average Citation | Publication Year |
|---|---|---|---|---|---|
| 1 | [37] | Millard, K | 260 | 37.14 | 2015 |
| 2 | [38] | Dronova, I | 176 | 16 | 2011 |
| 3 | [39] | Bwangoy, JRB | 169 | 14.08 | 2010 |
| 4 | [40] | Baker, C | 168 | 10.5 | 2006 |
| 5 | [41] | Mandianpari, M | 155 | 31 | 2017 |
| 6 | [42] | Han, XX | 147 | 21 | 2015 |
| 7 | [43] | van Beijma, S | 142 | 17.75 | 2014 |
| 8 | [44] | Liu, T | 138 | 34.5 | 2018 |
| 9 | [45] | Corcoran, JM | 130 | 14.44 | 2013 |
| 10 | [46] | Mahdianpari, M | 114 | 38 | 2019 |

### 2.5.2 Study Focus and Applications

Knowledge of the status and extent of wetlands is essential to a series of research questions and applications. Thus far, many studies have characterized wetlands and monitored, mapped, and assessed them over time using a variety of satellite datasets with different spatial and temporal resolutions [47, 48]. Satellite imagery, such as the Landsat series, Sentinel, SPOT, and MODIS, provide long-term spatial data archives to assess, monitor, and manage ecological environments. These data collections have been widely utilized in environmental studies, for instance, in LULC change analysis, wetland status monitoring and extent mapping, biomass estimation, soil moisture retrieval, inundation mapping, and water level monitoring [7, 49, 50, 51, 52], amongst others.

As depicted in Figure 2.9, satellite imagery is mainly applied in seven major application domains for wetland studies: (1) the generation of landscape-type thematic

maps for wetland types; (2) the dynamic change analysis of wetlands; (3) wetland vegetation mapping; (4) the survey and recognition of wetland extent; (5) the evaluation and estimation of biomass in wetland areas; (6) wetland hydrological characterization and surface water hydroperiod; and (7) soil and carbon estimation. The share of each of these applications within the reviewed literature is also presented in Figure 2.9. Of all reviewed publications, 51% investigate wetlands from the perspective of the classification of wetland classes. Following the classification, 14% of the publications analyzed wetlands' changes. Wetland vegetation mapping and wetland extent recognition are in third and fourth places, with a share of 12% and 7% among all reviewed papers. Since the classification and CD frameworks have the most significant shares, a brief discussion of these applications is presented below.

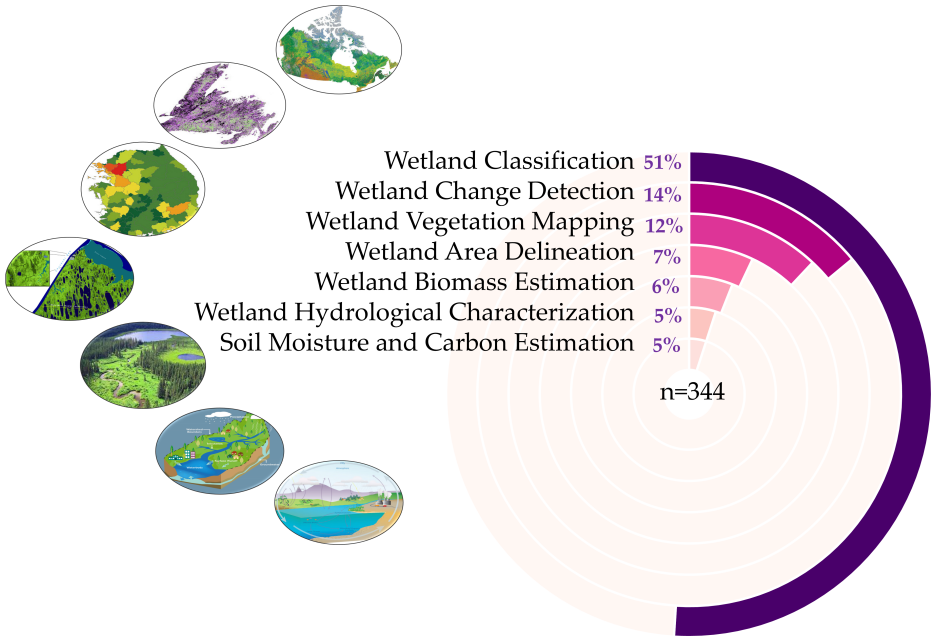



Figure 2.9: Overview of the diversity of application domains of RS Earth observations in wetland areas.

### Classification

Wetland cover classification arises from the monitoring and management needs to categorize wetland ecosystems into several types displaying different landscapes within wetlands. Traditional in situ surveys are too costly and slow to meet the demand for extensive and fast monitoring of wetland habitats [11]. The RS technology, in contrast,

offers labor- and cost-effective advantages for mapping and assessing wetlands due to its intuitive observations of the ground in the broad coverage area, along with timely, regular, and rapid monitoring capabilities [53, 54, 55].

With the current advancement in Earth observation instruments (e.g., multi/ hyperspectral, SAR, etc.), there are ever more types of airborne or space-borne images with different resolutions available (i.e., spatial/spectral/temporal resolution). This leads to significant demand for intelligent Earth observation based on RS imagery, enabling the smart identification and classification of wetland areas from airborne and space platforms. The problem of scene classification has emerged as an active research area in RS data analysis and has drawn remarkable attention in recent years, as it is essential for effectively interpreting remotely sensed images. It attempts to label given scene images correctly based on their contents with predefined semantic land cover categories [56]. Currently, satellite image data for Earth observation are being made continuously available to the public. Governmental programs, including the ESA's Copernicus and NASA, are putting considerable effort into making such data freely available for universities and institutions, researchers, scientists, and technology experts to use in order to inspire innovation and entrepreneurship.

### Change Detection

As one of the leading research topics in earth systems, land cover CD in terrestrial surfaces has profound implications for human society and ecosystems (especially in wetland ecosystem functioning) [57]. Due to their vulnerability and sensitivity to variations in the environment, wetlands have become key regions for monitoring land cover changes over time. Wetland ecosystems interact with the physical environment, including hydrology, meteorology, and topography, in a variety of ways. Land cover CD in wetland sites provides an understanding of the patterns of the spatial distribution of wetland surface cover and the complexity of its spatiotemporal variations [38].

As the most comprehensive and longest time-series RS image dataset available, Landsat imagery is one of the most suitable data sources, providing both appropriate spatial and spectral resolutions, as well as free-of-charge access. Moreover, in many developing countries, limited data resources make Landsat imagery an important data source for filling knowledge gaps in investigating local small-scale wetland dynamics.

Using satellite imagery for wetland CD involves a variety of methods, which can broadly be divided into two categories: (1) change enhancement approaches, including direct comparison, differentiation of vegetation indices, spectral mixture analysis, and fuzzy CD, and (2) 'from-to' change information extraction approaches [58, 59, 60]. The former methods (e.g., image differencing) do not indicate what types of land cover have been changed; they only provide information on whether there has been a change or not, and in some cases, measure the relative magnitude of that change. By contrast, the latter methods, such as the post-classification comparison approaches, are the most commonly used and effective CD techniques [61]. Post-classification comparison methods use separate classifications for images acquired at different times to produce different maps from which 'from-to' land-cover change trajectories can be detected [62]. In addition, 'from-to' quantitative information about the type of LULC changes can be gained from a cross-tabulated change matrix [63].

Among all wetland CD methods in our meta-analysis, the post-classification approach is the most-employed technique, with a share of n = 46 out of 49. Taking a time interval perspective, CD studies can be categorized into two categories: (1) long-term CD and (2) short-term CD. As depicted in Figure 2.10, short-term CD (i.e., CD studies within a period of (1) 1–5 years and (2) 5–10 years) has a share of 20%, and long-term CD (i.e., CD studies within a period of (1) 10–20 years, (2) 20–30 years, and (3) 30–40 years) has a share of 80% among all post-classification change analysis papers. Long-term CD provides a better understanding of wetland trends and sudden changes; therefore, it is helpful to protect and analyze the dynamics of wetlands.

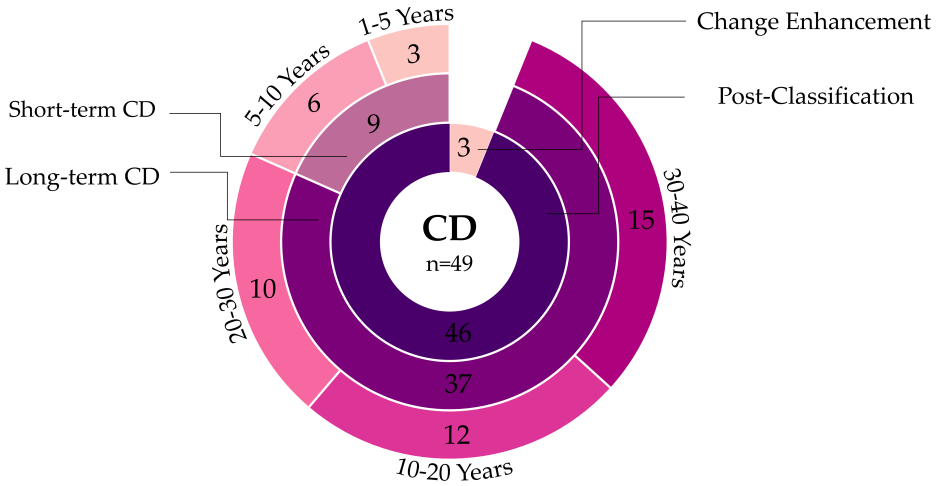



Figure 2.10: Frequency of short-term and long-term CD.

### 2.5.3 Case Study Analysis

The worldwide distribution of study regions grouped by countries of case studies is shown in Table 2.4. As shown, most studies were conducted in study areas in China (35%), the USA (19%), and Canada (18%). Additionally, the literature review found the following study areas were studied at least four times: South Africa (n = 12), India (n = 9), Australia (n = 9), France (n = 6), Indonesia (n = 6), Iran (n = 5), Brazil (n = 4), Turkiye (n = 4), and Sweden (n = 4).

Table 2.4: Overview of study site locations grouped by countries coupled with various scales of the study site's extent. Sites with four or more studies were included.

| # | Study Area (Country) | #Studies | VS | L | R | P | N | # | Study Area (Country) | #Studies | VS | L | R | P | N |
|---|---|---|---|---|---|---|---|---|---|---|---|---|---|---|---|
| 1 |  | 120 | 39 | 50 | 27 | 3 | 1 | 7 |  | 6 | 5 | 1 | 0 | 0 | 0 |
| 2 |  | 66 | 34 | 21 | 8 | 2 | 1 | 8 |  | 6 | 4 | 2 | 0 | 0 | 0 |
| 3 |  | 62 | 9 | 36 | 6 | 6 | 5 | 9 |  | 5 | 1 | 2 | 2 | 0 | 0 |
| 4 |  | 12 | 5 | 3 | 4 | 0 | 0 | 10 |  | 4 | 3 | 1 | 0 | 0 | 0 |
| 5 |  | 9 | 3 | 3 | 3 | 0 | 0 | 11 |  | 4 | 3 | 1 | 0 | 0 | 0 |
| 6 |  | 9 | 4 | 3 | 2 | 0 | 0 | 12 |  | 4 | 2 | 1 | 1 | 0 | 0 |

**Note:** very small (VS), large (L), regional (R), provincial (P), national (N).

Based on the extent of the study sites, the publications were categorized into five groups (see Table 2.4). To have consistency with [28], these divisions were considered in terms of the following five groups: (1) very small (less than 100 $km^2$), (2) local (between 100 $km^2$ and 3000 $km^2$), (3) regional (more than 3000 $km^2$ and less than a provincial scale), (4) provincial, and (5) national (country-wide) scales. This investigation shows that most wetland RS studies call attention to very small, local, and regional scales and that very few consider provincial or country-wide scales.

### 2.5.4 RS Data Used in Wetland Studies

#### Data Type

The use of satellite RS in environmental research studies has been widely adopted as a rapid scientific tool for monitoring and investigative purposes [7, 21, 64, 65], as shown in Figure 2.11. It offers a powerful alternative over-ground survey, providing a synoptic view, multispectral data, multitemporal coverage, and cost-effectiveness [36, 66]. With these improvements and advances in quality, volume, and diversity, spectral imagery is being used to study wetlands more effectively and with a wider variety of applications. These advances support increases in the quality, volume, and diversity of applications of spectral imagery in the study of wetlands, in particular, accurate assessment of their status and measuring the pattern of the changes, as well as the success of restoration efforts. Meanwhile, wetland studies conducted by optical and SAR imagery have by far the largest shares.

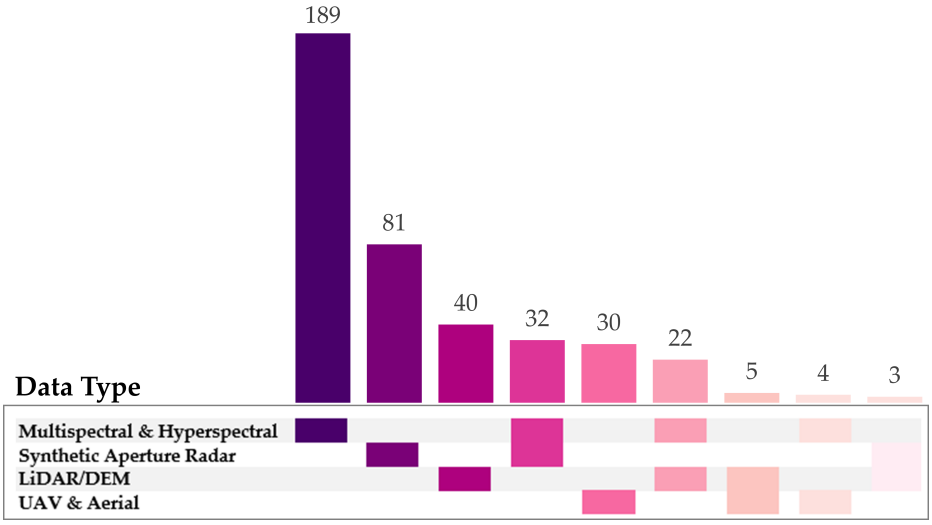



Figure 2.11: Distribution of employed data types and their combinations with the largest shares for multispectral and hyperspectral (46%), SAR (20%), and LiDAR/DEM (10%) data types.

A variety of applications have been proposed and studied for RS optical sensors, from small target evaluation to global issue resolution. In the wetland field of studies, in addition to providing information on vegetation cover and community type, optical sensors are capable of identifying and differentiating wetlands and vegetation zones, as well as mapping wetlands on a large scale, among other applications [67]. Over

the last two decades, improvement of satellite spatial resolution and reduced costs of multi- and hyperspectral sensors have increased the scope for applying spectral imaging to advance wetland study. Multispectral satellite imagery can be acquired at resolutions $< 5$ m, enabling examination of wetland systems at much finer scales and supporting longitudinal analyses of change over extended periods. However, due to their inability to penetrate clouds and atmospheric haze or a dense vegetated canopy, optical sensors are limited to daytime clear-sky image acquisition [24]. Even though optical satellite imagery successfully detects and monitors wetlands, the presence of cloud cover limits their usefulness, especially in coastal areas [14, 68, 69].

Unlike optical sensors, as an active RS system, SAR is not affected by atmospheric conditions, can detect sub-canopy soil and vegetation structural features, and does not rely on external sources of radiation (i.e., sunlight) for its operation. It has the ability to overcome the above limitations (unaffected by weather conditions) and can operate in all-weather and daylight-independent conditions [36, 70, 71], so it is well suited to wetland monitoring. SAR has proven to be a preferred alternative or supplemental source to optical images for wetland mapping, especially in coastal wetlands and intertidal zones [69, 72, 73]. However, several factors affect SAR data and its components, such as the effects of surface moisture content and roughness and instrument viewing direction, and incidence angle [74]. As a result, the collected backscattering SAR signals influenced by vegetation and soil properties carry information related to wetlands and soil's geometric structure and dielectric properties [73]. This makes SAR data essential to distinguish certain land cover classes such as "built-up" and "bare soil", or classes with different levels of moisture and inundation such as "heterogeneous wetland sites" and "intermittent water bodies".

Considering the advantages of optical and SAR data, the combination of optical and SAR imagery can offer the greatest potential for supporting wetland mapping and monitoring tasks, as described in [21]. It is critical, therefore, to explore the extent to which optical and SAR RS data may supplement the LULC studies, particularly in wetland regions. Our findings showed that multispectral and hyperspectral optical imagery and SAR data present the greatest portion of wetland studies. Regarding the data type usage, as shown in Figure 2.11, 247 studies employed multispectral and hyperspectral optical images, followed by SAR images (n = 116), LiDAR/DEM data (n = 65), and UAV/Aerial imagery (n = 39). Moreover, the integration of optical and SAR imagery includes 32 studies, followed by the integration of optical

and LiDAR/DEM with 22 studies.

### Single-Source Versus Multi-Source Data

Although individual RS data have proven successful in monitoring wetland areas, data fusion techniques employing multi-source satellite data sets can improve the determination of wetland hydrological, vegetation, and topographic characteristics, which are important indicators of wetland characteristics and offer the potential for improved wetland classification accuracy [21, 75, 76, 77]. For example, optical images can reflect the rich spectral information of objects, and SAR is capable of providing valuable geophysical parameters. The combination of polarimetric and optical data to classify wetlands fully exploits the spectral and backscattering characteristics of the habitat. In addition, it reduces radar speckle noise and enhances the separation between wetland objects, making it a helpful monitoring strategy. Many experts and geoscientists have recently utilized multi-source RS imagery to monitor wetlands with varying results [11]. Many works have attempted to employ multisource imagery to monitor wetlands considering data fusion and feature fusion techniques to use the complementary merit of different types of RS data. For instance, in a newly published paper, Jafarzadeh et al. [21] established a two-stream DL framework based on a graph convolutional network and convolutional neural network for wetland classification using Sentinel-1 and Sentinel-2 images. Based on their ablation analysis, the accuracy of classification reached its highest when two kinds of data sets were combined. By combining LiDAR and SAR data, Millard et al. [78] observed improved wetland extent mapping and classification accuracy of wetland types compared to individual data source analysis. The significant advancements and improvements in spaceborne RS, in parallel with the rise of the trend toward open-source data sharing, have led to opportunities for combining multiple data types in monitoring and fully understanding the unique characteristics of wetland environments.

Using multi-source satellite images helps in understanding, modeling, and projecting land change effectively by providing timely and spatially distributed information. In particular, moderate-resolution multispectral sensors (e.g., Landsat, SPOT, and ASTER) have been successfully used to study flooding and affected land cover, detect wetlands in heterogeneous landscapes, and monitor invasive plants. More recent studies reported high accuracies in obtaining wetland characteristics when fusing the

datasets from Sentinel-1 and Sentinel-2 sensors [21, 50, 73, 77]. This meta-analysis reveals that about 55% of studies benefited from multi-source or multi-sensor RS data combination, while the remaining utilized only a single-source or single-sensor imagery (see Figure 2.12).

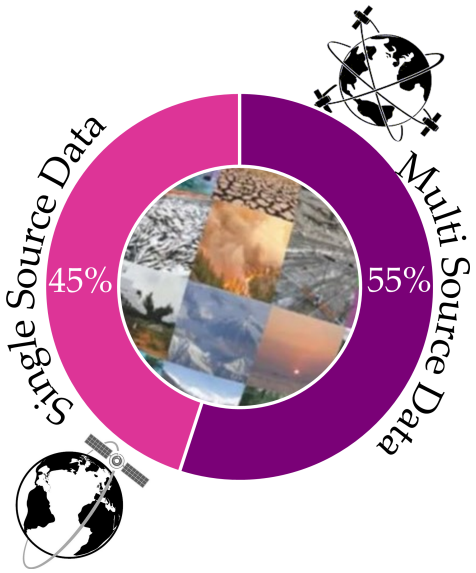



Figure 2.12: Frequency of single- and multi-source RS data usage in wetland studies.

### Sensor Type

Based on our search query in WoS, we can indicate an increase in the use of RS methods in wetland research during the last decade, which is likely a result of the greater availability of new RS data sets (e.g., Sentinel 1 and 2; Landsat 8) paired with the rapid development of ML approaches. As shown earlier, a variety of RS data have been applied to evaluate wetlands, including very high-resolution (VHR) satellite imagery, Landsat, and SAR.

The most broadly used wetland RS data source is Landsat multispectral imagery that, as of Landsat 8, is 30 m in spatial resolution for most spectral channels, with a repeat cycle of 16 days, including 11 bands, which is publicly accessible at no cost [12]. Scholars in a wide range of studies have achieved accurate wetland identification results through the incorporation of the Landsat dataset, specifically from the Landsat 8 Operational Land Imagery (OLI) satellite (e.g., [79, 80]). The limitations of approaches using data at this spatial resolution, such as the inability to exactly identify

wetland locations, are in turn balanced by the possibility of such data to rule out large-scale regions as not being likely to include wetlands. Landsat-5, which holds the Guinness World Record for the longest on-orbit operational time (from 1984 to 2012), was also widely applied to historical wetland mapping [7, 10, 45, 81, 82]. Because they provide more spatial and structural characteristics than spectral information, the high-resolution images obtained from the RapidEye, Quickbird, WorldView-2, and SPOT 5 satellites also have become one of the main sources for resources and environmental management and application [20, 83, 84, 85, 86, 87]. The utilization of optical and SAR data for wetland studies is growing. As shown in Table 2.5 and Table 2.6, various satellite data with different resolutions are used in different studies. Among optical sensors, the Landsat Archive (including Landsat 4, 5, 7, and 8) has the greatest share by far (with n = 201 studies), followed by Sentinel-2 and RapidEye with a share of n = 54 and n = 14 studies, respectively. In SAR-equipped satellites, Sentinel-1 (n = 45), RADARSAT-2 (n = 31), and ALOS PALSAR (n = 25) are the most used SAR data sets.

Along with varieties of RS data that have been engaged in wetland studies, employing the new generation of RS data provides promise for resolving the remaining challenges in this field. Meanwhile, it is recommended to utilize the RADARSAT Constellation Mission (RCM) and the upcoming NASA-ISRO SAR Mission (NISAR) in future wetland studies by establishing new methodologies.

### Data Type Resolution

The RS data types employed in wetland studies can be classified into three categories based on their spatial resolution: high-resolution (5 m), medium-resolution (5 to 30 m), and coarse-resolution (> 30 m). Figure 2.13 illustrates how frequently each of these data types is used in review papers. Medium-resolution images hold the largest share (with 66%) by far out of all data types. This is followed by high-resolution images, which take up 30% of the share, and coarse-resolution images, which take up 4%.

Table 2.5: List of the commonly used optical satellites in wetland studies ranked by the number of times they have been utilized in the papers.

| Satellite | Life Span | #Channels | Range | Image Type | | | Spatial Resolution | Repeat Cycle (Days) | #Studies | Ref. |
|---|---|---|---|---|---|---|---|---|---|---|
| | | | | Pan | MSI | HSI | | | | |
| Landsat-8 | 2013–now | 12 | B1–9 (0.43–1.38) | ✓ | ✓ | × | 15, 30, 100 m | 16 | 74 | [7, 10, 42, 81, 88, 89, 90, 91] |
| Landsat-5 | 1984–2013 | 8 | B1–5 (0.45–1.75) | × | ✓ | × | 30, 120 m | 16 | 62 | [7, 10, 42, 45, 81, 82, 92, 93] |
| Sentinel-2 | 2015–now | 12 | 0.443–2.190 | × | ✓ | × | 10, 20, 60 m | 5 | 54 | [21, 55, 89, 91, 94, 95, 96, 97, 98, 99] |
| Landsat-7 | 1999–now | 8 | B1–5 (0.45–1.75) | ✓ | ✓ | × | 15, 30, 60 m | 16 | 50 | [7, 10, 42, 81, 100] |
| Landsat-4 | 1982–2001 | 7 | B1–5 (0.45–1.75) | × | ✓ | × | 30, 120 m | 16 | 15 | [10, 42, 101, 102, 103] |
| RapidEye | 2008–now | 4 | 0.44–0.85 | ✓ | ✓ | × | 5 m | 1–5.5 | 14 | [104, 105, 106] |
| MODIS | 1999/2002–now | 36 | B1–19 (0.405–2.155) | × | ✓ | × | 250,500, 1000 m | 1–2 | 12 | [107, 108, 109, 110, 111] |
| WorldView-2 | 2009–now | 8 | 0.45–0.80 | ✓ | ✓ | × | 0.52, 2.4 m | 1.1 | 12 | [2, 86, 112] |
| Quickbird | 2001–now | 5 | 0.45–0.9 | ✓ | ✓ | × | 0.61, 2.4 m | 1–3.5 | 8 | [83, 84, 85, 113, 114] |
| Gaofen-1 | 2013–now | 5 | 0.45–0.89 | ✓ | ✓ | × | 2, 8 m | 4 | 8 | [115, 116, 117] |
| ASTER | 1999–now | 14 | B1–3B (0.52–0.86) | × | ✓ | × | 15, 30, 90 m | 4–16 | 7 | [91, 118, 119] |
| SPOT-5 | 2002 | 4 | 0.5–1.75 | ✓ | ✓ | × | 2.5, 5, 10 m | 2–3 | 5 | [83, 87] |
| Gaofen-5 | 2018–now | 330 | 0.39–2.51 | × | × | ✓ | 30 m | 2 | 5 | [95, 120] |
| Pléiade | 2011 | 4 | 0.43–0.95 | ✓ | ✓ | × | 0.5, 2 m | 26 | 3 | [121] |
| Gaofen-2 | 2014–now | 5 | 0.45–0.89 | ✓ | ✓ | × | 0.8, 3.2 m | 4 | 3 | [5] |

Table 2.6: List of the commonly used SAR satellites in wetland studies, ranked by the number of times they have been utilized in the papers.

| Satellite | Life Span | Polarization | Wavelength (cm)/Band | Repeat Cycle (Days) | #Studies | Ref. |
|---|---|---|---|---|---|---|
| Sentinel-1A, Sentinel-1B | 2014–Present, 2016–Present | Single/Dual | 5.54/C-band | 6 | 45 | [21, 82, 89, 96, 97, 115, 122] |
| RADARSAT-2 | 2007–Present | Single/Dual/Quad | 5.55/C-band | 24 | 31 | [41, 45, 78, 82, 106, 123, 124] |
| ALOS PALSAR | 2006–2011 | Quad | 23.6/L-band | 46 | 25 | [110, 124, 125, 126, 127, 128, 129] |
| TerraSAR-X | 2007–Present | Quad | 3.11/X-band | 11 | 9 | [41, 124, 130] |
| ENVISAT ASAR | 2002–2012 | Dual | 5.63/C-band | 35 | 6 | [110, 131] |
| Gaofen-3 | 2016–Present | Single/Dual/Quad | 5.4/C-band | 29 | 3 | [69] |
| Huan Jing-1C | 2012–Present | Single-VV | 3.13/S-band | 31 | 2 | [132] |
| ERS-1 | 1991–2000 | Single-VV | 5.66/C-band | 35, 3, 168 | 2 | [126] |
| ERS-2 | 1995–2011 | Single-VV | 5.66/C-band | 35 | 2 | [126] |

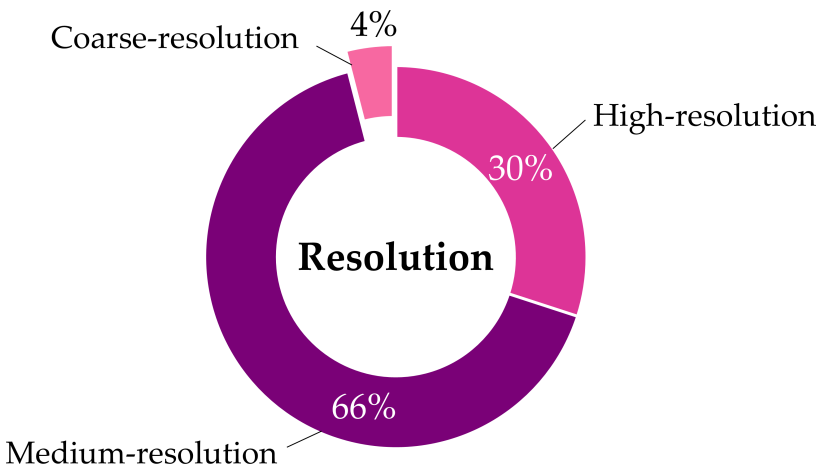



Figure 2.13: Frequency of high-resolution, medium-resolution, and coarse-resolution images used in wetland studies.

#### Single-Date Versus Multi-Date

Multi-date and time-series RS data has been widely conducted with many sensors to monitor the status of wetlands and detect land cover changes globally [6, 7, 109, 133]. There are a number of satellite missions, both optical and SAR systems, which provide long time-series and ongoing multi-temporal imageries with global coverage for LULC mapping, wetland monitoring, and CD efforts [7, 40]. Our systematic review provides insights into the available data types for investigating wetland covers in a multi-date manner. For example, of the optical sensors, Landsat archive, MODIS, and Sentinel-2, and among SAR missions, Sentinel-1 and RADARSAT-2 are suitable for large spatial and long time-series wetland studies. In some cases, such as the MODIS sensor, which provides a historical observation of the earth's surface, the coarse resolution of such imagery cannot precisely identify the details of the wetlands and smaller wetland sites. Looking at Figure 2.14, about two-thirds of the studies have applied multi-date RS data for wetland studies.

### 2.5.5 Methodology Analysis

#### ML Classifier Categories

In the aftermath of its introduction, land cover mapping algorithms have been refined and upgraded many times [134]. For instance, when it comes to water extraction, the

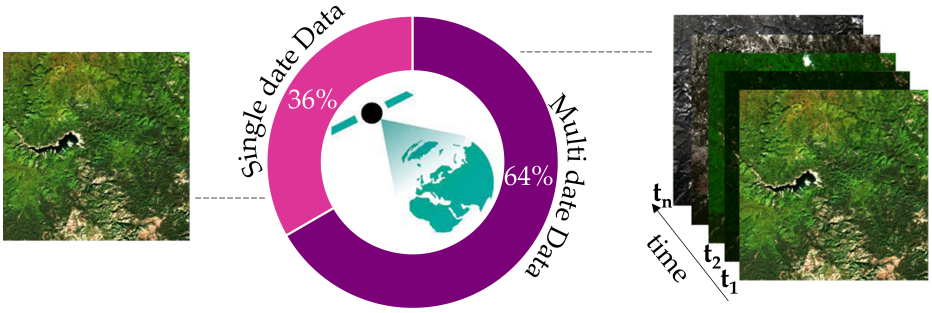



Figure 2.14: Frequency of single- and multi-date RS data usage in wetland studies.

procedure can be done considering three stages: visual interpretation, semi-automatic interpretation, and automatic interpretation [135]. In recent years, ML has emerged as the most common wetland extraction method for automatic interpretation, and supervised and unsupervised ML techniques for RS image classification have progressed greatly. The challenges and difficulty of discrimination among classes, however, continue to affect the accuracy of surface mapping and data extraction. Therefore, classification is still a difficult task due to confusion with different cover classes.

Various classification techniques have been used to deal with land cover classification and improve classification accuracy. At present, the use of shallow ML algorithms, such as support vector machines (SVMs), backpropagation (BP) neural networks, decision trees (DTs), random forest (RF), extreme gradient boosting (XGBoost), and K-Nearest Neighbors (KNN), have been widely applied to RS data in extracting wetland information and improving the accuracy of wetland classification and CD. These approaches are able to handle complex nonlinear relationships without taking into account the statistical assumptions. However, as a diverse type of land cover, wetlands involve a variety of spatial, temporal, and spectral characteristics, and no single algorithm has proven to meet all the needs of wetland monitoring and be optimal across all use cases [76]. The shallow ML algorithms work well in extracting information from wetland areas; however, they require a lot of prior knowledge to be trained and high learning costs to migrate models.

Since its inception, DL, a subfield of ML, is emerging as a powerful tool to address problems by learning from data. DL is a milestone data representation learning technology that has taken the world by storm due to its success. As a way to automate predictive analytics, DL allows trainable models composed of a sequence of processing layers and nonlinear mappings to learn representations of data with multiple levels

of abstraction [136]. A DL network has a strong function expression ability, can learn more complex training samples, and has good robustness for the classification of complex features such as wetland landscapes in RS images [21, 77, 137]. CNN is a breakthrough technique in DL, and it is a kind of feed-forward neural network, which has good performance in image processing and data mining. The artificial neurons in CNN models can respond to a part of the surrounding units in the coverage area. By the inclusion of several building blocks, such as convolutional layers and pooling layers in its structure, a CNN framework is capable of better extracting medium and high-level abstractions from the original images. Some scholars have applied it in wetland classification studies and have reported higher overall accuracy values than those obtained using shallow ML [21, 77, 96, 138].

ML algorithms' robustness and generalization capability have made them the major classification methods. Various ML and classification techniques have been used successfully and widely in wetland studies. Considering the structure of different methodologies employed during the last three decades, the classification algorithms were grouped into eight major categories in this paper: (1) ensemble learning; (2) decision tree; (3) Kernel-based; (4) distance-based; (5) DL-based; (6) ANN; (7) instance-based; (8) Bayesian (see Figure 2.15a and Figure 2.16). While there is an overlap between the ANN and DL categories, the former includes shallow, two- or three-layer networks, whereas the latter includes more complex and deeper networks. As illustrated in Figure 2.15b, the most common form of ML, deep or not, is supervised learning.

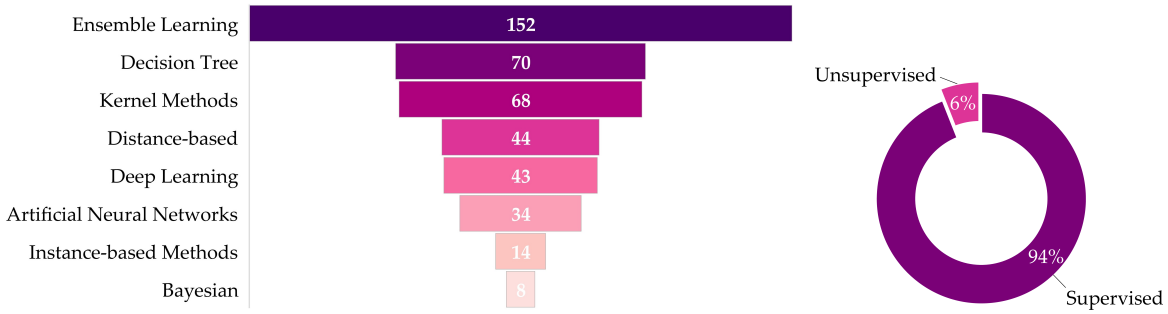



Figure 2.15: (a) Frequency of ML algorithms in wetland studies with (b) percentage of supervised and unsupervised approaches.

According to Figure 2.16, among these algorithms, CNN as a DL model, and RF as a ML model have drawn attention to wetland mapping. As far as the accuracy of

algorithms is concerned, DL models are usually the best to use. However, recent studies on challenging classification tasks using multi-source and multi-temporal RS data have pointed to the superiority of the RF approach. RF, as a tree-based ensemble method, has shown superior performance among other ML techniques and has become an often-used method in wetland identification and mapping. RF has several advantages, such as the ability to handle high-dimensional data while being less affected by noise, incorporating continuous and categorical data, and measuring descriptive variable importance [139]. Although many studies indicate that RF produces higher classification accuracy than traditional techniques, it is not usually the most accurate ML method (the reader is referred to [21] and Section 2.5.7 in this paper). The ensemble methods combine several base estimators' predictions, improving a single estimator's performance and accuracy [139]. In a recent study, a new ensemble-based model, called the multi-grained cascade forest (gcForest), was proposed by Zhou [140]. In this approach, several base estimators are stacked to form a layer-by-layer model. As the name implies, a multi-grained scanning technique is used to construct this estimator, and a cascade forest is included to enhance the depth and diversity of the traditional forest model. Shallow structure models combine spectral, structural, and semantic features for the classification of remotely sensed imagery [141]. However, the hetero-spectrum phenomenon in high-resolution RS image classification is very obvious. Therefore, in complex structures, such as heterogeneous wetlands, shallow structure models may be negatively affected by computing power and unable to learn the sample information adequately.

The selection of ML algorithms in RS applications such as wetland studies is subjected to several influential factors, such as sensor type and its spatial and spectral resolution, training sample size, and the complexity of the classification problem, etc. For instance, the RF model could be considered to be the most efficient if useful features can be derived from the RS imagery and fed to it. In the case that extracted features are not beneficial in classification, DL models could be the best selection as they have the ability to retrieve complex patterns and informative features from the satellite image data. For example, CNN has shown performance improvements over SVM and RF [21, 142]. However, the main problem with DL approaches is the lack of interpretability due to their hidden layers, "black box" nature [143]. Additionally, the efficiency of DL models strongly depends on the availability of a high number of

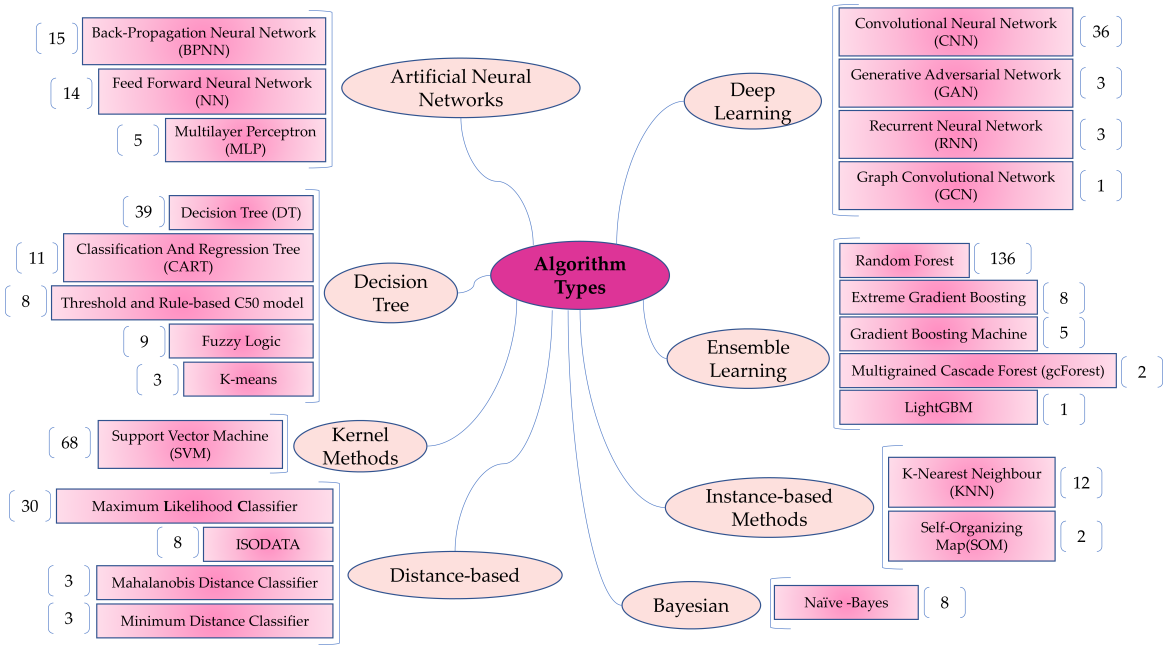



Figure 2.16: Number of studies employed different ML models in wetland studies.

training samples, i.e., ground truth data [21]. Moreover, DL models require specialized knowledge, are expensive to implement computationally, and require dedicated hardware to operate.

Overall, the direct comparisons of different kinds of methodologies might not be fair since the experiment settings, and the hyperparameter tuning process for different ML and DL models are not the same (e.g., the input features used for RF and other DL methods are different). With the advent of big data and the continuous addition of satellite-based data, we cannot rely on only one specific methodology for all RS applications. There is a need to develop ensemble and hybrid approaches to tackle this voluminous data coming from a variety of sources. As such, giving merit to a single approach is difficult, as past comparison-based studies and some review papers provide readers with often contradictory conclusions based on processing workload, input datasets, and the evaluated performance metrics, which is somewhat confusing.

### Google Earth Engine (GEE)

For the mapping and monitoring of wetlands over broad spatial scales and for long periods of time, long-term earth observation data archives, such as those provided

by the optical Landsat repository (1984 onwards), are crucial resources. Mapping wetlands on a long-time scale along with high spatial resolution requires collecting and storing large datasets and often involves complicated processing and manipulation. It is infeasible or time-consuming to use conventional image processing software, such as ENVI and ERDAS; thus, an effective platform is required. For such a system to be established, strong computing power and high capacity of data storage is needed, and these can be limiting factors for many decisionmakers around the world, especially in resource-poor regions. With GEE, users can freely access cloud-based computing resources and parallel processing for analysis on a global scale [7]. To provide benefits to the broader community, GEE offers an online integrated development environment using Earth Engine JavaScript, designed to ease geospatial data analysis and preparation complexities without the need for heavy data downloading and data-intensive processing. Additionally, GEE supports Python through its Earth Engine Python API, offering users the flexibility to perform geospatial analyses in both JavaScript and Python environments. It hosts petabyte-scale RS data, including the NASA's Landsat and ESA's Sentinel archives, crucially corrected to surface reflectance, providing a unique opportunity for developing and disseminating worldwide environmental monitoring systems. In addition to the data provision, GEE is equipped with many ML tools, such as RF Classification. Studies using GEE as an RS data provider with ML techniques have become more numerous since its advent in 2015. Such studies account for 11% of included studies (n = 40 of 344) in the current systematic review. More details of these publications have been presented in Figure 2.17 and Table 2.7.

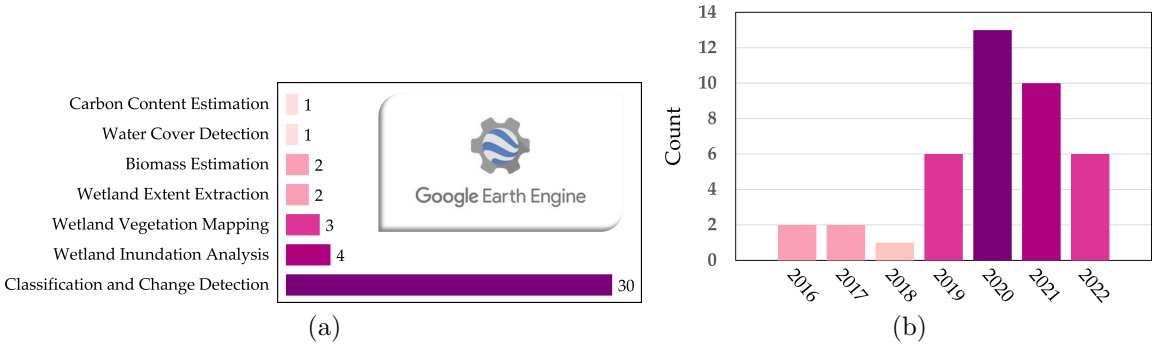



Figure 2.17: (a) Frequency of each type of wetland study using GEE. (b) Frequency of GEE-based wetland studies per year.

Table 2.7: List of included papers in the meta-analysis that applied GEE in wetland studies sorted by publication date.

| # | Ref. | Application Type | Publication Date | # | Ref. | Application Type | Publication Date |
|---|---|---|---|---|---|---|---|
| 1 | [144] | Change Detection | May, 2016 | 21 | [145] | Classification | Aug, 2020 |
| 2 | [146] | Wetland Inundation Analysis | Dec, 2016 | 22 | [147] | Classification | Sep, 2020 |
| 3 | [148] | Classification | Dec, 2017 | 23 | [7] | Change Detection | Nov, 2020 |
| 4 | [22] | Classification | Dec, 2017 | 24 | [149] | Wetland Extent Extraction | Dec, 2020 |
| 5 | [150] | Carbon Content and Biomass | May, 2018 | 25 | [151] | Wetland Vegetation Mapping | Feb, 2021 |
| 6 | [46] | Classification | Jan, 2019 | 26 | [152] | Classification | Jun, 2021 |
| 7 | [153] | Classification | Apr, 2019 | 27 | [154] | Change Detection | Jun, 2021 |
| 8 | [24] | Classification | Jun, 2019 | 28 | [127] | Classification | Aug, 2021 |
| 9 | [19] | Wetland Inundation Analysis | Jul, 2019 | 29 | [155] | Change Detection | Sep, 2021 |
| 10 | [156] | Classification | Oct, 2019 | 30 | [157] | Classification and Change Detection | Oct, 2021 |
| 11 | [158] | Change Detection | Oct, 2019 | 31 | [159] | Wetland Vegetation Mapping | Oct, 2021 |
| 12 | [160] | Classification | Jan, 2020 | 32 | [161] | Change Detection | Nov, 2021 |
| 13 | [96] | Classification | Jan, 2020 | 33 | [162] | Classification | Nov, 2021 |
| 14 | [163] | Inundation Analysis and Biomass | Feb, 2020 | 34 | [134] | Classification | Dec, 2021 |
| 15 | [164] | Classification | Mar, 2020 | 35 | [97] | Wetland Extent Extraction | Jan, 2022 |
| 16 | [51] | Wetland Vegetation Mapping | Apr, 2020 | 36 | [94] | Classification | Jan, 2022 |
| 17 | [165] | Classification | Apr, 2020 | 37 | [166] | Classification | Feb, 2022 |
| 18 | [99] | Classification | May, 2020 | 38 | [167] | Wetland Inundation Analysis | May, 2022 |
| 19 | [168] | Water Cover Detection | May, 2020 | 39 | [169] | Classification | May, 2022 |
| 20 | [170] | Classification | May, 2020 | 40 | [171] | Change Detection | Jun, 2022 |

### 2.5.6 Feature Selection and Derivation

The features used in wetlands research from optical data are mostly spectral reflectance characteristics, such as the normal difference vegetation index (NDVI), normal difference water index (NDWI), and soil-adjusted vegetation index (SAVI), etc. These feature indices have been widely used in monitoring and mapping wetlands [7, 46, 76, 99]. When identifying wetlands, relations to neighbor objects may be useful features because of the spatial relationship of objects in distribution. These features aid the identification of wetlands and improve the accuracy of classification. For instance, texture consists of visual patterns or spatial patterns of pixels that may have statistical properties, structural properties, or both [172]. The texture of imagery has been extensively investigated and studied as a supplement to spectral data for the analysis of wetland zones, and has proven effective [172, 173]. There are many ways to describe texture. The gray-level covariance co-occurrence matrix (GLCM) has proven effective for the identification of wetlands [174].

In the current meta-analysis, different feature sets employed in wetland studies are grouped as follows: (1) original spectral bands or backscattering coefficients; (2) spectral indices; (3) image texture components derived from the GLCM; (4) SAR polarimetric features (5) geometric features; and (6) topographic variables derived from digital terrain models (see Figure 2.18 and Table 2.8).

Rather than relying solely on a single feature category, the majority of wetland studies combine several features from multiple categories. Spectral indices and SAR polarimetric decompositions, followed by textural, topographical, and geometric features, are frequently used to determine the contribution of each feature category. According to several studies involving the feature selection process, the spectral and polarimetric features that are simple and easy to extract have been shown to be more powerful than other types of features in wetland studies and in discriminating class types.

### 2.5.7 Accuracy Assessment

Here, the reported overall accuracies were assessed and compared to comprehensively investigate the RS-based wetland studies. Figure 2.19a shows the histogram of the overall accuracies reported in wetland classification studies. Note that the papers

Table 2.8: Common features extracted from Optical and SAR imagery in wetland studies.

| Category | Imagery | Indicator/Band | Ref. |
|---|---|---|---|
| Imagery Features | Optical | blue band, red band, green band, red-edge band, near-infrared, shortwave-infrared | - |
| | SAR | Backscatter Coefficient (HH, HV, VH, VV) | - |
| Spectral Indices (vegetation/water/soil indices) | Optical | Normalized Difference Vegetation Index (NDVI) | [155, 156, 169, 175, 176, 177, 178, 179, 180] |
| | Optical | Normalized Difference Water Index (NDWI) | [155, 156, 169, 175, 176, 177, 180, 181] |
| | Optical | Enhanced Vegetation Index (EVI) | [169, 175] |
| | Optical | Simple Ratio (SR) | [169] |
| | Optical | Modified Normalized Difference Water Index (MNDWI) | [177] |
| | Optical | Soil-Adjusted Vegetation Index (SAVI) | [175, 176, 181] |
| | Optical | Modified Soil-Adjusted Vegetation Index-2 (MSAVI2) | [175] |
| | Optical | Modified Normalized Difference Water Index (MNDWI) | [175] |
| | Optical | Tasseled-Cap Transformation Brightness (TCB) | [175, 182] |
| | Optical | TC-Greenness (TCG) | [175, 182] |
| | Optical | TC-Wetness (TCW) | [175, 182] |
| | Optical | Green Chlorophyll Index (Clgreen) | [177] |
| Textural Metrics (GLCM) | Optical and SAR | Mean | [169, 176, 178] |
| | Optical and SAR | Variance | [169, 176] |
| | Optical and SAR | Homogeneity | [169, 176, 177, 178, 181, 183] |
| | Optical and SAR | Contrast | [169, 176, 178, 181, 183] |
| | Optical and SAR | Entropy | [169, 176, 178, 181, 183] |
| | Optical and SAR | Angular Second Moment | [169, 176, 183] |
| | Optical and SAR | Correlation | [177, 178, 181, 183] |
| | Optical and SAR | Standard Deviation | [177, 178] |
| | Optical and SAR | Dissimilarity | [177, 183] |
| SAR Polarimetric Features | SAR | Pauli | [125, 184, 185] |
| | SAR | Cloude–Pottier | [3, 41, 45, 69, 73, 125, 184, 185] |
| | SAR | Freeman–Durden | [3, 41, 45, 72, 185, 186] |
| | SAR | Yamaguchi | [69, 125, 184, 185, 186] |
| | SAR | Neumann | [69, 125, 185] |
| | SAR | Touzi | [41, 125, 185, 186] |
| | SAR | H/A/Alpha | [125, 184, 185] |
| | SAR | Single-Bounce Eigenvalue Relative Difference | [69, 185] |
| | SAR | Double-Bounce Eigenvalue Relative Difference | [69, 185] |
| | SAR | Shannon Entropy | [69, 73, 130, 187] |
| | SAR | The Total Power (Span) | [21, 69, 99, 160] |
| | SAR | Ratio | [21, 99, 130, 160] |
| | SAR | Radar Vegetation Index | [69] |
| Geometric/Contextual Features | Optical and SAR | Area | [176, 178] |
| | Optical and SAR | Shape Index | [176, 183] |
| | Optical and SAR | Border Index | [176, 183] |
| | Optical and SAR | Number of Pixels | [176] |
| | Optical and SAR | Perimeter | [176, 183] |
| Topographic Features | LiDAR/DEM | Elevation data | [175] |
| | LiDAR/DEM | SLOP | [175] |
| | LiDAR/DEM | Topographic Wetness Index | [175] |
| | LiDAR/DEM | Terrain Surface Texture | [175] |

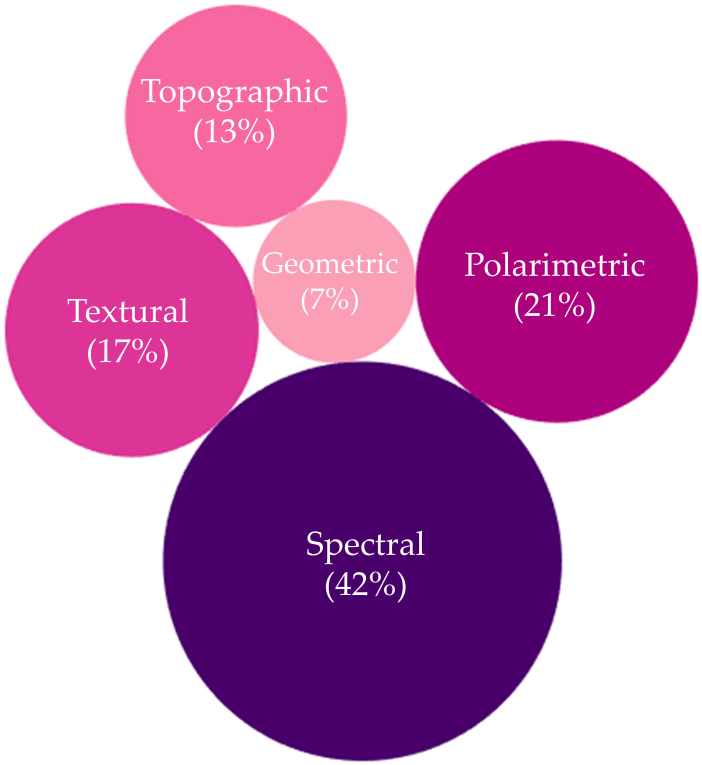



Figure 2.18: Percentage of studies that use each type of feature category. Note that as almost all studies have used either optical or SAR imagery features, the category of imagery features was excluded here.

(n = 67 out of 344) that did not report the overall accuracy of their classification methods have not been counted in this chart. According to Figure 2.19b, about 69% of the studies have an overall accuracy of greater than 85%. Additionally, studies of very small-scale areas yielded the highest overall accuracy, followed by investigations involving local and provincial study areas. The studies on a national scale, however, were found to have the lowest median overall accuracy. In Figure 2.19c, the overall accuracies based on the input data have been presented. Accordingly, the integration of optical and SAR datasets presents high classification accuracies in the case of wetland studies. Figure 2.19d depicts the reported overall accuracies from the methodological viewpoint. As can be seen, DL, ANN, and ensemble learning algorithms yielded the best classification results in the reviewed literature.

Supervised and object-based methodologies reported high median overall accuracies compared to unsupervised and pixel-based techniques, respectively (see Figure 2.19e and 2.19f. As shown in Figure 2.15b, the majority of studies (94%) employed supervised ML methods, while only 6% used unsupervised methods. The higher number of studies using supervised methods may contribute to the observed discrepancy in Figure 2.19e, where supervised methods show a much lower minimum overall accuracy compared to unsupervised methods. This could be due to the diverse range of supervised techniques and datasets used, which leads to a broader spread of results, including some lower-performing cases. In contrast, unsupervised methods, due to their less dependence on training data, might exhibit more consistent performance, though this does not necessarily translate to higher overall accuracy. Finally, Figure 2.19g represents the median overall accuracy reported in reviewed papers using high, medium, and coarse spatial resolution imagery. A median overall accuracy of more than 84% was achieved for all spatial resolution imagery. Studies using medium-resolution datasets achieved the highest median overall accuracies in wetland mapping, followed closely by those using high-resolution data.

### 2.5.8 Preprocessing and Processing Tools

Dealing with various RS datasets requires sufficient toolboxes and software. Several commercial and free open-source tools exist for RS image preprocessing and processing. Although great advances have been reached regarding toolbox development, a public release of processing software can further facilitate and promote experimentations. Figure 2.20 represents the most frequently employed tools and software for data preprocessing and processing in wetland studies (according to the reviewed literature). As shown, ArcGIS, ENVI, and Python programming packages (such as Scikit-learn, Keras, Tensorflow, PyTorch, Matplotlib, and Numpy) are the most popular and widely used tools for RS data processing when it comes to the study of wetland areas.

## 2.6 Future Perspective

As a part of the systematic review of the literature, this study also proposes the following three general suggestions for future research in order to shed light on issues

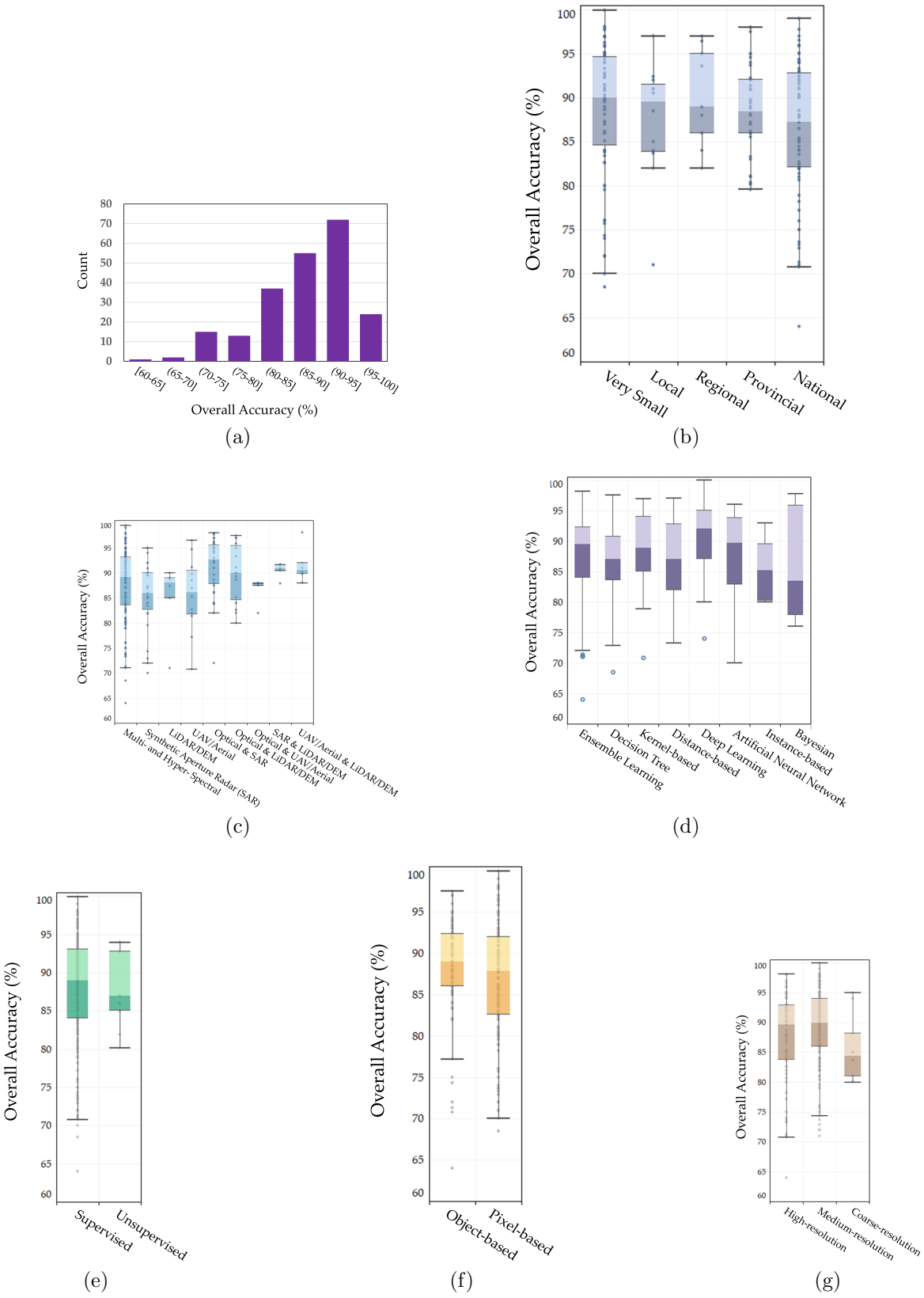



Figure 2.19: (a) The histogram of the overall accuracies reported in wetland classification papers. Box-and-whisker plots displaying the overall accuracies reported in RS-based wetland classification studies according to the (b) study extent, (c) utilized data type, (d) type of employed ML algorithm, (e) supervised or unsupervised models, (f) pixel-based or object-based methods, and (g) selected image resolution.




Figure 2.20: The main tools used for data preprocessing and processing in wetland studies. The larger the text, the more frequently the tool used in papers.

identified during the review process (Figure 2.21). Considering the ever-increasing stresses upon and loss of wetland areas, implementing the following suggestions in the future seems both appropriate and necessary, and has a high potential to make a difference to practitioners and policymakers.

1. Wetland sustainability policy: wetlands are at risk, and those around agricultural land or near urban areas have suffered huge losses with extended cultivation and urbanization. This indicates that upgrades and reinforcements of existing legislation, policies, programs, and strategic ecosystem plans are seriously required to protect and preserve wetlands habitat. Land use decisions are mostly influenced by agricultural policies and urban planners. On the one hand, agricultural policies try to act as an economic stimulus (economic gain trumps)

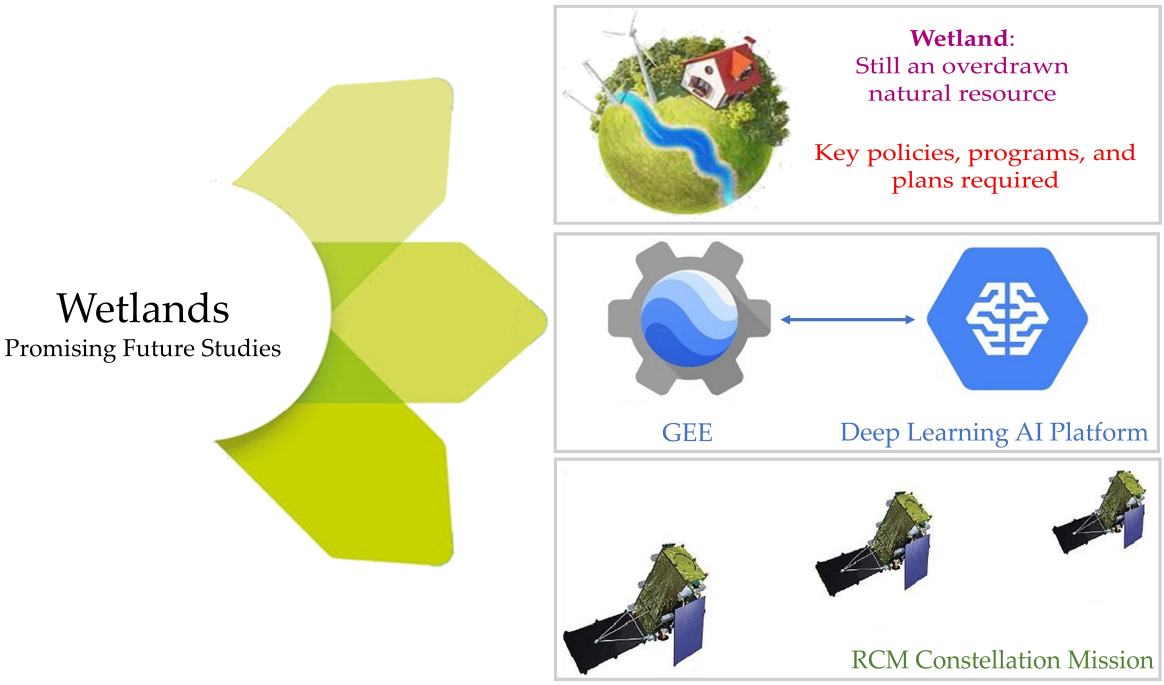



Figure 2.21: General overview of key recommendations for future studies to combat the challenges of wetland monitoring.

for crop production and cultivation expansion, which constitutes an encroachment on wetland areas. On the other hand, with the expansion of urbanization around wetlands, many people now live in and around wetlands and rely on their resources for their livelihoods. Moreover, wetlands near urban centers are under increasing developmental pressure for residential purposes. Accordingly, educating the community about the importance and benefits of wetlands and encouraging volunteer monitoring programs are perhaps the best ways to protect them. Indeed, developing community advocacy that is persistent, watchful, and active to empower communities to be more active stewards of wetlands would be wise to preserve wetlands. Doing so could minimize the adverse/negative effects of agricultural activities and urban expansion on neighboring and adjacent wetlands. As a consequence, decisions by local communities are critical to the successful sustainable management of wetlands.

2. The use of state-of-the-art DL models combined with GEE has the potential to make substantial progress toward wetland status monitoring, which has remained undocumented in the literature. Utilizing such a system would allow a

large area of wetlands, whether globally or nationally, to be studied for automatic and efficient monitoring, thereby minimizing human involvement in data processing and enhancing the accuracy of monitoring results. Therefore, intelligent monitoring and assessment of wetland status are essential for wetland management and strategy formulation.

3. Based on Figure 2.19c, SAR images show high potential for wetland monitoring. The recent deployment of SAR systems in RS, such as in the RADARSAT Constellation Mission (RCM), has resulted in a number of new applications [188]. This mission is a continuation of RADARSAT-1 and RADARSAT-2 and is conducted by the Canadian Space Agency (CSA) under the RADARSAT project. It offers a variety of imaging modes from 100 m low resolution to high 3 m resolution [188, 189]. As noted before, the primary advantage of SAR is that it provides repeatable data acquisition while being relatively unaffected by atmospheric effects, making it a reliable data acquisition technology. In the ongoing efforts to inventory wetlands and monitor their changes, RCM is expected to provide an essential source of C-band SAR data. Although the RCM is a Canadian commercial mission, given the high number of papers affiliated with Canadian researchers, it is somewhat strange that the RCM compact polarimetry data have not yet attracted the interest of wetland researchers. This is partly due to the lack of a suitable standard coverage, but one has been added by the CSA to improve the availability of suitable data. This study highly recommends the employment of promising new technologies and data for future wetland inventory and monitoring, including the upcoming NISAR mission.

## 2.7 Conclusions

In this study, the trend of worldwide RS-based wetland monitoring studies was established, exploring 344 papers published in the last three decades. Over fifteen sub-fields were summarized and highlighted, including ML approaches and their accuracies in wetland studies, RS data types and their corresponding accuracies, journals / conferences / publishers, authors affiliations, publications per year, the geographical distribution of case studies and the corresponding study extent, and paper citations. Through this, a comprehensive meta-analysis was used to discuss the utilization of

RS and ML tools in these subfields. Consequently, this paper addresses the role of RS and ML tools in supporting global wetland monitoring. Research opportunities and directions for further supporting wetlands studies were also presented in the paper. In summary, the general findings of this review paper concerning both technological and substantive viewpoints are as follows:

- A total of 88 journals have published the papers summarized in the present meta-analysis (with a share of 89%). The papers from the IGARSS conference, as well as a few from other international conference proceedings, were also included. About 67% of these publications were published between 2018 and 2022.

- More than half (51%) of the reviewed publications investigated wetlands from the perspective of classifying wetland zones, while 14% analyzed the changes within the wetlands. Wetland vegetation mapping and wetland extent recognition are in third and fourth places, with a share of 12% and 7% among all reviewed papers.

- Over 70% of the research studies have been conducted in China, the USA, and Canada, illustrating the need for wider international efforts to be undertaken in other countries in order to have consistent monitoring of wetlands across the globe. Over the past few years, the number of wetland studies has increased. In light of the increase in quality RS data availability, the launch of new RS platforms, as well as increased computing capabilities, and the growing interest in wetlands as part of climate change research, it is likely that this trend will continue.

- Slightly more than three-quarters of the studies have been conducted at areas with very small and local scales, whereas a few national-scale research papers have been published. More large-scale (e.g., continental-scale) studies are likely to be conducted as the number of satellites continues to increase and data become more widely available. The very recent ability of GEE to apply DL models has also opened up new possibilities for large-scale wetland classification research.

- The largest number of studies have been conducted on optical sensors using the Landsat archive (with 201 studies) and Sentinel-2 (with 54 studies), while SAR-based studies mostly employed data from Sentinel-1 (with 45 studies) and

RADARSAT-2 (with 31 studies) missions. This is likely partially due to the relatively long history of these datasets and low/no cost availability.

- Reviewed studies indicated that optical images had most often been used in the wetland monitoring tasks with 247 studies, followed by SAR datasets with 116 studies. A fusion of data types, including optical and SAR data, increases overall accuracy compared to each data type separately.

- A review of the published literature from the methodological viewpoint found that 152 studies adopted ensemble learning methods, 70 employed DT-based methods, and 68 utilized kernel-based methods. Further, among different classification approaches, CNN as a DL model, as well as RF as a ML model are the most successful classifiers for wetland mapping.

- As expected, spatial resolution was highly correlated with the overall accuracy of the wetland classification. This shows that wetland mapping may be improved by high/medium resolution RS imagery, at least until some minimum resolution threshold is reached.

- In comparison to pixel-based and unsupervised methods, object-based and supervised methods were mostly preferred for mapping and delineating wetlands owing to their simplicity and higher accuracy. On a national or continental scale, however, employing object-based analysis can be challenging.

## 2.8 Future Directions & Recommendations

While optical and SAR data have shown significant potential for wetland monitoring, their combination and utilization of complementary strengths may open opportunities to address some unexplored limitations, such as the lack of sufficient ground-truth samples in wetland study areas when using and training AI models.

Future research should prioritize this integration by proposing advanced DL frameworks that effectively merge the spectral information from multispectral imagery with the structural information from SAR data. Such frameworks can improve classification accuracy, particularly in complex wetland environments with heterogeneous land cover types. The upcoming chapter (Chapter 3) will address this by exploring the role of

combined C-band SAR and multispectral imagery in achieving robust wetland mapping, assessing the capacity of this synergy to enhance data-driven insights.

Additionally, advancements in SAR technology, particularly with the deployment of systems like the RCM, have unlocked a range of innovative applications. The high temporal resolution and consistent C-band SAR data from RCM offer an invaluable resource for Canadian wetland mapping, monitoring seasonal changes, and assessing phenological cycles. In the ongoing efforts to map and monitor wetlands, RCM is anticipated to play a crucial role by providing frequent, reliable data that can help detect subtle changes in wetland ecosystems, even in cloud-prone or low-light conditions where optical data may be limited.

Moreover, a review of the current literature indicates that RCM's CP-SAR data has not yet drawn substantial interest from wetland researchers. There is a pressing need for research that examines the application of these advanced SAR data to capture intricate wetland patterns and dynamic changes, particularly in ecologically sensitive or fragmented wetland regions. This thesis underscores the potential of CP in RCM data to revolutionize wetland research by offering a new layer of information that can enhance classification accuracy and reveal nuanced structural details in wetland habitats. This research (in Chapter 4 & 5) will focus on developing novel techniques tailored to the unique characteristics of wetland environments, exploiting CP to improve accuracy in delineating wetland types, detecting seasonal dynamics, and assessing hydrological impacts. By advocating for these advanced technologies, this work aims to set a precedent for future wetland mapping and monitoring practices that harness the full capabilities of RCM's CP data.

Lastly, the advent of cloud-based geospatial processing platforms, such as GEE, has revolutionized environmental monitoring by providing access to extensive datasets and robust computational capabilities. Additionally, the availability of LiDAR data has the potential to enhance the characterization of wetland structures, particularly in analyzing vegetation canopy height (VCH). Utilizing GEE, Chapter 6 will investigate the integration of VCH derived from LiDAR data across various wetland case studies, emphasizing its potential to improve wetland classification accuracy and deepen our understanding of wetland structures.

## 2.9 References

[1] S. Paul and S. Pal, "Predicting wetland area and water depth of ganges moribund deltaic parts of india," *Remote Sensing Applications: Society and Environment*, vol. 19, p. 100338, 2020.

[2] T. M. Berhane, C. R. Lane, Q. Wu, B. C. Autrey, O. A. Anenkhonov, V. V. Chepinoga, and H. Liu, "Decision-tree, rule-based, and random forest classification of high-resolution multispectral imagery for wetland mapping and inventory," *Remote sensing*, vol. 10, no. 4, p. 580, 2018.

[3] F. Mohammadimanesh, B. Salehi, M. Mahdianpari, M. Motagh, and B. Brisco, "An efficient feature optimization for wetland mapping by synergistic use of sar intensity, interferometry, and polarimetry data," *International journal of applied earth observation and geoinformation*, vol. 73, pp. 450–462, 2018.

[4] S. Mitra, R. Wassmann, and P. L. Vlek, "An appraisal of global wetland area and its organic carbon stock," *Current science*, vol. 88, no. 1, pp. 25–35, 2005.

[5] X. Meng, S. Zhang, and S. Zang, "Lake wetland classification based on an svm-cnn composite classifier and high-resolution images using wudalianchi as an example," *Journal of Coastal Research*, vol. 93, no. SI, pp. 153–162, 2019.

[6] M. Mahdianpari, H. Jafarzadeh, J. Granger, F. Mohammadimanesh, B. Brisco, B. Salehi, S. Homayouni, and Q. Weng, "Monitoring of 30 years wetland changes in newfoundland, canada," in *2021 IEEE International Geoscience and Remote Sensing Symposium IGARSS*, pp. 88–91, IEEE, 2021.

[7] M. Mahdianpari, H. Jafarzadeh, J. E. Granger, F. Mohammadimanesh, B. Brisco, B. Salehi, S. Homayouni, and Q. Weng, "A large-scale change monitoring of wetlands using time series landsat imagery on google earth engine: a case study in newfoundland," *GIScience & Remote Sensing*, vol. 57, no. 8, pp. 1102–1124, 2020.

[8] L. Cui, X. Zuo, Z. Dou, Y. Huang, X. Zhao, X. Zhai, Y. Lei, J. Li, X. Pan, and

W. Li, "Plant identification of beijing hanshiqiao wetland based on hyperspectral data," *Spectroscopy Letters*, vol. 54, no. 5, pp. 381–394, 2021.

[9] S. Ghosh, S. Dinda, N. D. Chatterjee, and K. Das, "Analyzing risk factors for shrinkage and transformation of east kolkata wetland, india," *Spatial Information Research*, vol. 26, pp. 661–677, 2018.

[10] H. Guo, Y. Cai, Z. Yang, Z. Zhu, and Y. Ouyang, "Dynamic simulation of coastal wetlands for guangdong-hong kong-macao greater bay area based on multi-temporal landsat images and flus model," *Ecological Indicators*, vol. 125, p. 107559, 2021.

[11] S. Mahdavi, B. Salehi, J. Granger, M. Amani, B. Brisco, and W. Huang, "Remote sensing for wetland classification: A comprehensive review," *GIScience & remote sensing*, vol. 55, no. 5, pp. 623–658, 2018.

[12] M. Guo, J. Li, C. Sheng, J. Xu, and L. Wu, "A review of wetland remote sensing," *Sensors*, vol. 17, no. 4, p. 777, 2017.

[13] M. Mahdianpari, J. E. Granger, F. Mohammadimanesh, B. Salehi, B. Brisco, S. Homayouni, E. Gill, B. Huberty, and M. Lang, "Meta-analysis of wetland classification using remote sensing: A systematic review of a 40-year trend in north america," *Remote Sensing*, vol. 12, no. 11, p. 1882, 2020.

[14] K. B. Dang, M. H. Nguyen, D. A. Nguyen, T. T. H. Phan, T. L. Giang, H. H. Pham, T. N. Nguyen, T. T. V. Tran, and D. T. Bui, "Coastal wetland classification with deep u-net convolutional networks and sentinel-2 imagery: A case study at the tien yen estuary of vietnam," *Remote Sensing*, vol. 12, no. 19, p. 3270, 2020.

[15] S. A. Romshoo and I. Rashid, "Assessing the impacts of changing land cover and climate on hokersar wetland in indian himalayas," *Arabian Journal of Geosciences*, vol. 7, pp. 143–160, 2014.

[16] A. Davranche, G. Lefebvre, and B. Poulin, "Wetland monitoring using classification trees and spot-5 seasonal time series," *Remote sensing of environment*, vol. 114, no. 3, pp. 552–562, 2010.

[17] L.-M. Rebelo, C. M. Finlayson, and N. Nagabhatla, "Remote sensing and gis for wetland inventory, mapping and change analysis," *Journal of environmental management*, vol. 90, no. 7, pp. 2144–2153, 2009.

[18] B. R. Felton, G. L. O'Neil, M.-M. Robertson, G. M. Fitch, and J. L. Goodall, "Using random forest classification and nationally available geospatial data to screen for wetlands over large geographic regions," *Water*, vol. 11, no. 6, p. 1158, 2019.

[19] Q. Wu, C. R. Lane, X. Li, K. Zhao, Y. Zhou, N. Clinton, B. DeVries, H. E. Golden, and M. W. Lang, "Integrating lidar data and multi-temporal aerial imagery to map wetland inundation dynamics using google earth engine," *Remote sensing of environment*, vol. 228, pp. 1–13, 2019.

[20] T. M. Berhane, C. R. Lane, Q. Wu, O. A. Anenkhonov, V. V. Chepinoga, B. C. Autrey, and H. Liu, "Comparing pixel-and object-based approaches in effectively classifying wetland-dominated landscapes," *Remote sensing*, vol. 10, no. 1, p. 46, 2017.

[21] H. Jafarzadeh, M. Mahdianpari, and E. W. Gill, "Wet-gc: a novel multimodel graph convolutional approach for wetland classification using sentinel-1 and 2 imagery with limited training samples," *IEEE Journal of Selected Topics in Applied Earth Observations and Remote Sensing*, vol. 15, pp. 5303–5316, 2022.

[22] J. N. Hird, E. R. DeLancey, G. J. McDermid, and J. Kariyeva, "Google earth engine, open-access satellite data, and machine learning in support of large-area probabilistic wetland mapping," *Remote sensing*, vol. 9, no. 12, p. 1315, 2017.

[23] E. R. DeLancey, J. Kariyeva, J. Cranston, and B. Brisco, "Monitoring hydro temporal variability in alberta, canada with multi-temporal sentinel-1 sar data," *Canadian Journal of Remote Sensing*, vol. 44, no. 1, pp. 1–10, 2018.

[24] E. R. DeLancey, J. Kariyeva, J. T. Bried, and J. N. Hird, "Large-scale probabilistic identification of boreal peatlands using google earth engine, open-access satellite data, and machine learning," *PloS one*, vol. 14, no. 6, p. e0218165, 2019.

[25] C. Wang, M. Jia, N. Chen, and W. Wang, "Long-term surface water dynamics analysis based on landsat imagery and the google earth engine platform: A

case study in the middle yangtze river basin," *Remote Sensing*, vol. 10, no. 10, p. 1635, 2018.

[26] N. Gorelick, M. Hancher, M. Dixon, S. Ilyushchenko, D. Thau, and R. Moore, "Google earth engine: Planetary-scale geospatial analysis for everyone," *Remote sensing of Environment*, vol. 202, pp. 18–27, 2017.

[27] S. Czapiewski and D. Szumińska, "An overview of remote sensing data applications in peatland research based on works from the period 2010–2021," *Land*, vol. 11, no. 1, p. 24, 2021.

[28] S. M. Mirmazloumi, A. Moghimi, B. Ranjgar, F. Mohseni, A. Ghorbanian, S. A. Ahmadi, M. Amani, and B. Brisco, "Status and trends of wetland studies in canada using remote sensing technology with a focus on wetland classification: A bibliographic analysis," *Remote Sensing*, vol. 13, no. 20, p. 4025, 2021.

[29] J. Montgomery, C. Mahoney, B. Brisco, L. Boychuk, D. Cobbaert, and C. Hopkinson, "Remote sensing of wetlands in the prairie pothole region of north america," *Remote Sensing*, vol. 13, no. 19, p. 3878, 2021.

[30] S. Gxokwe, T. Dube, and D. Mazvimavi, "Multispectral remote sensing of wetlands in semi-arid and arid areas: a review on applications, challenges and possible future research directions," *Remote Sensing*, vol. 12, no. 24, p. 4190, 2020.

[31] S. Adeli, B. Salehi, M. Mahdianpari, L. J. Quackenbush, B. Brisco, H. Tamiminia, and S. Shaw, "Wetland monitoring using sar data: A meta-analysis and comprehensive review," *Remote Sensing*, vol. 12, no. 14, p. 2190, 2020.

[32] L. Chasmer, C. Mahoney, K. Millard, K. Nelson, D. Peters, M. Merchant, C. Hopkinson, B. Brisco, O. Niemann, J. Montgomery, *et al.*, "Remote sensing of boreal wetlands 2: methods for evaluating boreal wetland ecosystem state and drivers of change," *Remote Sensing*, vol. 12, no. 8, p. 1321, 2020.

[33] L. Chasmer, D. Cobbaert, C. Mahoney, K. Millard, D. Peters, K. Devito, B. Brisco, C. Hopkinson, M. Merchant, J. Montgomery, *et al.*, "Remote sensing of boreal wetlands 1: Data use for policy and management," *Remote Sensing*, vol. 12, no. 8, p. 1320, 2020.

[34] B. Minasny, Ö. Berglund, J. Connolly, C. Hedley, F. de Vries, A. Gimona, B. Kempen, D. Kidd, H. Lilja, B. Malone, *et al.*, "Digital mapping of peatlands–a critical review," *Earth-Science Reviews*, vol. 196, p. 102870, 2019.

[35] D. Moher, A. Liberati, J. Tetzlaff, D. G. Altman, and t. PRISMA Group*, "Preferred reporting items for systematic reviews and meta-analyses: the prisma statement," *Annals of internal medicine*, vol. 151, no. 4, pp. 264–269, 2009.

[36] H. Jafarzadeh, M. Mahdianpari, S. Homayouni, F. Mohammadimanesh, and M. Dabboor, "Oil spill detection from synthetic aperture radar earth observations: A meta-analysis and comprehensive review," *GIScience & Remote Sensing*, vol. 58, no. 7, pp. 1022–1051, 2021.

[37] K. Millard and M. Richardson, "On the importance of training data sample selection in random forest image classification: A case study in peatland ecosystem mapping," *Remote sensing*, vol. 7, no. 7, pp. 8489–8515, 2015.

[38] I. Dronova, P. Gong, and L. Wang, "Object-based analysis and change detection of major wetland cover types and their classification uncertainty during the low water period at poyang lake, china," *Remote sensing of Environment*, vol. 115, no. 12, pp. 3220–3236, 2011.

[39] J.-R. B. Bwangoy, M. C. Hansen, D. P. Roy, G. De Grandi, and C. O. Justice, "Wetland mapping in the congo basin using optical and radar remotely sensed data and derived topographical indices," *Remote Sensing of Environment*, vol. 114, no. 1, pp. 73–86, 2010.

[40] C. Baker, R. Lawrence, C. Montagne, and D. Patten, "Mapping wetlands and riparian areas using landsat etm+ imagery and decision-tree-based models," *Wetlands*, vol. 26, no. 2, pp. 465–474, 2006.

[41] M. Mahdianpari, B. Salehi, F. Mohammadimanesh, and M. Motagh, "Random forest wetland classification using alos-2 l-band, radarsat-2 c-band, and terrasar-x imagery," *ISPRS Journal of Photogrammetry and Remote Sensing*, vol. 130, pp. 13–31, 2017.

[42] X. Han, X. Chen, and L. Feng, "Four decades of winter wetland changes in poyang lake based on landsat observations between 1973 and 2013," *Remote Sensing of Environment*, vol. 156, pp. 426–437, 2015.

[43] S. Van Beijma, A. Comber, and A. Lamb, "Random forest classification of salt marsh vegetation habitats using quad-polarimetric airborne sar, elevation and optical rs data," *Remote Sensing of Environment*, vol. 149, pp. 118–129, 2014.

[44] T. Liu, A. Abd-Elrahman, J. Morton, and V. L. Wilhelm, "Comparing fully convolutional networks, random forest, support vector machine, and patch-based deep convolutional neural networks for object-based wetland mapping using images from small unmanned aircraft system," *GIScience & remote sensing*, vol. 55, no. 2, pp. 243–264, 2018.

[45] J. M. Corcoran, J. F. Knight, and A. L. Gallant, "Influence of multi-source and multi-temporal remotely sensed and ancillary data on the accuracy of random forest classification of wetlands in northern minnesota," *Remote Sensing*, vol. 5, no. 7, pp. 3212–3238, 2013.

[46] M. Mahdianpari, B. Salehi, F. Mohammadimanesh, S. Homayouni, and E. Gill, "The first wetland inventory map of newfoundland at a spatial resolution of 10 m using sentinel-1 and sentinel-2 data on the google earth engine cloud computing platform," *Remote Sensing*, vol. 11, no. 1, p. 43, 2018.

[47] Y. Lin, J. Yu, J. Cai, N. Sneeuw, and F. Li, "Spatio-temporal analysis of wetland changes using a kernel extreme learning machine approach," *Remote Sensing*, vol. 10, no. 7, p. 1129, 2018.

[48] S. Munishi and G. Jewitt, "Degradation of kilombero valley ramsar wetlands in tanzania," *Physics and Chemistry of the Earth, Parts A/B/C*, vol. 112, pp. 216–227, 2019.

[49] T. Basu, A. Das, Q. B. Pham, N. Al-Ansari, N. T. T. Linh, and G. Lagerwall, "Development of an integrated peri-urban wetland degradation assessment approach for the chatra wetland in eastern india," *Scientific reports*, vol. 11, no. 1, p. 4470, 2021.

[50] A. Chatziantoniou, G. P. Petropoulos, and E. Psomiadis, "Co-orbital sentinel 1 and 2 for lulc mapping with emphasis on wetlands in a mediterranean setting based on machine learning," *Remote Sensing*, vol. 9, no. 12, p. 1259, 2017.

[51] B. Slagter, N.-E. Tsendbazar, A. Vollrath, and J. Reiche, "Mapping wetland characteristics using temporally dense sentinel-1 and sentinel-2 data: A case

study in the st. lucia wetlands, south africa," *International Journal of Applied Earth Observation and Geoinformation*, vol. 86, p. 102009, 2020.

[52] E. Yirsaw, W. Wu, X. Shi, H. Temesgen, and B. Bekele, "Land use/land cover change modeling and the prediction of subsequent changes in ecosystem service values in a coastal area of china, the su-xi-chang region," *Sustainability*, vol. 9, no. 7, p. 1204, 2017.

[53] X. Hu, P. Zhang, Q. Zhang, and J. Wang, "Improving wetland cover classification using artificial neural networks with ensemble techniques," *GIScience & Remote Sensing*, vol. 58, no. 4, pp. 603–623, 2021.

[54] L. Kumar and P. Sinha, "Mapping salt-marsh land-cover vegetation using high-spatial and hyperspectral satellite data to assist wetland inventory," *GIScience & Remote Sensing*, vol. 51, no. 5, pp. 483–497, 2014.

[55] A. Zhang, G. Sun, P. Ma, X. Jia, J. Ren, H. Huang, and X. Zhang, "Coastal wetland mapping with sentinel-2 msi imagery based on gravitational optimized multilayer perceptron and morphological attribute profiles," *Remote Sensing*, vol. 11, no. 8, p. 952, 2019.

[56] G. Cheng, X. Xie, J. Han, L. Guo, and G.-S. Xia, "Remote sensing image scene classification meets deep learning: Challenges, methods, benchmarks, and opportunities," *IEEE Journal of Selected Topics in Applied Earth Observations and Remote Sensing*, vol. 13, pp. 3735–3756, 2020.

[57] B. L. Turner, E. F. Lambin, and A. Reenberg, "The emergence of land change science for global environmental change and sustainability," *Proceedings of the National Academy of Sciences*, vol. 104, no. 52, pp. 20666–20671, 2007.

[58] M. Hussain, D. Chen, A. Cheng, H. Wei, and D. Stanley, "Change detection from remotely sensed images: From pixel-based to object-based approaches," *ISPRS Journal of photogrammetry and remote sensing*, vol. 80, pp. 91–106, 2013.

[59] A. Singh, "Review article digital change detection techniques using remotely-sensed data," *International journal of remote sensing*, vol. 10, no. 6, pp. 989–1003, 1989.

[60] T. Hu, J. Liu, G. Zheng, Y. Li, and B. Xie, "Quantitative assessment of urban wetland dynamics using high spatial resolution satellite imagery between 2000 and 2013," *Scientific Reports*, vol. 8, no. 1, p. 7409, 2018.

[61] H. Zhou, H. Jiang, G. Zhou, X. Song, S. Yu, J. Chang, S. Liu, Z. Jiang, and B. Jiang, "Monitoring the change of urban wetland using high spatial resolution remote sensing data," *International Journal of Remote Sensing*, vol. 31, no. 7, pp. 1717–1731, 2010.

[62] F. Yuan, K. E. Sawaya, B. C. Loeffelholz, and M. E. Bauer, "Land cover classification and change analysis of the twin cities (minnesota) metropolitan area by multitemporal landsat remote sensing," *Remote sensing of Environment*, vol. 98, no. 2-3, pp. 317–328, 2005.

[63] D. Lu, P. Mausel, E. Brondizio, and E. Moran, "Change detection techniques," *International journal of remote sensing*, vol. 25, no. 12, pp. 2365–2401, 2004.

[64] L. Zhao, J. Yang, P. Li, and L. Zhang, "Seasonal inundation monitoring and vegetation pattern mapping of the erguna floodplain by means of a radarsat-2 fully polarimetric time series," *Remote Sensing of Environment*, vol. 152, pp. 426–440, 2014.

[65] M. Boueshagh and M. Hasanlou, "Estimating water level in the urmia lake using satellite data: a machine learning approach," *The International Archives of the Photogrammetry, Remote Sensing and Spatial Information Sciences*, vol. 42, pp. 219–226, 2019.

[66] X. Na, S. Zang, L. Liu, and M. Li, "Wetland mapping in the zhalong national natural reserve, china, using optical and radar imagery and topographical data," *Journal of Applied Remote Sensing*, vol. 7, no. 1, pp. 073554–073554, 2013.

[67] E. Brown, M. Aitkenhead, R. Wright, and I. Aalders, "Mapping and classification of peatland on the isle of lewis using landsat etm+," *Scottish Geographical Journal*, vol. 123, no. 3, pp. 173–192, 2007.

[68] H. Su, W. Yao, Z. Wu, P. Zheng, and Q. Du, "Kernel low-rank representation with elastic net for china coastal wetland land cover classification using gf-5 hyperspectral imagery," *ISPRS Journal of Photogrammetry and Remote Sensing*, vol. 171, pp. 238–252, 2021.

[69] X. Zhang, J. Xu, Y. Chen, K. Xu, and D. Wang, "Coastal wetland classification with gf-3 polarimetric sar imagery by using object-oriented random forest algorithm," *Sensors*, vol. 21, no. 10, p. 3395, 2021.

[70] M. W. Lang and E. S. Kasischke, "Using c-band synthetic aperture radar data to monitor forested wetland hydrology in maryland's coastal plain, usa," *IEEE Transactions on Geoscience and Remote Sensing*, vol. 46, no. 2, pp. 535–546, 2008.

[71] S. W. P. Rodrigues and P. W. M. Souza-Filho, "Use of multi-sensor data to identify and map tropical coastal wetlands in the amazon of northern brazil," *Wetlands*, vol. 31, pp. 11–23, 2011.

[72] M. A. Merchant, J. R. Adams, A. A. Berg, J. L. Baltzer, W. L. Quinton, and L. E. Chasmer, "Contributions of c-band sar data and polarimetric decompositions to subarctic boreal peatland mapping," *IEEE Journal of Selected Topics in Applied Earth Observations and Remote Sensing*, vol. 10, no. 4, pp. 1467–1482, 2016.

[73] L. White, K. Millard, S. Banks, M. Richardson, J. Pasher, and J. Duffe, "Moving to the radarsat constellation mission: Comparing synthesized compact polarimetry and dual polarimetry data with fully polarimetric radarsat-2 data for image classification of peatlands," *Remote Sensing*, vol. 9, no. 6, p. 573, 2017.

[74] L. White, B. Brisco, M. Dabboor, A. Schmitt, and A. Pratt, "A collection of sar methodologies for monitoring wetlands," *Remote sensing*, vol. 7, no. 6, pp. 7615–7645, 2015.

[75] L. Chasmer, C. Hopkinson, T. Veness, W. Quinton, and J. Baltzer, "A decision-tree classification for low-lying complex land cover types within the zone of discontinuous permafrost," *Remote Sensing of Environment*, vol. 143, pp. 73–84, 2014.

[76] H. Jafarzadeh, M. Mahdianpari, and E. Gill, "Meta-learning for wetland classification using a combination of sentinel-1 and sentinel-2 imagery," *ISPRS Annals of the Photogrammetry, Remote Sensing and Spatial Information Sciences*, vol. 3, pp. 47–52, 2022.

[77] B. Hosseiny, M. Mahdianpari, B. Brisco, F. Mohammadimanesh, and B. Salehi, "Wetnet: A spatial–temporal ensemble deep learning model for wetland classification using sentinel-1 and sentinel-2," *IEEE transactions on geoscience and remote sensing*, vol. 60, pp. 1–14, 2021.

[78] K. Millard and M. Richardson, "Wetland mapping with lidar derivatives, sar polarimetric decompositions, and lidar–sar fusion using a random forest classifier," *Canadian Journal of Remote Sensing*, vol. 39, no. 4, pp. 290–307, 2013.

[79] S. Rapinel, J.-B. Bouzillé, J. Oszwald, and A. Bonis, "Use of bi-seasonal landsat-8 imagery for mapping marshland plant community combinations at the regional scale," *Wetlands*, vol. 35, pp. 1043–1054, 2015.

[80] G. Kaplan and U. Avdan, "Monthly analysis of wetlands dynamics using remote sensing data," *ISPRS International Journal of Geo-Information*, vol. 7, no. 10, p. 411, 2018.

[81] D. F. Muñoz, P. Muñoz, A. Alipour, H. Moftakhari, H. Moradkhani, and B. Mortazavi, "Fusing multisource data to estimate the effects of urbanization, sea level rise, and hurricane impacts on long-term wetland change dynamics," *IEEE Journal of Selected Topics in Applied Earth Observations and Remote Sensing*, vol. 14, pp. 1768–1782, 2021.

[82] A. Judah and B. Hu, "The integration of multi-source remotely-sensed data in support of the classification of wetlands," *Remote Sensing*, vol. 11, no. 13, p. 1537, 2019.

[83] S. Rapinel, L. Hubert-Moy, and B. Clément, "Combined use of lidar data and multispectral earth observation imagery for wetland habitat mapping," *International journal of applied earth observation and geoinformation*, vol. 37, pp. 56–64, 2015.

[84] R. Jahncke, B. Leblon, P. Bush, and A. LaRocque, "Mapping wetlands in nova scotia with multi-beam radarsat-2 polarimetric sar, optical satellite imagery, and lidar data," *International Journal of Applied Earth Observation and Geoinformation*, vol. 68, pp. 139–156, 2018.

[85] M. S. Gilmore, E. H. Wilson, N. Barrett, D. L. Civco, S. Prisloe, J. D. Hurd, and C. Chadwick, "Integrating multi-temporal spectral and structural information

to map wetland vegetation in a lower connecticut river tidal marsh," *Remote Sensing of Environment*, vol. 112, no. 11, pp. 4048–4060, 2008.

[86] R. A. Araya-López, J. Lopatin, F. E. Fassnacht, and H. J. Hernández, "Monitoring andean high altitude wetlands in central chile with seasonal optical data: A comparison between worldview-2 and sentinel-2 imagery," *ISPRS journal of photogrammetry and remote sensing*, vol. 145, pp. 213–224, 2018.

[87] M. Cao, G. Liu, and X. Zhang, "An object-oriented approach to map wetland vegetation: a case study of yellow river delta," in *2007 IEEE International Geoscience and Remote Sensing Symposium*, pp. 4585–4587, IEEE, 2007.

[88] J. Mallick, S. Talukdar, S. Pal, A. Rahman, *et al.*, "A novel classifier for improving wetland mapping by integrating image fusion techniques and ensemble machine learning classifiers," *Ecological Informatics*, vol. 65, p. 101426, 2021.

[89] S. Hakdaoui, A. Emran, B. Pradhan, C.-W. Lee, and S. C. Nguemhe Fils, "A collaborative change detection approach on multi-sensor spatial imagery for desert wetland monitoring after a flash flood in southern morocco," *Remote Sensing*, vol. 11, no. 9, p. 1042, 2019.

[90] H. Pan, "A feature sequence-based 3d convolutional method for wetland classification from multispectral images," *Remote Sensing Letters*, vol. 11, no. 9, pp. 837–846, 2020.

[91] S. Tahsin, S. C. Medeiros, and A. Singh, "Consistent long-term monthly coastal wetland vegetation monitoring using a virtual satellite constellation," *Remote Sensing*, vol. 13, no. 3, p. 438, 2021.

[92] S. Berberoglu, K. T. Yilmaz, and C. Özkan, "Mapping and monitoring of coastal wetlands of cukurova delta in the eastern mediterranean region," *Biodiversity & Conservation*, vol. 13, pp. 615–633, 2004.

[93] D. Pouliot, R. Latifovic, J. Pasher, and J. Duffe, "Assessment of convolution neural networks for wetland mapping with landsat in the central canadian boreal forest region," *Remote Sensing*, vol. 11, no. 7, p. 772, 2019.

[94] S. Gxokwe, T. Dube, and D. Mazvimavi, "Leveraging google earth engine platform to characterize and map small seasonal wetlands in the semi-arid environments of south africa," *Science of the Total Environment*, vol. 803, p. 150139, 2022.

[95] Y. Gao, W. Li, M. Zhang, J. Wang, W. Sun, R. Tao, and Q. Du, "Hyperspectral and multispectral classification for coastal wetland using depthwise feature interaction network," *IEEE Transactions on Geoscience and Remote Sensing*, vol. 60, pp. 1–15, 2021.

[96] E. R. DeLancey, J. F. Simms, M. Mahdianpari, B. Brisco, C. Mahoney, and J. Kariyeva, "Comparing deep learning and shallow learning for large-scale wetland classification in alberta, canada," *Remote Sensing*, vol. 12, no. 1, p. 2, 2019.

[97] H. Sahour, K. M. Kemink, and J. O'connell, "Integrating sar and optical remote sensing for conservation-targeted wetlands mapping," *Remote Sensing*, vol. 14, no. 1, p. 159, 2021.

[98] L. Wen and M. Hughes, "Coastal wetland mapping using ensemble learning algorithms: A comparative study of bagging, boosting and stacking techniques," *Remote Sensing*, vol. 12, no. 10, p. 1683, 2020.

[99] M. Mahdianpari, B. Brisco, J. E. Granger, F. Mohammadimanesh, B. Salehi, S. Banks, S. Homayouni, L. Bourgeau-Chavez, and Q. Weng, "The second generation canadian wetland inventory map at 10 meters resolution using google earth engine," *Canadian Journal of Remote Sensing*, vol. 46, no. 3, pp. 360–375, 2020.

[100] R. Frohn, B. Autrey, C. Lane, and M. Reif, "Segmentation and object-oriented classification of wetlands in a karst florida landscape using multi-season landsat-7 etm+ imagery," *International Journal of Remote Sensing*, vol. 32, no. 5, pp. 1471–1489, 2011.

[101] C. Doyle, T. Beach, and S. Luzzadder-Beach, "Tropical forest and wetland losses and the role of protected areas in northwestern belize, revealed from landsat and machine learning," *Remote Sensing*, vol. 13, no. 3, p. 379, 2021.

[102] A. H. Ehsani and M. Shakeryari, "Monitoring of wetland changes affected by drought using four landsat satellite data and fuzzy artmap classification method (case study hamoun wetland, iran)," *Arabian Journal of Geosciences*, vol. 14, no. 14, p. 1363, 2021.

[103] Y. Liu, R. Jin, and W. Zhu, "Conversion of natural wetland to farmland in the tumen river basin: Human and environmental factors," *Remote Sensing*, vol. 13, no. 17, p. 3498, 2021.

[104] M. Mahdianpari, M. Rezaee, Y. Zhang, and B. Salehi, "Wetland classification using deep convolutional neural network," in *IGARSS 2018-2018 IEEE International Geoscience and Remote Sensing Symposium*, pp. 9249–9252, IEEE, 2018.

[105] M. Rezaee, M. Mahdianpari, Y. Zhang, and B. Salehi, "Deep convolutional neural network for complex wetland classification using optical remote sensing imagery," *IEEE Journal of Selected Topics in Applied Earth Observations and Remote Sensing*, vol. 11, no. 9, pp. 3030–3039, 2018.

[106] M. Mahdianpari, B. Salehi, F. Mohammadimanesh, B. Brisco, S. Mahdavi, M. Amani, and J. E. Granger, "Fisher linear discriminant analysis of coherency matrix for wetland classification using polsar imagery," *Remote Sensing of Environment*, vol. 206, pp. 300–317, 2018.

[107] J. Jiang, A. Li, W. Deng, and J. Bian, "Construction of a new classifier integrated multiple sources and multi-temporal remote sensing data for wetlands," *Procedia Environmental Sciences*, vol. 2, pp. 302–314, 2010.

[108] M. Zarei, M. Tazeh, V. Moosavi, and S. Kalantari, "Investigating the capability of thermal-moisture indices extracted from modis data in classification and trend in wetlands," *Journal of the Indian Society of Remote Sensing*, vol. 49, pp. 2583–2596, 2021.

[109] L. Chen, Z. Jin, R. Michishita, J. Cai, T. Yue, B. Chen, and B. Xu, "Dynamic monitoring of wetland cover changes using time-series remote sensing imagery," *Ecological Informatics*, vol. 24, pp. 17–26, 2014.

[110] G. Tana, H. Letu, Z. Cheng, and R. Tateishi, "Wetlands mapping in north america by decision rule classification using modis and ancillary data," *IEEE*

*Journal of Selected Topics in Applied Earth Observations and Remote Sensing*, vol. 6, no. 6, pp. 2391–2401, 2013.

[111] L. Jing, Y. Zhou, Q. Zeng, S. Liu, G. Lei, C. Lu, and L. Wen, "Exploring wetland dynamics in large river floodplain systems with unsupervised machine learning: A case study of the dongting lake, china," *Remote Sensing*, vol. 12, no. 18, p. 2995, 2020.

[112] P. A. Rupasinghe and P. Chow-Fraser, "Mapping phragmites cover using worldview 2/3 and sentinel 2 images at lake erie wetlands, canada," *Biological Invasions*, vol. 23, no. 4, pp. 1231–1247, 2021.

[113] L. Kumar, P. Sinha, and S. Taylor, "Improving image classification in a complex wetland ecosystem through image fusion techniques," *Journal of Applied Remote Sensing*, vol. 8, no. 1, pp. 083616–083616, 2014.

[114] M. Laba, R. Downs, S. Smith, S. Welsh, C. Neider, S. White, M. Richmond, W. Philpot, and P. Baveye, "Mapping invasive wetland plants in the hudson river national estuarine research reserve using quickbird satellite imagery," *Remote sensing of Environment*, vol. 112, no. 1, pp. 286–300, 2008.

[115] J. Xiao, Y. Xiao, X. Sun, J. Huang, and H. Wang, "Land cover classification of huixian wetland based on sar and optical image fusion," in *2020 IEEE 3rd International Conference on Information Communication and Signal Processing (ICICSP)*, pp. 316–320, IEEE, 2020.

[116] N. Wu, R. Shi, W. Zhuo, C. Zhang, and Z. Tao, "Identification of native and invasive vegetation communities in a tidal flat wetland using gaofen-1 imagery," *Wetlands*, vol. 41, pp. 1–17, 2021.

[117] N. Sun, W. Zhu, and Q. Cheng, "Gf-1 and landsat observed a 40-year wetland spatiotemporal variation and its coupled environmental factors in yangtze river estuary," *Estuarine, Coastal and Shelf Science*, vol. 207, pp. 30–39, 2018.

[118] M. Amani, B. Salehi, S. Mahdavi, and B. Brisco, "Spectral analysis of wetlands using multi-source optical satellite imagery," *ISPRS journal of photogrammetry and remote sensing*, vol. 144, pp. 119–136, 2018.

[119] D. A. Novresiandi and R. Nagasawa, "Polarimetric synthetic aperture radar application for tropical peatlands classification: a case study in siak river transect, riau province, indonesia," *Journal of Applied Remote Sensing*, vol. 11, no. 1, pp. 016040–016040, 2017.

[120] C. Liu, R. Tao, W. Li, M. Zhang, W. Sun, and Q. Du, "Joint classification of hyperspectral and multispectral images for mapping coastal wetlands," *IEEE Journal of Selected Topics in Applied Earth Observations and Remote Sensing*, vol. 14, pp. 982–996, 2020.

[121] S. Niculescu, J.-B. Boissonnat, C. Lardeux, D. Roberts, J. Hanganu, A. Billey, A. Constantinescu, and M. Doroftei, "Synergy of high-resolution radar and optical images satellite for identification and mapping of wetland macrophytes on the danube delta," *Remote Sensing*, vol. 12, no. 14, p. 2188, 2020.

[122] A. O. Amoakoh, P. Aplin, K. T. Awuah, I. Delgado-Fernandez, C. Moses, C. P. Alonso, S. Kankam, and J. C. Mensah, "Testing the contribution of multi-source remote sensing features for random forest classification of the greater amanzule tropical peatland," *Sensors*, vol. 21, no. 10, p. 3399, 2021.

[123] J. Corcoran, J. Knight, B. Brisco, S. Kaya, A. Cull, and K. Murnaghan, "The integration of optical, topographic, and radar data for wetland mapping in northern minnesota," *Canadian Journal of Remote Sensing*, vol. 37, no. 5, pp. 564–582, 2011.

[124] F. Mohammadimanesh, B. Salehi, M. Mahdianpari, B. Brisco, and M. Motagh, "Multi-temporal, multi-frequency, and multi-polarization coherence and sar backscatter analysis of wetlands," *ISPRS Journal of Photogrammetry and Remote Sensing*, vol. 142, pp. 78–93, 2018.

[125] Y. Chen, X. He, J. Xu, R. Zhang, and Y. Lu, "Scattering feature set optimization and polarimetric sar classification using object-oriented rf-sfs algorithm in coastal wetlands," *Remote Sensing*, vol. 12, no. 3, p. 407, 2020.

[126] L. L. Bourgeau-Chavez, S. Endres, R. Powell, M. J. Battaglia, B. Benscoter, M. Turetsky, E. S. Kasischke, and E. Banda, "Mapping boreal peatland ecosystem types from multitemporal radar and optical satellite imagery," *Canadian Journal of Forest Research*, vol. 47, no. 4, pp. 545–559, 2017.

[127] M. Mahdianpari, B. Brisco, J. Granger, F. Mohammadimanesh, B. Salehi, S. Homayouni, and L. Bourgeau-Chavez, "The third generation of pan-canadian wetland map at 10 m resolution using multisource earth observation data on cloud computing platform," *IEEE journal of selected topics in applied earth observations and remote sensing*, vol. 14, pp. 8789–8803, 2021.

[128] L. San Martín, N. S. Morandeira, R. Grimson, M. Rajngewerc, E. B. González, and P. Kandus, "The contribution of alos/palsar-1 multi-temporal data to map permanently and temporarily flooded coastal wetlands," *International Journal of Remote Sensing*, vol. 41, no. 4, pp. 1582–1602, 2020.

[129] M. Zhang, F. Chen, B. Tian, and D. Liang, "Multi-temporal sar image classification of coastal plain wetlands using a new feature selection method and random forests," *Remote Sensing Letters*, vol. 10, no. 3, pp. 312–321, 2019.

[130] J. Betbeder, S. Rapinel, T. Corpetti, E. Pottier, S. Corgne, and L. Hubert-Moy, "Multitemporal classification of terrasar-x data for wetland vegetation mapping," *Journal of applied remote sensing*, vol. 8, no. 1, pp. 083648–083648, 2014.

[131] X. Na, S. Zang, Y. Zhang, and L. Liu, "Wetland mapping and flood extent monitoring using optical and radar remotely sensed data and ancillary topographical data in the zhalong national natural reserve, china," in *Earth Resources and Environmental Remote Sensing/GIS Applications IV*, vol. 8893, pp. 390–396, SPIE, 2013.

[132] P. Xu, Z. Niu, and P. Tang, "Comparison and assessment of ndvi time series for seasonal wetland classification," *International Journal of Digital Earth*, vol. 11, no. 11, pp. 1103–1131, 2018.

[133] Y. Cai, X. Li, M. Zhang, and H. Lin, "Mapping wetland using the object-based stacked generalization method based on multi-temporal optical and sar data," *International journal of applied earth observation and geoinformation*, vol. 92, p. 102164, 2020.

[134] Q. Liu, Y. Zhang, L. Liu, Z. Wang, Y. Nie, and M. K. Rai, "A novel landsat-based automated mapping of marsh wetland in the headwaters of the brahmaputra, ganges and indus rivers, southwestern tibetan plateau," *International*

*Journal of Applied Earth Observation and Geoinformation*, vol. 103, p. 102481, 2021.

[135] X. Yang, Q. Qin, H. Yésou, T. Ledauphin, M. Koehl, P. Grussenmeyer, and Z. Zhu, "Monthly estimation of the surface water extent in france at a 10-m resolution using sentinel-2 data," *Remote Sensing of Environment*, vol. 244, p. 111803, 2020.

[136] Y. LeCun, Y. Bengio, and G. Hinton, "Deep learning," *nature*, vol. 521, no. 7553, pp. 436–444, 2015.

[137] C. Yao, Y. Zhang, and H. Liu, "Application of convolutional neural network in classification of high resolution agricultural remote sensing images," *The international archives of the photogrammetry, remote sensing and spatial information sciences*, vol. 42, pp. 989–992, 2017.

[138] G. L. O'Neil, J. L. Goodall, M. Behl, and L. Saby, "Deep learning using physically-informed input data for wetland identification," *Environmental modelling & software*, vol. 126, p. 104665, 2020.

[139] H. Jafarzadeh, M. Mahdianpari, E. Gill, F. Mohammadimanesh, and S. Homayouni, "Bagging and boosting ensemble classifiers for classification of multispectral, hyperspectral and polsar data: a comparative evaluation," *Remote Sensing*, vol. 13, no. 21, p. 4405, 2021.

[140] Z.-H. Zhou, "andfeng j.. deep forest: towards an alternative to deep neural networks," in *Proceedings of the 26th International Joint Conference on Artificial Intelligence*, 2017.

[141] X. Huang and L. Zhang, "An svm ensemble approach combining spectral, structural, and semantic features for the classification of high-resolution remotely sensed imagery," *IEEE transactions on geoscience and remote sensing*, vol. 51, no. 1, pp. 257–272, 2012.

[142] S. S. Heydari and G. Mountrakis, "Meta-analysis of deep neural networks in remote sensing: A comparative study of mono-temporal classification to support vector machines," *ISPRS Journal of Photogrammetry and Remote Sensing*, vol. 152, pp. 192–210, 2019.

[143] T. Habib, J. Inglada, G. Mercier, and J. Chanussot, "Support vector reduction in svm algorithm for abrupt change detection in remote sensing," *IEEE Geoscience and Remote Sensing Letters*, vol. 6, no. 3, pp. 606–610, 2009.

[144] A. Alonso, R. Muñoz-Carpena, R. E. Kennedy, and C. Murcia, "Wetland landscape spatio-temporal degradation dynamics using the new google earth engine cloud-based platform: Opportunities for non-specialists in remote sensing," *Transactions of the ASABE*, vol. 59, no. 5, pp. 1331–1342, 2016.

[145] J. Muro, A. Varea, A. Strauch, A. Guelmami, E. Fitoka, F. Thonfeld, B. Diekkrüger, and B. Waske, "Multitemporal optical and radar metrics for wetland mapping at national level in albania," *Heliyon*, vol. 6, no. 8, 2020.

[146] Z. Tang, Y. Li, Y. Gu, W. Jiang, Y. Xue, Q. Hu, T. LaGrange, A. Bishop, J. Drahota, and R. Li, "Assessing nebraska playa wetland inundation status during 1985–2015 using landsat data and google earth engine," *Environmental monitoring and assessment*, vol. 188, pp. 1–14, 2016.

[147] V. L. Valenti, E. C. Carcelen, K. Lange, N. J. Russo, and B. Chapman, "Leveraging google earth engine user interface for semiautomated wetland classification in the great lakes basin at 10 m with optical and radar geospatial datasets," *IEEE Journal of selected topics in applied earth observations and remote sensing*, vol. 13, pp. 6008–6018, 2020.

[148] N. Farda, "Multi-temporal land use mapping of coastal wetlands area using machine learning in google earth engine," in *IOP Conference Series: Earth and Environmental Science*, vol. 98, p. 012042, IOP Publishing, 2017.

[149] S. Sun, Y. Zhang, Z. Song, B. Chen, Y. Zhang, W. Yuan, C. Chen, W. Chen, X. Ran, and Y. Wang, "Mapping coastal wetlands of the bohai rim at a spatial resolution of 10 m using multiple open-access satellite data and terrain indices," *Remote Sensing*, vol. 12, no. 24, p. 4114, 2020.

[150] K. B. Byrd, L. Ballanti, N. Thomas, D. Nguyen, J. R. Holmquist, M. Simard, and L. Windham-Myers, "A remote sensing-based model of tidal marsh aboveground carbon stocks for the conterminous united states," *ISPRS Journal of Photogrammetry and Remote Sensing*, vol. 139, pp. 255–271, 2018.

[151] N. Wu, R. Shi, W. Zhuo, C. Zhang, B. Zhou, Z. Xia, Z. Tao, W. Gao, and B. Tian, "A classification of tidal flat wetland vegetation combining phenological features with google earth engine," *Remote Sensing*, vol. 13, no. 3, p. 443, 2021.

[152] B. T. Lamb, M. A. Tzortziou, and K. C. McDonald, "A fused radar–optical approach for mapping wetlands and deepwaters of the mid–atlantic and gulf coast regions of the united states," *Remote Sensing*, vol. 13, no. 13, p. 2495, 2021.

[153] M. Amani, S. Mahdavi, M. Afshar, B. Brisco, W. Huang, S. Mohammad Javad Mirzadeh, L. White, S. Banks, J. Montgomery, and C. Hopkinson, "Canadian wetland inventory using google earth engine: The first map and preliminary results," *Remote Sensing*, vol. 11, no. 7, p. 842, 2019.

[154] Q. Zhu, Y. Wang, J. Liu, X. Li, H. Pan, and M. Jia, "Tracking historical wetland changes in the china side of the amur river basin based on landsat imagery and training samples migration," *Remote Sensing*, vol. 13, no. 11, p. 2161, 2021.

[155] M. Amani, S. Mahdavi, M. Kakooei, A. Ghorbanian, B. Brisco, E. R. DeLancey, S. Toure, and E. L. Reyes, "Wetland change analysis in alberta, canada using four decades of landsat imagery," *IEEE Journal of Selected Topics in Applied Earth Observations and Remote Sensing*, vol. 14, pp. 10314–10335, 2021.

[156] M. Amani, B. Brisco, M. Afshar, S. M. Mirmazloumi, S. Mahdavi, S. M. J. Mirzadeh, W. Huang, and J. Granger, "A generalized supervised classification scheme to produce provincial wetland inventory maps: An application of google earth engine for big geo data processing," *Big Earth Data*, vol. 3, no. 4, pp. 378–394, 2019.

[157] E. Fekri, H. Latifi, M. Amani, and A. Zobeidinezhad, "A training sample migration method for wetland mapping and monitoring using sentinel data in google earth engine," *Remote Sensing*, vol. 13, no. 20, p. 4169, 2021.

[158] J. Muro, A. Strauch, E. Fitoka, M. Tompoulidou, and F. Thonfeld, "Mapping wetland dynamics with sar-based change detection in the cloud," *IEEE Geoscience and Remote Sensing Letters*, vol. 16, no. 10, pp. 1536–1539, 2019.

[159] X. Long, X. Li, H. Lin, and M. Zhang, "Mapping the vegetation distribution and dynamics of a wetland using adaptive-stacking and google earth engine based

on multi-source remote sensing data," *International Journal of Applied Earth Observation and Geoinformation*, vol. 102, p. 102453, 2021.

[160] M. Mahdianpari, B. Salehi, F. Mohammadimanesh, B. Brisco, S. Homayouni, E. Gill, E. R. DeLancey, and L. Bourgeau-Chavez, "Big data for a big country: The first generation of canadian wetland inventory map at a spatial resolution of 10-m using sentinel-1 and sentinel-2 data on the google earth engine cloud computing platform," *Canadian journal of remote sensing*, vol. 46, no. 1, pp. 15–33, 2020.

[161] S. Shi, Y. Chang, Y. Li, Y. Hu, M. Liu, J. Ma, Z. Xiong, D. Wen, B. Li, and T. Zhang, "Using time series optical and sar data to assess the impact of historical wetland change on current wetland in zhenlai county, jilin province, china," *Remote Sensing*, vol. 13, no. 22, p. 4514, 2021.

[162] M. Amani, B. Brisco, S. Mahdavi, A. Ghorbanian, A. Moghimi, E. R. DeLancey, M. Merchant, R. Jahncke, L. Fedorchuk, A. Mui, *et al.*, "Evaluation of the landsat-based canadian wetland inventory map using multiple sources: challenges of large-scale wetland classification using remote sensing," *IEEE Journal of Selected Topics in Applied Earth Observations and Remote Sensing*, vol. 14, pp. 32–52, 2020.

[163] A. D. Campbell and Y. Wang, "Salt marsh monitoring along the mid-atlantic coast by google earth engine enabled time series," *PloS one*, vol. 15, no. 2, p. e0229605, 2020.

[164] J. Salinas, M. Eggerth, M. Miller, R. Meza, J. Chacaltana, J. Acuña, and G. Barroso, "Wetland mapping with multitemporal sentinel radar remote sensing in the southeast region of brazil," in *2020 IEEE Latin American GRSS & ISPRS Remote Sensing Conference (LAGIRS)*, pp. 669–674, IEEE, 2020.

[165] A. Hardy, G. Oakes, and G. Ettritch, "Tropical wetland (tropwet) mapping tool: the automatic detection of open and vegetated waterbodies in google earth engine for tropical wetlands," *Remote Sensing*, vol. 12, no. 7, p. 1182, 2020.

[166] Z. Zhang, N. Xu, Y. Li, and Y. Li, "Sub-continental-scale mapping of tidal wetland composition for east asia: A novel algorithm integrating satellite tide-level

and phenological features," *Remote Sensing of Environment*, vol. 269, p. 112799, 2022.

[167] J. Kool, S. Lhermitte, M. Hrachowitz, F. Bregoli, and M. E. McClain, "Seasonal inundation dynamics and water balance of the mara wetland, tanzania based on multi-temporal sentinel-2 image classification," *International Journal of Applied Earth Observation and Geoinformation*, vol. 109, p. 102766, 2022.

[168] A. Gulácsi and F. Kovács, "Sentinel-1-imagery-based high-resolution water cover detection on wetlands, aided by google earth engine," *Remote Sensing*, vol. 12, no. 10, p. 1614, 2020.

[169] J. Munizaga, M. García, F. Ureta, V. Novoa, O. Rojas, and C. Rojas, "Mapping coastal wetlands using satellite imagery and machine learning in a highly urbanized landscape," *Sustainability*, vol. 14, no. 9, p. 5700, 2022.

[170] X. Wang, X. Xiao, Z. Zou, L. Hou, Y. Qin, J. Dong, R. B. Doughty, B. Chen, X. Zhang, Y. Chen, *et al.*, "Mapping coastal wetlands of china using time series landsat images in 2018 and google earth engine," *ISPRS Journal of Photogrammetry and Remote Sensing*, vol. 163, pp. 312–326, 2020.

[171] L. Zhu, Y. Ke, J. Hong, Y. Zhang, and Y. Pan, "Assessing degradation of lake wetlands in bashang plateau, china based on long-term time series landsat images using wetland degradation index," *Ecological Indicators*, vol. 139, p. 108903, 2022.

[172] M. Laba, B. Blair, R. Downs, B. Monger, W. Philpot, S. Smith, P. Sullivan, and P. C. Baveye, "Use of textural measurements to map invasive wetland plants in the hudson river national estuarine research reserve with ikonos satellite imagery," *Remote Sensing of Environment*, vol. 114, no. 4, pp. 876–886, 2010.

[173] C. Wright and A. Gallant, "Improved wetland remote sensing in yellowstone national park using classification trees to combine tm imagery and ancillary environmental data," *Remote Sensing of Environment*, vol. 107, no. 4, pp. 582–605, 2007.

[174] J. Töyrä and A. Pietroniro, "Towards operational monitoring of a northern wetland using geomatics-based techniques," *Remote Sensing of Environment*, vol. 97, no. 2, pp. 174–191, 2005.

[175] P. Dubeau, D. J. King, D. G. Unbushe, and L.-M. Rebelo, "Mapping the dabus wetlands, ethiopia, using random forest classification of landsat, palsar and topographic data," *Remote Sensing*, vol. 9, no. 10, p. 1056, 2017.

[176] R. Geng, S. Jin, B. Fu, and B. Wang, "Object-based wetland classification using multi-feature combination of ultra-high spatial resolution multispectral images," *Canadian Journal of Remote Sensing*, vol. 46, no. 6, pp. 784–802, 2020.

[177] B. Fu, S. Xie, H. He, P. Zuo, J. Sun, L. Liu, L. Huang, D. Fan, and E. Gao, "Synergy of multi-temporal polarimetric sar and optical image satellite for mapping of marsh vegetation using object-based random forest algorithm," *Ecological Indicators*, vol. 131, p. 108173, 2021.

[178] A. Campbell, Y. Wang, M. Christiano, and S. Stevens, "Salt marsh monitoring in jamaica bay, new york from 2003 to 2013: a decade of change from restoration to hurricane sandy," *Remote Sensing*, vol. 9, no. 2, p. 131, 2017.

[179] B. Fu, Y. Wang, A. Campbell, Y. Li, B. Zhang, S. Yin, Z. Xing, and X. Jin, "Comparison of object-based and pixel-based random forest algorithm for wetland vegetation mapping using high spatial resolution gf-1 and sar data," *Ecological indicators*, vol. 73, pp. 105–117, 2017.

[180] K. R. Ahmed, S. Akter, A. Marandi, and C. Schüth, "A simple and robust wetland classification approach by using optical indices, unsupervised and supervised machine learning algorithms," *Remote Sensing Applications: Society and Environment*, vol. 23, p. 100569, 2021.

[181] M. Amani, B. Salehi, S. Mahdavi, J. E. Granger, B. Brisco, and A. Hanson, "Wetland classification using multi-source and multi-temporal optical remote sensing data in newfoundland and labrador, canada," *Canadian Journal of Remote Sensing*, vol. 43, no. 4, pp. 360–373, 2017.

[182] W.-Y. Chiu and I. Couloigner, "Modified fuzzy c-means classification technique for mapping vague wetlands using landsat etm+ imagery," *Hydrological processes*, vol. 20, no. 17, pp. 3623–3634, 2006.

[183] M. Jia, D. Mao, Z. Wang, C. Ren, Q. Zhu, X. Li, and Y. Zhang, "Tracking long-term floodplain wetland changes: A case study in the china side of the amur

river basin," *International Journal of Applied Earth Observation and Geoinformation*, vol. 92, p. 102185, 2020.

[184] H. Liu, Q. Jiang, Y. Ma, Q. Yang, P. Shi, S. Zhang, Y. Tan, J. Xi, Y. Zhang, B. Liu, *et al.*, "Object-based multigrained cascade forest method for wetland classification using sentinel-2 and radarsat-2 imagery," *Water*, vol. 14, no. 1, p. 82, 2022.

[185] F. Mohammadimanesh, B. Salehi, M. Mahdianpari, B. Brisco, and E. Gill, "Full and simulated compact polarimetry sar responses to canadian wetlands: Separability analysis and classification," *Remote Sensing*, vol. 11, no. 5, p. 516, 2019.

[186] F. Mohammadimanesh, B. Salehi, M. Mahdianpari, and M. Motagh, "A new hierarchical object-based classification algorithm for wetland mapping in newfoundland, canada," in *IGARSS 2018-2018 IEEE International Geoscience and Remote Sensing Symposium*, pp. 9233–9236, IEEE, 2018.

[187] J. Betbeder, S. Rapinel, S. Corgne, E. Pottier, and L. Hubert-Moy, "Terrasar-x dual-pol time-series for mapping of wetland vegetation," *ISPRS Journal of Photogrammetry and Remote Sensing*, vol. 107, pp. 90–98, 2015.

[188] M. Dabboor, I. Olthof, M. Mahdianpari, F. Mohammadimanesh, M. Shokr, B. Brisco, and S. Homayouni, "The radarsat constellation mission core applications: First results," *Remote Sensing*, vol. 14, no. 2, p. 301, 2022.

[189] A. A. Thompson*, "Overview of the radarsat constellation mission," *Canadian Journal of Remote Sensing*, vol. 41, no. 5, pp. 401–407, 2015.

# Chapter 3

# A Novel Multimodel Framework for Wetland Classification [1]

## 3.1 Preface

A version of this manuscript has been published in the *IEEE Journal of Selected Topics in Applied Earth Observations and Remote Sensing (JSTARS)*. I am the primary author of this work, alongside my co-authors, Masoud Mahdianpari and Eric Gill. I conceptualized and designed the study, developed the model, and conducted all the experiments and tests presented in this manuscript. Additionally, I was responsible for writing the paper and ensuring the technical content was accurately conveyed. The co-authors provided feedback, reviewing and offering comments on the manuscript. I revised the paper, incorporating their suggestions as well as addressing the feedback from the peer reviewers.

## 3.2 Abstract

Wetland is one of the most productive resources on Earth, and it provides vital habitats for several unique species of flora and fauna. Over the last decade, mapping

[1] Jafarzadeh, H., Mahdianpari, M. and Gill, E.W., 2022. Wet-GC: a novel multimodel graph convolutional approach for wetland classification using Sentinel-1 and 2 imagery with limited training samples. IEEE Journal of Selected Topics in Applied Earth Observations and Remote Sensing, 15, pp.5303-5316.

and monitoring wetlands by utilizing deep learning (DL) models and remote sensing data gained popularity due to the importance of wetland preservation. In general, DL-based methods have shown astonishing achievement in wetland classification, but some practical issues, such as limited training samples, still need to be addressed. Moreover, the performance of most of the DL approaches is decreased when moderate-resolution images with few features are used as input data. One solution to breaking the performance bottleneck of a single model is to fuse two or more of them. To this end, we strive to investigate and develop a multimodel DL algorithm for wetland classification based on the combination of a graph convolutional network (GCN) and a shallow convolutional neural network (CNN), which is called the Wet-GC algorithm hereinafter. In doing this, moderate-resolution Sentinel-1 (S1) synthetic aperture radar (SAR) and Sentinel-2 (S2) multispectral optical imagery are fed into the GCN and CNN models, respectively. As we know from the literature, the synergistic use of S1 SAR and S2 optical imagery can be used to extract different types of wetland features and increase the class discrimination possibility. Hence, wetland mapping by jointly using GCN and CNN has the ability to boost the wetland classification task. Findings indicate that the efficiency of Wet-GC with an overall accuracy (OA) of 88.68% outperforms the results obtained from random forest (OA = 84.88%), support vector machine (OA = 82.86%), extreme gradient boosting (OA = 86.55%), and ResNet50 (OA = 86.93%). The outcomes reveal that the Wet-GC architecture proposed in this article has an excellent capability to be applied over large areas with minimal need for training samples and can perform acceptably in supporting regional wetland mapping.

## 3.3 Introduction

Wetlands are most simply defined as areas that are at least periodically covered by or saturated with water and include active plants during each year's growing season and water saturation period [1, 2, 3, 4, 5]. Wetlands are some of the most productive resources on Earth and support a host of ecosystem services [1, 4, 6, 7]. In particular, they provide innumerable functions, such as natural drinking water filtration, flood and drought relief, shoreline erosion protection, soil conservation, biodiversity preservation, and carbon sequestration, to name a few [3, 6, 8, 9, 10]. Wetlands also have an impact on climate change in that they help regulate regional climate [4, 11]. As such,

these considerations confirm that wetlands can provide huge economical, ecological, cultural, recreational, and aesthetic worldwide benefits [12, 13, 14]. In spite of these positive impacts, due to human disturbance, wetlands have been polluted and drained severely over the past five decades as some regions' land covers have changed (e.g., wetlands conversion to urban or agricultural land use) [1, 3]. The loss in wetland areas has severe impacts on the valuable services they provide for humans and non-humans alike [3, 7, 15]. Therefore, improving the requirements for wetland studies and monitoring the status of wetlands is essential to maintaining such vital features of the landscape.

Remote sensing (RS) is the foremost source of spatial and temporal information about Earth's surface constitution [16]. Despite several advances in RS technology, certain factors make wetlands challenging to map through satellite imagery [17]. Of these factors, the main ones are 1) ecological similarities of wetland classes with each other (among types of wetlands are bog, fen, marsh, and swamp, as outlined and explained by the Canadian Wetland Classification System [18]) and also with other non-wetland classes (e.g., water, forest, agriculture,...) [19, 20, 21]; and 2) highly dynamic characteristics of wetland classes that substantially alter their reflectance and energy backscatter properties, especially within a growing season [22, 23]. However, these challenges can be overcome by selecting appropriate machine learning (ML) algorithms.

Given the need for up-to-date landscape information, along with broad-scale coverage of wetland areas (i.e., regional, national, and global context), satellite RS plays the main role as an efficient and cost-effective method in such a vital task [24, 25]. Different sensors in RS, however, capture a wide range of Earth surface information from different perspectives. Within the RS community, a particularly interesting challenge is how to effectively combine multiple complementary data sources. Previous studies highlight improvements in the performance of a variety of RS-based applications by integrating multisource/multisensor RS data. For instance, by using multisource moderate resolution RS data, Shen et al. [26] applied deep learning (DL) technique to predict the main factors for drought monitoring. In [27], a multiple-layers DL architecture was designed for change detection with multisource VHR satellite images. Li et al. [28] proposed a DL network to extract water bodies based on multisource RS data. The use of integrated features of multisource datasets has also contributed to the classification of wetland areas [29].

Specifically, optical and synthetic aperture radar (SAR) sensors are based on range and angular measurements and collect information about wetland vegetation's chemical and physical characteristics, respectively [8]. The combination of optical and SAR images has a number of advantages and can be applied to improve wetland mapping, thanks to the complementary information provided by both sources. The optical sensors obtain information from the reflection and emission characteristics of the Earth's surface, while the SAR sensors provide information based on the structural and dielectric properties of natural and man-made objects [30]. So, a feature that is not visible in the optical images may be visible in the SAR data (and vice versa), and using only the optical images can lead to misclassification. The inclusion of SAR data can avoid this misclassification, as features with similar spectral characteristics may have different distribution patterns in the SAR images. Therefore, incorporating both optical and SAR datasets adds more information on wetlands and consequently enhances the discrimination of different wetland types [31, 32, 33].

Fortunately, through the development of innovative models, numerous studies in the literature have attempted to deal with wetland classification challenges with a minimal need for in situ measurements. However, for the following reasons, most models related to large-scale scattering are not very effective in wetland classification.

1. Current large-scale satellite imagery does not use high spatial and spectral resolution sensors, and this imposes challenges in distinguishing classes exclusively by analyzing their spectra.

2. Cost and accessibility issues associated with some kinds of satellite images (e.g., high-resolution and hyperspectral data) prevent the utilization of several approaches in practice [34, 35].

3. A large amount of in situ measurements are not available for large-scale and inaccessible wetland areas, and since the efficiency of DL methods significantly depends on the availability of a large number of training samples, not every methodology is executable.

4. Wetland classes have considerable internal variability caused by the large spatial coverage of satellite retrieved data; thus, the class separability in a restricted neighborhood is a complex problem.

Considering the points raised previously, proposing a proper ML algorithm and utilizing available free-of-charge satellite imagery is still needed in order to make a significant contribution to wetland mapping.

To date, several DL approaches have been developed for diverse kinds of RS images, from coarse resolution to high-resolution satellite imagery and from multispectral to hyperspectral datasets with hundreds of bands. Owing to the impressive feature representation power of the convolutional neural network (CNN), it has been employed in a broad scope of RS applications such as image classification [36, 37], change detection [38], and semantic segmentation [39]. For classification purposes, for instance, Wang et al. [40] introduced a deep feature learning-based method to improve scene classification by incorporating rich hierarchical features of a CNN model. Liu et al. [41] proposed a scene classification approach based on Siamese CNN, which combines verification and identification models to boost performance. These two models are used to predict the input images' identity labels and measure the similarities between image pairs, respectively. To support arbitrary sizes of the input images without any resizing process, Xie et al. [42] designed a scale-free CNN to prevent information discard in high spatial resolution images and improve scene classification performance.

Several attempts have been made to use DL models for wetland classification in the last few years. For instance, in [43], a pretrained AlexNet model was applied to the RapidEye multispectral dataset to classify complex wetland land cover. Its results were compared with those of the random forest model. DeLancey et al. used optical and SAR images to investigate the effectiveness of deep CNN on large-scale wetland classification. They reported the successful discrimination of the wetland categories using CNN models [21]. Furthermore, in [44], an encoder-decoder CNN model was proposed to classify wetland classes using LiDAR and spectral indices as input. To provide a spatio-temporal architecture, Hosseiny et al. established a workflow named WetNet for wetland mapping considering 2D-CNN, 3D-CNN, and LSTM layers. The efficiency of their model was evaluated utilizing S1 and S2 images [29]. In a recent publication, Jamali and Mahdianpari [45] focused on the integration of CNN models with transformers and suggested a multimodel DL network for wetland classification by the integration of a modified version of VGG-16, a 3D-CNN, and the Swin transformer.

Benefiting from the fast development of DL approaches, the progress in RS image

classification has been accelerated. Several graph convolutional network (GCN) based methods have recently been proposed in the RS community. These studies have investigated the potential of such a powerful model for RS scene classification using optical data [46, 47]. In [48], a graph attention network, which is a modification of GCN, was suggested for hyperspectral image classification. To exploit the spatial information of a hyperspectral image as well as its spectral information, context-aware GCN, and multiscale GCN algorithms were established in [49] and [50], respectively. In addition, a nonlocal GCN, which took the whole hyperspectral image as input to learning graph representations, was explored in [51].

Given that the traditional GCN model utilizes the adjacency matrix, it suffers from a high computational cost, particularly in large-scale RS problems. To solve this issue, very recently, Hong et al. [52] proposed a minibatch GCN framework for hyperspectral image classification. Instead of feeding all the data into the network at once, this method proceeds in several batches, reducing the computational cost compared to the traditional GCN model. Despite the effectiveness of the GCN structure, there is no documented research on the application of this powerful model either for wetland classification or the combination of SAR and optical imagery. The literature review indicates that GCNs have not been widely applied to commonly used free publicly available satellite imagery (e.g., Sentinel and Landsat images) compared to hyperspectral data. Since these publicly available moderate-resolution datasets (e.g., 10–30 m) are extensively used in both RS-based academic and practical fields, there needs to be more research on the potential of GCNs on such imagery.

With the current status of DL algorithms employed in wetland mapping in mind, we will propose a new classification framework that combines GCNs and CNNs utilizing moderate-resolution S1 and S2 satellite imagery. The focus of this article lies in the prediction of wetland classes. Here, we summarize the contributions of this article in addressing the issues of large-scale wetland landscape classification through RS imagery and provide a framework to reach better results. In order to make the synergistic use of the S1 and S2 datasets, the proposed framework (i.e., Wet-GC) is devised in two branches as follows.

1. The GCN branch: The GCN architecture will be introduced first, focusing on incorporating the spatial context of images in wetland classification as the spectral context. As verified, this framework is able to produce good results in the

classification of hyperspectral benchmark datasets. To our knowledge, this article is the first one that modifies and employs such a potentially effective network for wetland classification.

2. The CNN branch: A simple shallow CNN architecture will also be introduced and added to the model as the second branch.

The main objective for creating a two-branch Wet-GC network in this article is to take advantage of each branch's unique capabilities when dealing with multisource data. The optical imagery contains rich spectral information that offers an opportunity to study land covers. Studies using DL have demonstrated that CNNs can learn image features automatically by collecting spectral contextual information from multispectral images. As a result, CNNs are frequently cited in the literature as effective models for classifying land covers using S2 optical data [53, 54]. As such, S2 is the input of the CNN branch of the proposed Wet-GC. With less contextual information available in SAR data, the CNN branch is inefficient for exploring S1 imagery, as frequently reported in the literature. Therefore, the Wet-GC approach employs a GCN branch to establish the directional associations between pixels in S1 SAR data. In comparison to the CNN branch, the GCN branch is more capable of polarimetric information extraction in SAR data. Thus, SAR data have been considered as input in the GCN branch of the proposed Wet-GC network.

In Section 3.4, the basic preliminaries of GCNs are presented. The details of the Wet-GC architecture are introduced in Section 3.5. Section 3.6 contains an introduction to the study area, datasets, and the experimental setup utilized in this article. Discussion of the results appears in Section 3.7. Finally, Section 3.8 concludes this article.

## 3.4 Related Work

This section provides basic preliminaries of GCNs and mini-GCNs and the related equations. First, consideration is given as to what a "graph" is. Subsequently, we will discuss constructing the adjacency matrix and using it with Fourier transform equations to express the convolution operation on a graph.

The neural network concept for directly processing graph data was first introduced

in [55]. In the case of RS data analysis, a graph is explained as the relations of spectral/ backscattering signatures in an image domain. A graph $G$ is defined by two components: $G = (V, E)$, in which $V$ denotes the vertices (i.e., the pixel vectors in the image domain) and $E$ denotes the edges (i.e., the similarities between the two $V_i$ and $V_j$ vertices) [52]. This similarity is defined by an adjacency matrix denoted as $A$, which is computed using the radial basis function (RBF) for any two $x_i$ and $x_j$ spectral signatures associated with the vertices $V_i$ and $V_j$ as given by

$$A_{ij} = \exp\left(-\frac{\|x_i - x_j\|^2}{\sigma^2}\right) \tag{3.1}$$

where the value for the $\sigma$ parameter controls the width of the RBF. By knowing both the adjacency matrix $A$ and the matrix trace of $A$ (sum of diagonal elements of the matrix $A$, i.e., $D_{i,i} = \sum_j A_{i,j}$ [52, 56]), the Laplacian matrix $L$ and the symmetric normalized Laplacian matrix ($L_{\text{sym}}$) can be computed as:

$$L = D - A \tag{3.2}$$

$$L_{\text{sym}} = D^{-\frac{1}{2}} L D^{-\frac{1}{2}} = I - D^{-\frac{1}{2}} A D^{-\frac{1}{2}} \tag{3.3}$$

In mathematics and, in particular, functional analysis, the "Convolution" is an operation involving two functions by the integral of the pointwise multiplication of those functions. We now briefly discuss graph convolutions and their related equations in the spectral domain. Through the practical Fourier and inverse Fourier transforms [52, 57], the convolution theorem of the given two functions $f$ and $g$ can be expressed as:

$$f(t) \otimes g(t) = \mathcal{F}^{-1}\{\mathcal{F}[f(t)] \cdot \mathcal{F}[g(t)]\} \tag{3.4}$$

where $\otimes$ denotes the convolution operation.

According to Equation 3.4, the convolution operation on a graph can be expressed in terms of the Fourier transform $\mathcal{F}$ and subsequently as a series of basis functions. In other words, as proven in [52], the eigenvectors of $L$, i.e., $U = (u_1, u_2, \ldots, u_n)$, are the same as the basis functions of $\mathcal{F}$ and expressed as:

$$L = U\Lambda U^{-1} \tag{3.5}$$

and since $U$ is an orthogonal matrix, i.e., its transpose ($U^T$) is equal to its inverse matrix ($U^{-1}$), then Equation 3.5 can be written as:

$$L = U\Lambda U^{-1} = U\Lambda U^T \tag{3.6}$$

where $\Lambda$ is a diagonal matrix of $L$'s eigenvalues. So that considering Equation 3.6, the Fourier transform and the inverse Fourier transform of the function $f$ on a graph is identical to:

$$\mathcal{GF}[f] = U^T f \tag{3.7}$$

$$f = U\mathcal{GF}[f] \tag{3.8}$$

Therefore, Equation 3.4 can be converted to:

$$\mathcal{G}\ [f \otimes g] = U\big\{\big[U^T f\big] . \big[U^T g\big]\big\} \tag{3.9}$$

If we write $U^T g$ as $g_\theta$ and consider doing some computational complexity simplification, the convolution on a graph can be formulated as:

$$\mathcal{G}\,[f \otimes g_\theta] \approx \theta\left(I + D^{-\frac{1}{2}} A D^{-\frac{1}{2}}\right) f. \tag{3.10}$$

Finally, by using Equation 3.10, the propagation rule for GCNs will be as follows:

$$H^{(\ell+1)} = h\left(\tilde{D}^{-\frac{1}{2}}\tilde{A}\tilde{D}^{-\frac{1}{2}}H^{(\ell)}W^{(\ell)} + b^{(\ell)}\right) \tag{3.11}$$

$$\tilde{A} = \ A + I, \quad \text{and} \ \ \tilde{D}_{i,i} = \sum_j \tilde{A}_{i,j}\ .$$

## 3.5 Proposed Methodology

The overall architecture of the proposed Wet-GC model is shown in Figure 3.1 and is composed of two parts: 1) feature extraction module, including the mini-GCN-based branch and the CNN-based branch; and 2) feature fusion module. The feature extraction module extracts different features by using both CNNs and GCNs. Also, the feature fusion module concatenates the resulted features as the final classification input. These steps will be discussed further in what follows.

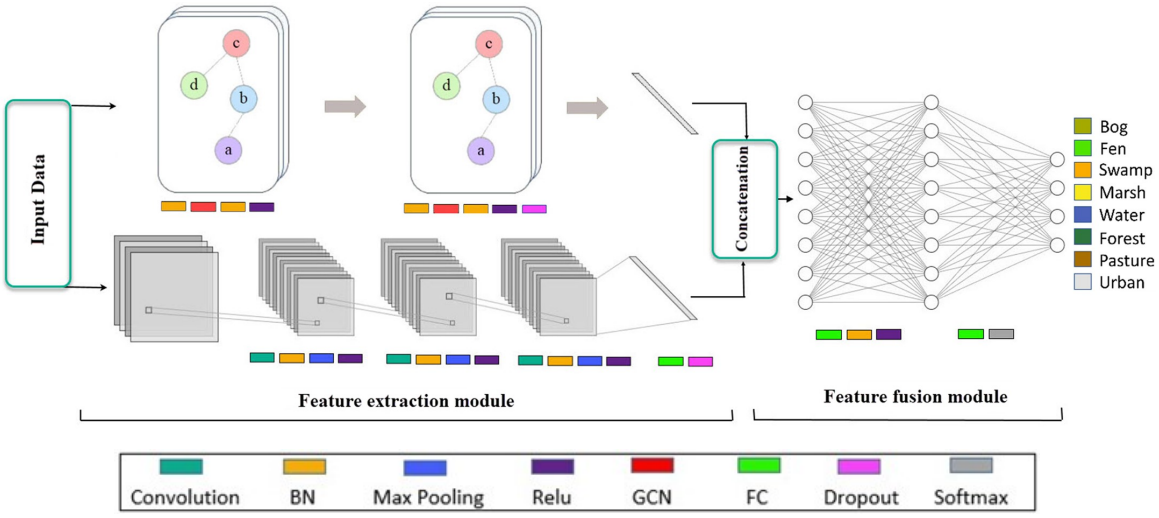



Figure 3.1: General flowchart of the proposed Wet-GC model. The feature extraction module extracts different features by using both CNNs and GCNs. The feature fusion module concatenates the resulting features as the final classification input.

### 3.5.1 Mini-GCN-Based Branch

GCN is a neural network that learns features by gradually aggregating information in the neighborhood. Figure 3.1 and Table 3.1 show the architecture of the proposed mini-GCN-based branch. There are some differences between traditional GCNs and mini-GCNs. For the GCNs, all the data usually are used as input at once, which requires a high volume of computations. However, the mini-GCN architecture offers three benefits over the well-known GCNs as follows.

1. It performs a minibatch learning procedure and consequently reduces the computational complexity of the Laplacian matrix and training process and performs

fast computations.

2. Minibatch learning acts as a feasible solution to combine the GCN and CNN architectures, and in fact, the mini-GCN procedure makes the GCN trainable in minibatch fashion, analogously to CNN architecture.

3. Minibatch learning also provides spatially local connectivity, which enables the mini-GCN to learn discriminative features from input graph-structured data.

Table 3.1: The mini-GCN configuration of the proposed Wet-GC framework.

| **Input Dimension** | D |
|---|---|
| Sequence | Layer Type |
| Block 1 | Batch Normalization<br>GCN Layer<br>Batch Normalization<br>ReLU Activation Function |
| Block 2 | Batch Normalization<br>GCN Layer<br>Batch Normalization<br>ReLU Activation Function<br>Dropout |

Considering Equation 3.11, the graph convolution in $S$ batches can be stated as:

$$H^{(\ell+1)} = h\left(\tilde{D}_S^{-\frac{1}{2}}\tilde{A}_S\tilde{D}_S^{-\frac{1}{2}}H_S^{(\ell)}W^{(\ell)} + b_S^{(\ell)}\right) \tag{3.12}$$

In the last equation, $S$ refers to both the $S$-th subgraph and batch in the training process of the network. The blocks' sequences utilized for the mini-GCN branch of this article are presented in Table 3.1.

### 3.5.2 CNN-Based Branch

As shown in Figure 3.1, the proposed CNN-based branch network has a simple and shallow structure. Generally, CNNs contain three layers: convolutional, pooling, and fully connected (FC) layers. The convolutional layer plays a crucial role in a CNN architecture, and convolution refers to a mathematical operation that merges the input

image and filters. This layer includes multiple filters with different sizes that slide across the image grid and learn different portions of input data. In fact, convolution is used for extracting a feature of data by using an arbitrary filter [58, 59]. Typically, after each convolutional layer, a pooling layer is added, which summarizes the features generated in the previous layer and lying within the region covered by the filter, thus, reducing the number of parameters and dimensionality of CNNs [34]. In a standard CNN, the final layer is the FC layer that classifies the features extracted from the last layer into different classes. The structure of the CNN model utilized in this article is presented in Table 3.2.

Table 3.2: CNN configuration of the proposed Wet-GC framework.

| **Input Dimension** | $7 \times 7 \times D$ | |
|---|---|---|
| **Sequence** | **Layer Type** | **Size** |
| Block 1 | Convolutional Layer | (2,2,64) |
| | Batch Normalization | - |
| | Max Pooling | (2×2) |
| | ReLU Activation Function | - |
| Block 2 | Convolutional Layer | (3,3,128) |
| | Batch Normalization | - |
| | Max Pooling | (2×2) |
| | ReLU Activation Function | - |
| Block 3 | Convolutional Layer | (3,3,256) |
| | Batch Normalization | - |
| | Max Pooling | (2×2) |
| | ReLU Activation Function | - |
| Block 4 | Fully Connected Layer | - |
| | Dropout | 0.3 |

### 3.5.3 Feature Fusion

There are three well-known and practical strategies, namely additive, elementwise multiplicative, and concatenation, which are used in DL and data processing to combine and fuse the output of different models. For the investigations at hand, as the last step of the Wet-GC architecture, the concatenation strategy is used to fuse/merge the outputs of the mini-GCN and CNN branches to yield a final classification map.

In fact, the final output of the proposed framework before entering the classifier is calculated through

$$H_{\text{Total}}^{(\ell+1)} = \left[ H_{\text{miniGCNs}}^{(\ell)}, H_{\text{CNNs}}^{(\ell)} \right] \tag{3.13}$$

In order to yield the final output of the Wet-GC network, a FC layer and then a Softmax classifier are applied to the concatenated data. The general overview of the proposed framework for wetland classification is presented in Algorithm 3.1.

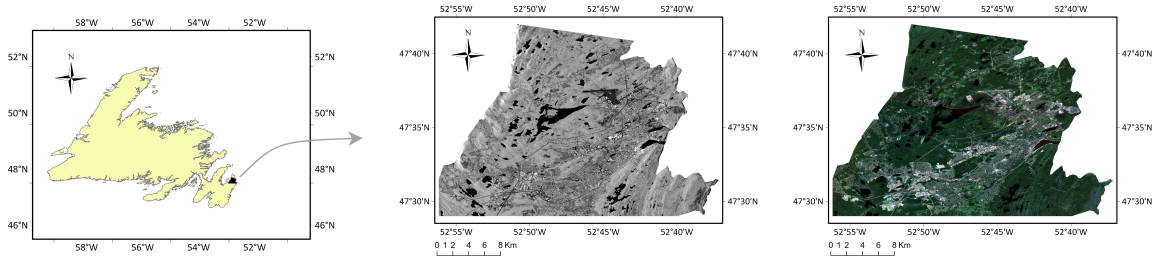
**Algorithm 3.1** : The Pseudocode of the Proposed Wet-GC Method for Wetland Classification.

*Step*1; {data preparation}
**Inputs:**
*CNN: input S2 data, batchsize*
*miniGCN: input S1 data, $\sigma$ value for RBF function*
**Outputs:**
*Patches for CNN branch, Laplacian matrix for GCN branch*
*Step*2; {Jointly using miniGCN and CNN farmework}
**Inputs:**
*number of epochs n for training,*
*CNN branch: x-train, x-test, y-train, y-test,*
*miniGCN branch: train-x, train-y, test-x, test-y, Laplacian matrix; minibatch size*
*LOOP Process:*
**for** $i = 1$ to $n$ **do**
    Feature extraction of the *lth* layer for miniGCN
    Feature extraction of the *lth* layer for CNN
    Calculate the loss
    Update the weight matrices
**end for**
Concatenate the outputs of two branches
Feature fusion
Calculate the network output and conduct label prediction.
**Output:**
*Predict label for input datasets*

## 3.6 Results

### 3.6.1 Study Site

Mapping wetlands via RS in Canada is a well-studied topic [19]. The province of Newfoundland is an island located on the eastern-most coast of Canada, and wetlands are a dominant feature of its landscape [3]. In this article, the case study is conducted over part of the Avalon area located in the eastern portion of the province [see Figure 3.2a].




(a) (b) (c)

Figure 3.2: (a) Location of the study site in Newfoundland province, Canada. (b) Grayscale VH band illustration of S1 imagery. (c) RGB illustration of S2 imagery.

### 3.6.2 Datasets

#### Field Data

The wetland ground-truth (GT) data that provides the basis for the multiyear reference dataset used in this article was obtained via field campaigns conducted in the summers of 2015 to 2020, initially carried out for use in a project to develop RS methods for mapping wetlands in Newfoundland and Labrador [3, 60].

#### Sentinel-1 Imagery

The S1 SAR data originated from the Level-1 ground range detected (GRD) interferometric wide swath product as ingested in the cloud-based geospatial processing platform Google Earth Engine (GEE) [61]. This GRD product consisted of S1 radar observations projected onto a regular 10-m grid [62]. GRD data provide dual-polarized

intensity (VV and VH) but lack phase and full polarimetric information, which constrains the potential for more advanced SAR feature extraction. These limitations are due to GEE currently supporting only GRD-level products. The S1 images taken from Jun. 1–Oct. 30, 2020, were selected for this article, and the median reflectance values of the collections were calculated. The primary features recorded by S1 over the case study are the VV and VH polarized backscatter values (in dB). However, the Span and Ratio features (see the formulas in Table 3.3) were also calculated and stacked to S1 data. A grayscale VH band illustration of S1 imagery from the study area is depicted in Figure 3.2b.

Table 3.3: The bands/features extracted from S1 & S2 imagery in this study.

| **Sensor** | **Spatial Resolution** | **Spectral Features** | **Formula/Symbol** |
|---|---|---|---|
| Sentinel-1 | 10 m | VV | $\sigma^0_{VV}$ |
| | | VH | $\sigma^0_{VH}$ |
| | | Span | $\lvert\sigma^0_{VV}\rvert^2 + \lvert\sigma^0_{VH}\rvert^2$ |
| | | Ratio | $\frac{\lvert\sigma^0_{VV}\rvert^2}{\lvert\sigma^0_{VH}\rvert^2}$ |
| Sentinel-2 | 10 m | Blue | B2 |
| | | Green | B3 |
| | | Red | B4 |
| | | NIR | B8 |

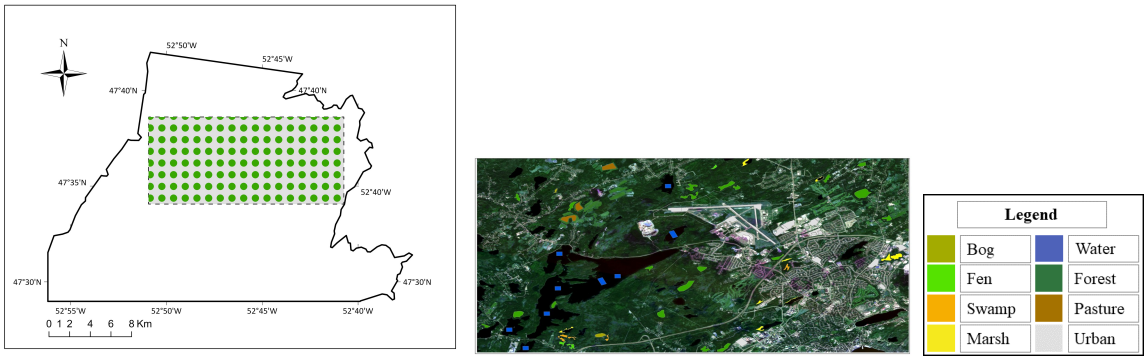
$\sigma^0_{XX}$ and $\sigma^0_{XY}$ denote co- and cross-polarized sigma nought in the logarithmic scale (dB).

### Sentinel-2 Imagery

The S2 data are provided in GEE as a Level-1C product representing Top-of-Atmosphere reflectance [63]. A composite based on the median reflectance values of the images taken from Jun. 1–Oct. 30, 2020, with a cloud cover of less than 10% was created. In this article, four bands of S2 image, namely the near-infrared (NIR), red, green, and blue bands, were selected and utilized. These bands have unique characteristics to delineate and discriminate wetland classes. Since water strongly absorbs NIR light, this band was chosen because of its usefulness in distinguishing water content from various land cover types. The Red band has the potential to delineate wetland classes because of its ability to detect chlorophyll absorption in vegetation. Meanwhile, the blue band can reflect the differences between soil and vegetation. The green band can

act as a valuable input for vegetation extraction as well as being used in a variety of vegetation indices. Excluding the green band may cause some indistinguishably in land covers (e.g., in our case, marsh, and water classes). Moreover, we tried to use only the S2 bands with 10-m spatial resolution (see Table 3.3). An RGB illustration of S2 imagery from the study area is depicted in Figure 3.2c.

As mentioned earlier, one of the key goals in this article is to develop a novel framework for wetland classification with limited training samples, and this explains the decision to combine GCNs and CNNs. To this end, instead of utilizing all GT data, the training samples are selected just from a portion of the whole study area, as depicted in Figure 3.3a. Note that the chosen area consists of reference data for all kinds of wetland and non-wetland classes mentioned in this article [see Figure 3.3b]. In addition, the selected GT dataset was randomly split into training and testing samples with a ratio of 10% to 90%, further reducing the training dataset. The number of training, validation, and testing samples for each category is listed in Table 3.4. Moreover, the number of pixels for the final classification accuracy assessment (number of pixels in test labels) is added to Table 3.4. Note that test labels listed in the last column of this table were selected from the entire region of the study area to illustrate the generalization capability of the proposed model.




(a) (b)

Figure 3.3: Snapshot of (a) a portion of the study area in which the reference training samples were selected. (b) Reference wetland and non-wetland data collected in the study area

Table 3.4: The number of selected training, validation, and testing pixels of wetland classes in the study area.

| Class | # Training Pixels | # Validation Pixels | # Testing Pixels | # Pixels in Test Labels |
|---|---|---|---|---|
| Bog | 584 | 175 | 5259 | 10509 |
| Fen | 237 | 72 | 2133 | 4257 |
| Forest | 306 | 92 | 2750 | 5500 |
| Marsh | 76 | 25 | 684 | 1072 |
| Pasture | 509 | 152 | 4578 | 9200 |
| Swamp | 69 | 23 | 621 | 1185 |
| Urban | 490 | 147 | 4403 | 8828 |
| Water | 249 | 74 | 2239 | 4476 |
| Total | 2520 | 760 | 22669 | 45027 |

### 3.6.3 Experimental Setup

#### Wetland Classification by Well-Known Models

There are numerous DL and ML models whose robustness has been established in the RS literature. Here, the investigation commences by applying some of these well-known models to S1 and S2 images. Since two different types of satellite datasets are used to investigate the proposed Wet-GC model, in order to maintain the integrity and provide a logical comparison, these datasets are stacked and utilized for the rest of the algorithms employed here. For comparison purposes and to evaluate the efficiency of the Wet-GC, several models, including random forest (RF), support vector machine (SVM), extreme gradient boosting (XGB), and ResNet50 [64] were selected as efficient classifiers for wetland classification, as reported in [29, 34, 65, 66]. Based on experience reported in [3] and [67], and trial and error, the optimum values for the parameters of RF, SVM, and XGB classifiers are defined and presented in Table 3.5. All of these models are trained using the limited training samples as explained previously.

#### Wetland Classification by Wet-GC

As noted, the primary purpose of the current research is to develop a novel framework for jointly using mini-GCN and CNN models based on S1 and S2 imagery. To this end, we combined the mini-GCN with a shallow CNN, both of which were discussed earlier. The implementation details of the Wet-GC model are provided in Table 3.6. Moreover, an ablation experiment (i.e., the accuracy that can be achieved with only a single branch of CNN and GCN models) was also conducted to better understand

Table 3.5: Implementation details for RF, SVM, and XGB classifiers.

| Classifier | Parameter Name | Parameter Value |
|---|---|---|
| RF | Number of decision trees | 150 |
| | Number of variables in each node split | 5 |
| | Minimum size of a terminal node | 2 |
| | Fraction of the input to bag per tree | 0.5 |
| | Number of random seeds | 5 |
| SVM | Regularization parameter | 3 |
| | Kernel type | RBF |
| | Degree of the polynomial kernel function | 6 |
| XGB | Maximum tree depth | 10 |
| | Number of gradient boosted trees | 150 |
| | Learning rate | 0.1 |

how each branch of the proposed method improves the wetland classification. The result of this scenario shows an improvement in classification accuracy as compared to several well-known models.

Table 3.6: Implementation details for the Wet-GC model.

| Classifier | Parameter Name | Parameter Value |
|---|---|---|
| Wet-GC | Base learning rate | 0.0001 |
| | Current learning rate | $(1 - (\text{Iter}/\text{maxIter}))^{0.5}$; Iter = 50 |
| | Number of epochs | 200 |
| | Minibatch size | 32 |
| | Dropout | 0.3 |

### 3.6.4 Classification Maps

The classification results of the models implemented here are shown in Figure 3.4. Eight distinct land cover classes are depicted on these maps, namely, bog, fen, swamp, marsh, water, forest, pasture, and urban. Furthermore, a zoomed-in representation of a small portion of the classified maps is included in Figure 3.5 to investigate and highlight the details of the classification results for different methods.

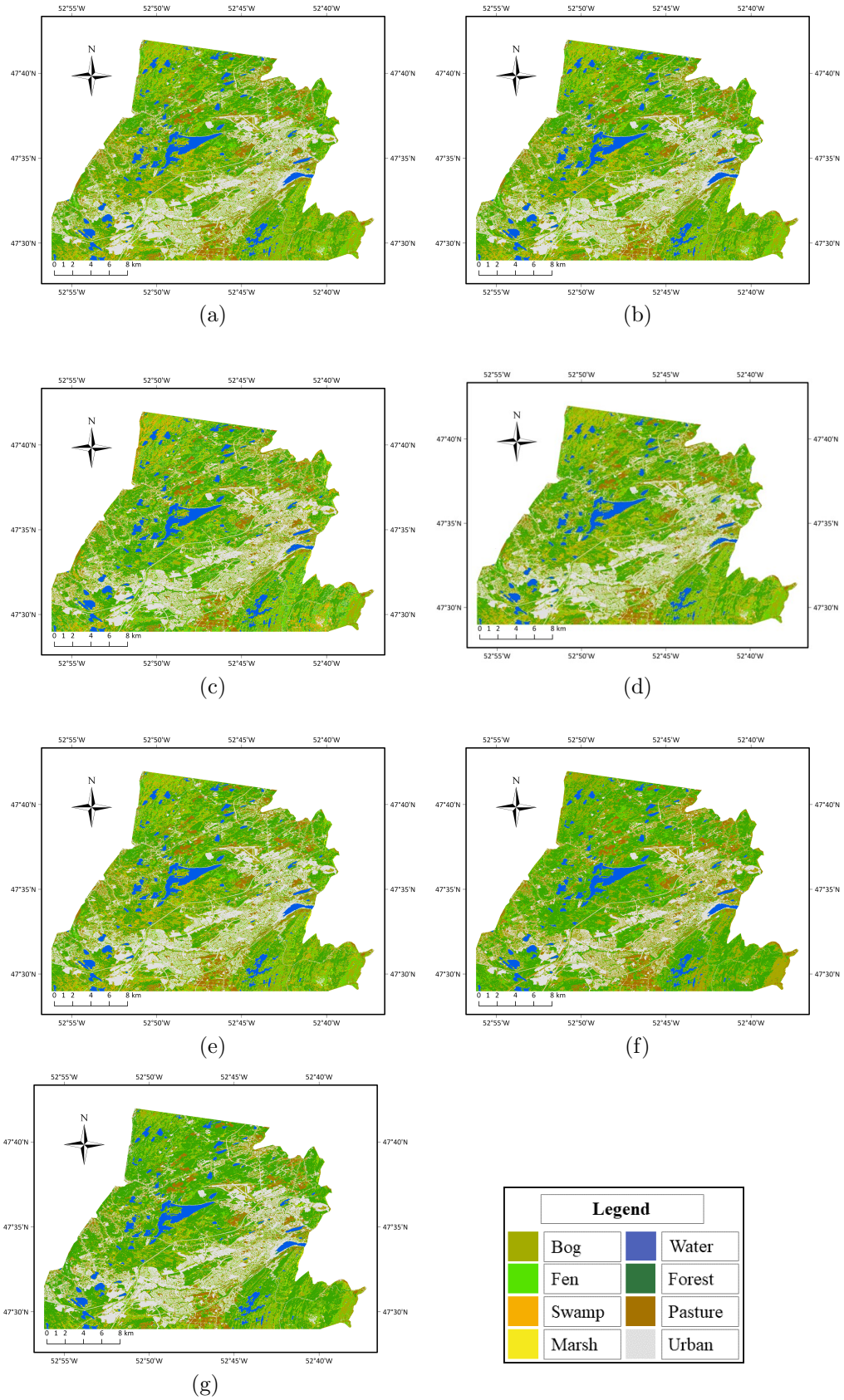



Figure 3.4: Resulting classification maps for different methods. (a) RF. (b) SVM. (c) XGB. (d) ResNet50. (e) GCN-branch. (f) CNN-branch. (g) Wet-GC.

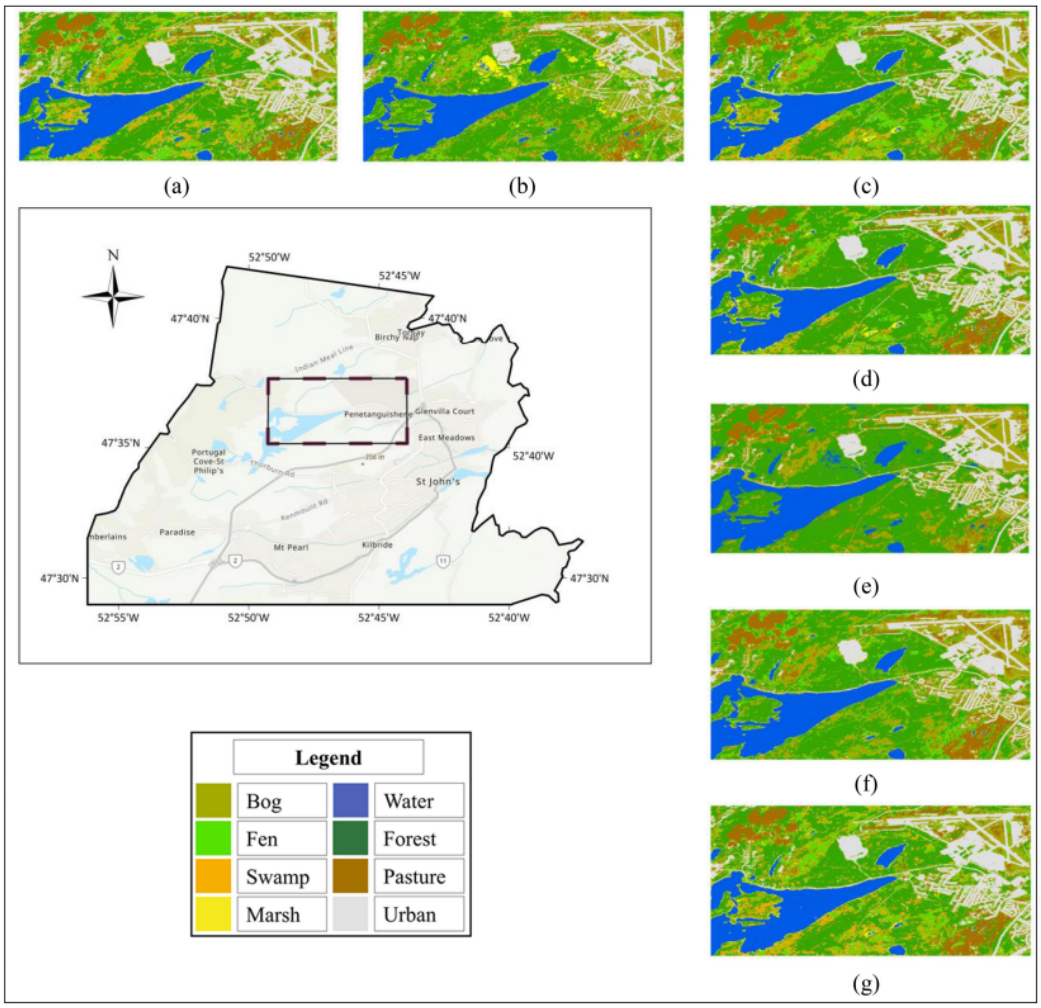



Figure 3.5: Zoomed-in representation of a small portion of the classification maps obtained by (a) RF, (b) SVM, (c) XGB, (d) ResNet50, (e) GCN-branch, (f) CNN-branch, and (g) Wet-GC.

### 3.6.5 Accuracy Assessment

One of the essential steps in RS applications is to assess the accuracy of the generated products. To this end, several accuracy assessment metrics have been proposed in the literature and applied for different applications. These applications mainly include classification, change detection, and target detection. For the purpose at hand, five metrics, including overall accuracy (OA), recall (sensitivity), specificity, precision, and the F-measure, are used. We refer readers for more information of these metrics to [68]. Moreover, the formulas for the mentioned metrics are presented in Table 3.7 in

which the components "TP," "TN," "FN," and "FP" indicate "True Positive," "True Negative," "False Negative," and "False Positive," respectively.

Table 3.7: Accuracy assessment metrics.

| **Criteria** | **Formula** |
|---|---|
| OA | $\frac{(TP+TN)}{(TP+FN+FP+TN)}$ |
| Recall | $\frac{TP}{(TP+FN)}$ |
| Specificity | $\frac{TN}{(TN+FP)}$ |
| Precision | $\frac{TP}{(TP+FP)}$ |
| F-measure | $\frac{2\times(Precision\times Recall)}{(Precision+Recall)}$ |

The quantitative assessment of the classification results of the RF, SVM, XGB, ResNet50, and Wet-GC is shown in Table 3.8. According to the results, the ResNet50 and XGB models perform better than RF and SVM models. This conclusion seems logical because the robustness of ResNet50 and XGB is also highlighted in comparative evaluation studies, such as appear in [67] and [66]. Although, given the small number of input features (i.e., four features of S1 data and four features of S2 data), it is expected to achieve low accuracy results for RF and SVM models; but the developed Wet-GC architecture has a relatively better performance compared to the other algorithms.

Table 3.8: The accuracy assessment indices of employed approaches in this study.

| **Methods** | **OA (%)** | **Recall** | **Specificity** | **Precision** | **F-score** |
|---|---|---|---|---|---|
| RF | 84.88 | 0.7180 | 0.9777 | 0.6987 | 0.7082 |
| SVM | 82.86 | 0.6922 | 0.9745 | 0.6713 | 0.6816 |
| XGB | 86.55 | 0.7181 | 0.9811 | 0.6887 | 0.7031 |
| ResNet50 | 86.93 | 0.7154 | 0.9780 | 0.6919 | 0.7172 |
| GCN-branch | 77.70 | 0.5696 | 0.9609 | 0.5888 | 0.5790 |
| CNN-branch | 79.01 | 0.6174 | 0.9665 | 0.6122 | 0.6135 |
| Wet-GC | 88.68 | 0.7567 | 0.9838 | 0.7484 | 0.7525 |

For further comparison, Figure 3.6 shows the confusion matrices of the classification maps. The columns of the confusion matrices denote the classes in the GT data, and the rows show the classes in the predicted maps. It should be noted that each element of the confusion matrices is shown as a percentage calculated from the total number of entries in each column.

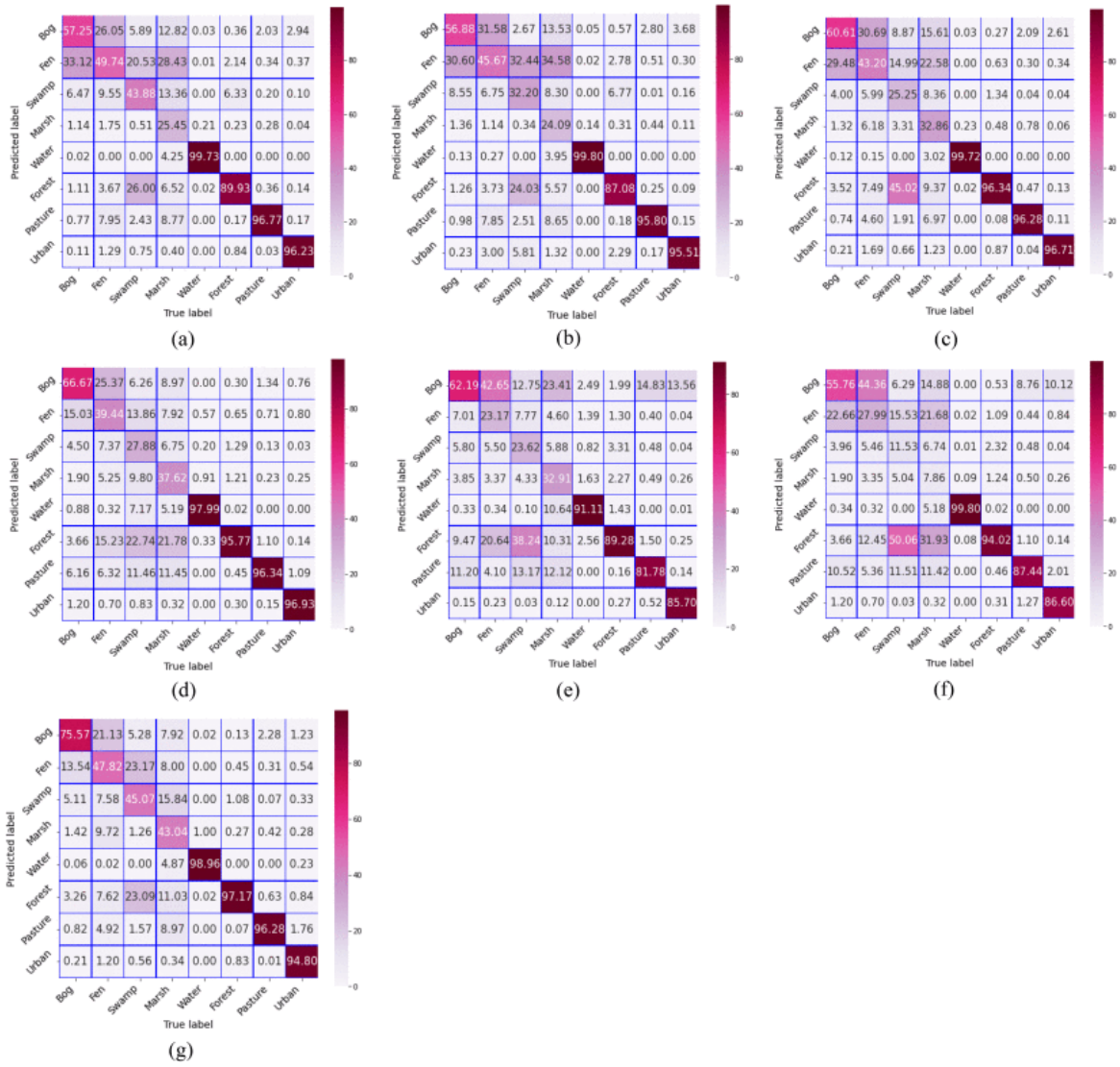



Figure 3.6: Confusion matrices summarizing the accuracy of results based on the evaluation of different algorithms. (a) RF. (b) SVM. (c) XGB. (d) ResNet50. (e) GCN-branch. (f) CNN-branch. (g) Wet-GC. Each entry of the confusion matrices is shown as a percentage calculated from the total number of entries in each column.

### 3.6.6 Computation Run-Time

In order to compare the classification models in terms of computation load, the approximate run-time required for all methods investigated in this article was added to Table 3.9. Although the Wet-GC and ResNet50 models perform well in the classification of wetland areas, they have the defect of taking a long time to run. The time complexity of the Wet-GC model is due to its two branch architecture and the use of a

graph-based structure. All models were run using the Google Colab Pro environment, which provides access to enhanced computational resources.

Table 3.9: Approximate execution time of the classification models.

| Methods | Processing time (minutes) |
|---|---|
| RF | 8 |
| SVM | 13 |
| XGB | 11 |
| ResNet50 | 77 |
| GCN-branch | 59 |
| CNN-branch | 42 |
| Wet-GC | 84 |

## 3.7 Discussion

The quantitative evaluation of the results reported in Table 3.8 and Figure 3.6 shows that the ResNet50 and XGB methods could correctly detect and classify most classes rather than RF and SVM. The performance of these models strongly depends on the number of input features and training samples. While the ResNet50 and XGB show better performances, the RF and SVM models failed to provide acceptable results. However, such models do not engender high expectations when using moderate-resolution data with fewer features and limited training samples as input.

Looking at the Wet-GC's result, we find that the classification accuracy has increased relatively. Of the classification results, the Wet-GC method generally produced the highest OA at 88.68%, followed by the ResNet50 at 86.93%, XGB at 86.55%, RF at 84.88%, and SVM at 82.86%. Though the XGB method produced recall and F-score close to that of RF, the RF method had a higher precision (RF precision was 0.6987 compared to 0.6887 XGB precision). In contrast, the XGB method produced a higher specificity compared to RF (Table 3.8, the XGB specificity was 0.9811, while the RF specificity was 0.9777). Overall, the highest scores of these parameters belong to the Wet-GC method, and the lowest scores are produced by the SVM method. The differences between recall, specificity, precision, and F-score parameters for the proposed method (Wet-GC) and the maximum accuracy obtained for these parameters among the other methods (i.e., SVM, RF, XGB, and ResNet50) are about 0.039,

0.003, 0.05, and 0.035, respectively.

The conclusion about the performance of Wet-GC can also be drawn when comparing the confusion matrices. According to Figure 3.6, wetland classes' classification has lower accuracy than non-wetland classes. Notably, all methods successfully classified over 87% of the non-wetland classes (i.e., water, forest, pasture, and urban). The Wet-GC model was the most successful approach for classifying the non-wetland classes among all the methods. However, the wetland classes were also identified with high accuracies when Wet-GC was applied. In the case of other methods, some misclassifications in wetland classes look relatively impressive. For instance, about 33% of bog classes were misclassified as fen in the RF method, and more than 30% of fen classes were misclassified as bog in the SVM method. In addition, in the XGB and ResNet50 models, about 25% and 28% of swamp classes, respectively, were classified correctly.

In distinguishing wetland classes, the Wet-GC method was also the best one. More than 43% of fen, swamp, and marsh classes were correctly classified in Wet-GC, and beyond 75% of bog classes. The efficiency of Wet-GC could be due to CNNs' nature, which is to extract and add new features for training the network, combined with the GCNs' nature, which is to explore the spatial relations of the pixels (in fact, the wetland classes). Moreover, all the models use the S1 and S2 images as stacked data and apply the classification procedure for the data at once. In contrast, the Wet-GC method deals with each dataset separately and through two branches, which are inherently designed for such datasets. In particular, the CNN branch handles the contextual information in S2 multispectral data, while the mini-GCN branch takes into account the spatial relationships of pixels in S1 data.

## 3.8 Conclusion

Wetlands are one of the most unique, valuable, and beautiful ecosystem types on Earth and perform a variety of ecological and socio-economic benefits. However, anthropogenic activities significantly threaten wetlands' capacity and their services. Hence, mapping these productive resources is crucial to monitor their status (changes and losses). RS-based approaches are time- and cost-effective solutions and superior to laborious fieldwork when dealing with large-scale wetland classification. Although

several DL-based models in the literature have achieved outstanding wetland classification performance, some complex scene classes are still easily misclassified when only a limited number of training samples are available. Thus, exploring new models that require fewer training samples remains a necessity.

This article proposed a novel Wet-GC workflow, which jointly uses the GCN and CNN models. The proposed approach was examined using S1 and S2 imagery and revealed promising results for the classification of wetlands' scenes with minimal need for training samples. This article is the first one investigating the GCN model's performance for large-scale wetland classification using the combination of SAR and optical imagery. The experimental results demonstrate the superiority of the developed framework over the RF, SVM, XGB, and ResNet50 methods. For future work, incorporating richer multispectral data and additional SAR data features to improve the Wet-GC architecture's efficiency and increase the discriminability of the wetland categories is suggested. It is also recommended to employ the proposed method for provincial-scale wetland classification with a variety of training sample sizes. A new study could also be conducted to examine the impacts of different ratios of training samples for each class when GCNs are used.

## 3.9 Future Directions & Recommendations

The success of the Wet-GC multimodal framework demonstrates the power of combining multispectral and SAR data, showing that employing diverse sources can yield robust classification results. However, further research is needed to address the remaining challenges and explore broader applications.

While the current multimodal framework using Sentinel-1 SAR and Sentinel-2 optical imagery shows significant promise, incorporating CP in DL data offers the opportunity to extract new scattering mechanisms and polarization features unique to wetlands. Such features are likely to improve classification accuracy by providing more insights into vegetation structure and hydrological states within Canada's varied wetland environments. By enriching feature sets, CP data stands to increase the precision of wetland mapping and tracking, especially in wetland landscapes, which is essential for monitoring biodiversity, hydrology, and carbon storage.

In view of the foregoing considerations, one major future direction would be the

utilization of CP data to capture features unique to Canada's wetlands, which are not readily available from other RS platforms. RCM CP-SAR data offers enhanced sensitivity to polarization-based scattering mechanisms, which can reveal differences in wetland vegetation and hydrology that traditional data sources may overlook. This could enable more precise mapping of specific wetland types and ecological conditions unique to Canada, deepening our understanding of wetland landscapes.

## 3.10 References

[1] M. Guo, J. Li, C. Sheng, J. Xu, and L. Wu, "A review of wetland remote sensing," *Sensors*, vol. 17, no. 4, p. 777, 2017.

[2] R. W. Tiner, *Wetland indicators: A guide to wetland formation, identification, delineation, classification, and mapping*. CRC press, 2016.

[3] M. Mahdianpari, H. Jafarzadeh, J. E. Granger, F. Mohammadimanesh, B. Brisco, B. Salehi, S. Homayouni, and Q. Weng, "A large-scale change monitoring of wetlands using time series landsat imagery on google earth engine: a case study in newfoundland," *GIScience & Remote Sensing*, vol. 57, no. 8, pp. 1102–1124, 2020.

[4] A. L. Gallant, "The challenges of remote monitoring of wetlands," 2015.

[5] G. Kaplan and U. Avdan, "Monthly analysis of wetlands dynamics using remote sensing data," *ISPRS International Journal of Geo-Information*, vol. 7, no. 10, p. 411, 2018.

[6] M. Mahdianpari, B. Brisco, J. E. Granger, F. Mohammadimanesh, B. Salehi, S. Banks, S. Homayouni, L. Bourgeau-Chavez, and Q. Weng, "The second generation canadian wetland inventory map at 10 meters resolution using google earth engine," *Canadian Journal of Remote Sensing*, vol. 46, no. 3, pp. 360–375, 2020.

[7] M. Mahdianpari, H. Jafarzadeh, J. Granger, F. Mohammadimanesh, B. Brisco, B. Salehi, S. Homayouni, and Q. Weng, "Monitoring of 30 years wetland changes

in newfoundland, canada," in *2021 IEEE International Geoscience and Remote Sensing Symposium IGARSS*, pp. 88–91, IEEE, 2021.

[8] M. Mahdianpari, B. Salehi, F. Mohammadimanesh, B. Brisco, S. Homayouni, E. Gill, E. R. DeLancey, and L. Bourgeau-Chavez, "Big data for a big country: The first generation of canadian wetland inventory map at a spatial resolution of 10-m using sentinel-1 and sentinel-2 data on the google earth engine cloud computing platform," *Canadian journal of remote sensing*, vol. 46, no. 1, pp. 15–33, 2020.

[9] C. Fang, Z. Tao, D. Gao, and H. Wu, "Wetland mapping and wetland temporal dynamic analysis in the nanjishan wetland using gaofen one data. spatial sci. 22, 259–271," 2016.

[10] D. Were, F. Kansiime, T. Fetahi, A. Cooper, and C. Jjuuko, "Carbon sequestration by wetlands: a critical review of enhancement measures for climate change mitigation," *Earth Systems and Environment*, vol. 3, pp. 327–340, 2019.

[11] C. H. Marshall, R. A. Pielke, and L. T. Steyaert, "Has the conversion of natural wetlands to agricultural land increased the incidence and severity of damaging freezes in south florida?," *Monthly Weather Review*, vol. 132, no. 9, pp. 2243–2258, 2004.

[12] G. D. Lynne, P. Conroy, and F. J. Prochaska, "Economic valuation of marsh areas for marine production processes," *Journal of environmental economics and management*, vol. 8, no. 2, pp. 175–186, 1981.

[13] C. N. Raphael and E. Jaworski, "Economic value of fish, wildlife, and recreation in michigan's coastal wetlands," *Coastal Management*, vol. 5, no. 3, pp. 181–194, 1979.

[14] R. Costanza, O. Pérez-Maqueo, M. L. Martinez, P. Sutton, S. J. Anderson, and K. Mulder, "The value of coastal wetlands for hurricane protection," *Ambio*, pp. 241–248, 2008.

[15] R. Gardner, S. Barchiesi, C. Beltrame, C. Finlayson, T. Galewski, I. Harrison, M. Paganini, C. Perennou, D. Pritchard, A. Rosenqvist, *et al.*, "State of the world's wetlands and their services to people: A compilation of recent analyses. 2015," *DOI: https://doi. org/10.2139/ssrn*, vol. 2589447, pp. 1–20.

[16] K. Schmidt and A. Skidmore, "Spectral discrimination of vegetation types in a coastal wetland," *Remote sensing of Environment*, vol. 85, no. 1, pp. 92–108, 2003.

[17] T. Landmann, M. Schramm, R. R. Colditz, A. Dietz, and S. Dech, "Wide area wetland mapping in semi-arid africa using 250-meter modis metrics and topographic variables," *Remote Sensing*, vol. 2, no. 7, pp. 1751–1766, 2010.

[18] S. C. Zoltai and D. H. Vitt, "Canadian wetlands: environmental gradients and classification," *Vegetatio*, vol. 118, pp. 131–137, 1995.

[19] S. Mahdavi, B. Salehi, J. Granger, M. Amani, B. Brisco, and W. Huang, "Remote sensing for wetland classification: A comprehensive review," *GIScience & remote sensing*, vol. 55, no. 5, pp. 623–658, 2018.

[20] F. M. Henderson and A. J. Lewis, "Radar detection of wetland ecosystems: a review," *International journal of remote sensing*, vol. 29, no. 20, pp. 5809–5835, 2008.

[21] E. R. DeLancey, J. F. Simms, M. Mahdianpari, B. Brisco, C. Mahoney, and J. Kariyeva, "Comparing deep learning and shallow learning for large-scale wetland classification in alberta, canada," *Remote Sensing*, vol. 12, no. 1, p. 2, 2019.

[22] A. L. Gallant, S. G. Kaya, L. White, B. Brisco, M. F. Roth, W. Sadinski, and J. Rover, "Detecting emergence, growth, and senescence of wetland vegetation with polarimetric synthetic aperture radar (sar) data," *Water*, vol. 6, no. 3, pp. 694–722, 2014.

[23] E. S. Kasischke, K. B. Smith, L. L. Bourgeau-Chavez, E. A. Romanowicz, S. Brunzell, and C. J. Richardson, "Effects of seasonal hydrologic patterns in south florida wetlands on radar backscatter measured from ers-2 sar imagery," *Remote sensing of environment*, vol. 88, no. 4, pp. 423–441, 2003.

[24] S. O. Mabwoga and A. K. Thukral, "Characterization of change in the harike wetland, a ramsar site in india, using landsat satellite data," *SpringerPlus*, vol. 3, pp. 1–11, 2014.

[25] M. J. McCarthy, E. J. Merton, and F. E. Muller-Karger, "Improved coastal wetland mapping using very-high 2-meter spatial resolution imagery," *International*

*Journal of Applied Earth Observation and Geoinformation*, vol. 40, pp. 11–18, 2015.

[26] R. Shen, A. Huang, B. Li, and J. Guo, "Construction of a drought monitoring model using deep learning based on multi-source remote sensing data," *International Journal of Applied Earth Observation and Geoinformation*, vol. 79, pp. 48–57, 2019.

[27] H. Chen, C. Wu, B. Du, L. Zhang, and L. Wang, "Change detection in multisource vhr images via deep siamese convolutional multiple-layers recurrent neural network," *IEEE Transactions on Geoscience and Remote Sensing*, vol. 58, no. 4, pp. 2848–2864, 2019.

[28] M. Li, P. Wu, B. Wang, H. Park, H. Yang, and Y. Wu, "A deep learning method of water body extraction from high resolution remote sensing images with multisensors," *IEEE Journal of Selected Topics in Applied Earth Observations and Remote Sensing*, vol. 14, pp. 3120–3132, 2021.

[29] B. Hosseiny, M. Mahdianpari, B. Brisco, F. Mohammadimanesh, and B. Salehi, "Wetnet: A spatial–temporal ensemble deep learning model for wetland classification using sentinel-1 and sentinel-2," *IEEE transactions on geoscience and remote sensing*, vol. 60, pp. 1–14, 2021.

[30] D. Amarsaikhan, H. Blotevogel, J. Van Genderen, M. Ganzorig, R. Gantuya, and B. Nergui, "Fusing high-resolution sar and optical imagery for improved urban land cover study and classification," *International Journal of Image and Data Fusion*, vol. 1, no. 1, pp. 83–97, 2010.

[31] S. Van Beijma, A. Comber, and A. Lamb, "Random forest classification of salt marsh vegetation habitats using quad-polarimetric airborne sar, elevation and optical rs data," *Remote Sensing of Environment*, vol. 149, pp. 118–129, 2014.

[32] J. Zhang, "Multi-source remote sensing data fusion: status and trends," *International Journal of Image and Data Fusion*, vol. 1, no. 1, pp. 5–24, 2010.

[33] M. Mahdianpari, B. Salehi, F. Mohammadimanesh, S. Homayouni, and E. Gill, "The first wetland inventory map of newfoundland at a spatial resolution of 10 m using sentinel-1 and sentinel-2 data on the google earth engine cloud computing platform," *Remote Sensing*, vol. 11, no. 1, p. 43, 2018.

[34] A. Jamali, M. Mahdianpari, B. Brisco, J. Granger, F. Mohammadimanesh, and B. Salehi, "Deep forest classifier for wetland mapping using the combination of sentinel-1 and sentinel-2 data," *GIScience & Remote Sensing*, vol. 58, no. 7, pp. 1072–1089, 2021.

[35] M. Amani, B. Salehi, S. Mahdavi, and B. Brisco, "Spectral analysis of wetlands using multi-source optical satellite imagery," *ISPRS journal of photogrammetry and remote sensing*, vol. 144, pp. 119–136, 2018.

[36] E. Maggiori, Y. Tarabalka, G. Charpiat, and P. Alliez, "Convolutional neural networks for large-scale remote-sensing image classification," *IEEE Transactions on geoscience and remote sensing*, vol. 55, no. 2, pp. 645–657, 2016.

[37] W. Zhang, P. Tang, and L. Zhao, "Remote sensing image scene classification using cnn-capsnet," *Remote Sensing*, vol. 11, no. 5, p. 494, 2019.

[38] Q. Wang, Z. Yuan, Q. Du, and X. Li, "Getnet: A general end-to-end 2-d cnn framework for hyperspectral image change detection," *IEEE Transactions on Geoscience and Remote Sensing*, vol. 57, no. 1, pp. 3–13, 2018.

[39] B. Yu, L. Yang, and F. Chen, "Semantic segmentation for high spatial resolution remote sensing images based on convolution neural network and pyramid pooling module," *IEEE Journal of Selected Topics in Applied Earth Observations and Remote Sensing*, vol. 11, no. 9, pp. 3252–3261, 2018.

[40] G. Wang, B. Fan, S. Xiang, and C. Pan, "Aggregating rich hierarchical features for scene classification in remote sensing imagery," *IEEE Journal of Selected Topics in Applied Earth Observations and Remote Sensing*, vol. 10, no. 9, pp. 4104–4115, 2017.

[41] X. Liu, Y. Zhou, J. Zhao, R. Yao, B. Liu, and Y. Zheng, "Siamese convolutional neural networks for remote sensing scene classification," *IEEE Geoscience and Remote Sensing Letters*, vol. 16, no. 8, pp. 1200–1204, 2019.

[42] J. Xie, N. He, L. Fang, and A. Plaza, "Scale-free convolutional neural network for remote sensing scene classification," *IEEE Transactions on Geoscience and Remote Sensing*, vol. 57, no. 9, pp. 6916–6928, 2019.

[43] M. Rezaee, M. Mahdianpari, Y. Zhang, and B. Salehi, "Deep convolutional neural network for complex wetland classification using optical remote sensing imagery," *IEEE Journal of Selected Topics in Applied Earth Observations and Remote Sensing*, vol. 11, no. 9, pp. 3030–3039, 2018.

[44] G. L. O'Neil, J. L. Goodall, M. Behl, and L. Saby, "Deep learning using physically-informed input data for wetland identification," *Environmental modelling & software*, vol. 126, p. 104665, 2020.

[45] A. Jamali and M. Mahdianpari, "Swin transformer and deep convolutional neural networks for coastal wetland classification using sentinel-1, sentinel-2, and lidar data," *Remote Sensing*, vol. 14, no. 2, p. 359, 2022.

[46] Y. Gao, J. Shi, J. Li, and R. Wang, "Remote sensing scene classification based on high-order graph convolutional network," *European Journal of Remote Sensing*, vol. 54, no. sup1, pp. 141–155, 2021.

[47] B. Liu, K. Gao, A. Yu, W. Guo, R. Wang, and X. Zuo, "Semisupervised graph convolutional network for hyperspectral image classification," *Journal of Applied Remote Sensing*, vol. 14, no. 2, pp. 026516–026516, 2020.

[48] A. Sha, B. Wang, X. Wu, and L. Zhang, "Semisupervised classification for hyperspectral images using graph attention networks," *IEEE Geoscience and Remote Sensing Letters*, vol. 18, no. 1, pp. 157–161, 2020.

[49] S. Wan, C. Gong, P. Zhong, S. Pan, G. Li, and J. Yang, "Hyperspectral image classification with context-aware dynamic graph convolutional network," *IEEE Transactions on Geoscience and Remote Sensing*, vol. 59, no. 1, pp. 597–612, 2020.

[50] S. Wan, C. Gong, P. Zhong, B. Du, L. Zhang, and J. Yang, "Multiscale dynamic graph convolutional network for hyperspectral image classification," *IEEE Transactions on Geoscience and Remote Sensing*, vol. 58, no. 5, pp. 3162–3177, 2019.

[51] L. Mou, X. Lu, X. Li, and X. X. Zhu, "Nonlocal graph convolutional networks for hyperspectral image classification," *IEEE Transactions on Geoscience and Remote Sensing*, vol. 58, no. 12, pp. 8246–8257, 2020.

[52] D. Hong, L. Gao, J. Yao, B. Zhang, A. Plaza, and J. Chanussot, "Graph convolutional networks for hyperspectral image classification," *IEEE Transactions on Geoscience and Remote Sensing*, vol. 59, no. 7, pp. 5966–5978, 2020.

[53] V. Mazzia, A. Khaliq, and M. Chiaberge, "Improvement in land cover and crop classification based on temporal features learning from sentinel-2 data using recurrent-convolutional neural network (r-cnn)," *Applied Sciences*, vol. 10, no. 1, p. 238, 2019.

[54] D. Ienco, R. Interdonato, R. Gaetano, and D. H. T. Minh, "Combining sentinel-1 and sentinel-2 satellite image time series for land cover mapping via a multi-source deep learning architecture," *ISPRS Journal of Photogrammetry and Remote Sensing*, vol. 158, pp. 11–22, 2019.

[55] M. Gori, G. Monfardini, and F. Scarselli, "A new model for learning in graph domains," in *Proceedings. 2005 IEEE international joint conference on neural networks, 2005.*, vol. 2, pp. 729–734, IEEE, 2005.

[56] D. Hong, N. Yokoya, N. Ge, J. Chanussot, and X. X. Zhu, "Learnable manifold alignment (lema): A semi-supervised cross-modality learning framework for land cover and land use classification," *ISPRS journal of photogrammetry and remote sensing*, vol. 147, pp. 193–205, 2019.

[57] C. D. McGillem and G. R. Cooper, "Continuous and discrete signal and system analysis," *(No Title)*, 1991.

[58] K. He, X. Zhang, S. Ren, and J. Sun, "Spatial pyramid pooling in deep convolutional networks for visual recognition," *IEEE transactions on pattern analysis and machine intelligence*, vol. 37, no. 9, pp. 1904–1916, 2015.

[59] H. Lee and H. Kwon, "Going deeper with contextual cnn for hyperspectral image classification," *IEEE Transactions on Image Processing*, vol. 26, no. 10, pp. 4843–4855, 2017.

[60] M. Mahdianpari, B. Salehi, F. Mohammadimanesh, and M. Motagh, "Random forest wetland classification using alos-2 l-band, radarsat-2 c-band, and terrasar-x imagery," *ISPRS Journal of Photogrammetry and Remote Sensing*, vol. 130, pp. 13–31, 2017.

[61] N. Gorelick, M. Hancher, M. Dixon, S. Ilyushchenko, D. Thau, and R. Moore, "Google earth engine: Planetary-scale geospatial analysis for everyone," *Remote sensing of Environment*, vol. 202, pp. 18–27, 2017.

[62] K. Van Tricht, A. Gobin, S. Gilliams, and I. Piccard, "Synergistic use of radar sentinel-1 and optical sentinel-2 imagery for crop mapping: A case study for belgium," *Remote Sensing*, vol. 10, no. 10, p. 1642, 2018.

[63] B. Slagter, N.-E. Tsendbazar, A. Vollrath, and J. Reiche, "Mapping wetland characteristics using temporally dense sentinel-1 and sentinel-2 data: A case study in the st. lucia wetlands, south africa," *International Journal of Applied Earth Observation and Geoinformation*, vol. 86, p. 102009, 2020.

[64] K. He, X. Zhang, S. Ren, and J. Sun, "Deep residual learning for image recognition," in *Proceedings of the IEEE conference on computer vision and pattern recognition*, pp. 770–778, 2016.

[65] H. Liu, Q. Jiang, Y. Ma, Q. Yang, P. Shi, S. Zhang, Y. Tan, J. Xi, Y. Zhang, B. Liu, *et al.*, "Object-based multigrained cascade forest method for wetland classification using sentinel-2 and radarsat-2 imagery," *Water*, vol. 14, no. 1, p. 82, 2022.

[66] M. Mahdianpari, B. Salehi, M. Rezaee, F. Mohammadimanesh, and Y. Zhang, "Very deep convolutional neural networks for complex land cover mapping using multispectral remote sensing imagery," *Remote Sensing*, vol. 10, no. 7, p. 1119, 2018.

[67] H. Jafarzadeh, M. Mahdianpari, E. Gill, F. Mohammadimanesh, and S. Homayouni, "Bagging and boosting ensemble classifiers for classification of multispectral, hyperspectral and polsar data: a comparative evaluation," *Remote Sensing*, vol. 13, no. 21, p. 4405, 2021.

[68] H. Jafarzadeh and M. Hasanlou, "An unsupervised binary and multiple change detection approach for hyperspectral imagery based on spectral unmixing," *IEEE Journal of Selected Topics in Applied Earth Observations and Remote Sensing*, vol. 12, no. 12, pp. 4888–4906, 2019.

# Chapter 4

# Wetland Classification Using CP-SAR & DL

## 4.1 Preface

I am the primary author of this work, with Masoud Mahdianpari and Eric Gill as co-authors. I conceptualized and designed the study, developed the model, and conducted all experiments and tests. Additionally, I was responsible for writing the manuscript and ensuring the conveyance of technical content. My co-authors contributed by providing valuable feedback, reviewing the manuscript, and offering insightful comments. I revised the manuscript accordingly, incorporating their suggestions.

## 4.2 Abstract

Wetland mapping plays an important role in environmental monitoring, particularly in assessing biodiversity dynamics. This study presents a deep-learning (DL) based model, which integrates RADARSAT Constellation Mission (RCM) compact polarimetric (CP) synthetic aperture radar (SAR) and Sentinel-2 (S2) optical data for wetland classification. The model integrates spatial, spectral, and polarimetric information through two primary input streams: (1) RCM CP Backscratching channels and S2 spectral bands and (2) polarimetric decomposition features. These features are first processed separately to extract representations and then fused using an adaptive

weighted fusion mechanism. Additionally, the model employs a polarization-aware cross-attention mechanism to capture cross-modality interactions between the spatial-spectral and polarimetric features, enhancing the model's ability to focus on crucial areas in the wetlands. Experimental results and a comparative analysis with well-known DL models demonstrated the effectiveness of this model in wetland mapping.

## 4.3 Introduction

Wetlands are unique ecosystems characterized by the presence of water, either permanently or seasonally, which significantly influences their biological productivity [1]. These ecosystems are vital for biodiversity conservation, hydrological regulation, and carbon storage. Globally, wetlands are considered one of the most productive ecosystems, making their mapping and monitoring crucial for effective environmental management.

In recent years, the advent of remote sensing (RS) technologies has revolutionized the monitoring and assessment of wetlands. Among the various RS methods, Synthetic Aperture Radar (SAR) has proven to be highly effective due to its ability to capture detailed information regardless of weather conditions or time of day. The RADARSAT Constellation Mission (RCM) provides a unique opportunity to utilize high-resolution C-band SAR data, specifically the compact polarization (CP) channels, to enhance our understanding of wetland dynamics [2].

Traditional classification techniques often struggle with the heterogeneous and dynamic nature of wetland landscapes. Wetlands exhibit varying vegetation types, water bodies, and soil conditions that can be difficult to classify using conventional methods. Therefore, there is an increasing demand for innovative approaches that can capture the intricate spatial relationships within wetland ecosystems. In this context, deep learning (DL) techniques have shown great promise in overcoming the limitations of traditional methods. For instance, Convolutional Neural Networks (CNNs), Long Short-Term Memory (LSTM) networks, and more recently, transformer-based architectures, have been successfully applied to RS tasks, including land cover classification and environmental monitoring. However, the complexity and scale of wetland ecosystems necessitate the development of new frameworks capable of capturing the spatial and contextual relationships within satellite imagery, specifically when considering

the nature of advanced SAR data sources.

This paper presents a novel DL framework specifically designed for wetland classification using RCM CP-SAR data. The proposed framework integrates advanced techniques, including feature fusion and a contextual attention mechanism, to introduce a new procedure capable of discriminating wetland classes using small sets of input features. Through the use of multi-branch architecture and feature fusion strategies, the model integrates information from SAR channels and derived components. Additionally, the dynamic weighting mechanism within the model enables it to adaptively prioritize different features depending on the specific context of the input data.

SAR data has gained significant prominence in various RS applications due to its weather-, illumination-, and time-independent properties. In particular, it has been extensively applied to wetland type identification and vegetation index formulation [3]. The interaction of SAR signals with vegetation and soil properties, influenced by key parameters such as wavelength, polarization, and incidence angle, determines the reflected backscattering signals, which contain useful information about the surface's geometric and dielectric properties [4, 5, 6].

Among various SAR systems, the RADARSAT Constellation Mission (RCM) provides significant opportunities for wetland monitoring and mapping in Canada. By using a CP configuration and using single-transmit polarization, the power requirements are substantially lower than those of full polarimetric (FP) modes [7]. Several studies have explored the use of simulated CP-SAR data to assess the potential of the CP acquisition mode, as described by [8], in a range of applications such as wetland classification [9] and crop inventory mapping [10]. Due to limited availability of CP data, many researchers have relied on simulated CP data generated from the FP acquisition mode, with RADARSAT-2 FP data being predominantly used for these applications. Additionally, research has indicated that CP parameters are sensitive to variations in land cover types [11].

Polarimetric decomposition is a vital technique for extracting meaningful polarimetric parameters from SAR data, providing insights into the physical characteristics of natural surfaces and aiding in land cover mapping. As SAR technology has advanced, especially with the advent of regional coverage and high-resolution data

offered by RCM, innovative methodologies for wetland monitoring have become increasingly relevant. This research focuses on evaluating the significance of RCM CP-SAR data in wetland mapping with a focus on CP data and developing a CP-aware DL model.

The primary objective of this study is to evaluate the potential of RCM CP-SAR data for wetland mapping using DL. A secondary goal is to develop a simplified yet efficient DL model to capture CP features and enhance wetland mapping. These efforts aim to advance satellite-based wetland monitoring by employing advanced artificial intelligence techniques that address the unique characteristics of the data and the specific nature of wetland ecosystems.

The structure of the paper is organized as follows: Section 4.4 provides a concise overview of the decomposition features utilized in this study. Section 4.5 describes the study area and details the data preparation process. The methodology, including the proposed model, experimental results, and comparative analysis, is presented in Section 4.6. Finally, Section 4.7 summarizes the findings and concludes the study.

## 4.4 The $m$-$\delta$ and $m$-$\chi$ Decompositions Review

The compact system measures a projection of the complex scattering matrix **s** onto a transmitted electromagnetic field $\mathbf{E}_i$, as shown in Equation 4.1.

$$\begin{aligned} \vec{E} = \begin{bmatrix} E_{\mathrm{CH}} \\ E_{\mathrm{CV}} \end{bmatrix} &= \frac{1}{\sqrt{2}} \begin{bmatrix} \mathrm{S_{HH}} & \mathrm{S_{HV}} \\ \mathrm{S_{VH}} & \mathrm{S_{VV}} \end{bmatrix} \begin{bmatrix} 1 \\ \pm i \end{bmatrix} \\ &= \frac{1}{\sqrt{2}} \begin{bmatrix} \mathrm{S_{HH}} \pm i\mathrm{S_{HV}} \\ \mathrm{S_{VH}} \pm i\mathrm{S_{VV}} \end{bmatrix} \end{aligned} \tag{4.1}$$

In the circularly polarized transmit mode, the + sign is for left-hand and the - sign is for right-hand circular. The RCM CP-SAR system employs a right-handed circularly polarized transmit signal while coherently recording both the horizontal and vertical components (H + V) of the backscattered signal in its system [2]. This configuration is achieved by applying a 90-degree phase shift to the H and V feeds [8]. One can extract the characteristics of the observed surface using the four-element Stokes vector,

as defined in Equation 4.2, which is commonly used to describe the polarization information obtained from the observed scene:

$$\boldsymbol{g_s} = \begin{bmatrix} g_0 \\ g_1 \\ g_2 \\ g_3 \end{bmatrix} = \begin{bmatrix} \langle |E_{\mathrm{CH}}|^2 + |E_{\mathrm{CV}}|^2 \rangle \\ \langle |E_{\mathrm{CH}}|^2 - |E_{\mathrm{CV}}|^2 \rangle \\ 2\Re\langle E_{\mathrm{CH}} E_{\mathrm{CV}}^* \rangle \\ 2\Im\langle E_{\mathrm{CH}} E_{\mathrm{CV}}^* \rangle \end{bmatrix} . \tag{4.2}$$

Various parameters can be derived from the Stokes vector, including the degree of polarization $m$, the relative phase $\delta$, and the ellipticity angle $\chi$, which are defined as follows:

$$m = \frac{\sqrt{g_1^2 + g_2^2 + g_3^2}}{g_0}, \tag{4.3}$$

$$\delta = \arg(g_2 + j g_3), \tag{4.4}$$

$$\sin 2\chi = -\frac{g_3}{m g_0}. \tag{4.5}$$

The total backscattered energy, represented by the Stokes component $g_0$, along with the polarimetric features $m$, $\delta$, and $\chi$, were used to compute the $m$-$\delta$ decomposition [8] (see Equation 4.7) and the $m$-$\chi$ [12] decomposition (see Equation 4.6).

$$\begin{bmatrix} P_{\mathrm{d}} \\ P_{\mathrm{v}} \\ P_{\mathrm{s}} \end{bmatrix}_{m-\delta} = \begin{bmatrix} \sqrt{\frac{g_0 m(1 \mp \sin\delta)}{2}} \\ \sqrt{g_0(1-m)} \\ \sqrt{\frac{g_0 m(1 \pm \sin\delta)}{2}} \end{bmatrix}, \tag{4.6}$$

$$\begin{bmatrix} P_{\mathrm{d}} \\ P_{\mathrm{v}} \\ P_{\mathrm{s}} \end{bmatrix}_{m-\chi} = \begin{bmatrix} \sqrt{\frac{g_0 m(1 \pm \sin 2\chi)}{2}} \\ \sqrt{g_0(1-m)} \\ \sqrt{\frac{g_0 m(1 \mp \sin 2\chi)}{2}} \end{bmatrix}. \tag{4.7}$$

In Equations 4.6 and 4.7, the $+$ and $-$ signs correspond to the left-hand and right-hand circular transmit modes, respectively. The formulations for both decompositions are nearly identical, with the parameters $\delta$ and $\chi$ serving as indicators of single-bounce

and double-bounce scattering. It is important to note that single- and double-bounce reflections exhibit distinct signatures in the left-hand and right-hand polarization states. Additionally, the random polarized component $P_{\mathrm{v}}$ is solely dependent on $m$. In scattering processes dominated by multiple reflections, such as in highly vegetated wetlands, $P_{\mathrm{v}}$ may surpass either $P_{\mathrm{s}}$ or $P_{\mathrm{d}}$. From the observation, we can deduce that in the right-hand CP case, $\delta$ will be $-90^{\circ}$ for the surface scattering and $90^{\circ}$ for the double-bounce scattering, and $\chi$ will be $45^{\circ}$ for the surface scattering and $-45^{\circ}$ for the double-bounce scattering.

## 4.5 Study Area and Dataset

### 4.5.1 Study Area

Encompassing a geographical area from W82°11′28.04″ to W82°57′8.07″ longitude and N54°0′5.53″ to N55°3′42.53″ latitude, the experiment was conducted in a small part of the Hudson Bay Lowlands. The 'lowlands' include adjacent areas of flat terrain and wetlands. The Hudson Bay Lowlands refer to that vast tract of land that rises from the tidal flats around the southern part of Hudson Bay and James Bay to form lowland plains 150–400 km wide. This region is one of the three largest wetlands in the world, and although there are areas of inorganic surface sediments and bedrock, more than 80% of the lowlands are covered by wetlands. To manage the computational workload and ensure a focused evaluation and comparison, classification maps were generated from two locations (as shown in Figure 4.1) of this wetland region. This wetland landscape hosts bog, fen, marsh, and water classes.

### 4.5.2 Satellite Imagery and Pre-processing

In this study, we processed two Single Look Complex (SLC) RCM frames acquired in July 2021. The images captured in StripMap beam mode have a nominal spatial resolution of 5 meters. The coverage area of these two image frames, which encompass the study area as depicted in Figure 4.4, is detailed in Table 4.1.

The RCM images were preprocessed using SNAP software following standard procedures outlined in [7]. The preprocessing began with calibration to convert the digital

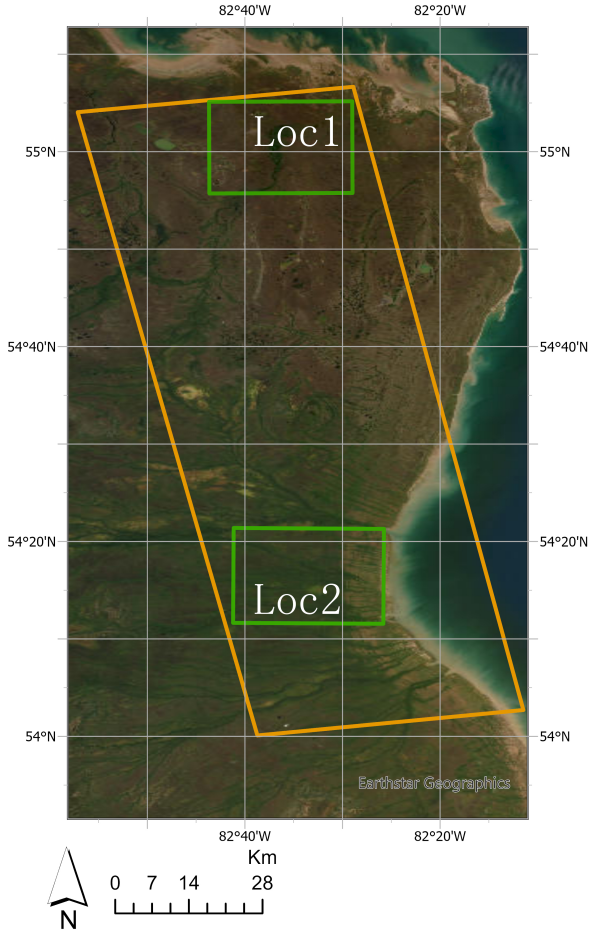



Figure 4.1: Study area with coverage of a portion of two RCM images.

CH and CV channels into sigma-naught ($\sigma^0$) backscatter coefficient in decibels. To minimize speckle noise and create ground-range square pixels, the images were multilooked with two looks in both azimuth and range directions ($2 \times 2$). Next, the $2 \times 2$ covariance matrix ($\mathbf{C}_2$) for each SAR image pixel was generated using the Polarimetric Matrix Generation toolbox in SNAP. This facilitated polarimetric decomposition to analyze scattering mechanisms. To correct geometric distortions caused by topography, terrain correction was applied to the $\mathbf{C}_2$ matrix using SNAP's Range Doppler Terrain Correction module and the SRTM 1 arc-second DEM [13, 14]. Speckle noise was further reduced by applying a $3 \times 3$ Boxcar filter. Finally, a subset of the data was used to cover the region of interest for analysis. In addition, as a complementary data source to SAR imagery, four bands of 10-meter spatial resolution surface reflectance from Sentinel-2 imagery were processed and extracted using Google Earth Engine during July over the study area.

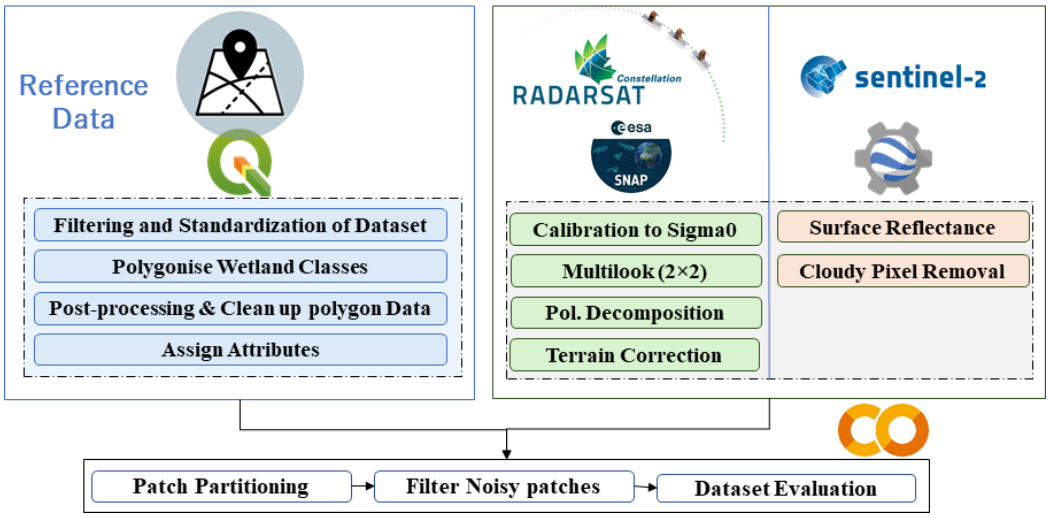



Figure 4.2: Preparation of training sample patches used in this study.

Table 4.1: The characteristics of RCM images utilized in this study.

| # | Satellite | Acquisition Date | Orbit Pass | Beam Mode | Resolution (rg×az) | Polarization | Looking Direction | Swath width |
|---|---|---|---|---|---|---|---|---|
| 1 | RCM1 | 2021-July | Ascending | High Resolution (StripMap) | 2.8 m×2.5 m | (RH, RV) | Right Looking | 30 km |
| 2 | RCM2 | 2021-July | | | | | | |

### 4.5.3 Reference Data and Sample Patches Partitioning

Obtaining reliable ground-truth data remains a critical challenge for supervised classification, especially in large and complex study areas. Ground-truth labels are typically acquired through field surveys, which provide high-fidelity and firsthand information [15, 16]. However, these field campaigns are often constrained by significant demands on time and human resources.

Reference data for this work were generated and polygonized using the wetland inventory map as described in [17]. To ensure the accuracy of the generated labels, the reference data were further augmented through careful cross-validation with high-resolution satellite imagery. This validation process enabled reliable polygonization and labeling, providing a robust foundation for the analyses conducted in this work.

In our workflow to create image patches from the polygonized reference areas, each image patch is associated with one land-cover class label. To create and split image patches from RCM and S2 data, neighborhoods of size of $d \times d$ pixels in/around the polygons is extracted. Then, each class polygon is tracked to cut the image blocks

to a pre-set patch size from the image composite. To determine the optimum $d$, we analyzed the performance of multiple well-known DL approaches (i.e., ResNet50, DenseNet121, and InceptionResNetV2) with different image patch sizes. Generally:

- If the patch size is very small, it may capture finer details but potentially result in a loss of contextual information for classification.
- If the patch size is very large, it may introduce unnecessary noise and include information from neighboring classes.

Hence, different values of $d$ have been chosen, specifically, $d = [10, 20, 30, 40]$ - to investigate the correlation between overall accuracy and the image patch size $d$. To conduct this analysis, a set of image patches (generated from both RCM and S2 data) was chosen for each image patch size. Each set comprises 100 image patches per class, and the average overall accuracies across these sets were subsequently compared. Figure 4.3 shows that for $d = 10$ and $d = 40$, the overall accuracy decreases sharply. This decline is due to the significant loss of fine-grained details in smaller patches ($d = 10$) and an excessive focus on coarse features, which leads to oversimplification ($d = 40$). This imbalance in spatial representation negatively impacts the models' ability to accurately classify intricate patterns within the images, resulting in a notable reduction in accuracy. When $d = 30$, notable increases in overall accuracy are observed. This improvement can be attributed to the optimal balance in capturing spatial information within the image patches. Accordingly, in this study, image patches with a size of $30 \times 30$ were utilized for our investigations.

## 4.6 Methodology and Experimental Design

### 4.6.1 Proposed Method

This study presents the proposed method, a new architecture designed for wetland classification through the integration of dual-modality data and feature interaction techniques. The proposed framework uses CP backscatter channels from RCM imagery, four spectral channels from S2 imagery, and polarimetric decomposition features, fuses them adaptively using a weighted mechanism, and enhances cross-modality

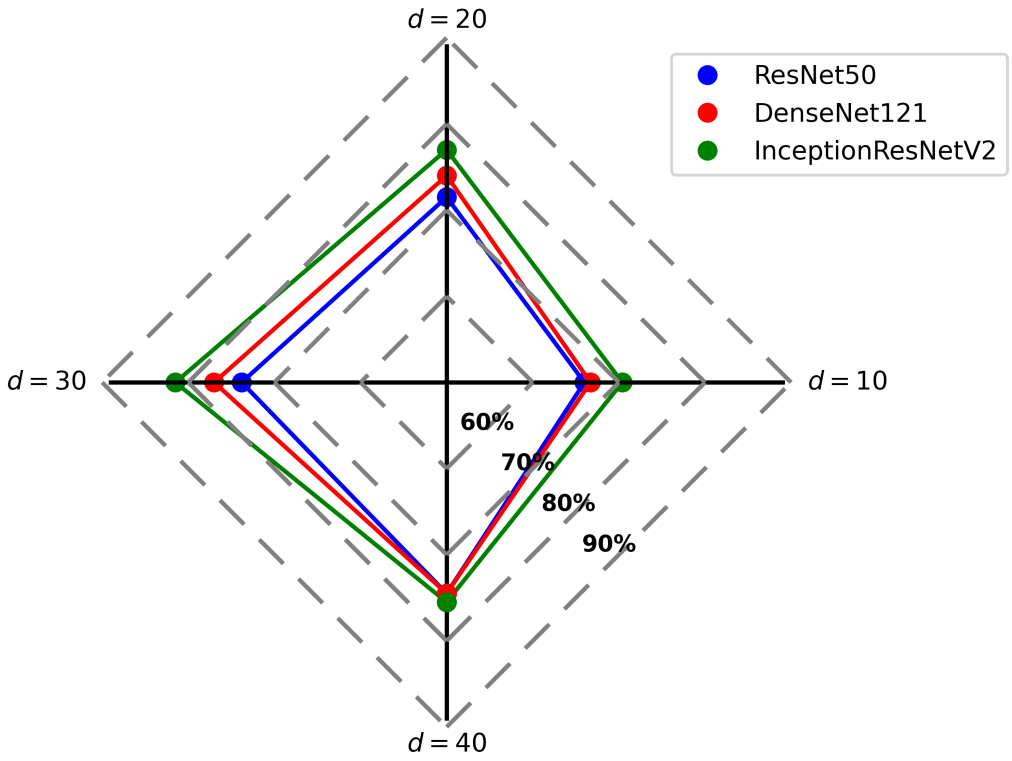



Figure 4.3: Evaluating the effect of different image patch sizes on the accuracy of DL models.

interactions through an attention module. Figure 4.4 presents a simple representation of the proposed model, with the detailed methodology outlined below.

### Input Data Preparation

The input to the proposed model comprises two complementary data modalities:

- **SAR and Optical Data**: The RCM's $CH$ and $CV$ backscatter intensities, represented as:

$$\mathbf{X}_{\text{CHCV}} \in \mathbb{R}^{H \times W \times 2},$$

where $H$ and $W$ denote the spatial dimensions of the input data. Also, four spectral bands from Sentinel-2 imagery, represented as:

$$\mathbf{X}_{\text{Sentinel2}} \in \mathbb{R}^{H \times W \times 4}$$

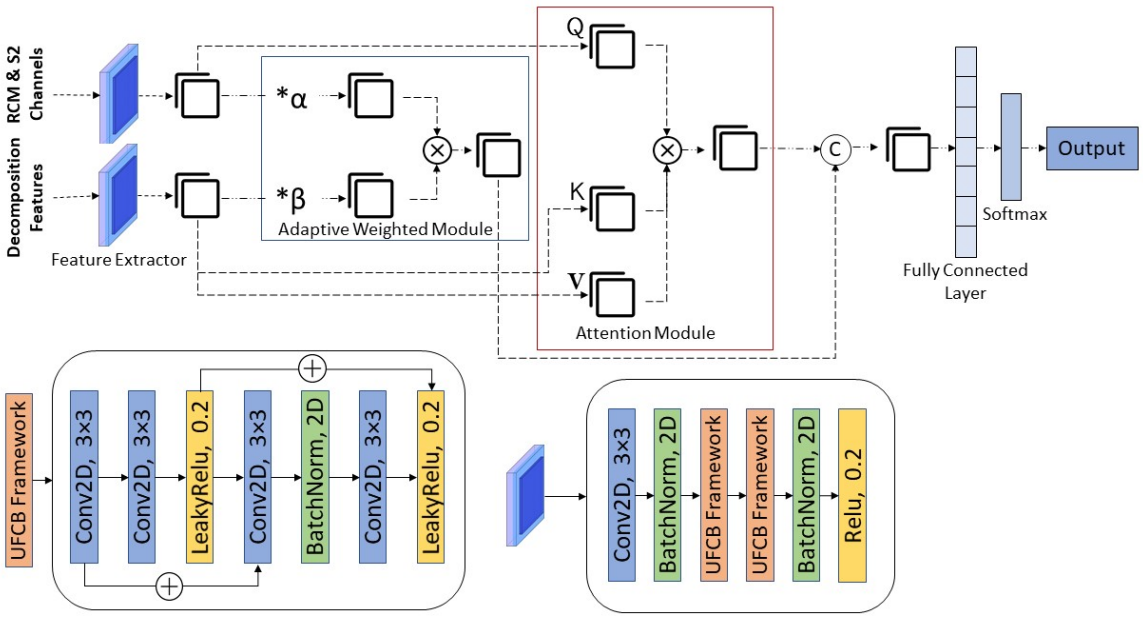



Figure 4.4: Illustration of the proposed model architecture.

- **Polarimetric Decomposition Features**: Key decomposition metrics, such as $m - \chi$ and $m - \delta$, derived from the CP-SAR dataset, represented as:

$$\mathbf{X}_{\text{Decomp}} \in \mathbb{R}^{H \times W \times D},$$

  where $D = 6$ is the number of decomposition features.

These inputs enable the model to capture both spatial-spectral and polarimetric characteristics, critical for accurate wetland classification.

### Dual-Stream Feature Extraction

To process the complementary input modalities, the architecture employs two parallel independent CNN streams. Separate processing allows the network to specialize in extracting complementary information from distinct input types.

The SAR and optical (SO) stream extracts spatial and spectral features:

$$\mathbf{F}_{\text{SO}} = \text{CNN}_{\text{SO}}(\mathbf{X}_{\text{SO}}),$$

while the Decomposition stream extracts polarimetric features:

$$\mathbf{F}_{\text{Decomp}} = \text{CNN}_{\text{Decomp}}(\mathbf{X}_{\text{Decomp}}).$$

$\text{CNN}_{\text{SO}}$ and $\text{CNN}_{\text{Decomp}}$ include a series of convolutional layers for feature extraction. These modules incorporate convolution, batch normalization, unequal feature cascade blocks (UFCB), and max-pooling layers to extract features and learn detailed information from the inputs. A convolution kernel size of 3 is used to enhance the precision of features across multiple scales. The UFCB, as proposed in [18], is designed to efficiently capture local features while enabling a hierarchical representation of these features (refer to Figure 4.2). By connecting the initial and intermediate convolution layers, along with the corresponding activation operations, through mathematical addition, UFCB helps mitigate the issue of feature loss that arises as network depth increases.

### Adaptive Weighted Fusion

An adaptive weighted fusion mechanism is introduced to integrate the features from the two modalities. Let $\mathbf{F}_{\text{SO}}$ and $\mathbf{F}_{\text{Decomp}}$ represent the feature vectors obtained from the respective streams. The model computes modality-specific weights $\alpha$ and $\beta$ as:

$$\begin{aligned} \alpha &= \sigma(\mathbf{W}_\alpha \mathbf{F}_{\text{SO}} + b_\alpha), \\ \beta &= \sigma(\mathbf{W}_\beta \mathbf{F}_{\text{Decomp}} + b_\beta), \end{aligned} \tag{4.8}$$

where $\sigma$ denotes the sigmoid activation function, and $\mathbf{W}_\alpha, \mathbf{W}_\beta, b_\alpha, b_\beta$ are learnable parameters.

The fused feature representation is computed as:

$$\mathbf{F}_{\text{fused}} = \alpha \cdot \mathbf{F}_{\text{SO}} + \beta \cdot \mathbf{F}_{\text{Decomp}}. \tag{4.9}$$

This mechanism dynamically adjusts the contribution of each modality, ensuring optimal feature integration. Dynamic weighting ensures that the model prioritizes the more informative stream based on input variability. It adapts to diverse wetland environments, where spatial or polarimetric information may dominate depending on conditions.

### Cross-Modality Attention Mechanism

To further enhance the interaction between features, the model incorporates a polarization - aware attention mechanism, inspired by transformer architectures. The attention mechanism computes the interaction between modalities by defining the query, key, and value as [19, 20]:

$$\begin{aligned} \mathbf{Q} &= \mathbf{W}_q \mathbf{F}_{\text{SO}}, \\ \mathbf{K} &= \mathbf{W}_k \mathbf{F}_{\text{Decomp}}, \\ \mathbf{V} &= \mathbf{W}_v \mathbf{F}_{\text{Decomp}}, \end{aligned} \tag{4.10}$$

where $\mathbf{W}_q, \mathbf{W}_k, \mathbf{W}_v \in \mathbb{R}^{F \times F}$ are learnable projection matrices. Here, we decided to generate the $\mathbf{Q}$ based on the CP channels and S2 spectral bands; it tries to capture which aspects of the other feature set (in our case, decomposition features) should be attended. The decomposition stream, in turn, provides the context or content (the $\mathbf{K}$ and $\mathbf{V}$) that will be used by the $\mathbf{Q}$ to determine how much attention is given to each part of the decomposition information. This is necessary as it allows the model to focus on crucial cross-modality interactions between spatial and polarimetric features. It also ensures stability and mitigates vanishing gradient issues, enhancing the depth and expressiveness of the model.

The attention weights are computed as:

$$\text{Attention}(\mathbf{Q}, \mathbf{K}) = \text{softmax}\left(\frac{\mathbf{Q}\mathbf{K}^\top}{\sqrt{F}}\right) \tag{4.11}$$

and the attention-enhanced representation is given by:

$$\mathbf{F}_{\text{attn}} = \text{Attention}(\mathbf{Q}, \mathbf{K})\mathbf{V}. \tag{4.12}$$

The final feature representation is obtained by combining the fused features with the attention-enhanced features:

$$\mathbf{F}_{\text{sum}} = \text{Concat}(\mathbf{F}_{\text{fused}}, \mathbf{F}_{\text{attn}}) \tag{4.13}$$

and finally, $\mathbf{F}_{\text{sum}}$, is passed through a series of fully connected layers for classification.

The output is computed as:

$$\hat{y} = \text{softmax}(\mathbf{W}_{\text{class}}\mathbf{F}_{\text{sum}} + b_{\text{class}}) \tag{4.14}$$

where $\hat{y}$ represents the predicted wetland class probabilities, $\mathbf{W}_{\text{class}}$ and $b_{\text{class}}$ denote the learnable weight matrix and bias vector of the classification layer, respectively.

Through a dual-modality feature integration, the proposed model combines spatial backscattering information and polarimetric decomposition features, capturing complementary information for wetland classification. By employing an adaptive weighted fusion, it dynamically balances feature contributions, emphasizing the most informative modality during training. The integration of these components ensures robust performance for wetland classification, particularly in heterogeneous environments. The pseudocode of the proposed method is presented in Algorithm 4.1.

### 4.6.2 Classification and Output

The training of the models used in this study involved selecting key hyperparameters, including the number of layers, batch size, dropout rate, and epochs, through a process of trial and testing. A learning rate was set to 0.001 and a batch size of 32 was chosen to balance model performance and memory constraints, and the model was trained for 100 epochs. The dataset was split into training, validation, and test sets using a ratio of 70:15:15, ensuring a representative distribution of the data for model evaluation. For the training process, a varying number of image patches were sampled from the dataset for each class: bog (300 patches), fen (300 patches), marsh (100 patches), and water (200 patches). Note that the number of patches is not the same for all classes, as it reflects the distribution of class instances in our study area.

Using the aforementioned configurations, the classification results of the proposed model were compared with those of other well-known DL architectures, including ResNet50, DenseNet121, and InceptionResNetV2. The comparative performance of these models is illustrated in Figure 4.5, with results evaluated across four accuracy metrics: Overall Accuracy, Precision, Recall, and F1-Score. From the results, it is evident that the proposed model achieves competitive performance, with results closely aligning with those of InceptionResNetV2, a state-of-the-art DL model. While InceptionResNetV2 outperforms the proposed model, this outcome is expected given its

**Algorithm 4.1** Architecture of the Proposed Method.

**Input:** $\mathbf{X}_{\text{RCM}}$, $\mathbf{X}_{m-\chi}$, $\mathbf{X}_{m-\delta}$ {Input features from RCM, S2, $m-\chi$, and $m-\delta$.}
**Output:** $\hat{y}$ {Predicted class labels for each patch.}
**Step 1: Input Preprocessing**
Extract backscatter channels from RCM: $\mathbf{X}_{\text{RCM}} = [\mathbf{CH}, \mathbf{CV}]$
Extract spectral channels from Sentinel-2: $\mathbf{X}_{\text{S2}} = [\mathbf{b2}, \mathbf{b3}, \mathbf{b4}, \mathbf{b8}]$
So, $\mathbf{X}_{\text{SO}} = [\mathbf{CH}, \mathbf{CV}, \mathbf{b2}, \mathbf{b3}, \mathbf{b4}, \mathbf{b8}]$
Extract polarimetric decomposition features for $m-\chi$:
$\mathbf{X}_{m-\chi} = [m_{\chi_1}, m_{\chi_2}, m_{\chi_3}]$
Extract polarimetric decomposition features for $m-\delta$:
$\mathbf{X}_{m-\delta} = [m_{\delta_1}, m_{\delta_2}, m_{\delta_3}]$
So, $\mathbf{X}_{Decomp} = [m_{\chi_1}, m_{\chi_2}, m_{\chi_3}, m_{\delta_1}, m_{\delta_2}, m_{\delta_3}]$
**Step 2: Feature Extraction using CNNs**
Pass $\mathbf{X}_{\text{SO}}$ through convolutional layers:
$\mathbf{F}_{\text{SO}} = \text{CNN}(\mathbf{X}_{\text{SO}})$
Pass $\mathbf{X}_{Decomp}$ through convolutional layers:
$\mathbf{F}_{Decomp} = \text{CNN}(\mathbf{X}_{Decomp})$
**Step 3: Cross-Attention for Feature Fusion**
Compute the attention scores for each feature set $i \in \{\mathbf{F}_{\text{SO}}, \mathbf{F}_{\text{Decomp}}\}$:
$\mathbf{Q}_i = \mathbf{W}_Q \mathbf{F}_i, \quad \mathbf{K}_i = \mathbf{W}_K \mathbf{F}_i, \quad \mathbf{V}_i = \mathbf{W}_V \mathbf{F}_i$
$\mathbf{A}_i = \text{Softmax}\left(\frac{\mathbf{Q}_i \mathbf{K}_i^\top}{\sqrt{d_k}}\right) \mathbf{V}_i$
Aggregate the attended features:
$\mathbf{F}_{\text{attn}} = \text{Concat}(\mathbf{A}_{\text{SO}}, \mathbf{A}_{Decomp})$
**Step 4: Adaptive Weighted Fusion**
Compute dynamic fusion weights $\alpha_i$:
$\alpha_i = \frac{\exp(\mathbf{w}_i^\top \mathbf{F}_i)}{\sum_{j=1}^{3} \exp(\mathbf{w}_j^\top \mathbf{F}_j)}$
Compute the weighted fused feature:
$\mathbf{F}_{\text{fusion}} = \sum_{i=1}^{3} \alpha_i \cdot \mathbf{F}_i$
**Step 5: Classification Head**
$\mathbf{F}_{\text{sum}} = \text{Concat}(\mathbf{F}_{\text{attn}}, \mathbf{F}_{\text{Fusion}})$
Pass $\mathbf{F}_{\text{sum}}$ through fully connected layers:
$\mathbf{F}_{\text{fc}} = \text{MLP}(\mathbf{F}_{\text{fusion}})$
Compute final class predictions using Softmax:
$\hat{y} = \text{Softmax}(\mathbf{F}_{\text{fc}})$
**Step 6: Return Predicted Labels**
**Return** $\hat{y}$

more complex architecture and greater depth. However, the proposed model's ability to achieve near-parity with such a robust model while being computationally less demanding underscores its efficiency. Moreover, the proposed model surpasses both

ResNet50 and DenseNet121 in terms of classification accuracy. This result demonstrates the effectiveness of incorporating polarization-aware cross-attention mechanisms and adaptive weighted fusion of features, which enhances the model's ability to capture intricate spatial and contextual information from CP-SAR data. The comparable performance of the proposed model to established models emphasizes its suitability for wetland mapping. Figure 4.6 illustrates the classification map of the study area generated using the proposed model.

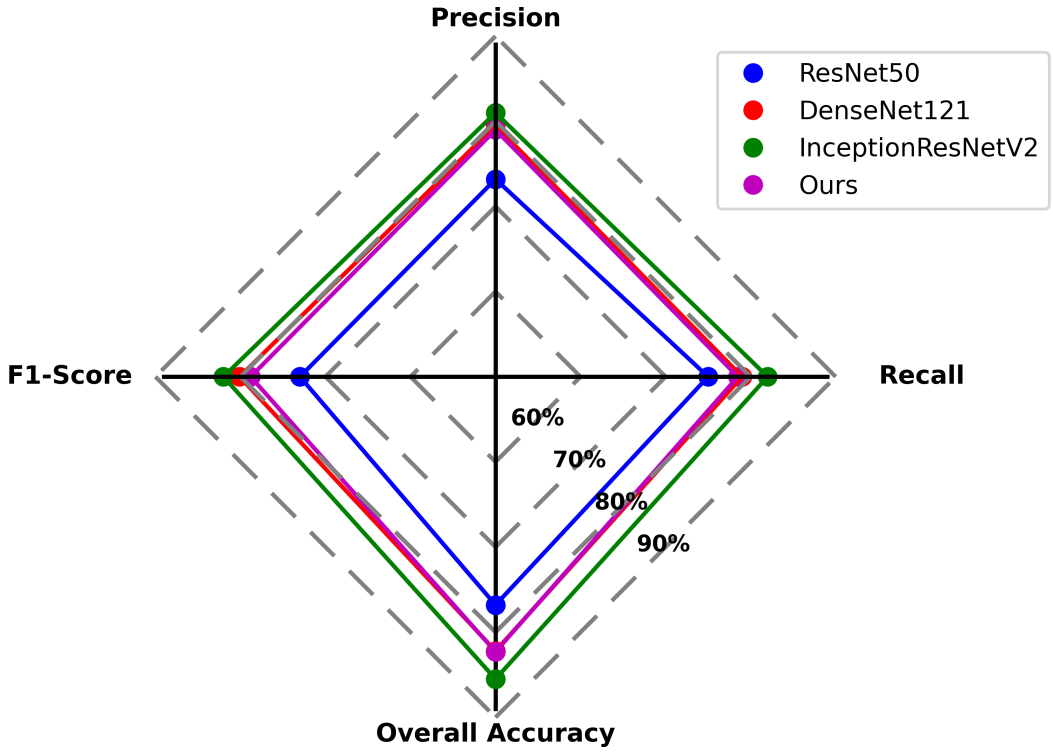



Figure 4.5: Comparative analysis of classification accuracy across employed DL models.

## 4.7 Conclusion

The study introduced a DL model designed for wetland classification using RCM CP-SAR data. By combining two feature extraction streams—one for CH/CV channels and another for polarimetric decomposition features—the model captured complementary information in different streams. The integration of adaptive weighted fusion and the polarization-aware cross-attention transformer allowed the network to focus

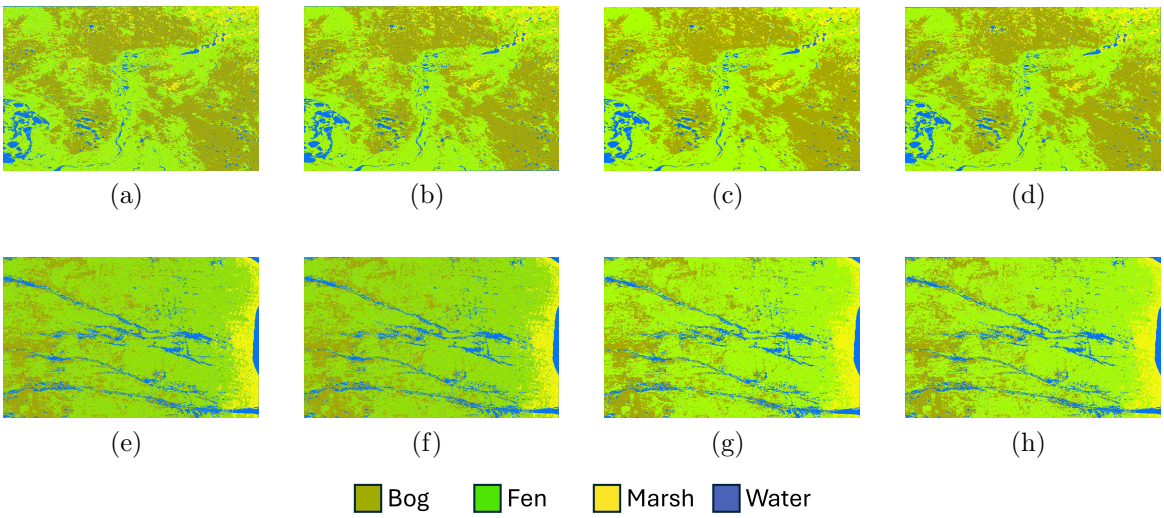



Figure 4.6: Classification results for Location 1: (a) ResNet50, (b) DenseNet121, (c) InceptionResNetV2, and (d) Ours. Classification results for Location 2: (e) ResNet50, (f) DenseNet121, (g) InceptionResNetV2, and (h) Ours.

on interactions between these modalities, leading to improved performance. With an overall classification accuracy of nearly 82.5% on the RCM dataset, this model demonstrated its potential for application in real-world scenarios for monitoring and managing wetland ecosystems. Despite the marginal gap between the accuracy of the proposed model and InceptionResNetV2, the ability of the proposed model to deliver near-comparable results with fewer computational resources positions it as a good technique in the field of wetland classification. The study also highlighted the potential sensitivity of CP in discriminating wetland classes and improving accuracy. Moving forward, further enhancements could include the incorporation of additional RS data and exploration of domain-specific tuning, contributing to a more robust and scalable framework for environmental applications.

## 4.8 Future Directions & Recommendations

While the current chapter highlighted the effectiveness of CP-SAR data for classification, future work could expand on these findings by transitioning from single-date data to multi-temporal CP-SAR datasets. Although the success of single-date RCM imagery presented here shows promise, incorporating time-series data would provide a

dynamic, temporal perspective, crucial for capturing variations and long-term changes in wetland ecosystems. Future studies should explore how time-series analysis can be used to help detect subtle fluctuations in wetland vegetation, water levels, and soil conditions. This temporal approach could be especially valuable in monitoring wetland health over time, allowing for early detection of ecological changes or shifts in species composition. By integrating time-series CP-SAR data, researchers can achieve a more comprehensive view of wetland dynamics, helping to identify trends.

Another key recommendation is the application of an advanced and unique polarization decomposition method to extract more detailed information from the radar signals in CP mode. Decomposition techniques have the potential to separate the different scattering mechanisms - such as volume, surface, and double-bounce scattering - that are characteristic of wetland environments. This could provide richer insights into wetland types and conditions, leading to more precise delineation and characterization compared to conventional SAR imagery.

## 4.9 References

[1] M. Morris, C. Chew, J. T. Reager, R. Shah, and C. Zuffada, "A novel approach to monitoring wetland dynamics using cygnss: Everglades case study," *Remote Sensing of Environment*, vol. 233, p. 111417, 2019.

[2] M. Dabboor, I. Olthof, M. Mahdianpari, F. Mohammadimanesh, M. Shokr, B. Brisco, and S. Homayouni, "The RADARSAT Constellation Mission core applications: First results," *Remote Sensing*, vol. 14, no. 2, p. 301, 2022.

[3] D. Mandal, V. Kumar, D. Ratha, J. M. Lopez-Sanchez, A. Bhattacharya, H. McNairn, Y. S. Rao, and K. Ramana, "Assessment of rice growth conditions in a semi-arid region of india using the Generalized Radar Vegetation Index derived from RADARSAT-2 polarimetric SAR data," *Remote Sensing of Environment*, vol. 237, p. 111561, 2020.

[4] S. Dey, N. Bhogapurapu, S. Homayouni, A. Bhattacharya, and H. McNairn, "Unsupervised classification of crop growth stages with scattering parameters

from dual-pol Sentinel-1 SAR data," *Remote Sensing*, vol. 13, no. 21, p. 4412, 2021.

[5] P. Ferrazzoli, S. Paloscia, P. Pampaloni, G. Schiavon, D. Solimini, and P. Coppo, "Sensitivity of microwave measurements to vegetation biomass and soil moisture content: A case study," *IEEE Transactions on Geoscience and Remote Sensing*, vol. 30, no. 4, pp. 750–756, 1992.

[6] M. W. Davidson, T. Le Toan, F. Mattia, G. Satalino, T. Manninen, and M. Borgeaud, "On the characterization of agricultural soil roughness for radar remote sensing studies," *IEEE Transactions on Geoscience and Remote Sensing*, vol. 38, no. 2, pp. 630–640, 2000.

[7] L. Dingle Robertson, H. McNairn, X. Jiao, C. McNairn, and S. O. Ihuoma, "Monitoring crops using compact polarimetry and the RADARSAT constellation mission," *Canadian Journal of Remote Sensing*, vol. 48, no. 6, pp. 793–813, 2022.

[8] R. K. Raney, "Hybrid-polarity SAR architecture," *IEEE Transactions on Geoscience and Remote Sensing*, vol. 45, no. 11, pp. 3397–3404, 2007.

[9] M. Mahdianpari, B. Salehi, F. Mohammadimanesh, and B. Brisco, "An assessment of simulated compact polarimetric SAR data for wetland classification using random forest algorithm," *Canadian Journal of Remote Sensing*, vol. 43, no. 5, pp. 468–484, 2017.

[10] F. Charbonneau, B. Brisco, R. Raney, H. McNairn, C. Liu, P. Vachon, J. Shang, R. DeAbreu, C. Champagne, A. Merzouki, *et al.*, "Compact polarimetry overview and applications assessment," *Canadian Journal of Remote Sensing*, vol. 36, no. sup2, pp. S298–S315, 2010.

[11] J. D. Ballester-Berman and J. M. Lopez-Sanchez, "Time series of hybrid-polarity parameters over agricultural crops," *IEEE Geoscience and Remote Sensing Letters*, vol. 9, no. 1, pp. 139–143, 2011.

[12] R. K. Raney, J. T. Cahill, G. W. Patterson, and D. B. J. Bussey, "The m-chi decomposition of hybrid dual-polarimetric radar data with application to lunar craters," *Journal of Geophysical Research: Planets*, vol. 117, no. E12, 2012.

[13] V. F. Rodriguez-Galiano, B. Ghimire, J. Rogan, M. Chica-Olmo, and J. P. Rigol-Sanchez, "An assessment of the effectiveness of a random forest classifier for land-cover classification," *ISPRS journal of photogrammetry and remote sensing*, vol. 67, pp. 93–104, 2012.

[14] L. Dingle Robertson, A. Davidson, H. McNairn, M. Hosseini, S. Mitchell, D. De Abelleyra, S. Verón, and M. H. Cosh, "Synthetic Aperture Radar (SAR) image processing for operational space-based agriculture mapping," *International Journal of Remote Sensing*, vol. 41, no. 18, pp. 7112–7144, 2020.

[15] L. Zhong, L. Hu, and H. Zhou, "Deep learning based multi-temporal crop classification," *Remote sensing of environment*, vol. 221, pp. 430–443, 2019.

[16] X.-P. Song, P. V. Potapov, A. Krylov, L. King, C. M. Di Bella, A. Hudson, A. Khan, B. Adusei, S. V. Stehman, and M. C. Hansen, "National-scale soybean mapping and area estimation in the United States using medium resolution satellite imagery and field survey," *Remote sensing of environment*, vol. 190, pp. 383–395, 2017.

[17] M. Mahdianpari, B. Brisco, J. Granger, F. Mohammadimanesh, B. Salehi, S. Homayouni, and L. Bourgeau-Chavez, "The third generation of pan-canadian wetland map at 10 m resolution using multisource earth observation data on cloud computing platform," *IEEE Journal of Selected Topics in Applied Earth Observations and Remote Sensing*, vol. 14, pp. 8789–8803, 2021.

[18] J. Wang, Y. Feng, X. Tong, Z. Lei, M. Xi, Y. Zhou, and P. Tang, "Classification evaluation and improvement of airborne polsar images for land use mapping using deep learning," *Geocarto International*, vol. 39, no. 1, p. 2401937, 2024.

[19] H. Chen and Z. Shi, "A spatial-temporal attention-based method and a new dataset for remote sensing image change detection," *Remote Sensing*, vol. 12, no. 10, p. 1662, 2020.

[20] S. Lu, M. Liu, L. Yin, Z. Yin, X. Liu, and W. Zheng, "The multi-modal fusion in visual question answering: a review of attention mechanisms," *PeerJ Computer Science*, vol. 9, p. e1400, 2023.

# Chapter 5

# Wetland Characterization Using Compact Polarimetric SAR Data [1]

## 5.1 Preface

A version of this manuscript has been published in the *IEEE Transactions on Geoscience and Remote Sensing (TGRS)*. I am the primary author of this work, along with my co-authors: Abhinav Verma, Masoud Mahdianpari, Eric W. Gill, Avik Bhattacharya, and Saeid Homayouni. I was responsible for designing and conceptualizing the study, preprocessing all the data, and developing the methodologies used in this research. I conducted all experiments and analyses and wrote the manuscript. After completing the initial draft, I revised the manuscript based on feedback from all co-authors, ensuring that their suggestions were incorporated. I also made further revisions to address the reviewers' comments. All co-authors provided editorial input and scientific insights, which were crucial in improving the quality and clarity of the paper. They also reviewed and commented on the manuscript throughout the process.

[1] Jafarzadeh, H., Verma, A., Mahdianpari, M., Gill, E.W., Bhattacharya, A. and Homayouni, S., 2024. Compact-polarimetric SAR signature analysis for wetland characterization using RADARSAT constellation mission. IEEE Transactions on Geoscience and Remote Sensing, 62, pp.1-16.

## 5.2 Abstract

Effective monitoring of wetlands plays a pivotal role in comprehending and managing these ecologically vital ecosystems. This study assesses the potential of C-band Synthetic Aperture Radar (SAR) imagery in compact polarization (CP) mode, utilizing the RADARSAT Constellation Mission (RCM), for wetland characterization. We introduce the compact-polarimetric signature (CPS) as a novel descriptor to delineate wetlands, including bog, fen, and marsh classes. Additionally, we propose an alternative decomposition technique ($\mu - \chi$) to segment the total power into three components: odd-bounce scattering ($P_s$), double-bounce scattering ($P_d$), and random scattering ($P_v$). For our evaluation, we selected a test site in New Brunswick, Canada, and acquired a series of RCM datasets covering this region. The time-series CPS plots yield valuable insights, elucidating the scattering mechanisms of different wetland classes. Notably, these plots reveal that during the active season, characterized by changing vegetation structures, the scattered waves exhibit variations, leading to changes in received power and the purity parameter ($\mu$). Furthermore, the observed variations in the proposed power components demonstrate a significant discriminatory capacity among wetlands. The $P_s$, $P_d$, and $P_v$ components effectively distinguish bog, fen, and marsh classes, respectively, capturing the unique characteristics of each wetland type. These findings carry considerable potential for advancing wetland characterization through the RCM CP-SAR mission. The improved discriminative ability among different wetland classes is a valuable contribution to the broader field of wetland ecology and management. This advancement potentially empowers precise wetland classification, facilitating well-informed decision-making in wetland preservation and resource allocation. The applications of these findings extend to ecosystem monitoring, environmental impact assessments, and the long-term evaluation of wetland health. Eventually, this contributes to developing more effective wetland conservation and management strategies.

## 5.3 Introduction

Wetlands are intricate ecological systems situated in the transition zone between terrestrial and aquatic environments. They are characterized by the presence of water, either permanently or temporarily, near or at the soil surface, facilitating various

aquatic processes [1, 2]. These unique ecosystems exhibit diversity in hydrology, soil types, and vegetation communities, encompassing a range of forms, including swamps, marshes, bogs, fens, and open waters, as classified by the Canadian Wetland Classification System (CWCS) [3, 4].

Often referred to as the "kidneys of the Earth," wetlands provide crucial services and functions to both the environment and human societies. These services include water purification and regulation, erosion control, nutrient cycling, filtration of pollutants, provision of habitat for a diverse range of flora and fauna, and opportunities for recreation and tourism [5, 6, 7]. Additionally, wetlands play a significant role in carbon sequestration, contributing to efforts to mitigate the impacts of climate change.

Despite their vital ecological role, wetlands face threats stemming from human activities, including urbanization, agriculture, and industrial development. These activities result in habitat loss, degradation, and fragmentation [8]. Therefore, the continuous monitoring and analysis of wetlands are imperative to ensure their protection, restoration, and long-term sustainability. Remote sensing technology has emerged as a practical and invaluable tool for assessing and monitoring dynamic environments worldwide, including wetland ecosystems [9]. This technology enables large-scale and repetitive observations of these systems.

In particular, SAR (Synthetic Aperture Radar) imagery offers distinct advantages for observing wetland environments. SAR can penetrate clouds and vegetation, making it operational and capable of collecting data regardless of weather conditions and sun illumination [10, 11]. The essential SAR parameters, such as the acquisition wavelength, polarization, and incidence angle of the transmitted electromagnetic signal, play a pivotal role in shaping the scattering responses received from diverse targets [12].

Critical vegetation and soil characteristics influence the backscattered SAR signals in wetlands. The geometric structure and dielectric properties of these natural features unveil important surface properties, including target size, water content, and roughness [13, 14]. In recent years, rapidly advancing Earth Observation (EO) SAR technologies have provided a wealth of observational data for wetlands [15]. Canada's Earth-observing RADARSAT Constellation Mission (RCM) is a cutting-edge remote

sensing platform offering exceptional wetland characterization and mapping opportunities. Launched in 2019, this constellation comprises three identical C-band SAR satellites operating in closely coordinated orbits, resulting in a four-day repeat cycle. RCM, as the successor to the RADARSAT-2 mission, introduces a range of operational polarization modes using the Compact-Polarimetric (CP) architecture, marking a significant shift in SAR acquisition modalities [16]. These advancements significantly enhance the operational capabilities for ecosystem monitoring [17].

While traditional SAR systems, with numerous examples spanning over half a century, predominantly operated in acquisition modes employing linear polarizations, the RCM represents a noteworthy departure from this convention [18]. RCM employs circular polarization for transmission and linear orthogonal pairs of horizontal (H) and vertical (V) polarizations for reception. This innovative paradigm shift effectively provides spaceborne SAR polarimetry capabilities almost on par with traditional full-polarimetric (FP) imaging radars. Notably, this approach simplifies the radar's design, reduces data costs and mass, widens the swath coverage compared to FP-SAR, and introduces a new class of dual-polarized radar systems [17].

Previous studies have conducted pre-launch assessments of the RCM utilizing simulated CP data generated from RADARSAT-2 for wetland monitoring applications. In an initial evaluation, Dabboor et al. [19] assessed RCM's potential for monitoring wetlands by focusing on detecting changes within the wetlands of Manitoba. They utilized simulated CP data in the 5 m imaging mode, and the results demonstrated comparability with those obtained from RADARSAT-2 FP data.

Subsequently, Dabboor et al. [11] expanded the research by investigating the potential of simulated CP data of the 16 m imaging mode for multi-temporal change detection over wetlands. Mahdianpari et al. [20] analyzed simulated RCM CP for mapping various wetland, upland, and urban classes in Newfoundland. Their findings provided valuable insights into the potential of RCM CP data for large-scale wetland mapping. In another study, Olthof et al. [21] evaluated the performance of RCM in mapping open water and flooded vegetation by analyzing CP options from different imaging modes (5 m, 16 m, and 30 m). The collective findings of these studies highlighted the potential of the RCM CP acquisition mode, making it a strong candidate to produce valuable sets of products for wetland monitoring.

Studies utilizing simulated RCM CP-SAR data have highlighted the efficiency of

enhanced radar target information in monitoring complex dynamic ecosystems such as wetlands. These studies generally employ the Stokes vector elements from simulated RCM datasets for wetland characterization. Additionally, several other studies utilized: backscatter coefficient (i.e., $\sigma^0_{RH}$ and $\sigma^0_{RV}$), wave descriptors (i.e., correlation coefficient, relative phase, degree of polarization, and wave entropy), and decomposition parameters (i.e., odd-bounce, even-bounce, and diffused scattering powers) to advance our understanding of wetland dynamics.

Nevertheless, it's essential to emphasize the validation of these methods by utilizing real CP-SAR imagery from RCM. Despite the significant progress, exploring the full potential of RCM CP-SAR data for ecosystem monitoring is needed, emphasizing wetland characterization in real-world scenarios. This research gap requires to be addressed as ecosystem/wetland mapping is one of the RCM's core applications. The initial assessment of RCM's linear dual-polarized imagery indicated its potential for discriminating wetland classes, especially when integrated with optical remote sensing data [17]. Therefore, one must investigate the unique capabilities of RCM CP-SAR data in the context of wetland monitoring.

Thorough and innovative remote sensing tools are crucial in understanding the complex nature of wetlands comprising diverse types and dynamic spatial patterns. The RCM, with its advanced features, holds promise in this regard. This study proposes a novel approach to analyze the RCM CP datasets by exploring the scattering mechanisms from wetlands. Our research contributes new insights to wetland characterization and augments the existing radar wetland monitoring approaches using SAR data. Through this investigation, we demonstrate the potential of RCM datasets, paving the way for more robust and accurate wetland mapping and characterizing using RCM CP-SAR imagery.

Over the past five decades, radar polarimetry has been a subject of continuous research, with recent developments in target characterization highlighted in Refs. [22, 23, 24]. As radar technology has advanced, there has been a growing demand for innovative techniques to effectively differentiate between various land cover types. However, traditional linear transmit-receive basis configurations have limitations in capturing the complete range of target scattering responses. These limitations stem from the fixed antenna orientation ($\psi$) and ellipticity ($\chi$) associated with these configurations. To overcome these limitations and obtain comprehensive scattering responses, van

Zyl et al. [25] explored the possibility of simulating received power using various combinations of transmit-receive antenna polarization bases. This approach enables the acquisition of optimal scattering information from the target.

In radar polarimetry, the term "polarimetric signature (PS)" denotes the synthesized received power of a target at various orientation-ellipticity angles representing the polarization basis of the transmitting and receiving antenna [26, 27]. The PS comprehensively represents a target's polarimetric response, enabling a deeper understanding of its physical characteristics and scattering mechanisms [28, 29]. PS finds application in diverse fields, including crop monitoring [30] and identifying and characterizing human-made targets [31]. Moreover, numerous polarimetric decomposition methods have been proposed for characterizing target scattering mechanisms. In the context of CP-SAR data, Raney [32, 33] proposed two decomposition methods: $m-\delta$ and $m-\chi$. The $m-\delta$ decomposition relies on the purity of the transmitted wave polarization and performs optimally when the incident wave is perfectly circular. On the other hand, the $m-\chi$ decomposition is robust to variations in transmission polarization, offering distinct advantages in certain scenarios. The present study also assesses the scattering power obtained using the $m-\chi$ decomposition technique over the wetland areas.

Raney et al. [33] effectively demonstrated the effectiveness of the $m-\chi$ decomposition in distinguishing between even bounce and odd bounce scattering ambiguities, particularly in the context of lunar crater walls. They suggested that employing a three-component approach ($m-\chi-\psi$) becomes more advantageous when one possesses prior knowledge of the ellipticity of the transmitting polarized wave. Building on this concept, Bhattacharya et al. [34] introduced the $S-\Omega$ decomposition, where $\Omega$ is dependent on the ellipticity and orientation angles of both the transmitted and received waves, denoted as $(\chi_r, \psi_r, \chi_t, \psi_t)$.

Considering the availability of CP-SAR data in the recent EO missions, this study extends the concept of PS by introducing a novel descriptor known as Compact-Polarimetric Signature (CPS), specifically designed for use with RCM imagery. This innovative approach leverages multi-date RCM images to investigate various wetland-type ecological conditions and their evolving structures at different growth stages.

Furthermore, building upon the progress made by previous decomposition methods, we propose a new approach to decompose the total received power using the

derived CPS. The primary objective of this article is to analyze the CPS and its power components across various wetland classes, aiming to distinguish between different types of wetlands and improve their efficient delineation and characterization.

This paper is organized as follows. Section 5.4 outlines the proposed methodology for generating CPS for wetland characterization and introduces a novel three-component scattering decomposition approach for CP-SAR data. Section 5.5 provides information about the RCM imagery, ground-truth datasets used in this study, and the data pre-processing steps. Section 5.6 offers a detailed analysis of the results obtained from the proposed approaches, highlighting their advantages and limitations. Finally, Section 5.7 concludes the paper by suggesting remarks on the potential applications and future directions of the proposed wetland monitoring and management approaches.

## 5.4 Methodology

In this section, we introduce a novel descriptor known as the CPS and present an innovative approach for decomposing the total power ($g_0$). The comprehensive methodology is outlined in the flowchart shown in Figure 5.1.

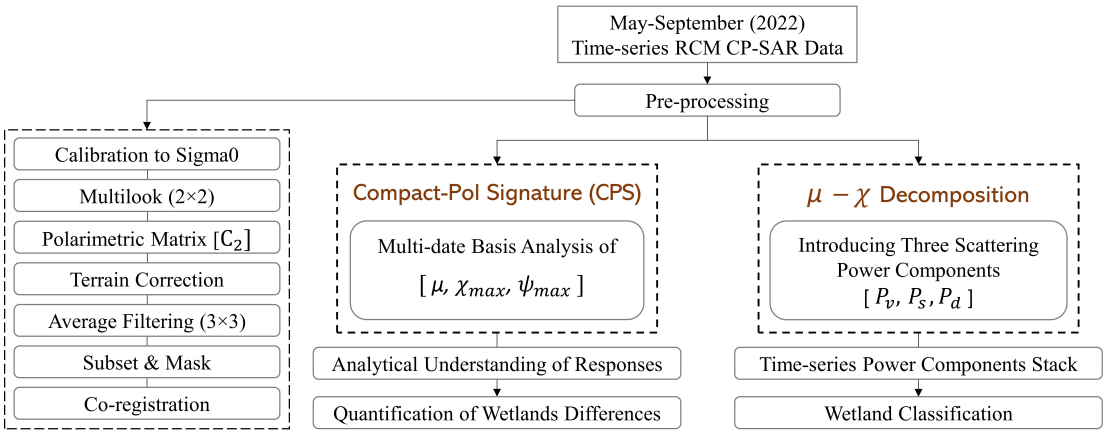



Figure 5.1: Flow diagram depicting the processing steps for analyzing wetland signatures based on RCM datasets. The process involves three major steps: (1) pre-processing of SAR datasets, (2) the proposed method, which explores wetlands CPS through multi-date basis analyses, along with introducing $\mu - \chi$ decomposition power, and (3) wetland classification.

### 5.4.1 Compact-polarimetric Signature (CPS)

In exploring SAR data, PS provides information about the response of a target as a function of the incident and backscattered polarizations. Determining scattering power involves considering four wave polarization variables: the transmit antenna $(\chi_t, \psi_t)$ and the receive antenna $(\chi_r, \psi_r)$ states. However, dealing with all these independent variables can be challenging for observation. To facilitate the visualization, van Zyl et al., [25] proposed simplifying the scenario by restricting the backscattered polarizations to either match the incident wave polarization or be orthogonal. This deliberate choice results in the computation of co-polarized and cross-polarized responses for each incident polarization. These responses are then depicted in two surface plots known as the co-pol and cross-pol signatures, offering a more accessible and focused representation.

The Stokes vector that defines the polarization state of the transmitting ($\boldsymbol{g_t}$) and receiving antenna ($\boldsymbol{g_r}$), along with the Kennaugh matrix $\mathbf{K}$ is used to calculate the received power ($P$). The Kennaugh matrix $\mathbf{K}$ is a $4\times4$ real-valued matrix derived from the complex scattering matrix $\mathbf{S}$. It provides a physically meaningful representation of the polarimetric characteristics of a target and is defined as

$$\mathbf{K} = \frac{1}{2}\mathbf{A}^*(\mathbf{S}\otimes\mathbf{S}^*)\mathbf{A}^H, \quad \mathbf{A} = \begin{bmatrix} 1 & 0 & 0 & 1 \\ 1 & 0 & 0 & -1 \\ 0 & 1 & 1 & 0 \\ 0 & j & -j & 0 \end{bmatrix}$$

where $\otimes$ denotes the Kronecker product and $j = (-1)^{1/2}$. This formulation enables the received power to be synthesized as a bilinear product of the transmit and receive Stokes vectors, allowing for polarization state analysis from polarimetric SAR data.

By changing the polarization state of the transmit and receive antennas, one can synthesize the received power $P(\chi_r, \psi_r, \chi_t, \psi_t)$ for FP-SAR data. This synthesis involves varying the ellipticity $(\chi)$ and orientation $(\psi)$ angles of both the transmit

$(\chi_t, \psi_t)$ and receive $(\chi_r, \psi_r)$ antennas, as follows:

$$\begin{aligned} P_{\mathrm{FP}}(\chi_r, \psi_r) &= \boldsymbol{g_r}^T \mathbf{K}\, \boldsymbol{g_t} \\ &= \begin{bmatrix} 1 \\ \cos 2\chi_r \cos 2\psi_r \\ \cos 2\chi_r \sin 2\psi_r \\ \sin 2\chi_r \end{bmatrix}^T \mathbf{K} \begin{bmatrix} 1 \\ \cos 2\chi_t \cos 2\psi_t \\ \cos 2\chi_t \sin 2\psi_t \\ \sin 2\chi_t \end{bmatrix} \end{aligned} \tag{5.1}$$

where $\mathbf{K}$ is the recorded data in a particular basis and $\boldsymbol{g_r}$ and $\boldsymbol{g_t}$ are the Stokes vectors defined by the polarization state of the receiving and transmitting antenna, the superscript $T$ denotes vector transpose. The ellipticity $(\chi)$ and the orientation angle $(\psi)$ vary between $-45°$ to $45°$ and $0°$ to $180°$, respectively. $P_{\mathrm{FP}}$ (of size $91 \times 181$) is the synthesized received power displayed in a 2D or 3D plot to obtain the PS of one pixel. This matrix size corresponds to an angular resolution of $1°$ for both $\chi$ and $\psi$, enabling fine-grained sampling of the polarization states.

Verma et al., [29, 35], extended the concept of PS from FP-SAR data to dual- and CP-SAR data. CP-SAR systems utilize circular polarization transmission, represented as either Left-Handed (L) or Right-Handed (R) circular polarization, and coherently receive the linear horizontal (H) and vertical (V) polarized components. This configuration allows the scattered wave information to be obtained using the $2 \times 1$ element complex Jones vector $\vec{\mathbf{E}} = \begin{bmatrix} E_{\mathrm{CH}} & E_{\mathrm{CV}} \end{bmatrix}^T$, where the subscript $C$ denotes the transmit polarization handedness. In the CP mode, it's important to note that we measure a projection of the $2 \times 2$ complex scattering matrix $\mathbf{S}$, as indicated below:

$$\begin{aligned} \vec{E} = \begin{bmatrix} E_{\mathrm{CH}} \\ E_{\mathrm{CV}} \end{bmatrix} &= \frac{1}{\sqrt{2}} \begin{bmatrix} \mathrm{S_{HH}} & \mathrm{S_{HV}} \\ \mathrm{S_{VH}} & \mathrm{S_{VV}} \end{bmatrix} \begin{bmatrix} 1 \\ \pm i \end{bmatrix} \\ &= \frac{1}{\sqrt{2}} \begin{bmatrix} \mathrm{S_{HH}} \pm i\mathrm{S_{HV}} \\ \mathrm{S_{VH}} \pm i\mathrm{S_{VV}} \end{bmatrix} \end{aligned} \tag{5.2}$$

where the $+$ sign is for L circular transmit and $-$ is for R circular transmit, and $\mathrm{S_{HH}}$, $\mathrm{S_{HV}}$, $\mathrm{S_{VH}}$, and $\mathrm{S_{VV}}$ are the complex scattering coefficients. The Jones vector is then

utilized to form a $2 \times 2$ Hermitian semi-definite wave covariance matrix $\mathbf{C_2}$ as,

$$\mathbf{C_2} = \begin{bmatrix} \langle |E_{\mathrm{CH}}|^2 \rangle & \langle E_{\mathrm{CH}} E_{\mathrm{CV}}^* \rangle \\ \langle E_{\mathrm{CV}} E_{\mathrm{CH}}^* \rangle & \langle |E_{\mathrm{CV}}|^2 \rangle \end{bmatrix}. \tag{5.3}$$

One can then compute the four elements of the Stokes vector ($\boldsymbol{g_s}$) using the elements of $\mathbf{C_2}$ as,

$$\boldsymbol{g_s} = \begin{bmatrix} g_0 \\ g_1 \\ g_2 \\ g_3 \end{bmatrix} = \begin{bmatrix} \langle |E_{\mathrm{CH}}|^2 + |E_{\mathrm{CV}}|^2 \rangle \\ \langle |E_{\mathrm{CH}}|^2 - |E_{\mathrm{CV}}|^2 \rangle \\ 2\Re\langle E_{\mathrm{CH}} E_{\mathrm{CV}}^* \rangle \\ 2\Im\langle E_{\mathrm{CH}} E_{\mathrm{CV}}^* \rangle \end{bmatrix} \quad . \tag{5.4}$$

The polarization state of the scattered wave can be described using the Stokes vector, denoted as $\boldsymbol{g_s}$. It's worth noting that both the polarization basis of the transmit and receive antennas is synthesized within the range of $-45^\circ \leq \chi_{t,r} \leq 45^\circ$, and $-90^\circ \leq \psi_{t,r} \leq 90^\circ$ in the full-polarimetric signature (FPS). Thus, in FPS, one measures the power received when the receiving antenna polarization is the same as the transmitting antenna (i.e., co-pol signature) and when the transmitting antenna and the receiving antenna polarization are orthogonal to that of the transmitting antenna (i.e., cross-pol signature). So, by systematically varying and recording these polarization states within the specified angular ranges, the FPS provides a comprehensive view of how the radar wave interacts with the target, enabling detailed polarization analysis and information extraction.

Unlike the FP mode, the CP mode employs a fixed transmit antenna polarization, which can be either L or R circular polarization. In this mode, the polarization state of the receive antenna is synthesized over a specific angular range, specifically ($-45^\circ \leq \chi_r \leq 45^\circ$, and $0^\circ \leq \psi_r \leq 180^\circ$). Consequently, in the CP mode, the received power is calculated as follows:

$$\begin{aligned} P_{\mathrm{CP}}(\chi_r, \psi_r) &= \boldsymbol{g_r}^T \, \mathbf{K} \, \boldsymbol{g_t} \\ &= \boldsymbol{g_r}^T \, \boldsymbol{g_s} \\ &= \begin{bmatrix} 1 \\ \cos 2\chi_r \cos 2\psi_r \\ \cos 2\chi_r \sin 2\psi_r \\ \sin 2\chi_r \end{bmatrix}^T \boldsymbol{g_s} \end{aligned} \tag{5.5}$$

where $\boldsymbol{g_s} = \mathbf{K}\,\boldsymbol{g_t}$ describes the polarization state of the scattered wave, and the superscript $T$ denotes the vector transpose. We then represent the synthesized received power, denoted as $P_{\mathrm{CP}}$, using a 2D plot. We obtain the CPS of size $91 \times 181$ since the received power is computed for all possible combinations of ellipticity angles ($-45°$ to $45°$) and orientation angles ($0°$ to $180°$) of the scattered wave while varying it by a step size of $1°$. We display the ellipticity and orientation angles in the CPS plot along the $x$ and $y$ axis, respectively. The received power, obtained by varying the polarization state of the receiving antenna, is represented using a color bar.

### 5.4.2 Three Scattering Power Components

In radar polarimetry, one aims to differentiate scattering mechanisms from targets, i.e., a clear distinction between odd-bounce, even-bounce, and random scattering. In this respect, Raney et al., [33], Cloude et al., [36], Bhattacharya et al., [34], Kumar et al., [37] and Dey et al., [22] proposed decomposition methods for CP-SAR data. These decomposition techniques employ various approaches to splitting the polarized scattered power into components related to even and odd-bounce scattering mechanisms. In contrast, the unpolarized power component is associated with diffuse scattering.

However, in this work, we propose an alternative approach to decompose the total power ($g_0$) using a parameter $\mu$ derived from the CPS (Figure 5.2). We define the parameter $\mu$ as the ratio of the total polarized power to the maximum received power,

$$\mu = 1 - \frac{P_{\mathrm{min}}}{P_{\mathrm{max}}} = \frac{P_{\mathrm{max}} - P_{\mathrm{min}}}{P_{\mathrm{max}}} \tag{5.6}$$

where $P_{\mathrm{max}}$ and $P_{\mathrm{min}}$ are respectively the maximum and the minimum received powers. The quantity, $P_{\mathrm{max}} - P_{\mathrm{min}}$, equals the total polarized power. However, note that the ratio, $P_{\mathrm{min}}/P_{\mathrm{max}}$, is similar to the pedestal height that one can obtain from FP co-pol signature [25]. The pedestal height indicates the amount of scattering randomness exhibited by the target. Thus, one can consider that $\mu$ measures the amount of scattering purity. It is related to the degree of polarization ($m$) as,

$$\begin{aligned} m &= \frac{P_{\mathrm{max}} - P_{\mathrm{min}}}{P_{\mathrm{max}} + P_{\mathrm{min}}} \\ &= \mu \left( \frac{P_{\mathrm{max}}}{g_0} \right) \end{aligned} \tag{5.7}$$

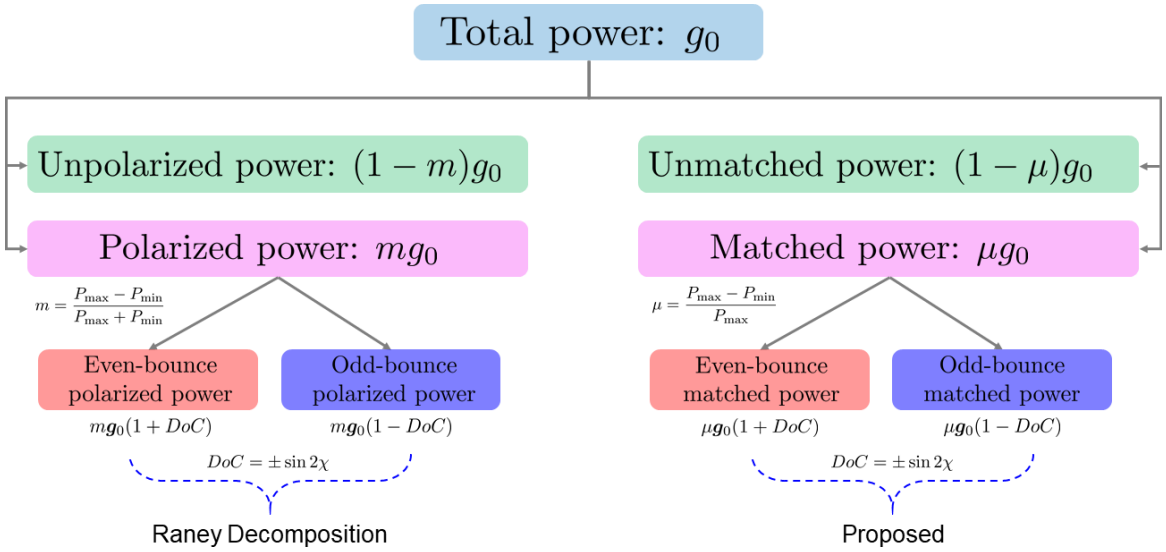



Figure 5.2: A representation of decomposition of the total power ($g_0$) using the Raney decomposition and the proposed method.

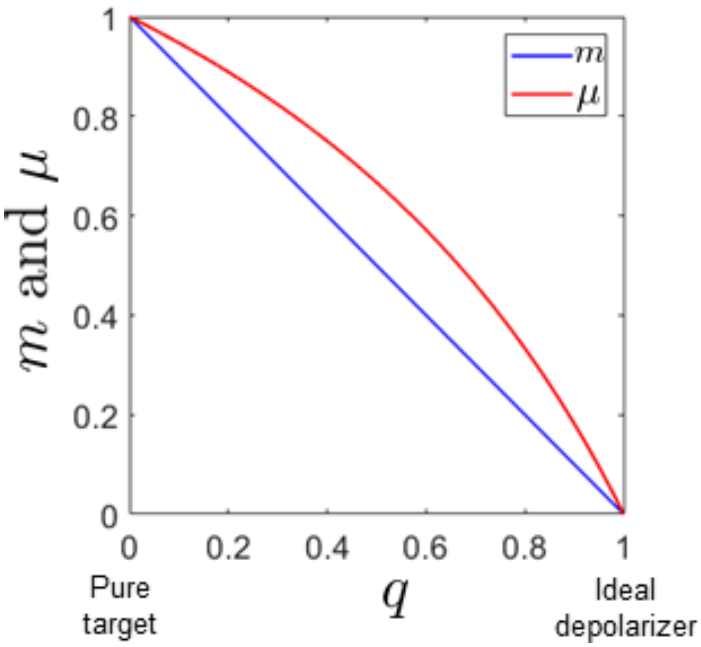



Figure 5.3: The values of $m$ and $\mu$ for a mixture of pure target and random volume (ideal depolarizer) target. $q$ represents the mixture proportion. The target is pure for $q = 0$, while for $q = 1$, it becomes a complete depolarizer.

We describe the relationship between $m$ and $\mu$ using the following three cases:

- **Case I (Completely polarized wave):** For a completely polarized wave from

a pure target ($q = 0$ in Figure 5.3), the maximum received power (i.e., $P_{\max}$) is equal to the total power (i.e., $g_0$). Hence, $m$ and $\mu$ are identical for a completely polarized wave. This case is shown in Figure 5.3 for a trihedral target.

- **Case II (Completely unpolarized wave):** In the case of a completely unpolarized wave from an ideal depolarizer target ($q = 1$ in Figure 5.3), the maximum and the minimum received power are both equal to half the total power (i.e., $P_{\max} = P_{\min} = g_0/2$). Thus, for a completely unpolarized wave scattered from an ideal depolarizer, $m$ and $\mu$ are identically equal to 0 (Figure 5.3).

- **Case III (Partially polarized wave):** For a partially polarized wave, $0.5 < P_{\max}/g_0 < 1$. Hence, for such a case, $\mu > m$. It can also be inferred from Figure 5.3 that for a mixture of a trihedral target and an ideal depolarizer (i.e., the target is neither pure nor ideal depolarizer), we observe $\mu > m$.

We illustrate the alternate approach to decompose the total power ($g_0$) in Figure 5.2. Here, using $\mu$, we first split $g_0$ into a sum of matched power $\mu g_0$ and unmatched power $(1-\mu)g_0$. The maximum power ($P_{\max}$) is obtained when the scattered wave's polarization state matches the receiving antenna's polarization state. Similarly, the minimum power ($P_{\min}$) is obtained when the polarization state of the scattered wave is completely unmatched (i.e., orthogonal) to the polarization state of the receiving antenna. One should note that it is possible as we synthesize all the polarization bases of the receiving antenna in this study.

We perform the decomposition of the total power ($g_0$) using both $\mu$ and parameters obtained from the Stokes vector ($\boldsymbol{g_s}$), as follows:

$$P_v = g_0\,(1-\mu) \tag{5.8}$$

$$P_s = \frac{1}{2}\mu\, g_0\,(1 - DoC) \tag{5.9}$$

$$P_d = \frac{1}{2}\mu\, g_0\,(1 + DoC) \tag{5.10}$$

where $P_v$ is the unmatched power, $P_s$ is the odd-bounce matched power, and $P_d$ is the even-bounce matched power. The degree of circularity $DoC = \pm \sin 2\chi$ depends upon the handedness of the transmitted circular polarized wave. The $\pm$ sign represents L and R circular transmit polarization, respectively. Here, $\chi$ represents the ellipticity angle of the scattered wave.

Unlike traditional CP decompositions that typically split the total power $g_0$ into polarized and unpolarized components, our approach entails splitting $g_0$ into matched and unmatched power components. We can express the difference between the two quantities as:

$$\Delta = g_0(\mu - m) \geq 0. \tag{5.11}$$

The excess power over the polarized component can be determined by evaluating the values of $\Delta$ in the following three scenarios:

- **Case I (Completely polarized wave):** For a completely polarized wave, since $\mu = m$, we obtain $\Delta = 0$. This condition implies no difference between the powers computed using the two methods (i.e., Raney decomposition and proposed) for a completely polarized wave.
- **Case II (Completely unpolarized wave):** In the case of a completely unpolarized wave, we observe both $\mu$ and $m$ equal to 0. Hence, similar to Case I, one would observe no change in the powers computed using the two methods ($\Delta = 0$).
- **Case III (Partially polarized wave):** For a partially polarized wave, we observed $\mu > m$. Hence, one would observe $\Delta > 0$ in this case. The powers obtained using the two methods will vary for a partially polarized wave.

Hereafter, we refer to the proposed method as the $\mu - \chi$ decomposition. We utilize the three power components presented in this section for wetlands classification. To accomplish this, we extracted the three powers for the five RCM images, forming a time-series dataset. These components were stacked together to form a comprehensive input for our wetland classification framework. By leveraging the information within the power components, we aimed to capture the distinctive scattering characteristics of wetland areas throughout the temporal sequence. Using the stacked power component input, the random forest (RF) algorithm effectively classified wetlands. This approach enables the use of the full potential of CP data, enhancing the accuracy and reliability of wetland mapping endeavors.

## 5.5 Study Area and Dataset

This section outlines the study area, the multi-temporal RCM data, the pre-processing steps applied to SAR data, and the reference wetland data used in the analysis. The processing flow diagram of the study, which focuses on the multi-date analysis of CP-SAR features in wetland characterization, is shown in Figure 5.1. The diagram also highlights the pre-processing steps involved in the RCM data analysis.

### 5.5.1 Study Site

The study area is located in the southeastern coastal region of the province of New Brunswick, Canada, with a geographical extent from W64°37′50″ to W65°3′0″ longitude and from N45°34′30″ to N45°46′0″ latitude, covering an approximate area of 409.85 $km^2$ (Figure 5.4). As illustrated, the most dominant wetland classes in this area are bogs, fens, and marshes. To evaluate the effectiveness of the proposed methodology in wetland class discrimination, we conducted an assessment using RCM imagery in this selected study area.

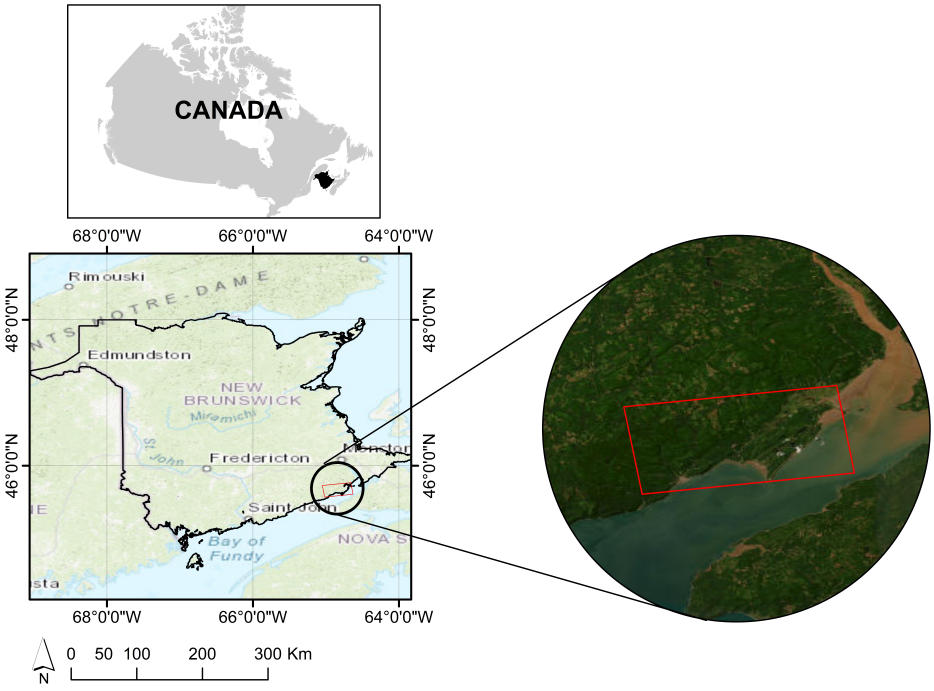



Figure 5.4: A close-up view of the study area located within the province of New Brunswick, Canada.

### 5.5.2 RCM Time-series Data Acquisition

For wetland signature analysis, 5 Single Look Complex (SLC) RCM frames (all in ascending imaging mode) were acquired from 26 May to 23 September 2022, spanning the duration of wetland growth - at 5 m nominal spatial resolution and with the supported Strip Map beam mode. The coverage areas of the obtained RCM images over the study area are depicted in Figure 5.4, and their details are tabulated in Table 5.1. Note that the selected RCM images were acquired at identical incidence angles to enable a meaningful comparison of the polarimetric characteristics of the targets and to ensure that no other factors will affect the scattering responses from the targets, as it is expected to affect the polarimetric backscatter from the targets [38, 39].

Table 5.1: Characteristics OF RCM Time-series images used in this study

| # | Satellite | Acquisition Date | Orbit Pass | Beam Mode | Polarization Channel | Resolution (rg×az) | Looking Direction | #Looks (rg×az) | Incidence Angle | Swath Width | Noise Floor |
|---|---|---|---|---|---|---|---|---|---|---|---|
| 1 | RCM3 | 2022-05-26 | Ascending | High Res. (StripMap) | RH, RV | 2.8 m × 2.5 m | Right Looking | 1×1 | 49.29°-50.85° | 30 Km | -19 dB |
| 2 | RCM3 | 2022-06-07 | | | | | | | | | |
| 3 | RCM1 | 2022-07-17 | | | | | | | | | |
| 4 | RCM2 | 2022-08-14 | | | | | | | | | |
| 5 | RCM3 | 2022-09-23 | | | | | | | | | |

### 5.5.3 Pre-processing of RCM Data

SAR data pre-processing is a crucial step in various EO applications, particularly in land cover characterization and classification. In this study, we pre-processed RCM images using the SNAP free open-source software. The pre-processing workflow encompasses several key steps: calibration, multi-looking, geo-coding, average filtering, and co-registration. All of these are illustrated in Figure 5.1.

The pre-processing sequence begins with calibration, where the digital data from two channels (RH and RV) of the RCM images, which constitute the elements of the scattering matrix, are converted into the sigma naught ($\sigma^0$) backscattering coefficient expressed in decibels (dB). Following calibration, a multi-looking approach involves a two-look process (i.e., $2 \times 2$) in the azimuth and range directions. This step serves to mitigate speckle noise and yield square ground range pixels. Subsequently, for each pixel, the $2 \times 2$ covariance matrix ($\mathbf{C_2}$) is computed for polarimetric decomposition and identifying distinct scattering mechanisms. The entire process is performed using the "Polarimetric Matrix Generation" toolbox.

Following the multi-looking step, geo-coding was applied to ensure accurate geographical registration. This was achieved using SNAP's `Range Doppler Terrain Correction` algorithm, utilizing the SRTM 1 arc-sec DEM. The goal was to ensure that all pixels within the images were correctly positioned on the Earth's surface. To further enhance data quality, an average filtering procedure was introduced. This step employed a $3 \times 3$ pixel window to reduce the impact of speckle noise. Subsequently, the data were subseted and co-registered to cover the designated test site. With these preparations in place, the CPS analyses and decomposition process utilizing the $\mathbf{C_2}$ matrices were initiated. This approach enabled the extraction of SAR-based features from the RCM data.

### 5.5.4 Reference Data

The wetland reference dataset used in this study (see Figure 5.5) was based on ground-truth data collected and updated by the Department of Environment and Local Government (http://www.snb.ca/geonb1/e/dc/catalogue-E.asp) for New Brunswick, Canada. The purpose of this dataset was to support the Watercourse and Wetland Alteration (WAWA) program and to alert primary users to the location of wetlands and possible regulatory obligations for land development. The dataset includes wetlands of provincial, national, or international importance and various wetland types such as marshes, bogs, and fens. An overview of the wetland classes investigated in this article is presented in sub-section 5.6.1. This ground truth was further augmented with the wetland inventory map (generated in [4]) to increase the number of reference wetland boundaries that are of interest in this study.

In our methodology, we allocate a portion of the ground-truth dataset for testing purposes to assess the accuracy of the RF classification. Typically, random sampling approaches divide the data into training and testing sets. However, one significant challenge associated with random sampling methods is the potential information leakage between the training and testing datasets, where pixels from the same polygon may be selected in both sets [40]. To overcome this challenge, our study employs a polygon-sampling approach. This procedure involves splitting the ground-truth data into equal-sized training and testing samples, each comprising 50 % of the data.

To achieve this balance, we first systematically organize reference polygons within each class based on their size. Subsequently, we allocate these sorted polygons to the

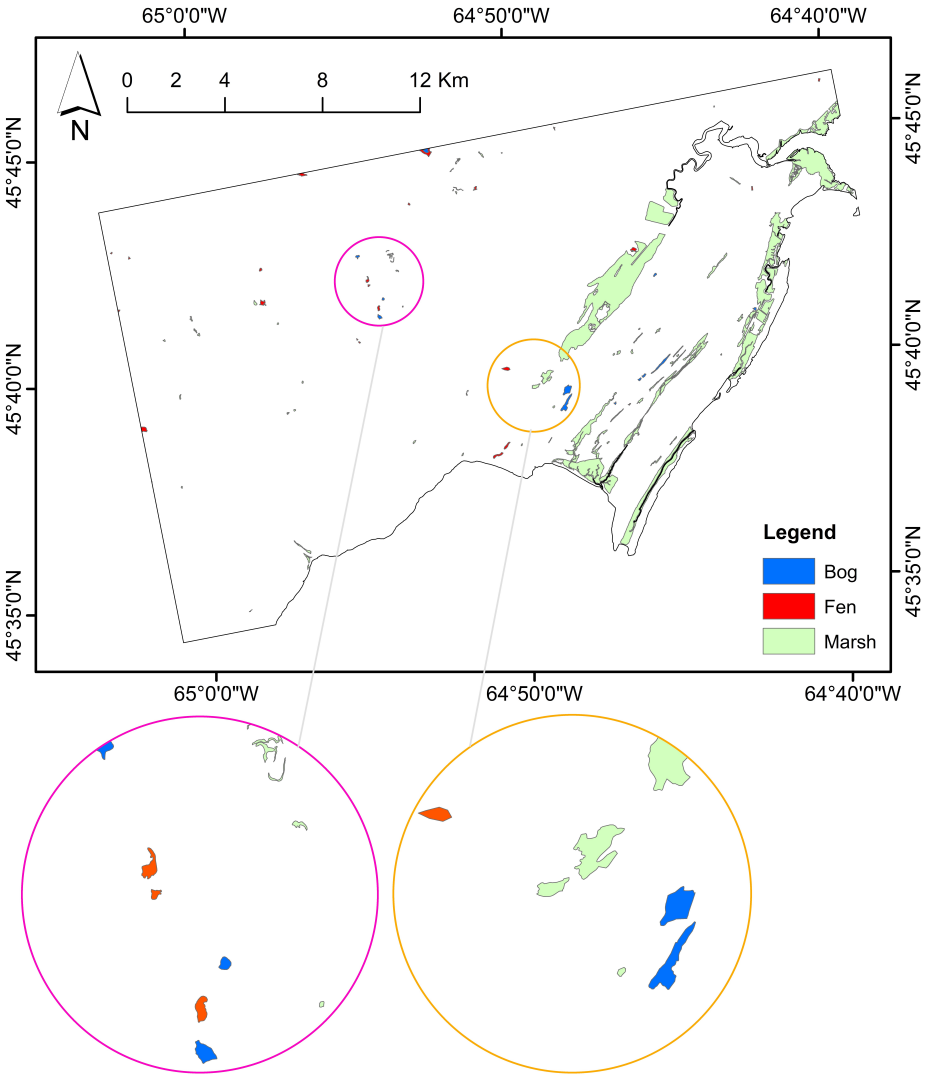



Figure 5.5: The ground-truth data for three wetland classes in the study area, including fen, bog, and marsh.

testing and training categories. Since wetland classes often exhibit a wide variation in polygon size, random assignment of reference samples to testing and training groups can result in substantial pixel count imbalances. However, our alternative assignment strategy ensures that the testing and training groups maintain comparable pixel counts for each class. Table 5.2 indicates the total number of training and testing polygons in supervised classification.

Table 5.2: Number of Reference Wetland and Non-Wetland Ground-Truth Polygons.

| # | Class | #Polygons |
|---|---|---|
| 1 | Marsh | 106 |
| 2 | Fen | 49 |
| 3 | Bog | 35 |
| 4 | Forest | 132 |
| 5 | Water | 45 |
| 6 | Barren | 38 |
| 7 | Shrubland | 38 |

## 5.6 Results and Discussion

This section explores the extensive analysis and findings derived from our study, offering valuable contributions to wetland characterization using CP-SAR data. Our investigation includes comparing CPS trends regarding their efficacy in discerning different wetland types. Additionally, we explore the behavior and significance of three power components, namely $P_v$, $P_s$, and $P_d$, representing the wetlands' ecological and scattering characteristics. These analyses contribute to a deeper understanding of wetland dynamics and lay the foundation for the subsequent classification of wetland areas.

### 5.6.1 Ecological Characteristics and Dynamics of Wetlands

Wetlands in Canada exhibit distinct types that are shaped by various factors. Notably, three key factors play a significant role [41, 3]: (1) Hydrology, including seasonal water level fluctuations and the volume of water flow within wetlands; (2) Chemistry, encompassing nutrient availability, acidity, and alkalinity; and (3) Biotic factors, such as the establishment of a ground layer dominated by either brown mosses or sphagnum mosses and the presence or absence of a tree layer. These factors collectively contribute to the diverse characteristics and classification of wetland types found in Canada and affect scattering responses from wetland areas during the growing season.

During summer in the southeastern coastal region of New Brunswick, higher temperatures and precipitation levels promote robust vegetation growth. Changes in vegetation structure and alignment throughout the summer lead to variations in scatterer orientation and, in turn, may be reflected in changes in the orientation and ellipticity of the backscattered SAR signals (i.e., CPS). If the vegetation becomes more uniformly aligned in a particular direction, the orientation of the CPS could shift accordingly. Soil moisture content is another factor that can influence the received signal properties, with shifts in the water table and precipitation altering the dielectric properties of soil and vegetation. As such, the following summarizes the main ecological aspects and dynamics of the three aforementioned wetland classes.

Bog wetlands are often enclosed depressions filled by precipitation (surface water) to varying depths across the wetland [42, 43]. Bogs are isolated from mineralized soil waters and rely solely on rainfall as their primary source of water and nutrients [43]. Sphagnum mosses, lichens, and black spruce trees dominate the plant community. They are characterized by acidity, primarily from the production of humic acid during decomposition processes and uronic acid production by sphagnum mosses; therefore, they have limited base cation content. Due to the nutrient-poor environment and acidic conditions, plant growth in bogs is often slow. This slow growth rate influences the overall dynamics of the bog ecosystem, leading to the development of specialized and highly adapted plant species.

The ombrotrophic nature of bogs significantly hinders water flow, leading to the retention of nutrients within sphagnum mosses and accumulated peat (at least 40 cm of peat are present) [41, 3]. The slow decomposition of organic matter in waterlogged conditions leads to carbon accumulation in peat. This, in turn, results in reduced mineralization processes [3]. As a result, the production rate in the ground layer of bogs tends to remain relatively similar to that of fens. However, the growth of vascular plants is restricted in bogs.

Fen wetlands are characterized by a predominant accumulation of peats [43], and the peat layer is at least 40 cm thick. They are generally more elongated and linear in shape compared to bogs. The chemical composition of the adjacent mineral soil deposits influences the development of fens. Rich fens, known for having bicarbonate, exhibit an alkaline nature. Both brown moss and graminoid vegetation dominate these fens and feature a significant presence of sedges [43, 41, 3]. Extreme-rich fen

Table 5.3: CPS Responses of Bog, Fen, And Marsh Wetlands for Some Specific Ellipticity ($\chi$) and Orientation ($\psi$) Angles.

| **Parameters** | | **Bog Wetlands** | | | | | **Fen Wetlands** | | | | | **Marsh Wetlands** | | | | |
|---|---|---|---|---|---|---|---|---|---|---|---|---|---|---|---|---|
| $\chi$ | $\psi$ | 26 May | 07 June | 17 July | 14 Aug. | 23 Sep. | 26 May | 07 June | 17 July | 14 Aug. | 23 Sep. | 26 May | 07 June | 17 July | 14 Aug. | 23 Sep. |
| 0° | 0° | 0.50 | 0.56 | 0.64 | 0.88 | **0.88** | 0.64 | **0.49** | 0.70 | 0.57 | **0.59** | 0.98 | **0.99** | 0.63 | 0.94 | 0.82 |
| 0° | 90° | 0.96 | 0.94 | 0.74 | 0.60 | **0.47** | 0.76 | **0.89** | 0.87 | 0.80 | **0.99** | 0.74 | **0.38** | 0.91 | 0.54 | 0.75 |
| 0° | 45° | 0.67 | 0.62 | 0.70 | 0.90 | 0.92 | 0.65 | 0.78 | 0.62 | 0.96 | 0.84 | 0.80 | 0.60 | 0.83 | 0.62 | 0.88 |
| 45° | 0° | 0.85 | 0.85 | 0.77 | 0.89 | 0.63 | 0.99 | 0.90 | 0.90 | 0.78 | 0.83 | 0.90 | 0.68 | 0.94 | 0.64 | 0.60 |
| −45° | 0° | 0.61 | 0.64 | 0.62 | 0.60 | 0.72 | 0.42 | 0.47 | 0.66 | 0.61 | 0.75 | 0.83 | 0.69 | 0.60 | 0.84 | 0.97 |
| $\mu$ | | **0.79** | 0.61 | **0.66** | 0.51 | 0.64 | **0.59** | 0.61 | **0.43** | 0.60 | 0.41 | **0.27** | 0.63 | **0.46** | 0.51 | 0.42 |
| $\chi_{\max}$ | | 13° | 13° | 7° | 17° | −4° | 37° | 22° | 17° | 8° | 5° | 7° | 0° | 24° | −12° | −31° |
| $\psi_{\max}$ | | 97° | 106° | 50° | 24° | 25° | 111° | 78° | 121° | 56° | 83° | 166° | 173° | 169° | 164° | 35° |

The entries with emphasized values discussed in CPS analysis are bold-faced.

wetlands typically exhibit basic conditions and contain marl deposits in their wetter areas. Moderate-rich fens, on the other hand, have acidic conditions.

Rich fens are often fed by a steady source of groundwater or water originating from the surrounding uplands. This ample water flow contributes to their mesotrophic nature. Moreover, the vascular plant component in rich fens may exhibit greater production than poor fens due to a slightly higher decomposition rate, making more nutrients available [41]. From vegetation and chemical perspectives, poor fens exhibit more similarities to bogs than rich fens. However, in terms of hydrology, poor fens align more closely with the characteristics of rich fens.

Marsh wetlands are characterized by the absence of tree or shrub cover, primarily dominated by emergent herbaceous or non-woody plants distinguishing them from other types of wetlands [20, 43]. Unlike non-patterned fens, marshes are periodically or permanently flooded with standing water and are commonly located along the margins of streams and lakes, as well as in confined basins associated with shallow open waters, which results in fluctuating water levels [44, 43]. They are strongly influenced by both surface water and groundwater, resulting in substantial water flow. Consequently, marshes exhibit abundant nutrient availability, such as nitrogen and phosphorus, leading to high productivity of vascular plants. However, the elevated decomposition rates in marshes also contribute to their nutrient-rich conditions. Bryophytes are typically sparse in marshes due to their inability to compete with vascular plants under eutrophication conditions and fluctuating water levels [41].

The combined effects of surface and groundwater influence create a well-regulated wetland environment. The absence of trees in marshes can be attributed to regional climatic factors and the recurring presence of wet conditions. Therefore, marshes represent wetlands that embody eutrophic and temporally dynamic conditions, inhibiting the development of a well-established bryophytes layer primarily due to the vigorous growth of vascular plants. The rapid decomposition processes, coupled with the limited development of the ground layer, impede significant peat accumulation. Moreover, the vegetation composition of marshes is greatly influenced by chemical variations [3].

### 5.6.2 Analysis of CPS over Wetlands

As discussed above, CPS provides the synthesized received power at ellipticity ($\chi$) and orientation angle ($\psi$). The variations in the received power at different $\chi$ and $\psi$ can provide valuable information about the characteristics of the vegetation within the wetlands during the summer months, as this period corresponds to active growth and development of vegetation. Here, we discuss the multi-date CPS of various wetland classes: bog, fen, and marsh. This analysis provides a valuable perspective on wetland monitoring and discrimination, elucidating the dynamic changes and unique characteristics associated with these ecosystems.

The backscatter at C-band frequency in wetland regions is influenced by vegetation's canopy, cylindrical stems, and interactions with the underneath soil/water. SAR backscatter intensity is significantly correlated with changes in the dielectric properties of the canopy, as they influence the radar signal's interaction with the vegetation and the underlying surface [45]. These factors contribute to the variability in backscattered signals. Using CPS, one can measure these variations better in terms of received power at all polarization states of the wave. Table 5.3 shows the received power at specific values of $\chi$ and $\psi$. To better visualize the CPS, we normalize the received power at all polarization states with the maximum received power (i.e., $P_{\text{max}}$).

The temporal variation in the CPS of the different wetland classes is evident in Figures 5.6-5.8. This variation indicates the sensitivity of the CPS to various physical and structural changes in the wetlands. During the initial acquisition dates, the CPS of the bog was found to be similar to a vertical dipole (Figure 5.6a). This similarity may also be inferred from the comparatively high value of received power at $\chi = 0$ and $\psi = 90$ (i.e., linear vertical wave) on this date as shown in Table 5.3. It can be related to the surface roughness of the wetland class during this period. The parameter $\mu$ that measures the amount of scattering purity was found to be $\approx 0.50$ during the initial acquisitions (Figure 5.9).

Further, as the depressions in the bog wetlands become filled with water, we observe the CPS to be similar to a trihedral canonical target. Due to the dominant surface scattering from this wetland, the $\mu$ was found to increase on 17 July (Figure 5.9). However, at a later stage, we observed the values of $\mu$ to reduce, indicating growth in the vegetation in this wetland.

In the case of fens, we found the CPS during the early acquisitions similar to a trihedral canonical target (Figure 5.7a). The high received power at $\chi = 45°$ (while the transmitted $\chi = -45°$) implies the surface scattering mechanism. It is possibly due to the smooth accumulated peats in the fen wetlands. Similarly, the $\mu$ values during the initial acquisitions were high, indicating pure scattering (Figure 5.9). However, with the change in the structural and physical properties of the vegetation present in this wetland, we found the values of $\mu$ at the later acquisition dates to decrease. The CPS of fen during the later stages also indicates the same (Figure 5.7).

Furthermore, one can note from Figure 5.8a that the CPS of marsh on 26 May is similar to a random scatterer. It can also be inferred from the low value of $\mu$ during this period (Figure 5.9). It is possibly due to the interaction of the incident C-band waves with the underneath rough surface, as the vegetation may be young and sparse during the initial acquisitions. As the water level increases, on 7 June, we observed the CPS to be similar to a horizontal dipole ($\chi = 0°$ and $\psi = 0°$ or $180°$). It can be related to the extended interaction of the incident C-band wave with underneath water. The value of $\mu$ significantly increased during this acquisition.

Later, as the vegetation in the marsh wetlands grows, we observe the $\mu$ values to decrease again (Figure 5.9). The CPS over this wetland can also be related to a dihedral during the later stages. It is possibly because of the multiple scattering of the C-band wave from the grown vegetation components and the underneath surface.

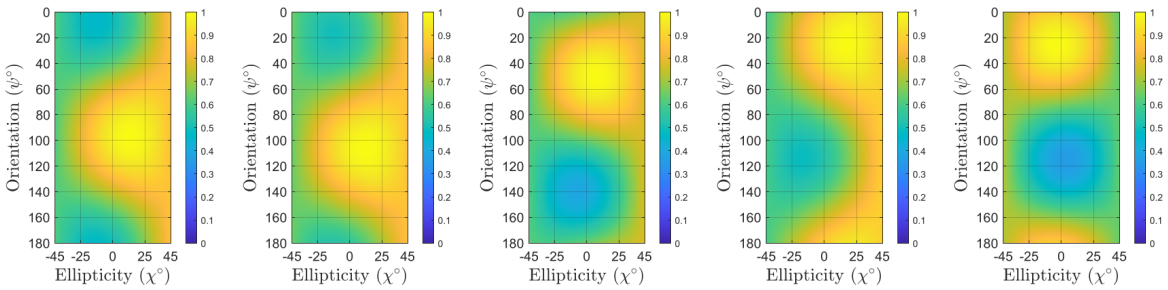



Figure 5.6: Temporal variation of CPS for the bog class, showing changes in received power over time: (a) 26 May, (b) 07 June, (c) 17 July, (d) 14 August, and (e) 23 September. Contours represent the received power, with brighter (yellow) colors indicating higher received power levels.

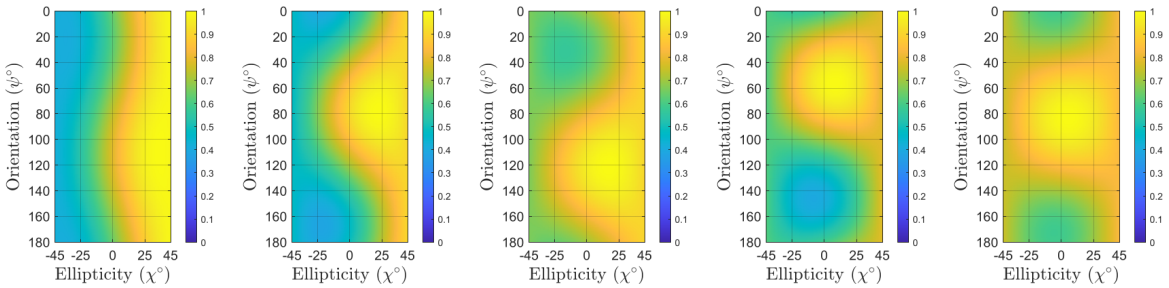



Figure 5.7: Temporal variation of CPS for the fen class, showing changes in received power over time: (a) 26 May, (b) 07 June, (c) 17 July, (d) 14 August, and (e) 23 September. Contours represent the received power, with brighter (yellow) colors indicating higher received power levels.

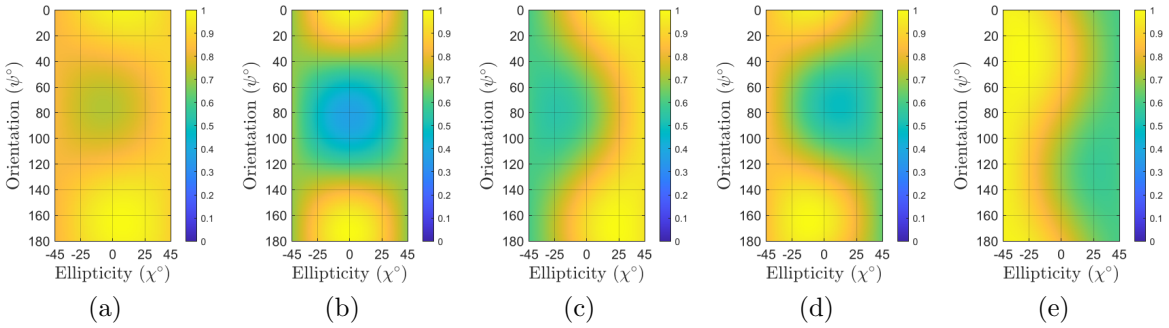



Figure 5.8: Temporal variation of CPS for the marsh class, showing changes in received power over time: (a) 26 May, (b) 07 June, (c) 17 July, (d) 14 August, and (e) 23 September. Contours represent the received power, with brighter (yellow) colors indicating higher received power levels.

Previous studies have demonstrated that wetland classes, specifically bog and fen wetlands, often exhibit similar backscattering responses, making it challenging to distinguish between these wetland classes [45]. However, by analyzing CPS behavior at some specific polarization states, one can observe relatively high variations in the response of different wetland types. With the availability of temporal data sets, this becomes even more interesting.

In particular, the differences in CPS values between bogs and fens become apparent when examining the CPS of the two wetlands on 23 September. We found the received power to be significantly distinct for $\chi = 0^\circ$ and $\psi = 90^\circ$ (i.e., for a linear vertical wave). Similarly, the fen and marsh wetlands were highly separable on 7 June for $\chi = 0^\circ$ and $\psi = 0^\circ$ (i.e., for a linear horizontal wave) (Table 5.3).

Further, the $\mu$ parameter can also discriminate between these three wetlands. For instance, the marsh wetland can be separated from the others during the early stages. Similarly, bog wetlands can be discriminated from the fen and marsh wetlands as the vegetation matures (Figure 5.9). Notably, the polarization states for the bog class in the early and late growing season, unlike fen and marsh wetlands, tend to be preserved.

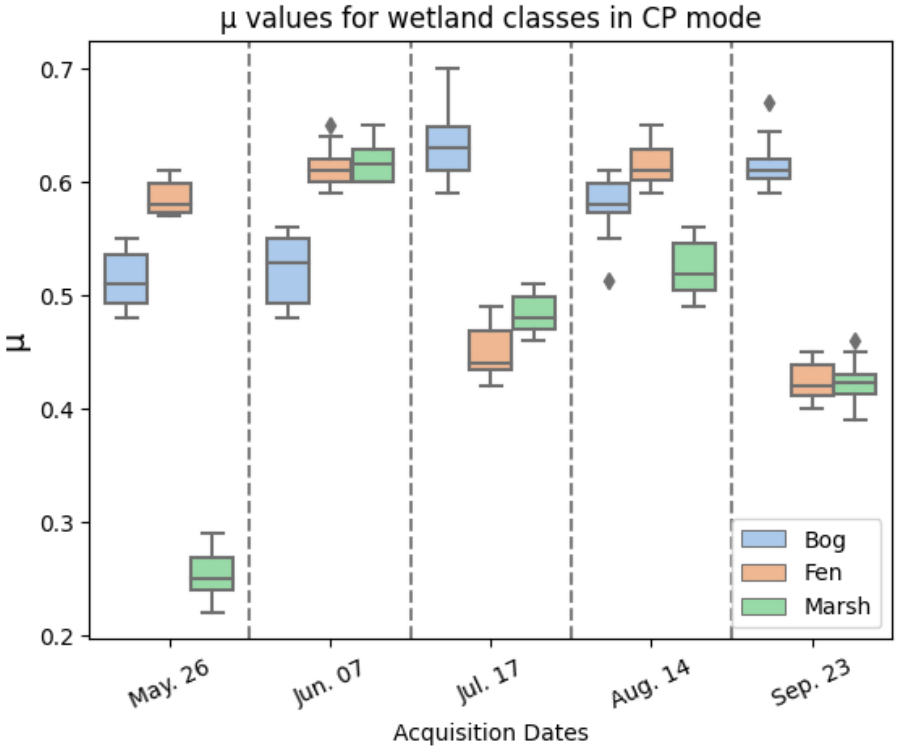


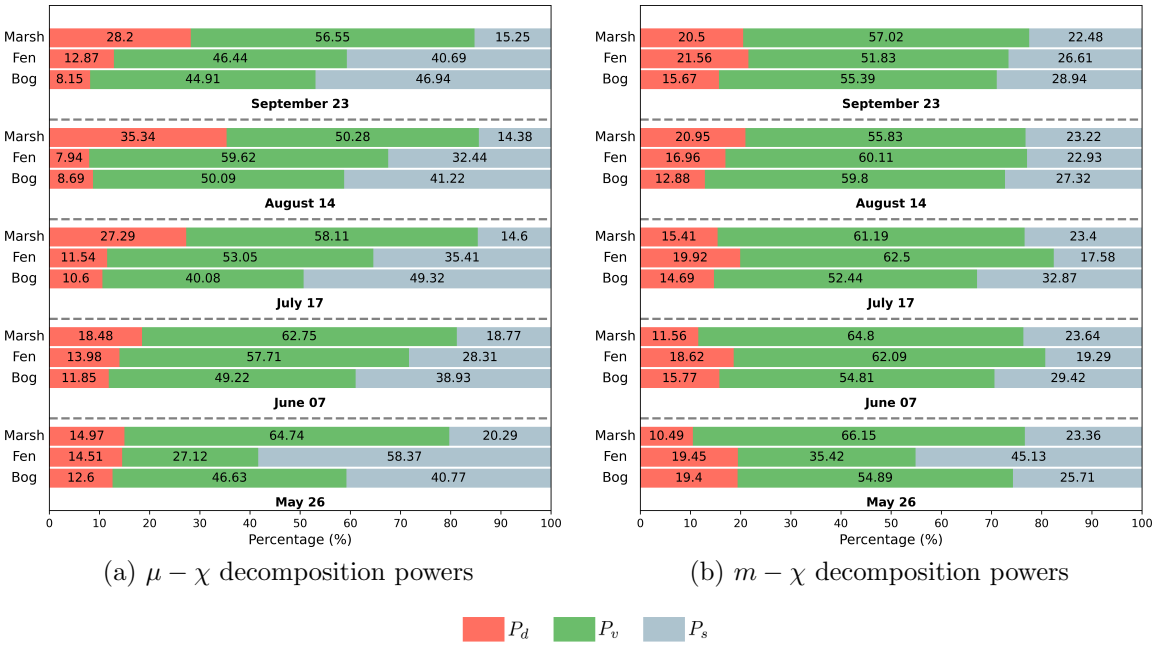

Figure 5.9: Values of $\mu$ for three wetland classes (bog, fen, and marsh) in CP mode.

### 5.6.3 Analysis of the Scattering Power Components over Wetlands

Using the CPS, we derive a parameter $\mu$, which is used to obtain the three scattering power components explained in Section 5.4. The proposed scattering power components provide valuable insights into the scattering mechanisms observed over the wetlands. The three scattering powers, $P_s$, $P_d$, and $P_v$, are the odd-bounce, even-bounce, and random scattering components, respectively. The scattering power

components are computed using the $\mu - \chi$ and the $m - \chi$ decomposition techniques (Figure 5.10).

In principle, the difference between the two decomposition techniques is the choice of parameters $\mu$ and $m$. The parameter $m$ is the ratio of the polarized power to the total scattered power ($g_0$), whereas the parameter $\mu$ is the ratio of the polarized power to the maximum received power ($P_{\max}$). The parameter $m$ that only depends on the transmit antenna polarization basis quantifies the overall polarization structure. In our approach, we synthesize the polarization basis of the receiving antenna to match its polarization basis to that of the scattered wave. Thus, the parameter $\mu$ derived from CPS quantifies the polarization structure better with respect to the dominant scattering phenomena. We show an RGB representation of the obtained power components using $\mu - \chi$ for the three aforementioned wetland classes in Figure 5.11.




(a) $\mu - \chi$ decomposition powers

(b) $m - \chi$ decomposition powers

Figure 5.10: Scattering powers (%) computed over wetlands using (a) $\mu - \chi$ and (b) $m - \chi$ decomposition technique.

Over the bog wetland class, using $\mu - \chi$ we found the $P_s = 40.77\,\%$ and $P_v = 46.63\,\%$ to be dominant during the initial acquisition dates. Similarly, using $m - \chi$ we observed the $P_s$ and $P_v$ to be $25.71\,\%$ and $54.89\,\%$, respectively. The comparatively low $P_v$ and high $P_s$ obtained using $\mu - \chi$ is due to excess power over the polarized component measured in $\mu$ (Figure 5.10). The high $P_s$ and $P_v$ components can be due

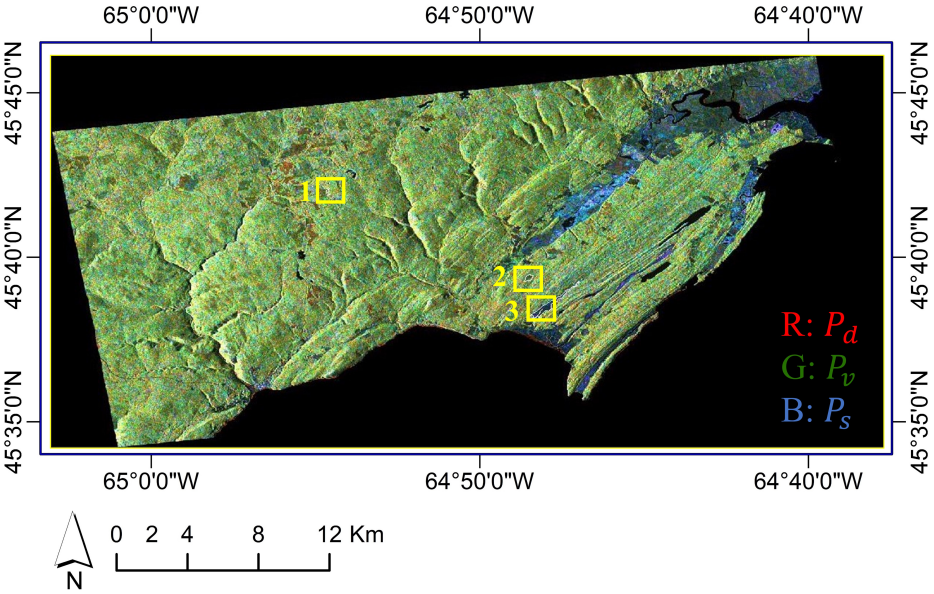
to the mixed surface and random scattering from the rough wetland surface. However, later, as the bog wetland becomes filled with water, we found the $P_s = 49.32\,\%$ to be dominant, indicating dominant surface scattering. Further, an increase in the $P_v$ component was observed due to the vegetation present in the bog wetland during the later acquisition dates. A similar trend was also observed from the powers computed using the $m - \chi$ decomposition technique. A comparatively low $P_v$ component in $\mu - \chi$ compared to $m - \chi$ is due to relatively high values of $\mu$ because of the surface scattering from underneath the surface of the sparsely vegetated bog wetland.

In the case of the fen, our analysis using the $\mu - \chi$ method revealed that on 26 May, the dominant component was $P_s$, accounting for approximately 58.37 % of the total scattering power. This finding can be attributed to the prevalent surface scattering resulting from the smooth accumulated peat in the fen. Similarly, when employing the $m - \chi$ decomposition method, we also observed the dominance of the $P_s$ component, along with a substantial presence of the $P_v$ component (as illustrated in Figure 5.10). However, as the volume of vegetation in this wetland increased during subsequent acquisition dates, we noticed a significant rise in the $P_v$ component. Specifically, the $P_v$ component, as obtained from both $\mu - \chi$ and $m - \chi$ decompositions, increased notably, reaching approximately 60 %.

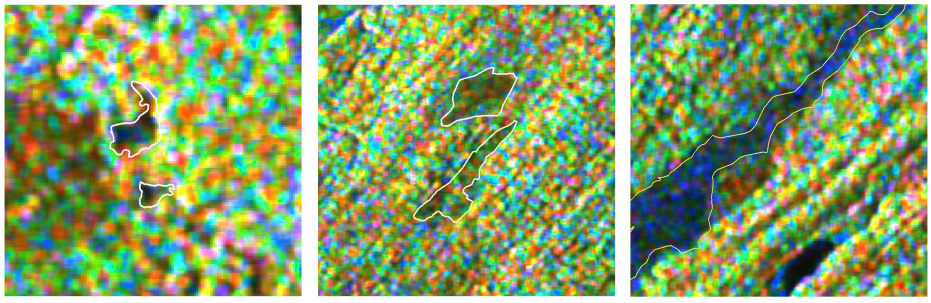
The scattering power components computed over the marsh wetlands resulted in a significant $P_v$ power component of 64.74 % and 66.15 % obtained from $\mu - \chi$ and $m - \chi$ decomposition, respectively (Figure 5.10). This is likely due to the random scattering from the underneath rough surface, as the vegetation may be young and sparse during the initial acquisitions. Nevertheless, we found the $P_v$ component to be reduced during the subsequent two acquisitions, possibly due to rising water levels. Later, as the vegetation in the marsh wetland grows, we found the $P_d = 35.34\,\%$ and $P_v = 50.28\,\%$ component to be dominant. This indicates multiple scattering from the grown vegetation components and the underneath wetland surface. One could note from Figure 5.10 that the $P_d$ component in $\mu - \chi$ is higher compared to $m - \chi$ as the $\mu$ parameter effectively characterizes the intricate multiple scattering phenomena within densely vegetated regions and the underneath marsh wetland surface.

We observed temporal variations in the scattering power components amongst the three wetland types. This variation in the scattered power can be helpful in the discrimination of the wetland classes from one another. In the following sub-section,

we show the usefulness of the proposed scattering power components in discriminating the three wetland classes.




(a)




(b)

Figure 5.11: (a) The RGB representation of scattering power components extracted from $\mu - \chi$ technique in the vegetation peak using RCM image acquired on 14 August. (b) The zoomed-in areas highlight the variations in scattering powers among different wetland types.

### 5.6.4 Classification of Wetlands

In the present study, RF was used as the classifier for wetland mapping as it is a good 'first-choice algorithm' [46]. RF is an easy-to-use ensemble bagging machine learning approach. It is known as one of the computationally efficient, robust, and

non-linear non-parametric classifiers in literature, especially for classifying crop types and heterogeneous wetland environments [20, 47, 48]. The following two significant aspects led to the selection of RF in our study.

Firstly, this method is less sensitive to noisy data sets; therefore, it is less affected in special cases, such as SAR image processing, where speckle degrades the radiometric quality of images. Secondly, RF can handle multiple input features while remaining non-over-fitted [20, 49]. This attribute also contributed to the present study since time-series polarimetric features were extracted and integrated as the input of the classification procedure. There are two main user-defined hyper-parameters for the RF model, including the number of trees (Ntree) and the number of features (Mtry) [40]. According to our sensitivity analysis and multiple runs of the model, the Ntree was set to 100, and the Mtry was set to the square root of the total number of features in this paper.

We compared two sets of inputs for wetland mapping using RF: one utilizing the three scattering power components derived from the $\mu-\chi$ decomposition and the other utilizing the three power components from the $m-\chi$ decomposition. Each input set consisted of the three power components extracted from each temporal RCM image. The classification maps obtained by these two sets of inputs are shown in Figure 5.12a and Figure 5.12c, respectively. The overall classification accuracy (OA) using the $\mu-\chi$ decomposition was found to be 87.45 %, while the $m-\chi$ decomposition achieved an OA of 83.57 %.

The classification accuracy results indicate that the $\mu-\chi$ decomposition outperformed the $m-\chi$ decomposition. We observed relatively higher accuracies (see Figure 5.12b and Figure 5.12d) for the classification of wetland classes using the proposed method compared to the $m-\chi$ decomposition as shown in the confusion matrices. Specifically, the $\mu-\chi$ decomposition approach resulted in an increase of 5 % accuracy in discriminating spectrally similar wetland classes, such as bog and fen. These findings suggest that the power components derived from the $\mu-\chi$ decomposition provide more discriminative information for better classifying wetland classes throughout the temporal sequence of RCM CP-SAR images. Therefore, the $\mu-\chi$ decomposition parameters demonstrated their potential to enhance the accuracy and reliability of wetland mapping compared to the $m-\chi$ decomposition parameters.

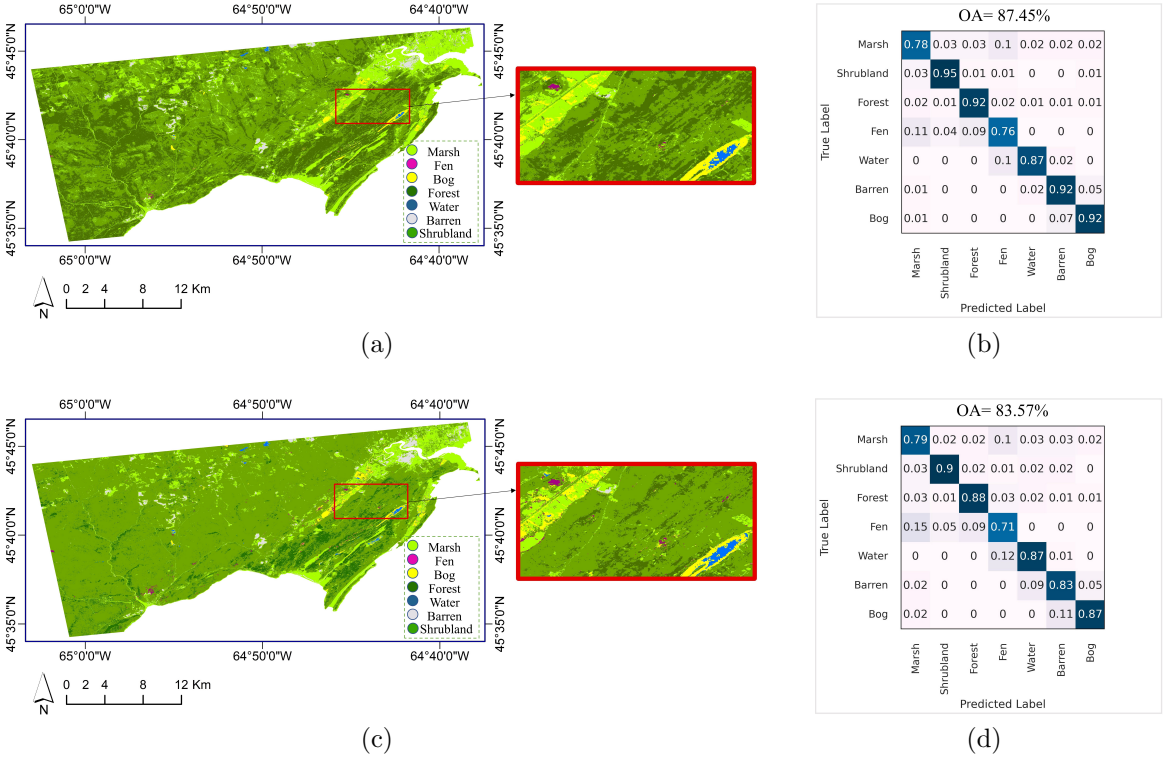



Figure 5.12: The classification maps obtained via time-series of scattering power components extracted using (a) the proposed $\mu - \chi$ decomposition and (c) the $m - \chi$ decomposition along with the corresponding confusion matrices (b) and (d), respectively.

## 5.7 Conclusion

This study investigated scattering response behavior in wetland environments using multi-temporal C-band RCM CP data sets. We specifically focused on three wetland types: bog, fen, and marsh, each characterized by its distinct structural attributes. We examined the variations in scattering responses using CPS at different acquisition dates.

As a result, the time-series CPS plots revealed intriguing patterns. During the active season, when vegetation structure changes, we observed significant variations in scattered waves, underscoring the unique scattering mechanisms inherent to each wetland type. Notably, these temporal variations in CPS indicated its sensitivity to various physical and structural changes within the wetlands. Moreover, we analyzed the distinctive wave ellipticity and orientation angles at the $P_{\max}$ for the three wetland

classes. Notably, the polarization states and scattering purity ($\mu$) for wetlands provide an additional dimension to the study. For instance, unlike fen and marsh wetlands, in the early and late growing seasons, the polarization states of the incidence waves tend to be preserved for the bog class.

We also proposed an alternative approach to decompose the total scattering power from the wetlands into a sum of matched and unmatched powers. We then used these descriptors to introduce an alternative scattering decomposition technique (i.e., $\mu-\chi$) utilizing the elements of the Stokes vector into three components: odd-bounce scattering, double-bounce scattering, and random scattering. This alternative decomposition approach outperformed the conventional method for wetland classification, yielding higher accuracy. The OA using the $\mu - \chi$ decomposition was found to be 87.45 % compared to 83.57 % while utilizing the $m - \chi$ decomposition. The findings provided valuable insights into the behavior of SAR backscattering during the wetland growing cycle.

Future research should explore the impact of critical imaging parameters, particularly the incidence angles of RCM observations, on CPS and the $\mu - \chi$ decomposition method. This exploration is essential for gaining a deeper understanding of the scattering mechanisms for diverse wetland classes. Variations in incidence angles have the potential to significantly influence how radar signals interact with wetland surfaces, unveiling different facets of the underlying scattering processes. For instance, different incidence angles may highlight subtle surface roughness or vegetation structure variations that are pivotal for distinguishing and characterizing wetlands. Such investigation will enable a comprehensive examination of how varying incidence angles affect the correlation between polarimetric parameters and biophysical variables. Moreover, it can provide valuable insights into selecting the optimal incidence angle for effective wetland monitoring.

In moving towards operational wetland characterization using SAR observations, validating and assessing the proposed methods' sensitivity using multifrequency observations is crucial, particularly at L-band. This offers a unique opportunity to examine the frequency-dependent behavior of wetland classes. Different frequencies penetrate the vegetation canopy to varying degrees, interact with subsurface features, and respond differently to changes in biophysical variables. Such assessments will strengthen the reliability of our proposed methods and contribute to the development

of operational wetland monitoring frameworks.

This study introduced an innovative descriptor and decomposition technique to interpret wetlands' intricate scattering responses using CP-SAR data. By decoding radar signals into their components and gaining insights into wetland dynamics, we equip environmental researchers and planners with a powerful toolset for assessing wetland behavior and tracking changes over time, benefiting informed decisions toward the preservation and sustainable use of these vital natural resources.

## 5.8 Future Directions & Recommendations

As illustrated in the literature review and the progress achieved in this thesis through the development of new AI techniques and the utilization of advanced EO data sources, each EO dataset offers unique efficiencies and advantages for wetland mapping and characterization. The complementary nature of these datasets, such as the structural detail provided by SAR and the spectral richness of the optical imager, highlights the potential for enhanced wetland analysis when these data sources are effectively integrated.

Despite these advancements, a critical gap remains in the comprehensive use of multi-source EO data for wetland studies. Specifically, there is a notable absence of studies that investigate the elevation information of wetland vegetation from LiDAR and synergistically employ SAR, optical, and LiDAR data for wetland mapping and monitoring within a unified framework, such as GEE. Such integration in GEE would not only streamline data access and processing but also facilitate large-scale, cloud-based analyses with significant computational efficiency. By addressing these gaps, future research can contribute significantly to the field of wetland science, advancing mapping and monitoring practices.

## 5.9 References

[1] M. Morris, C. Chew, J. T. Reager, R. Shah, and C. Zuffada, "A novel approach to monitoring wetland dynamics using cygnss: Everglades case study," *Remote Sensing of Environment*, vol. 233, p. 111417, 2019.

[2] R. W. Tiner, *Wetland indicators: A guide to wetland formation, identification, delineation, classification, and mapping*. CRC press, 2016.

[3] B. Warner and C. Rubec, "The canadian wetland classification system, national wetlands working group," *Wetlands Research Centre. University of Waterloo, Waterloo, Ontario*, 1997.

[4] M. Mahdianpari, B. Brisco, J. Granger, F. Mohammadimanesh, B. Salehi, S. Homayouni, and L. Bourgeau-Chavez, "The third generation of pan-canadian wetland map at 10 m resolution using multisource earth observation data on cloud computing platform," *IEEE Journal of Selected Topics in Applied Earth Observations and Remote Sensing*, vol. 14, pp. 8789–8803, 2021.

[5] S. Mahdavi, B. Salehi, J. Granger, M. Amani, B. Brisco, and W. Huang, "Remote sensing for wetland classification: A comprehensive review," *GIScience & Remote Sensing*, vol. 55, no. 5, pp. 623–658, 2018.

[6] M. Guo, J. Li, C. Sheng, J. Xu, and L. Wu, "A review of wetland remote sensing," *Sensors*, vol. 17, no. 4, p. 777, 2017.

[7] R. Jahncke, B. Leblon, P. Bush, and A. LaRocque, "Mapping wetlands in nova scotia with multi-beam radarsat-2 polarimetric sar, optical satellite imagery, and lidar data," *International Journal of Applied Earth Observation and Geoinformation*, vol. 68, pp. 139–156, 2018.

[8] Y. Gao, W. Li, M. Zhang, J. Wang, W. Sun, R. Tao, and Q. Du, "Hyperspectral and multispectral classification for coastal wetland using depthwise feature interaction network," *IEEE Transactions on Geoscience and Remote Sensing*, vol. 60, pp. 1–15, 2021.

[9] K. Schmidt and A. Skidmore, "Spectral discrimination of vegetation types in a coastal wetland," *Remote sensing of Environment*, vol. 85, no. 1, pp. 92–108, 2003.

[10] M. W. Lang and E. S. Kasischke, "Using c-band synthetic aperture radar data to monitor forested wetland hydrology in maryland's coastal plain, usa," *IEEE Transactions on Geoscience and Remote Sensing*, vol. 46, no. 2, pp. 535–546, 2008.

[11] M. Dabboor, S. Banks, L. White, B. Brisco, A. Behnamian, Z. Chen, and K. Murnaghan, "Comparison of compact and fully polarimetric sar for multitemporal wetland monitoring," *IEEE Journal of Selected Topics in Applied Earth Observations and Remote Sensing*, vol. 12, no. 5, pp. 1417–1430, 2019.

[12] G. Lefebvre, A. Davranche, L. Willm, J. Campagna, L. Redmond, C. Merle, A. Guelmami, and B. Poulin, "Introducing wiw for detecting the presence of water in wetlands with landsat and sentinel satellites," *Remote sensing*, vol. 11, no. 19, p. 2210, 2019.

[13] L. White, K. Millard, S. Banks, M. Richardson, J. Pasher, and J. Duffe, "Moving to the radarsat constellation mission: Comparing synthesized compact polarimetry and dual polarimetry data with fully polarimetric radarsat-2 data for image classification of peatlands," *Remote Sensing*, vol. 9, no. 6, p. 573, 2017.

[14] L. White, B. Brisco, M. Dabboor, A. Schmitt, and A. Pratt, "A collection of sar methodologies for monitoring wetlands," *Remote sensing*, vol. 7, no. 6, pp. 7615–7645, 2015.

[15] R. J. Zomer, A. Trabucco, and S. L. Ustin, "Building spectral libraries for wetlands land cover classification and hyperspectral remote sensing," *Journal of environmental management*, vol. 90, no. 7, pp. 2170–2177, 2009.

[16] L. Dingle Robertson, H. McNairn, X. Jiao, C. McNairn, and S. O. Ihuoma, "Monitoring crops using compact polarimetry and the radarsat constellation mission," *Canadian Journal of Remote Sensing*, vol. 48, no. 6, pp. 793–813, 2022.

[17] M. Dabboor, I. Olthof, M. Mahdianpari, F. Mohammadimanesh, M. Shokr, B. Brisco, and S. Homayouni, "The radarsat constellation mission core applications: First results," *Remote Sensing*, vol. 14, no. 2, p. 301, 2022.

[18] R. K. Raney, B. Brisco, M. Dabboor, and M. Mahdianpari, "Radarsat constellation mission's operational polarimetric modes: A user-driven radar architecture," *Canadian Journal of Remote Sensing*, vol. 47, no. 1, pp. 1–16, 2021.

[19] M. Dabboor, L. White, B. Brisco, and F. Charbonneau, "Change detection with compact polarimetric sar for monitoring wetlands," *Canadian Journal of Remote Sensing*, vol. 41, no. 5, pp. 408–417, 2015.

[20] M. Mahdianpari, B. Salehi, F. Mohammadimanesh, and B. Brisco, "An assessment of simulated compact polarimetric sar data for wetland classification using random forest algorithm," *Canadian Journal of Remote Sensing*, vol. 43, no. 5, pp. 468–484, 2017.

[21] I. Olthof and T. Rainville, "Evaluating simulated radarsat constellation mission (rcm) compact polarimetry for open-water and flooded-vegetation wetland mapping," *Remote Sensing*, vol. 12, no. 9, p. 1476, 2020.

[22] S. Dey, A. Bhattacharya, D. Ratha, D. Mandal, and A. C. Frery, "Target characterization and scattering power decomposition for full and compact polarimetric sar data," *IEEE Transactions on Geoscience and Remote Sensing*, vol. 59, no. 5, pp. 3981–3998, 2020.

[23] S. Dey, A. Bhattacharya, A. C. Frery, C. López-Martínez, and Y. S. Rao, "A model-free four component scattering power decomposition for polarimetric sar data," *IEEE Journal of Selected Topics in Applied Earth Observations and Remote Sensing*, vol. 14, pp. 3887–3902, 2021.

[24] H. Maurya, A. Bhattacharya, A. K. Mishra, and R. K. Panigrahi, "Hybrid three-component scattering power characterization from polarimetric sar data isolating dominant scattering mechanisms," *IEEE Transactions on Geoscience and Remote Sensing*, vol. 60, pp. 1–15, 2022.

[25] J. J. Van Zyl, H. A. Zebker, and C. Elachi, "Imaging radar polarization signatures: Theory and observation," *Radio science*, vol. 22, no. 04, pp. 529–543, 1987.

[26] H. A. Zebker, J. J. Van Zyl, and D. N. Held, "Imaging radar polarimetry from wave synthesis," *Journal of Geophysical Research: Solid Earth*, vol. 92, no. B1, pp. 683–701, 1987.

[27] H. A. Zebker and J. J. Van Zyl, "Imaging radar polarimetry: A review," *Proceedings of the IEEE*, vol. 79, no. 11, pp. 1583–1606, 1991.

[28] J. Strzelczyk and S. Porzycka-Strzelczyk, "Identification of coherent scatterers in sar images based on the analysis of polarimetric signatures," *IEEE Geoscience and remote sensing letters*, vol. 11, no. 4, pp. 783–787, 2013.

[29] A. Verma, S. Dey, N. Bhogapurapu, C. López-Martínez, and A. Bhattacharya, "Dual polarimetric sar signature for human-made target characterization," in *2021 IEEE International India Geoscience and Remote Sensing Symposium (InGARSS)*, pp. 520–523, IEEE, 2021.

[30] A. Verma, D. Haldar, and A. Bhattacharya, "Polarimetric signature analysis of various crop-types using multi-source dual-frequency sar data," *Geocarto International*, vol. 37, no. 25, pp. 8860–8881, 2022.

[31] S. R. Cloude and E. Pottier, "A review of target decomposition theorems in radar polarimetry," *IEEE transactions on geoscience and remote sensing*, vol. 34, no. 2, pp. 498–518, 1996.

[32] R. K. Raney, "Hybrid-polarity sar architecture," *IEEE Transactions on Geoscience and Remote Sensing*, vol. 45, no. 11, pp. 3397–3404, 2007.

[33] R. K. Raney, J. T. Cahill, G. W. Patterson, and D. B. J. Bussey, "The m-chi decomposition of hybrid dual-polarimetric radar data with application to lunar craters," *Journal of Geophysical Research: Planets*, vol. 117, no. E12, 2012.

[34] A. Bhattacharya, S. De, A. Muhuri, M. Surendar, G. Venkataraman, and A. Das, "A new compact polarimetric sar decomposition technique," *Remote sensing letters*, vol. 6, no. 12, pp. 914–923, 2015.

[35] A. Verma, S. Dey, C. López-Martínez, and A. Bhattacharya, "Radar target scattering signature for earth observation," in *2022 URSI Regional Conference on Radio Science (USRI-RCRS)*, pp. 1–4, 2022.

[36] S. R. Cloude, D. G. Goodenough, and H. Chen, "Compact decomposition theory," *IEEE Geoscience and Remote Sensing Letters*, vol. 9, no. 1, pp. 28–32, 2011.

[37] V. Kumar, D. Mandal, A. Bhattacharya, and Y. Rao, "Crop characterization using an improved scattering power decomposition technique for compact polarimetric sar data," *International Journal of Applied Earth Observation and Geoinformation*, vol. 88, p. 102052, 2020.

[38] B. Brisco, F. Ahern, S.-H. Hong, S. Wdowinski, K. Murnaghan, L. White, and D. K. Atwood, "Polarimetric decompositions of temperate wetlands at c-band," *IEEE journal of selected topics in applied earth observations and remote sensing*, vol. 8, no. 7, pp. 3585–3594, 2015.

[39] F. T. Ulaby, D. Held, M. C. Donson, K. C. McDonald, and T. B. Senior, "Relating polaization phase difference of sar signals to scene properties," *IEEE Transactions on Geoscience and Remote Sensing*, no. 1, pp. 83–92, 1987.

[40] M. Mahdianpari, H. Jafarzadeh, J. E. Granger, F. Mohammadimanesh, B. Brisco, B. Salehi, S. Homayouni, and Q. Weng, "A large-scale change monitoring of wetlands using time series landsat imagery on google earth engine: a case study in newfoundland," *GIScience & Remote Sensing*, vol. 57, no. 8, pp. 1102–1124, 2020.

[41] S. Zoltai and D. Vitt, "Canadian wetlands: environmental gradients and classification," *Vegetatio*, vol. 118, pp. 131–137, 1995.

[42] R. W. Tiner, M. W. Lang, and V. V. Klemas, "Remote sensing of wetlands: applications and advances," 2015.

[43] M. Dabboor and B. Brisco, "Wetland monitoring and mapping using synthetic aperture radar," *Wetl. Manag. Assess. Risk Sustain. Solut*, vol. 1, p. 13, 2018.

[44] F. M. Grings, P. Ferrazzoli, J. C. Jacobo-Berlles, H. Karszenbaum, J. Tiffenberg, P. Pratolongo, and P. Kandus, "Monitoring flood condition in marshes using em models and envisat asar observations," *IEEE Transactions on Geoscience and Remote Sensing*, vol. 44, no. 4, pp. 936–942, 2006.

[45] F. Mohammadimanesh, B. Salehi, M. Mahdianpari, B. Brisco, and M. Motagh, "Multi-temporal, multi-frequency, and multi-polarization coherence and sar backscatter analysis of wetlands," *ISPRS Journal of Photogrammetry and Remote Sensing*, vol. 142, pp. 78–93, 2018.

[46] S. E. Franklin, E. M. Skeries, M. A. Stefanuk, and O. S. Ahmed, "Wetland classification using radarsat-2 sar quad-polarization and landsat-8 oli spectral response data: A case study in the hudson bay lowlands ecoregion," *International Journal of Remote Sensing*, vol. 39, no. 6, pp. 1615–1627, 2018.

[47] V. F. Rodriguez-Galiano, B. Ghimire, J. Rogan, M. Chica-Olmo, and J. P. Rigol-Sanchez, "An assessment of the effectiveness of a random forest classifier for land-cover classification," *ISPRS journal of photogrammetry and remote sensing*, vol. 67, pp. 93–104, 2012.

[48] Z. Akhavan, M. Hasanlou, M. Hosseini, and H. McNairn, "Decomposition-based soil moisture estimation using uavsar fully polarimetric images," *Agronomy*, vol. 11, no. 1, p. 145, 2021.

[49] M. Belgiu and O. Csillik, "Sentinel-2 cropland mapping using pixel-based and object-based time-weighted dynamic time warping analysis," *Remote Sensing of Environment*, vol. 204, pp. 509–523, Jan. 2018.

# Chapter 6

# Advancing Wetland Mapping with Multi-Source Data Integration [1]

## 6.1 Preface

A version of this manuscript has been published in the MDPI Sensors journal. I am the first author, along with my co-authors: Masoud Mahdianpari, Eric W. Gill, and Fariba Mohammadimanesh. I was responsible for the conceptualization, methodology, formal analysis, visualization, and writing of the manuscript. The co-authors reviewed and provided comments and suggestions on the manuscript. To further improve the clarity and quality of the work, I revised the paper based on their feedback as well as that of the reviewers.

## 6.2 Abstract

Wetlands are amongst Earth's most dynamic and complex ecological resources, serving productive and biodiverse ecosystems. Enhancing the quality of wetland mapping

[1] Jafarzadeh, H., Mahdianpari, M., Gill, E.W. and Mohammadimanesh, F., 2024. Enhancing Wetland Mapping: Integrating Sentinel-1/2, GEDI Data, and Google Earth Engine. Sensors, 24(5), p.1651.

through Earth observation (EO) data is essential to improving management and conservation practices. However, the achievement of reliable and accurate wetland mapping faces challenges due to the heterogeneous and fragmented landscape of wetlands, along with spectral similarities among different wetland classes. The present study aims to produce advanced 10 m spatial resolution wetland classification maps for four pilot sites on the island of Newfoundland in Canada. Employing a comprehensive and multidisciplinary approach, this research leverages the synergistic use of optical, synthetic aperture radar (SAR), and light detection and ranging (LiDAR) data. It focuses on ecological and hydrological interpretation using multi-source and multi-sensor EO data to evaluate their effectiveness in identifying wetland classes. The diverse data sources include Sentinel-1 and -2 satellite imagery, Global Ecosystem Dynamics Investigation (GEDI) LiDAR footprints, the Multi-Error-Removed Improved-Terrain (MERIT) Hydro dataset, and the European ReAnalysis (ERA5) dataset. Elevation data and topographical derivatives, such as slope and aspect, were also included in the analysis. The study evaluates the added value of incorporating these new data sources into wetland mapping. Using the Google Earth Engine (GEE) platform and the Random Forest (RF) model, two main objectives are pursued: (1) integrating the GEDI LiDAR footprint heights with multi-source datasets to generate a 10 m vegetation canopy height (VCH) map and (2) seeking to enhance wetland mapping by utilizing the VCH map as an input predictor. Results highlight the significant role of the VCH variable derived from GEDI samples in enhancing wetland classification accuracy, as it provides a vertical profile of vegetation. Accordingly, VCH reached the highest accuracy with a coefficient of determination ($R^2$) of 0.69, a root-mean-square error (RMSE) of 1.51 m, and a mean absolute error (MAE) of 1.26 m. Leveraging VCH in the classification procedure improved the accuracy, with a maximum overall accuracy of 93.45%, a kappa coefficient of 0.92, and an F1 score of 0.88. This study underscores the importance of multi-source and multi-sensor approaches incorporating diverse EO data to address various factors for effective wetland mapping. The results are expected to benefit future wetland mapping studies.

## 6.3 Introduction

Wetlands are highly productive, yet they are the most vulnerable ecosystems, straddling terrestrial and aquatic systems [1, 2]. Due to their ecological richness, multifunctionality, and conservation concerns, wetlands are often referred to as "the kidney of the Earth" [3] and have drawn the attention of scientific communities. They offer a diverse range of services that contribute to human well-being and nature, serving as protective buffers against flood and storm damage, improving water quality, promoting aquatic and plant biomass productivity, stabilizing shorelines, aiding in plant collection and retaining contaminants [4]. However, wetlands face degradation in terms of coverage and biodiversity due to natural and human-induced disturbances, such as global warming, rising sea levels, and agricultural activities [5, 6]. As such, accurate mapping and consistent monitoring are crucial for managing and conserving wetland resources, protecting them from degradation, evaluating restoration efforts and ensuring future sustainability [7, 8].

With a view toward mitigating the existing environmental and biodiversity crises, global biodiversity changes can be monitored using several measures referred to as essential biodiversity variables (EBVs) [9]. EBVs function as a health indicator of an ecosystem and can be defined as metrics reporting on ecosystem dynamics and biodiversity. Ecological traits, species populations, diverse community compositions, as well as ecosystem function and structure are some of the more salient EBVs related to wetlands. Most of these variables can be inferred, if not measured directly, through remote sensing techniques. In general, the utility of remote sensing in characterizing EBVs and biodiversity is being increasingly acknowledged. Remote sensing data can provide insight into some EBVs; thus, it is important to accurately link EBVs with remote sensing data to facilitate long-term global monitoring [10]. Within this framework, vegetation canopy height (VCH) and structure hold great potential in developing EBVs for wetland landscapes. Launching these concepts (e.g., VCH) acts as a new toolkit for assessing the state of wetland realms and determining effective action toward monitoring tasks. VCH provides a perspective of the vertical dimension of vegetation, offering valuable information on habitat diversity, species richness assessment, and ecosystem resilience to environmental changes [11, 12]. Furthermore, the quantitative assessment of wetland vegetation characteristics, including canopy height and vegetation cover fraction, contributes crucial insights for effective

ecosystem management practices [13, 14].

The difficulty of accessing wetlands and their heterogeneous nature pose significant challenges for classifying and assessing their cover types, both spatially and temporally [15, 16]. Inexpensive remote sensing data offer synoptic, repeated, and reliable observations, making them favorable for monitoring the natural environment [1]. The integration of multiple sensors and measurements, such as optical and Synthetic Aperture Radar (SAR), enables space-based remote sensing systems to perform large-scale assessments of vegetation cover and biomass, surpassing the capabilities of traditional ground-based field measurements. However, relying solely on optical or SAR datasets tends to overlook some vegetation properties and structures due to the uncertainties inherent in the data sources.

So far, numerous studies have been carried out utilizing multi-source remotely sensed data to map, monitor, and assess the global wetlands from local to subcontinental scales [16, 17]. These studies have primarily focused on SAR and optical imagery [18, 19]. In contrast, the current study goes beyond the existing approaches by exploring additional features contributing to comprehensive wetland characterizations. We recognize that wetlands exhibit diverse forms and can be characterized in multiple ways, necessitating the consideration of a broader range of features.

In this context, the present work explores new aspects in terms of using multi-source and multi-sensor data. It evaluates the ability of different Earth observation (EO) datasets for wetland classification, focusing on NASA's Global Ecosystem Dynamics Investigation (GEDI) LiDAR data. Taking these capabilities into account has the potential to boost the remote sensing toolbox for wetland habitat monitoring by adding LiDAR-derived VCH, which includes the vertical structure of vegetation and additionally provides information complementary to that obtained from optical and SAR imagery. Incorporating supplementary data can offer a unique understanding of wetland characteristics beyond responses achieved with conventional remote sensing imagery, including features such as vegetation height, density, biomass distribution, etc.

Previous research efforts have illustrated the potential of integrating space-borne LiDAR—particularly GEDI—with optical and SAR imagery to conduct a detailed assessment of canopy height and biomass. Due to limited sampling and spatial resolution of grids, LiDAR measurements rely on either accepting sampling errors using

statistical methods or integrating them with other remote sensing data. This allows the leveraging of accurate but sparse LiDAR data to calibrate less accurate continuous datasets (compared to full-cover LiDAR products). In [20], Qi et al. improved forest height modeling by incorporating simulated GEDI LiDAR data and TanDEM-X InSAR data in sites located in the United States and Costa Rica. In addition, canopy height mapping for Chinese forests was achieved by Liu et al. through the integration of GEDI and ICESat-2 data [21]. Dorado-Roda et al. integrated airborne LiDAR and GEDI data in their study [22], estimating the canopy height maps and biomass in Mediterranean forests. Furthermore, biomass estimation was explored in [23] over Sonoma County in California, USA, leveraging simulated data from three missions: GEDI, ICESat-2, and the NASA–Indian Space Research Organization (ISRO) SAR (NISAR).

Building on this, advancements in cloud-based computing resources and open-access data policies for high-resolution EO datasets have revolutionized large-scale wetland monitoring [24]. The availability of datasets, particularly from Landsat and Sentinel archives, has enhanced the understanding of wetland ecosystems, facilitating effective management and conservation [25]. Google Earth Engine (GEE) exemplifies this innovative technology by providing access to vast amounts of satellite data and a web-based workbench environment for geospatial data analysis, incorporating image processing and machine learning (ML) algorithms [6, 26]. Its parallel processing architecture enables the storage and analysis of a massive volume of geospatial data that speed up the mapping and monitoring tasks [27], supporting diverse applications [28, 29].

This study seeks to enhance the accuracy of wetland mapping by integrating free-access EO data sources in the GEE cloud-computing environment. Despite the scientific accomplishments and the availability of various data sources, a knowledge gap exists in the application of remotely sensed data for VCH at the species level across different wetland ecosystems. At its core, this study evaluates the potential of footprint space-borne LiDAR samples in estimating gridded VCH within a unique Newfoundland ecosystem across four pilot sites and determines the effect of the VCH as an input predictor for accurate wetland mapping.

In summary, this study pursues the following main objectives:

- Firstly, it establishes an ML-based approach to integrate GEDI footprints with

multi-source EO data to generate VCH maps for wetland regions using GEE. The efficiency of GEDI-derived canopy height is also assessed under diverse terrain and land cover conditions distributed across the study sites. This integration focuses on exploring the potential of combining space-borne LiDAR point samples from GEDI footprints to generate VCH maps.

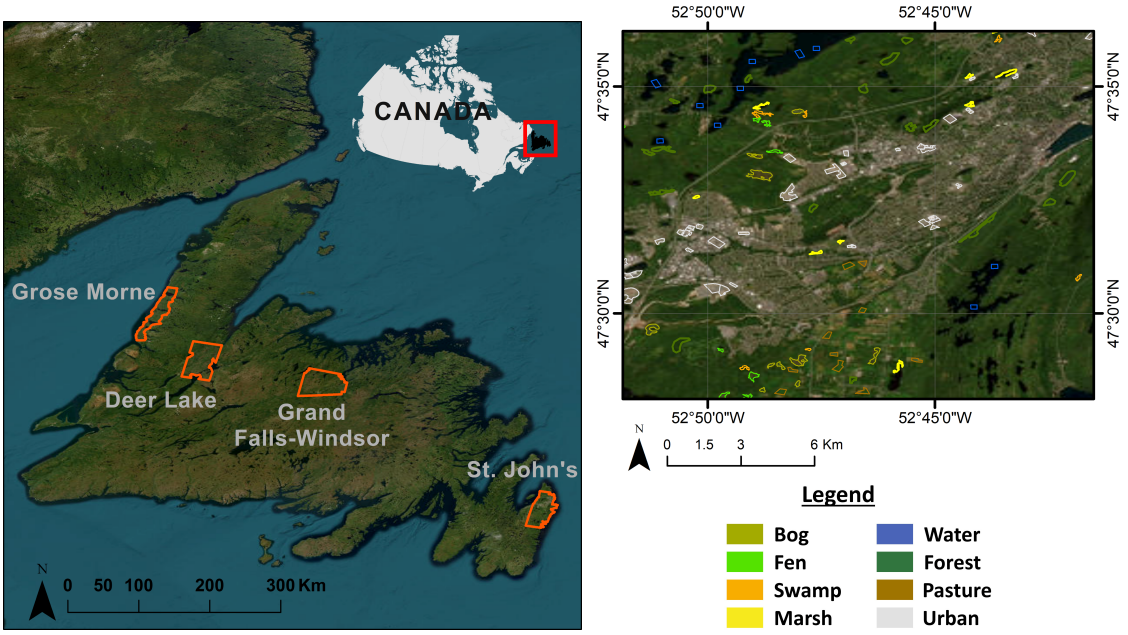
- Secondly, the study utilizes the combined VCH dataset and multi-source EO data to produce wetland classification maps. This step is crucial for investigating the importance of VCH to achieving enhanced wetland mapping.

Sections 6.4 and 6.5 provide a comprehensive overview of the study sites, multi-source and multi-sensor datasets, and the applied methodology. The results are presented in Section 6.6, and the significance of the employed methodology is discussed in Section 6.7. Finally, Section 6.8 draws the conclusions.

## 6.4 Study Sites and Datasets

### 6.4.1 Study Sites

To apply the proposed workflow, we chose four sub-provincial scale sites on the Island of Newfoundland, Canada, as study areas (see Figure 6.1). The total area covered by satellite imagery in these pilot sites is about 4229 $km^2$. The predominant land cover types are categorized into two general groups: (1) wetlands (i.e., bog, fen, swamp, and marsh) and (2) non-wetlands (i.e., deep water, forest, pasture, urban). The non-wetland areas are also of interest due to their potential as areas for development or land use change.




(a) (b)

Figure 6.1: (**a**) An overview of the Island of Newfoundland and pilot sites; (**b**) a representation of collected field data in St. John's area.

The first pilot site, the city of St. John's in the Avalon Peninsula area, situated in the southeast within the Maritime Barren eco-region, encounters an oceanic climate characterized by misty, cool summers and relatively temperate winters. Both Grand Falls-Windsor in the north-central region and Deer Lake in the northern area, designated as the second and third pilot sites, lie within the Central Newfoundland eco-region. These areas exhibit a continental climate characterized by cool summers and cold winters. On the far west coast in the Northern Peninsula eco-region, our fourth pilot site, Gros Morne, experiences a maritime-type climate with cool summers and mild winters [4].

These pilot sites represent the diverse regional characteristics of the landscape and vegetation across the island, with varying latitudes, longitudes, elevations, slopes, canopy heights, and canopy covers. They feature a range of geological formations, vegetation types, and climate conditions [6], allowing for a comparative analysis of the GEDI mission and its integration with other data sources. Detailed information on each pilot site can be found in Table 6.1.

Table 6.1: Study sites and the geological characteristics.

| Pilot Site | Area (km$^2$) | Elevation (m) | | Vegetation | Slope (Degrees) | | Land Covers | |
|---|---|---|---|---|---|---|---|---|
| | | Mean | Max | Mean Height (m) | Mean | Max | Wetland & Non-Wetland | |
| St. John's | 896 | 142.33 | 288 | 5.88 | 4.42 | 74.52 | Bog, Fen, Marsh, Swamp, | Water, Forest, Pasture, Urban |
| Grand Falls-Windsor | 1304 | 135.77 | 509 | 5.81 | 3.23 | 38.64 | | |
| Deer Lake | 1241 | 137.57 | 455 | 6.57 | 3.42 | 46.80 | | |
| Gros Morne | 788 | 61.96 | 500 | 6.08 | 3.87 | 80.09 | | |

### 6.4.2 Reference Data Repository

Wetland reference data collected from field campaigns are a valuable resource for geoscientists conducting research in the field of wetland ecology and management. It provides a wealth of information that can be utilized for various objectives, such as training and testing models for wetland identification and mapping, understanding the ecological characteristics of wetlands in a specific region, and tracking changes in wetland conditions over time. In this study, the reference samples of wetland/non-wetland classes were collected via field campaigns by multiple organizations. These campaigns involved visiting, identifying, and collecting data from all mentioned pilot sites (see Figure 6.1).

A size-based sorting approach was implemented for in-situ recorded reference polygons to enhance the accuracy and assessment robustness. This involved categorizing polygons based on their size and subsequently allocating them to either training or testing sets alternately. This method guaranteed the independence of the samples used to generate the training and testing polygons. Furthermore, the alternative assignment strategy aimed to achieve a balanced distribution, with ≈50% of polygons assigned to each group. The balanced allocation ensured that both the training and testing sets consisted of an equal number of small and large polygons. By doing so, the pixel counts were kept similar, effectively addressing the substantial variations in intra-wetland sizes. Table 6.2 indicates the total number of reference polygons assigned for each land cover type.

Table 6.2: Number of reference ground-truth polygons for each land cover class.

| # | **Class** | # **Polygons** |
|---|---|---|
| 1 | Bog | 185 |
| 2 | Fen | 185 |
| 3 | Marsh | 150 |
| 4 | Swamp | 157 |
| 5 | Water | 90 |
| 6 | Forest | 184 |
| 7 | Pasture | 155 |
| 8 | Urban | 193 |

### 6.4.3 Multi-Source/Multi-Sensor Data Collection on GEE and Pre-Processing

This study introduced and utilized a combination of multi-source EO data for classification, thereby fusing the strengths inherent in each dataset and enhancing the ability to discriminate different wetland classes. These include Sentinel-1 and -2 imagery, point-based height measurements from GEDI, the Merit Hydro dataset, ERA5, and elevation data with topographical derivatives. It is hypothesized that, with additional information, wetland areas can be identified and classified based on surface structure and hydrologic characteristics that may otherwise be indistinguishable in optical or SAR data. The GEE platform was used to acquire and pre-process all datasets. The subsequent sections provide a detailed overview of each data source.

#### SAR and Optical Data

This study utilized the European Space Agency's (ESA) Sentinel-1 C-band (≈5.5 cm wavelength) SAR imagery, which offers all-weather and all-time observations [30]. Our analysis considered the backscattering coefficient products derived from dual-band cross-polarization VV + VH, with a pixel size of 10 m. A composite summer image was generated by calculating the mean values of backscattering data spanning from June to September 2021 (four months). This approach is employed to mitigate the impact of speckle noise inherent in SAR images [31].

In addition, ESA's Sentinel-2 optical multispectral imagery, a constellation of a

pair of identical satellites, was utilized. These satellites collectively cover the Earth's surface every five days, providing imagery with 10 m, 20 m, and 60 m spatial resolution across 13 spectral bands [30]. A summer composite of the Sentinel-2 surface reflectance products was generated by employing the four-month extraction of Sentinel-2 observations and determining the median values across all pixels. This approach effectively helped to reduce the effects of cloudy and other unwanted pixels [31].

Further, to match the pixel size of Sentinel-1, the Sentinel-2 composite was upsampled to a 10 m pixel size for all spectral bands.

### GEDI Relative Height (RH) Data

Since its launch in December 2018, the GEDI instrument has revolutionized the study of vegetation structure. It is a laser altimeter with a full-waveform footprint dedicated exclusively to collecting unique data on the height and density of vegetation [32]. The GEDI data available in the GEE environment are created by selecting a subset of variables from NASA's GEDI level 2A (L2A) Global Footprint-Level Elevation and the Height Metrics Product [33].

The relevant variables of the product to be used in the current study are relative vegetation canopy height metrics (ranging from RH0 to RH100), capturing the height above the ground. For instance, RH50 represents the height of medium energy returns, while RH100 specifies the top of the canopy height. As the RH100 is associated with the first returned pulse and depends on signal-to-noise ratio (SNR) measurements, it may contain noise [34], leading to inaccurate estimates in complex canopy areas. Comparisons with GEDI-simulated waveforms indicate that RH95 is the most reliable estimate of canopy height [35], while RH100 consistently underestimates canopy heights. Hence, RH95 was employed as the vegetation stand height for the wetland to forest covers in this work, and was utilized as reference data for training and testing the prediction model. Remarkably, GEDI footprints have a diameter of 25 m and are spaced 60 m apart along a ground track [36]. A representation of GEDI footprints in the St. John's area is illustrated in Figure 6.2. Note that the GEDI observations for each pilot site were split into two training and testing parts with 70% and 30% ratios. The details on GEDI training and testing dataset quantity are presented in Table 6.3.

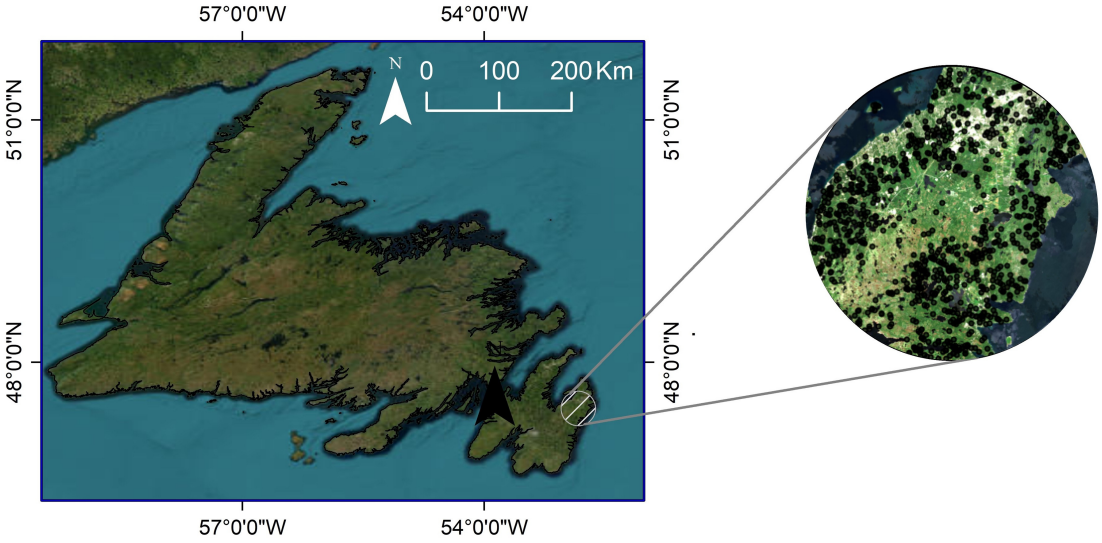



Figure 6.2: A visual example of the distribution of GEDI RH95 points on GEE in the St. John's site.

Table 6.3: Partitioning of GEDI Waveforms (N) into training and validation sets.

| **Pilot Site** | **N** | **Train** | **Test** |
|---|---|---|---|
| St. John's | 3266 | 2286 | 980 |
| Grand Falls-Windsor | 5514 | 3860 | 1654 |
| Deer Lake | 5786 | 4050 | 1736 |
| Gros Morne | 5915 | 4140 | 1775 |

GEDI LiDAR observations may include outliers caused by factors such as topography, photon return, and atmospheric conditions [37]. Here, the RH metric data are refined by defining stricter screening conditions to exclude the outliers and provide good-quality GEDI data collection. The following processing steps are involved in data filtering:

- Filtering based on a quality flag parameter is performed on GEDI observations, removing measurements with a quality flag value of zero. A value of 1 indicates a valid waveform, while a value of 0 indicates an invalid waveform.
- The ESA has developed a comprehensive global land cover map at a spatial resolution of 10 m, utilizing Sentinel-1 and -2 datasets [38]. This map, known

as ESA WorldCover V100, delineates 11 distinct land cover classes based on the classification system of the United Nations (UN) Food and Agriculture Organization (FAO). These classes include tree cover, shrubland, grassland, cropland, build-up, bare/sparse vegetation, snow-ice, permanent water bodies, herbaceous wetland, mangroves, and moss-lichen. Our study utilized the ESA land cover map to mask out non-vegetated regions in VCH maps.

- GEDI points were further screened using a defined threshold and multiple model-runs. Accordingly, the average canopy height was considered as the threshold for filtering GEDI RH metric data, calculated based on the GEDI-V27 product—a global canopy height map available from GEE with a 30 m spatial resolution [39]. GEDI points with a height value greater than twice the determined threshold at each pilot site were excluded from the analysis.

### Merit Hydro

The Multi-Error-Removed Improved-Terrain (MERIT) Hydro dataset presents a global flow direction map at 3-arc-sec resolution. This map is derived from the MERIT digital elevation model (DEM) and multiple water body datasets [40]. Despite being recently released, this dataset is increasingly being used for hydrological applications, including the global reconstruction of river flows [41] and the modeling of floodplain inundation dynamics [42]. Within this study, we incorporated two parameters derived from the MERIT Hydro dataset: (1) flow accumulation parameter [43] and (2) height above nearest drainage (HAND) parameter [44]. The HAND parameter represents the elevation difference between a pixel in a DEM and the nearest drainage network, while flow accumulation quantifies the cumulative weight of all pixels flowing into each downslope pixel. The inclusion of these parameters in wetland mapping is motivated by the close correlation between wetland ecosystems, topography, and hydrology, thereby introducing novel aspects to the analysis.

### ERA5

The supplementary climate data utilized in this study were acquired from the global ERA5 dataset, the fifth-generation European ReAnalysis [45]. It supplies global hourly measurements of various atmospheric and weather-related variables such as

temperature, precipitation, wind, and pressure. It is accessible in a regular latitude–longitude grid with 31 km spatial resolution. In this work, temperature and precipitation data were collected from ERA5 at a spatial resolution of 30 km, and the average monthly temperature and precipitation were calculated.

#### SRTM-DEM

The 30 m (1-arc-second) Shuttle Radar Topography Mission (SRTM) DEM [46] was originally designed by NASA to deliver the first consistent and relatively high-quality elevation data on a near-global scale [47]. The SRTM-DEM (V4), available in the GEE database, is the reprocessed version that addresses data voids and facilitates its ease of use.

Besides the elevation, both aspect and slope parameters were computed and integrated into our analysis. These terrain-related variables contribute valuable information for understanding the topographical characteristics of the pilot sites, enabling comprehensive interpretation of the wetland environments under investigation.

Considering all the abovementioned geospatial data sources, different features were extracted (listed in Table 6.4). Each variable was selected in accordance with its unique ability to capture wetland information.

## 6.5 Methods

### 6.5.1 Methodology Overview

Accurate estimation of VCH is essential for understanding ecosystem dynamics and biodiversity. To achieve this, we developed a process flow diagram outlining the different research stages. Figure 6.3 depicts the process flow diagram for the present study. The first phase involves data acquisition and pre-processing, followed by extracting various features. In the second phase, VCH and classification maps are obtained and assessed. The adopted approach relies on only publicly and freely accessible datasets that are widely available, allowing for easy adaptation to other heterogeneous wetland settings. Detailed overviews of each stage are provided in the following subsections.

Table 6.4: List of predictors used for VCH prediction and wetland cover classification in this study.

| Data Source | Band/Variable | Equation | Description |
|---|---|---|---|
| Sentinel-2 Optical | B2 (Blue) | - | Sentinel-2 multispectral bands |
| | B3 (Green) | - | |
| | B4 (Red) | - | |
| | B5 (VRE1) | - | |
| | B6 (VRE2) | - | |
| | B7 (VRE3) | - | |
| | B8 (NIR) | - | |
| | B8A (NNIR) | - | |
| | B11 (SWIR1) | - | |
| | B12 (SWIR2) | - | |
| Spectral Indices | NDVI | $\frac{NIR-\text{Red}}{NIR+\text{Red}}$ | Normalized Difference Vegetation Index |
| | SAVI | $1.5 \times \frac{(NIR-\text{Red})}{NIR+\text{Red}+0.5}$ | Soil Adjusted Vegetation Index |
| | EVI | $2 \times \frac{(NIR-\text{Red})}{NIR+6\times\text{Red}-7.5\times\text{Blue}+1}$ | Enhanced Vegetation Index |
| | NDWI | $\frac{\text{Green}-\text{NIR}}{\text{Green}+\text{NIR}}$ | Normalized Difference Water Index |
| | GNDVI | $\frac{\text{NIR}-\text{Green}}{\text{NIR}+\text{Green}}$ | Green Normalized Difference Vegetation Index |
| | RENDVI | $\frac{\text{NNIR}-\text{VRE2}}{\text{NNIR}+\text{VRE2}}$ | Red Edge Normalized Difference Vegetation Index |
| | NBR | $\frac{\text{NIR}-\text{SWIR2}}{\text{NIR}+\text{SWIR2}}$ | Normalized Burn Ratio |
| | NDSI | $\frac{\text{Green}-\text{SWIR1}}{\text{Green}+\text{SWIR1}}$ | Normalized Difference Snow Index |
| Sentinel-1 SAR | VH, VV | - | Sentinel-1 linear Polarizations |
| | Span | $\lvert VV\rvert^2 + \lvert VH\rvert^2$ | Sentinel-1 total scattered power |
| | Ratio | $\frac{VV}{VH}$ | Sentinel-1 cross-polarization ratio |
| | RVI | $\frac{VH\times 4}{VH+VV}$ | Radar Vegetation Index |
| GEDI | RH95 | - | Relative Height |
| MERIT Hydro-Hydrography | Flow | $F_{out} = F_{in} + F_{local}$ | Flow accumulation, where $F_{in}$ is flow received and $F_{local}$ is flow produced |
| | HAND | $H_{point} - H_{drainage}$ | Height Above Nearest Drainage, where $H_{point}$ is the DEM elevation and $H_{drainage}$ is the drainage elevation |
| ERA5–Climate | Precip | - | Average monthly precipitation |
| | Temp | - | Average monthly temperature |
| SRTM Topographic DEM | Elevation | - | Height of elevation |
| | Slope | $\sqrt{D_x^2 + D_y^2}$ | Rate of change of elevation, where $D_x$ is horizontal distance and $D_y$ is vertical distance |
| | Aspect | $\arctan\left(\frac{dy}{dx}\right)$ | Direction of slope |

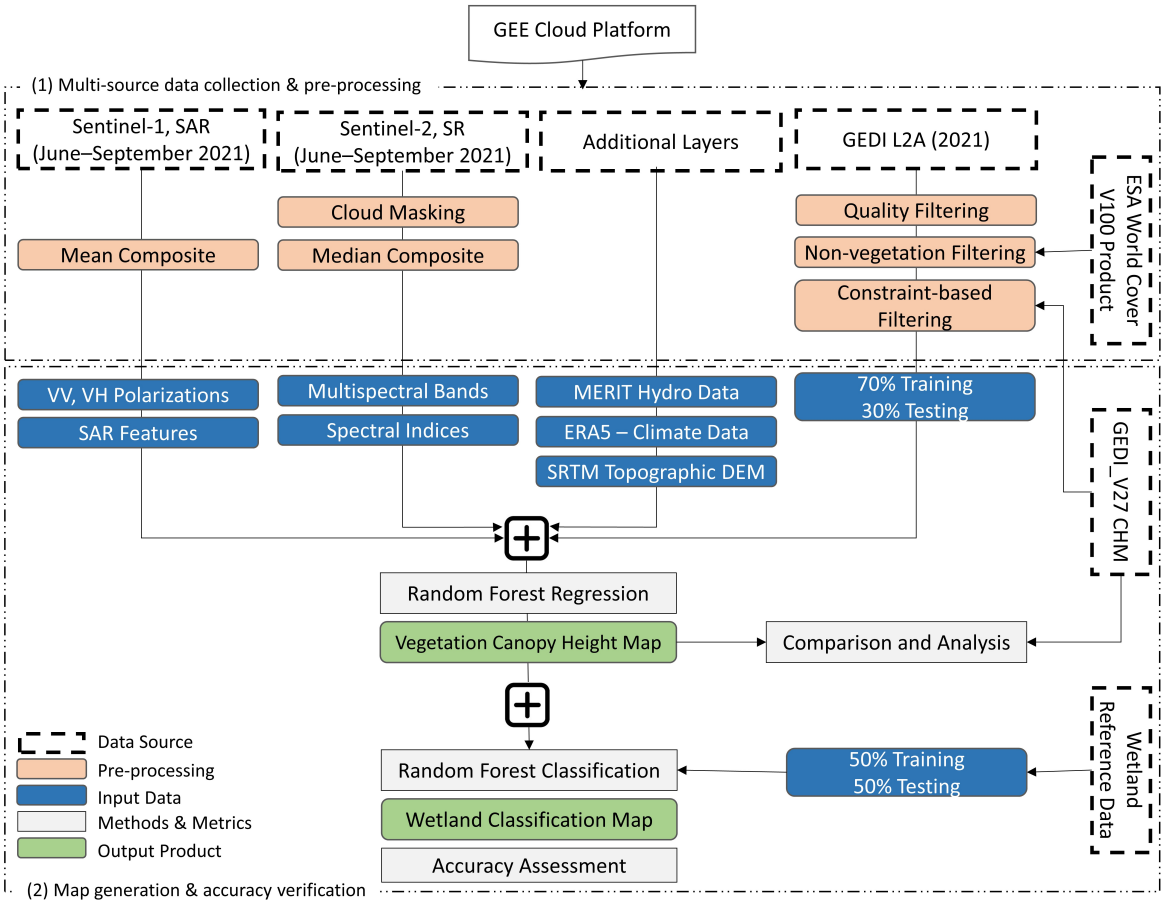



Figure 6.3: A representation of the approach developed for VCH and wetland mapping utilizing multi-source and multi-sensor remote sensing data.

### 6.5.2 Vegetation Canopy Height (VCH) Model

While several ML algorithms are available in the literature, Random Forest (RF), as a good 'first-choice algorithm', is proving to be a fairly accurate, computationally efficient, and easy-to-use ML algorithm for classification and regression compared to other methods [48]. RF is a versatile and robust method capable of handling the complex non-linear relations between the input and target variables [49]. It requires less data setup and model parameterization and makes fewer assumptions, making it suitable for high-dimensional datasets. The bootstrapping technique and parallel computing in RF reduce prediction error and accelerate the process [50]. Importantly, the RF algorithm offers a mechanism for estimating variable importance, enabling researchers to identify the most influential remote sensing features for accurate mapping.

Despite being able to penetrate the canopy to reach the ground and measure the height of the canopy, there are spatial discontinuities in GEDI footprints across the Earth's surface. The ancillary optical or SAR remote sensing datasets are often integrated to generate spatially continuous and consistent canopy height maps [32]. However, it should be noted that the method for predicting canopy height may not always be accurate due to factors such as the saturation of spectral reflectance in complex vegetation structures. This study includes additional important features in interpolating GEDI points to overcome such issues in retrieving canopy height and making the prediction model more stable.

As listed in Table 6.4, the inputs to the RF regression model consisted of 30 independent variables: 18 optical surface reflectance bands and spectral indices; 5 SAR-derived features; 2 MERIT Hydrography bands; 2 ERA5–Climate bands; and 3 SRTM DEM-derived features. A stacked GeoTiff image was exported with these multi-source metrics stored as separate bands. By incorporating these diverse inputs, the RF approach interpolated the pre-processed and filtered LiDAR footprints from space-borne GEDI into a surface covering the entire wetland areas.

To enhance the performance of the RF model in VCH prediction, a sensitivity analysis was conducted using $R^2$ values to optimize the hyperparameters. Within the GEE platform, RF allows for the adjustment of several hyperparameters, including the number of decision trees (nTree), minimum leaf population, number of variables per split, and bag fraction. The sensitivity analysis was initially performed on the Deer Lake pilot site, and the findings were subsequently applied to the remaining pilot sites. The analysis of model accuracy demonstrated the influence of varying hyperparameter values on the RF model's performance. For instance, adjusting nTree from 100 to 250 resulted in a change in model accuracy from 0.62 to 0.69. However, it was observed that an optimum nTree value of approximately 200 yielded the same accuracy as a larger nTree. Specifically, a negative correlation was observed between $R^2$ and the minimum leaf population. Lower minimum leaf populations were found to achieve higher model accuracy, reaching up to 0.61. On the other hand, the variables per split and bag fraction parameters demonstrated positive correlations with $R^2$. Increasing the number of variables per split and incorporating larger fractions of samples for training the model improved the accuracy. The optimal values for these two parameters were determined to be 15 and 0.8, respectively.

### 6.5.3 Wetland Cover Classification

To create a high-accuracy wetland classification map, the VCH layer was integrated with the feature set mentioned in Section 6.4. This comprehensive approach equipped the RF classification model with 31 independent variables, optimizing the inputs for wetland mapping. By integrating these features, we aimed to capture the unique surface structure and hydrological characteristics of wetland types for better discrimination. To further explore the classification performance, we also employed the CART (Classification and Regression Trees) method as an alternative approach, and its classification results were compared with those of the RF model.

### 6.5.4 Accuracy Assessment

The accuracy assessment of VCH maps was conducted by calculating key statistical parameters employing three regression error metrics: Coefficient of determination ($R^2$), Root Mean Squared Error (RMSE), and Mean Absolute Error (MAE) based on canopy height reference data from GEDI products. Below are the expressions for these metrics:

$$R^2 = 1 - \frac{\sum_{i=1}^{n}(x_i - y_i)^2}{\sum_{i=1}^{n}(y_i - \bar{y})^2} \tag{6.1}$$

$$RMSE = \sqrt{\frac{1}{n}\sum_{i=1}^{n}(x_i - y_i)^2} \tag{6.2}$$

$$MAE = \frac{1}{n}\sum_{i=1}^{n}|x_i - y_i|, \tag{6.3}$$

where the variables $x$, $y$, and $\bar{y}$ represent the modeled canopy height, reference values, and the average of reference values, respectively.

Additionally, the accuracy of classification maps was assessed using widely recognized metrics: Overall Accuracy (OA), Kappa Coefficient (KC), and F1-score. The formulas for these metrics are provided below:

$$OA = \frac{TP + TN}{TP + FN + FP + TN} \tag{6.4}$$

$$F1 = \frac{2TP}{2TP + FP + FN} \tag{6.5}$$

$$KC = \frac{PCC - P_e}{1 - P_e}, \tag{6.6}$$

$$PCC = \frac{TN + TP}{N}, \tag{6.7}$$

$$P_e = \frac{(TP + FP)(TP + FN) + (FN + TN)(FP + TN)}{N^2}, \tag{6.8}$$

where $N = TP + FP + TN + FN$, with $TP/FP$ denoting true/false positives, and similarly, $TN/FN$ denoting true/false negatives.

## 6.6 Experimental Results

### 6.6.1 VCH Maps and Validation

As seen in Figure 6.4, the visual comparison of the generated VCH maps reveals a clear representation of covered wetland height variations. The study areas differ in their characteristics with respect to species composition, site quality (e.g., topography, climate, and hydrology), and slightly varying ranges of canopy heights. The possible inferences for better performance and relatively poor performance of the geostatistical-interpolated VCH maps are discussed below.

To validate the VCH, predictions were compared to the observed and independent testing part of RH95 values for each study site and quantified by deriving statistical measures (i.e., $R^2$, RMSE, and MAE). In addition, a scatterplot was drawn in relation to GEDI RH95 data (i.e., observed values) and modeled canopy stand height data (i.e., predicted values) to assess systematic over/under predictions across regions along the range of RH95. The obtained scatter plots with the statistical values are shown in Figure 6.5.

It is worth mentioning that RH95 does not equate to canopy height. In recent years, several studies have investigated the limitations and uncertainties associated with GEDI observations. For example, refs. [51, 5] examined the effect of possible horizontal geolocation inaccuracies and uncertainties on the reliability of GEDI's forest canopy height estimates. Overall, incorrect ground elevation identification, atmospheric attenuation and thick cloud cover, topography within the footprint, and

uncertainty in SNR at the top of the canopy may all result in variations between canopy height estimates and RH95. These factors lead to instability in the accuracy of GEDI observations in complex structure wetland areas. Whereas this study provided good-quality data, some inherent errors remain. Accordingly, even with a high level of model accuracy, the results obtained may still be subject to potential errors. In the following discussion, we will explore these potential errors and their impact on the results drawn from our analysis.

The discrepancy between the 25 m width of GEDI's observation footprints and the upsampled Sentinel-1 and -2 10 m pixel size can cause issues with straightforward footprint-to-pixel matching. This means that the points in the area observed by GEDI would be sparse when directly matching with the higher resolution imagery from Sentinel-1 and -2; however, vegetation canopy height may vary greatly on adjacent pixels. This spatial misalignment may partly explain why, as seen in Figure 6.5, the prediction model does not fully capture the variability in canopy height observed by GEDI. These discrepancies can ultimately affect classification accuracy, especially in heterogeneous wetland environments. Specifically, neither GEDI footprints nor interpolated canopy height maps can be an exact representation of VCH, and in-situ records are required to decrease the uncertainties and diminish the effect of these technical issues. To explore the potential improvements in generating canopy height maps in this study, the GEDI validation data were compared with the GEDI-V27 global forest canopy height map, which specifically includes only integer values (see Figure 6.6).

According to Figure 6.6, it was found that, for all investigated sites, the VCH maps produced in this study exhibit a superior performance to the reference GEDI-V27 data. The limited accuracy of the GEDI-V27 data can be attributed to two primary factors; on the one hand, it is attributed to the bias of geographic positioning, particularly in complex areas with significant elevation variations, which leads to a lower accuracy of the GEDI-V27 product. On the other hand, the GEDI-V27 product was generated based on a global study area; therefore, the accuracy is lower in small-scale test sites. As an example, for the Deer Lake site, the proposed approach produced a VCH map with an $R^2$ of 0.69, an RMSE of 1.51 m, and an MAE of 1.26 m (Figure 6.5) as compared to the GEDI-V27 product with an $R^2$ of 0.38, an RMSE of 3.10 m, and an MAE of 2.45 m (Figure 6.6). Due to the absence of in-situ measurements of canopy height, our study was unable to further investigate the causes for these differences,

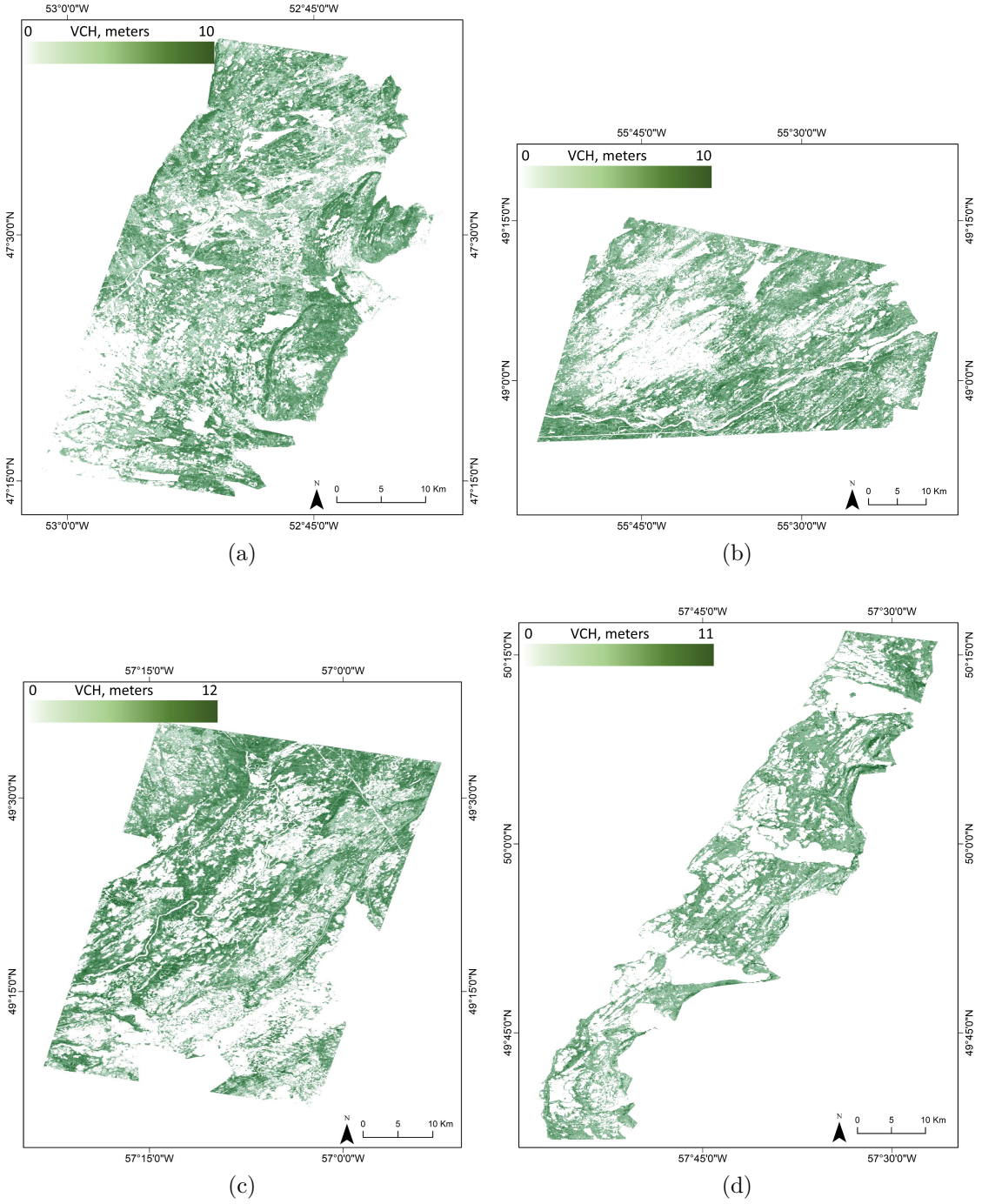



Figure 6.4: VCH maps for the year 2021 were produced through the integration of GEDI data (June–September 2021) and multi-source EO datasets for (**a**) St. John's, (**b**) Grand Falls-Windsor, (**c**) Deer Lake, and (**d**) Gros Morne.

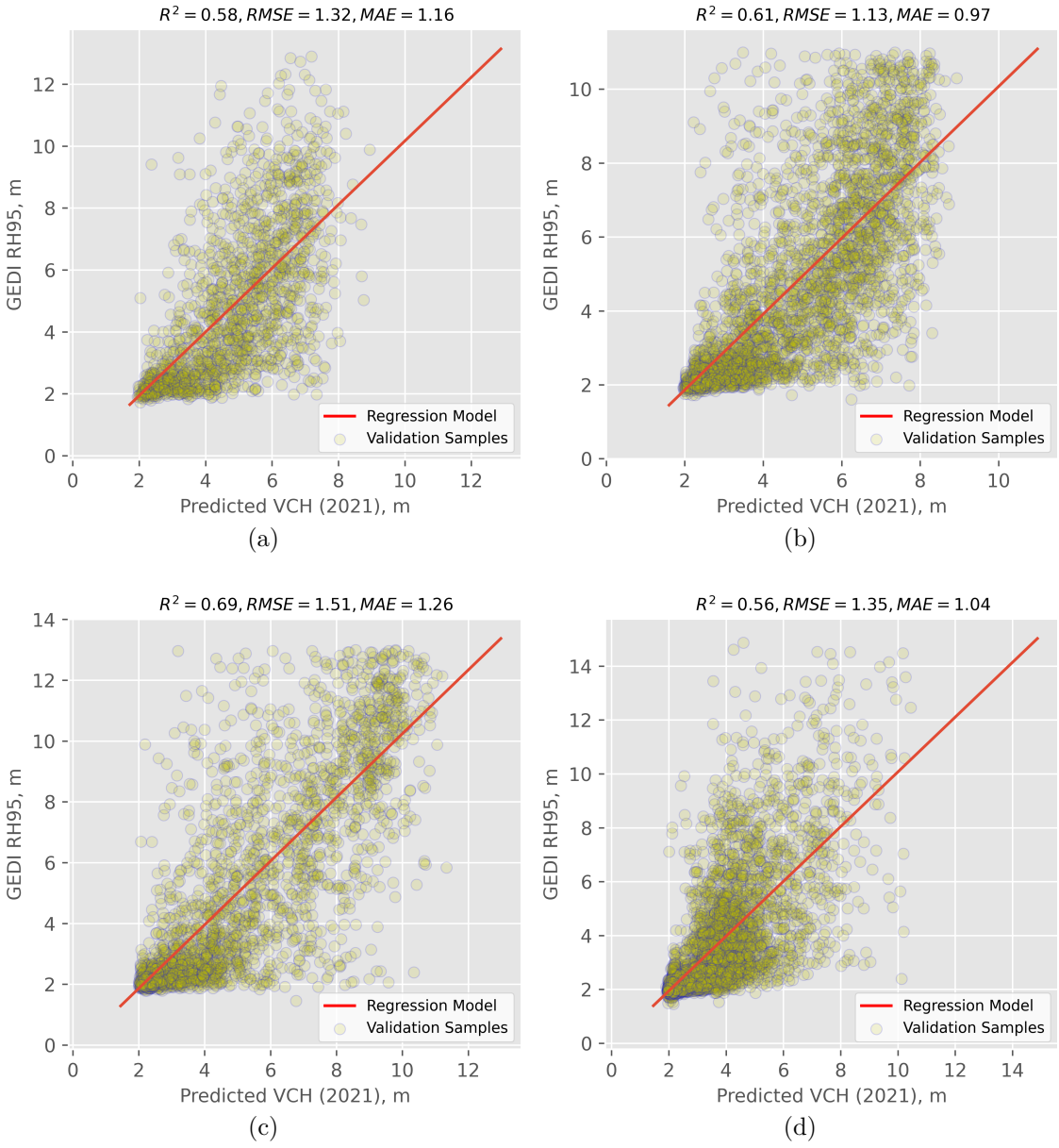



Figure 6.5: The correlation between the generated VCH and GEDI validation data for the four pilot sites in the study area: (**a**) St. John's, (**b**) Grand Falls-Windsor, (**c**) Deer Lake, and (**d**) Gros Morne. The figures show the scatter plots of the generated VCH data against the GEDI validation data for each of the four pilot sites. Each plot includes individual data points (dots) and a best-fit line (solid red line) between the two datasets.

thereby restricting the progress in increasing the accuracy of the VCH maps.

### 6.6.2 Wetland Classification Map and Validation

Following the validation of the generated VCH maps with GEDI data, the height layers were stacked with a set of features to provide high-accuracy wetland classification maps. The classification maps illustrating eight wetland and non-wetland covers (i.e., bog, fen, swamp, marsh, deep water, forest, pasture, and urban) are shown in Figure 6.7.

One of the primary objectives of this study was to assess how well the geostatistical-interpolated VCH from space-borne LiDAR data affects wetland mapping. Initially, the classification was performed with stacked inputs consisting of all variables/features, excluding VCH maps. The results of this initial classification, based on the RF method, yielded an OA range of 82.72% to 88.69% across all wetland sites. The inclusion of the VCH variable derived from GEDI LiDAR increased the number of correctly identified wetland classes, leading to an OA ranging from 86.11% to 93.45%. Adding VCH to the mapping workflow significantly improved the classification results in each area of interest, as evidenced by the comparison between OA values obtained with or without VCH. For instance, at the Deer Lake pilot site, the accuracy increased from 88.69% without VCH to 93.45% with VCH combined with all data sources. This notable improvement in wetland classification demonstrates the importance of integrating GEDI-derived VCH in the mapping process.

Both sets of classification results obtained from the RF and CART models are included in Table 6.5 for a comprehensive comparison.

The efficiency of VCH in wetland mapping is further confirmed by investigating the variable importance values in the RF model. In Figure 6.8, each predictor's importance value was determined to indicate the most significant features in the wetland classification process. As seen in Figure 6.8a, there are some general trends for all pilot sites, although some differences exist as well. For instance, the spectral bands of Sentinel-2 show the highest importance for St. John's and the lowest for Gros Morne pilot sites. Specifically, VCH is among the most significant factors in mapping wetland areas in our study sites. It is ranked in the top three important features along with Elevation and VRE1; see Figure 6.8b.

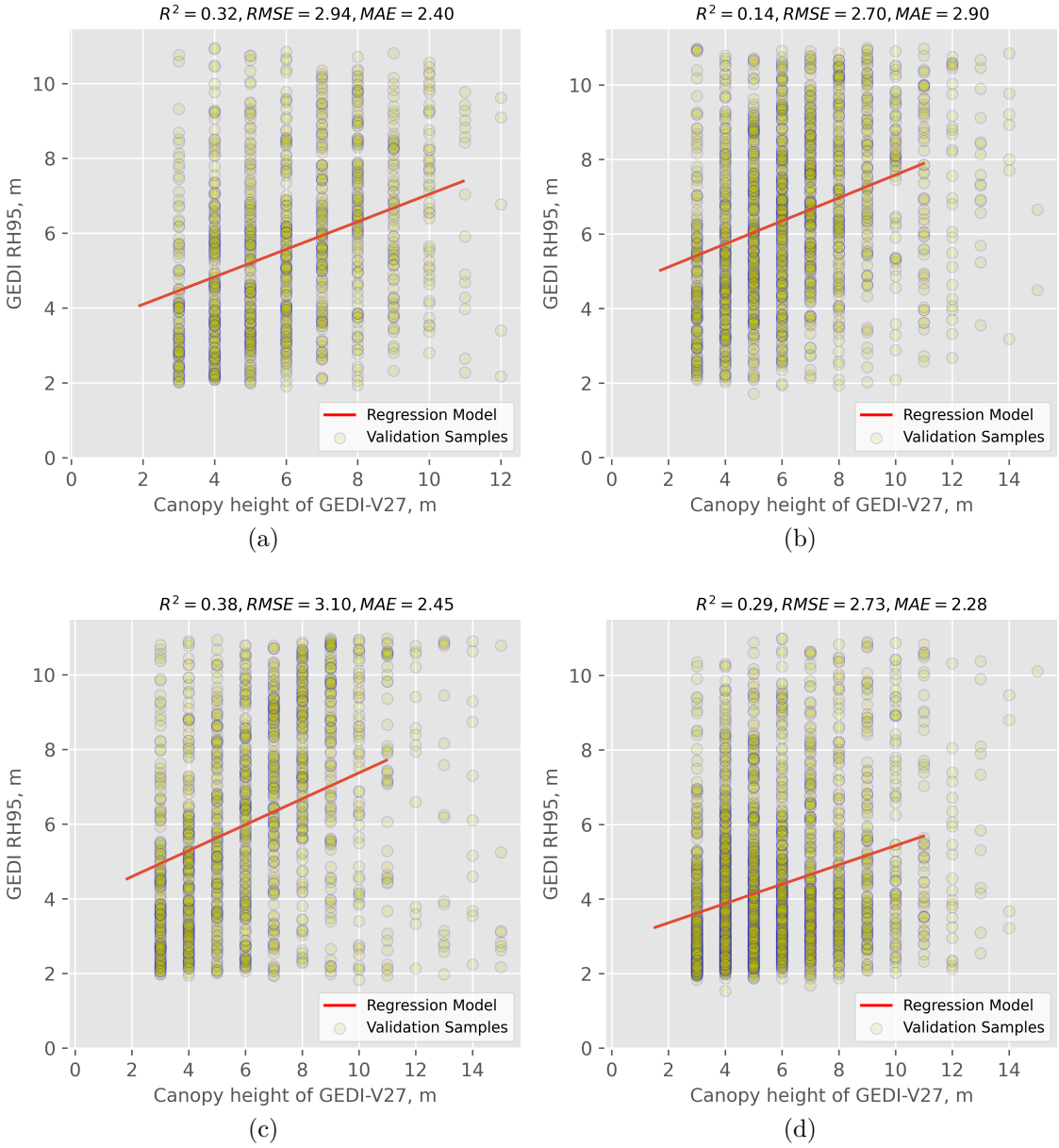



Figure 6.6: The correlation between the GEDI RH95 observations and GEDI-V27 in wetland areas using the same validation samples of our methodology: (**a**) St. John's, (**b**) Grand Falls-Windsor, (**c**) Deer Lake, and (**d**) Gros Morne. The figures show the scatter plots of the GEDI-V27 canopy height data against the GEDI validation data for each of the four pilot sites. Each plot includes individual data points (dots) and a best-fit line (solid red line) between the two datasets.

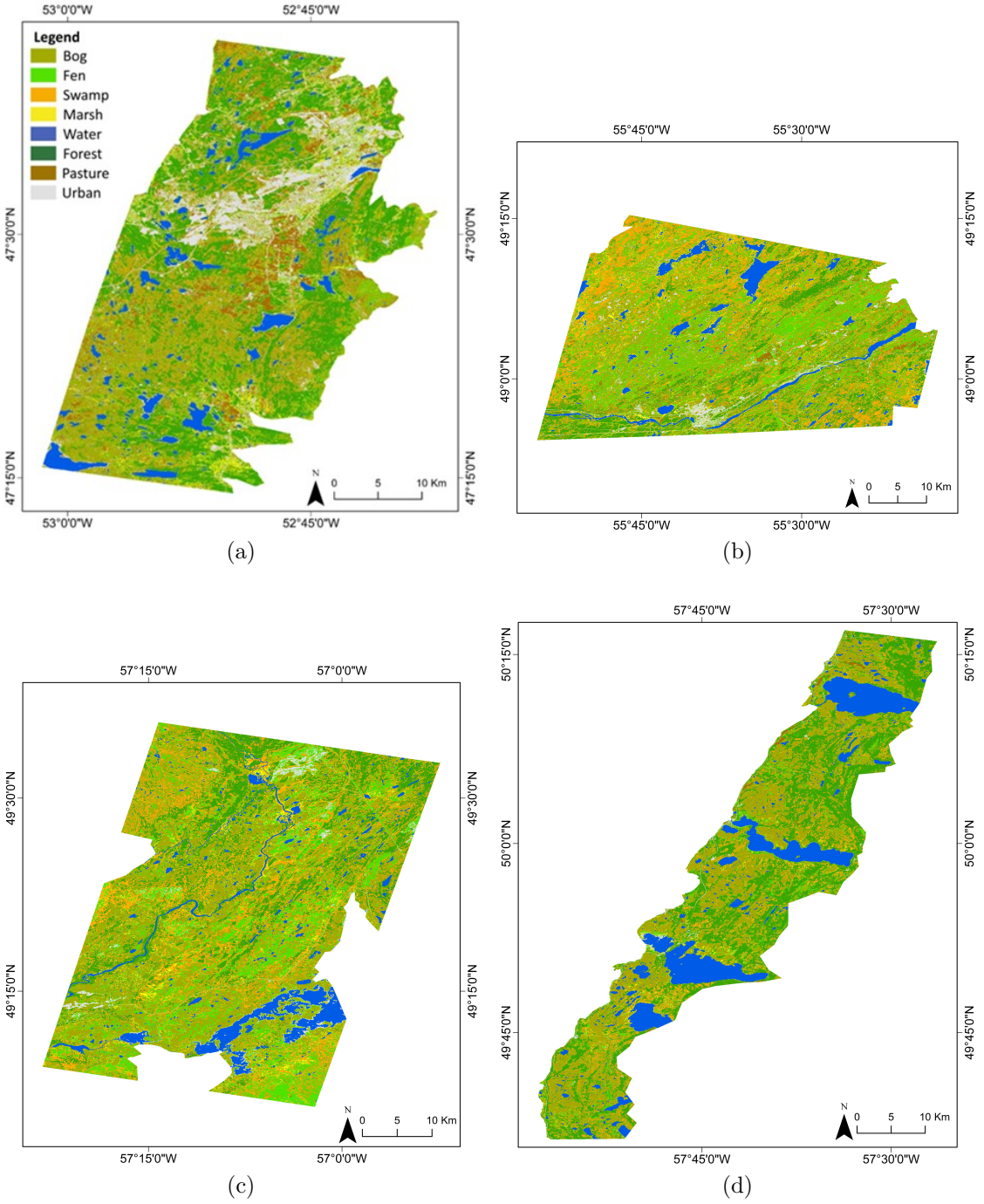
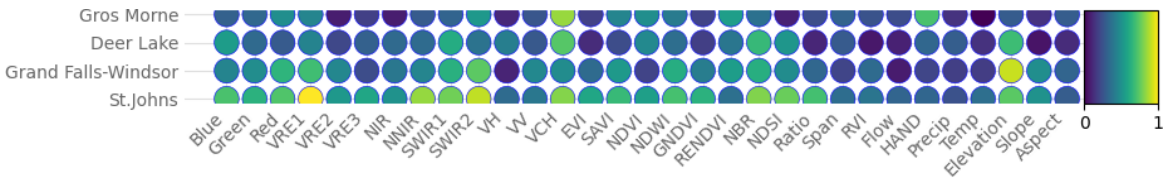


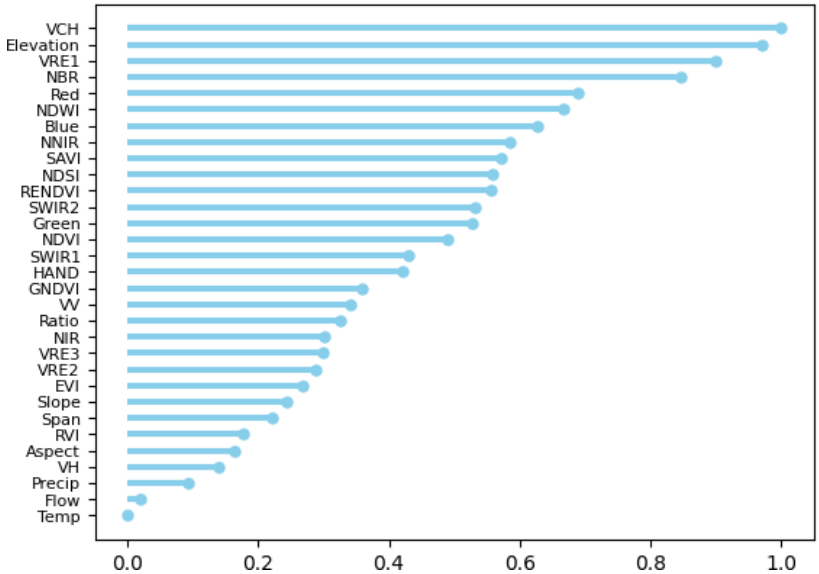

Figure 6.7: Wetland classification maps for the year 2021 were produced through the integration of VCH and metrics/features derived from multi-source EO datasets for (**a**) St. John's, (**b**) Grand Falls-Windsor, (**c**) Deer Lake, and (**d**) Gros Morne.

Table 6.5: Validation results for RF and CART models.

| Pilot Site | Method | VCH Included | | | VCH Excluded | |
|---|---|---|---|---|---|---|
| | | OA (%) | Kappa | F1-Score | OA (%) | Kappa |
| St. John's | RF | 91.66 | 0.89 | 0.86 | 86.22 | 0.82 |
| | CART | 88.09 | 0.83 | 0.83 | 82.87 | 0.79 |
| Grand Falls-Windsor | RF | 86.11 | 0.83 | 0.81 | 84.80 | 0.81 |
| | CART | 84.80 | 0.82 | 0.80 | 79.62 | 0.76 |
| Deer Lake | RF | 93.45 | 0.92 | 0.88 | 88.69 | 0.86 |
| | CART | 88.70 | 0.86 | 0.84 | 85.21 | 0.83 |
| Gros Morne | RF | 90.91 | 0.85 | 0.84 | 82.72 | 0.73 |
| | CART | 84.21 | 0.80 | 0.75 | 78.88 | 0.72 |




(a)




(b)

Figure 6.8: (**a**) The normalized importance of factors used in the wetland classification process of pilot sites, (**b**) the average value of the variables' importance.

In summary, according to validation results, the estimated VCH maps, derived from the integration of multi-source and multi-sensor data, represent a significant advancement in the characterization of wetland ecosystems. The spatially explicit information provided by these maps offers valuable insights into the complex dynamics of vegetation structure and land cover within our study areas. These considerations, in turn, contribute to a deeper understanding of ecosystem dynamics, biodiversity distribution, and land use patterns. Moreover, the integration of VCH maps adds an additional layer of enhancement to wetland mapping, boosting accuracy and reliability.

## 6.7 Discussion

### 6.7.1 Leveraging GEDI Data for Large-Scale VCH Mapping

Utilizing laser-based technology, the GEDI mission offers the capability to produce canopy height maps at both high resolution and on a large-scale [52]. This groundbreaking approach provides a multitude of advantages for VCH compared to alternative methods [39]. In the following, some of the key advantages of GEDI data and the opportunities for vegetation studies are highlighted:

- GEDI data yield the 3D structure of the Earth with 25 m diameter footprints [52], ensuring fine spatial resolution for accurately portraying landscape topography and VCH.
- Unlike passive sensor satellite-based methods, GEDI's laser instrument penetrates dense canopies, providing height measurements even in heavily vegetated regions [53]. This unique capability facilitates the creation of VCH maps as closely as possible to the real world.
- GEDI's fine spatial resolution, penetration ability through the dense canopies, and information on vertical vegetation structure make it a versatile tool for various applications, particularly large-scale VCH mapping.
- While airborne laser scanning (ALS) data may offer higher accuracy in VCH estimation, they present limitations in terms of coverage and cost. GEDI's

space-borne LiDAR, providing global coverage, emerges as a valuable resource for VCH measurements in regions with limited ALS data availability. Additionally, the cost-effectiveness and consistent dataset provided by GEDI since 2019 eliminate concerns about aligning and matching data from various sources collected at different times. This ensures a standardized approach to estimating VCH.

### 6.7.2 Leveraging VCH Data Across Environmental Domains

The VCH data play a crucial role in mapping wetlands, especially in complex and densely vegetated environments. In this study, we applied the integration of VCH with other EO data for wetland mapping across four distinct pilot sites in Newfoundland. The utilization of a 10 m GEDI-derived VCH map resulted in an average improvement of ≈5% improvement in OA and ≈0.07 in kappa considering all pilot sites.

This underscores the critical role of VCH as a fundamental tool for wetland mapping, providing valuable information on the structural characteristics of these ecosystems. The synergy achieved by integrating VCH maps with other remote sensing data notably enhances the precision of wetland class discrimination. As wetlands continue to face environmental pressures, the use of VCH, complemented by multi-sensor datasets, represents a robust approach for comprehensive wetland mapping, thereby supporting informed conservation and management strategies.

Beyond enhancing wetland mapping, GEDI measurements of canopy height, canopy vertical structures, and surface elevation have the potential application in various environmental and ecological domains [12, 54]:

- Forest structure and aboveground biomass estimation: these measurements provide valuable insights into forest canopy height and structure, enabling accurate estimation of biomass and carbon stocks in forests.
- Land surface dynamics: they can be used to monitor changes in land surface elevation, vegetation dynamics, water cycling processes, and terrain characteristics.
- Biodiversity conservation: these data aid in habitat mapping and characterizing, species distribution modeling, and biodiversity monitoring.

## 6.8 Conclusions

Accurate wetland mapping is important for effective conservation and restoration planning, as it is vital for monitoring efforts and developing emergency response strategies for natural disasters. This study focused on advancing wetland mapping through the integration of multi-source and multi-sensor remote sensing datasets via GEE. The objective was to introduce complementary EO data and assess their impact on enhancing wetland classification. Exploring GEDI footprints, Merit Hydro, and ERA5 data sources aimed to compensate for the shortcomings associated with relying solely on optical and SAR imagery. Transitioning to an advanced wetland characterization approach, VCH, serving as a representative structural variable, was assessed, and emerged as a key feature for wetland classification in this study. Importantly, optimizing VCH maps and other EO data sources demonstrated their responsiveness to wetland mapping tasks, yielding promising results. The efficiency of VCH was confirmed across all four pilot sites, affirming its effectiveness for wetland studies. While acknowledging that the VCH maps generated in this study are not the perfect representation of canopy heights, comparative analyses of classification maps indicate progress in achieving high-accuracy wetland maps using VCH. This suggests that the near-to-real state estimation of wetlands' canopy holds high potential for increasing wetland mapping accuracy. This conclusion holds true across all study sites, emphasizing the need to extend the research to include the implementation of VCH maps for large-scale wetland mapping (e.g., provincial scale) in future endeavors. Supportive airborne LiDAR data and in-situ measurements are also necessary for a comprehensive assessment and validation of VCH maps.

## 6.9 References

[1] E. Adam, O. Mutanga, and D. Rugege, "Multispectral and hyperspectral remote sensing for identification and mapping of wetland vegetation: a review," *Wetlands ecology and management*, vol. 18, pp. 281–296, 2010.

[2] M. Amani, S. Mahdavi, M. Kakooei, A. Ghorbanian, B. Brisco, E. R. DeLancey,

S. Toure, and E. L. Reyes, "Wetland change analysis in alberta, canada using four decades of landsat imagery," *IEEE Journal of Selected Topics in Applied Earth Observations and Remote Sensing*, vol. 14, pp. 10314–10335, 2021.

[3] M. Chen, X. Xu, X. Wu, and C. Mi, "Centennial-scale study on the spatial-temporal evolution of riparian wetlands in the yangtze river of china," *International Journal of Applied Earth Observation and Geoinformation*, vol. 113, p. 102874, 2022.

[4] M. Mahdianpari, B. Salehi, F. Mohammadimanesh, S. Homayouni, and E. Gill, "The first wetland inventory map of newfoundland at a spatial resolution of 10 m using sentinel-1 and sentinel-2 data on the google earth engine cloud computing platform," *Remote Sensing*, vol. 11, no. 1, p. 43, 2018.

[5] A. Liu, X. Cheng, and Z. Chen, "Performance evaluation of gedi and icesat-2 laser altimeter data for terrain and canopy height retrievals," *Remote Sensing of Environment*, vol. 264, p. 112571, 2021.

[6] M. Mahdianpari, H. Jafarzadeh, J. E. Granger, F. Mohammadimanesh, B. Brisco, B. Salehi, S. Homayouni, and Q. Weng, "A large-scale change monitoring of wetlands using time series landsat imagery on google earth engine: a case study in newfoundland," *GIScience & Remote Sensing*, vol. 57, no. 8, pp. 1102–1124, 2020.

[7] K. Peng, W. Jiang, P. Hou, Z. Wu, Z. Ling, X. Wang, Z. Niu, and D. Mao, "Continental-scale wetland mapping: A novel algorithm for detailed wetland types classification based on time series sentinel-1/2 images," *Ecological Indicators*, vol. 148, p. 110113, 2023.

[8] M. Jia, D. Mao, Z. Wang, C. Ren, Q. Zhu, X. Li, and Y. Zhang, "Tracking long-term floodplain wetland changes: A case study in the china side of the amur river basin," *International Journal of Applied Earth Observation and Geoinformation*, vol. 92, p. 102185, 2020.

[9] H. M. Pereira, S. Ferrier, M. Walters, G. N. Geller, R. H. Jongman, R. J. Scholes, M. W. Bruford, N. Brummitt, S. H. Butchart, A. Cardoso, *et al.*, "Essential biodiversity variables," *Science*, vol. 339, no. 6117, pp. 277–278, 2013.

[10] P. Vihervaara, A.-P. Auvinen, L. Mononen, M. Törmä, P. Ahlroth, S. Anttila, K. Böttcher, M. Forsius, J. Heino, J. Heliölä, *et al.*, "How essential biodiversity variables and remote sensing can help national biodiversity monitoring," *Global Ecology and Conservation*, vol. 10, pp. 43–59, 2017.

[11] S. Luo, C. Wang, F. Pan, X. Xi, G. Li, S. Nie, and S. Xia, "Estimation of wetland vegetation height and leaf area index using airborne laser scanning data," *Ecological Indicators*, vol. 48, pp. 550–559, 2015.

[12] E. Quiros, M.-E. Polo, and L. Fragoso-Campón, "Gedi elevation accuracy assessment: a case study of southwest spain," *IEEE Journal of Selected Topics in Applied Earth Observations and Remote Sensing*, vol. 14, pp. 5285–5299, 2021.

[13] O. Mutanga, E. Adam, and M. A. Cho, "High density biomass estimation for wetland vegetation using worldview-2 imagery and random forest regression algorithm," *International Journal of Applied Earth Observation and Geoinformation*, vol. 18, pp. 399–406, 2012.

[14] S. C. Popescu, K. Zhao, A. Neuenschwander, and C. Lin, "Satellite lidar vs. small footprint airborne lidar: Comparing the accuracy of aboveground biomass estimates and forest structure metrics at footprint level," *Remote Sensing of Environment*, vol. 115, no. 11, pp. 2786–2797, 2011.

[15] J. E. Houlahan, P. A. Keddy, K. Makkay, and C. S. Findlay, "The effects of adjacent land use on wetland species richness and community composition," *Wetlands*, vol. 26, no. 1, pp. 79–96, 2006.

[16] S. Van Beijma, A. Comber, and A. Lamb, "Random forest classification of salt marsh vegetation habitats using quad-polarimetric airborne sar, elevation and optical rs data," *Remote Sensing of Environment*, vol. 149, pp. 118–129, 2014.

[17] B. Fu, Y. Wang, A. Campbell, Y. Li, B. Zhang, S. Yin, Z. Xing, and X. Jin, "Comparison of object-based and pixel-based random forest algorithm for wetland vegetation mapping using high spatial resolution gf-1 and sar data," *Ecological indicators*, vol. 73, pp. 105–117, 2017.

[18] H. Jafarzadeh, M. Mahdianpari, and E. W. Gill, "Wet-gc: A novel multimodel

graph convolutional approach for wetland classification using sentinel-1 and 2 imagery with limited training samples," *IEEE Journal of Selected Topics in Applied Earth Observations and Remote Sensing*, vol. 15, pp. 5303–5316, 2022.

[19] B. Slagter, N.-E. Tsendbazar, A. Vollrath, and J. Reiche, "Mapping wetland characteristics using temporally dense sentinel-1 and sentinel-2 data: A case study in the st. lucia wetlands, south africa," *International Journal of Applied Earth Observation and Geoinformation*, vol. 86, p. 102009, 2020.

[20] W. Qi, S.-K. Lee, S. Hancock, S. Luthcke, H. Tang, J. Armston, and R. Dubayah, "Improved forest height estimation by fusion of simulated gedi lidar data and tandem-x insar data," *Remote Sensing of Environment*, vol. 221, pp. 621–634, 2019.

[21] X. Liu, Y. Su, T. Hu, Q. Yang, B. Liu, Y. Deng, H. Tang, Z. Tang, J. Fang, and Q. Guo, "Neural network guided interpolation for mapping canopy height of china's forests by integrating gedi and icesat-2 data," *Remote Sensing of Environment*, vol. 269, p. 112844, 2022.

[22] I. Dorado-Roda, A. Pascual, S. Godinho, C. A. Silva, B. Botequim, P. Rodríguez-Gonzálvez, E. González-Ferreiro, and J. Guerra-Hernández, "Assessing the accuracy of gedi data for canopy height and aboveground biomass estimates in mediterranean forests," *Remote Sensing*, vol. 13, no. 12, p. 2279, 2021.

[23] L. Duncanson, A. Neuenschwander, S. Hancock, N. Thomas, T. Fatoyinbo, M. Simard, C. A. Silva, J. Armston, S. B. Luthcke, M. Hofton, *et al.*, "Biomass estimation from simulated gedi, icesat-2 and nisar across environmental gradients in sonoma county, california," *Remote Sensing of Environment*, vol. 242, p. 111779, 2020.

[24] J. N. Hird, E. R. DeLancey, G. J. McDermid, and J. Kariyeva, "Google earth engine, open-access satellite data, and machine learning in support of large-area probabilistic wetland mapping," *Remote sensing*, vol. 9, no. 12, p. 1315, 2017.

[25] W. Turner, C. Rondinini, N. Pettorelli, B. Mora, A. K. Leidner, Z. Szantoi, G. Buchanan, S. Dech, J. Dwyer, M. Herold, *et al.*, "Free and open-access satellite data are key to biodiversity conservation," *Biological Conservation*, vol. 182, pp. 173–176, 2015.

[26] P. Pérez-Cutillas, A. Pérez-Navarro, C. Conesa-García, D. A. Zema, and J. P. Amado-Álvarez, "What is going on within google earth engine? a systematic review and meta-analysis," *Remote Sensing Applications: Society and Environment*, vol. 29, p. 100907, 2023.

[27] H. A. Zurqani, C. J. Post, E. A. Mikhailova, M. A. Schlautman, and J. L. Sharp, "Geospatial analysis of land use change in the savannah river basin using google earth engine," *International journal of applied earth observation and geoinformation*, vol. 69, pp. 175–185, 2018.

[28] M. Amani, A. Ghorbanian, S. A. Ahmadi, M. Kakooei, A. Moghimi, S. M. Mirmazloumi, S. H. A. Moghaddam, S. Mahdavi, M. Ghahremanloo, S. Parsian, *et al.*, "Google earth engine cloud computing platform for remote sensing big data applications: A comprehensive review," *IEEE Journal of Selected Topics in Applied Earth Observations and Remote Sensing*, vol. 13, pp. 5326–5350, 2020.

[29] H. Tamiminia, B. Salehi, M. Mahdianpari, L. Quackenbush, S. Adeli, and B. Brisco, "Google earth engine for geo-big data applications: A meta-analysis and systematic review," *ISPRS Journal of Photogrammetry and Remote Sensing*, vol. 164, pp. 152–170, 2020.

[30] D. Poursanidis and N. Chrysoulakis, "Remote sensing, natural hazards and the contribution of esa sentinels missions," *Remote Sensing Applications: Society and Environment*, vol. 6, pp. 25–38, 2017.

[31] F. Mohseni, M. Amani, P. Mohammadpour, M. Kakooei, S. Jin, and A. Moghimi, "Wetland mapping in great lakes using sentinel-1/2 time-series imagery and dem data in google earth engine," *Remote Sensing*, vol. 15, no. 14, p. 3495, 2023.

[32] M. Torresani, D. Rocchini, A. Alberti, V. Moudrỳ, M. Heym, E. Thouverai, P. Kacic, and E. Tomelleri, "Lidar gedi derived tree canopy height heterogeneity reveals patterns of biodiversity in forest ecosystems," *Ecological Informatics*, vol. 76, p. 102082, 2023.

[33] S. P. Healey, Z. Yang, N. Gorelick, and S. Ilyushchenko, "Highly local model calibration with a new gedi lidar asset on google earth engine reduces landsat forest height signal saturation," *Remote Sensing*, vol. 12, no. 17, p. 2840, 2020.

[34] W. Qi, S. Saarela, J. Armston, G. Ståhl, and R. Dubayah, "Forest biomass estimation over three distinct forest types using tandem-x insar data and simulated gedi lidar data," *Remote Sensing of Environment*, vol. 232, p. 111283, 2019.

[35] C. Wang, A. J. Elmore, I. Numata, M. A. Cochrane, L. Shaogang, J. Huang, Y. Zhao, and Y. Li, "Factors affecting relative height and ground elevation estimations of gedi among forest types across the conterminous usa," *GIScience & Remote Sensing*, vol. 59, no. 1, pp. 975–999, 2022.

[36] N. C. Coops, P. Tompalski, T. R. Goodbody, M. Queinnec, J. E. Luther, D. K. Bolton, J. C. White, M. A. Wulder, O. R. van Lier, and T. Hermosilla, "Modelling lidar-derived estimates of forest attributes over space and time: A review of approaches and future trends," *Remote Sensing of Environment*, vol. 260, p. 112477, 2021.

[37] M. Musthafa, G. Singh, and P. Kumar, "Comparison of forest stand height interpolation of gedi and icesat-2 lidar measurements over tropical and sub-tropical forests in india," *Environmental Monitoring and Assessment*, vol. 195, no. 1, p. 71, 2023.

[38] D. Zanaga, R. Van De Kerchove, W. De Keersmaecker, N. Souverijns, C. Brockmann, R. Quast, J. Wevers, A. Grosu, A. Paccini, S. Vergnaud, *et al.*, "Esa worldcover 10 m 2020 v100. 2021," 2021. Available online: https://developers.google.com/earth-engine/datasets/catalog/ESA_WorldCover_v100 (1 November 2023).

[39] P. Potapov, X. Li, A. Hernandez-Serna, A. Tyukavina, M. C. Hansen, A. Kommareddy, A. Pickens, S. Turubanova, H. Tang, C. E. Silva, *et al.*, "Mapping global forest canopy height through integration of gedi and landsat data," *Remote Sensing of Environment*, vol. 253, p. 112165, 2021.

[40] D. Yamazaki, D. Ikeshima, J. Sosa, P. D. Bates, G. H. Allen, and T. M. Pavelsky, "Merit hydro: A high-resolution global hydrography map based on latest topography dataset," *Water Resources Research*, vol. 55, no. 6, pp. 5053–5073, 2019.

[41] P. Lin, M. Pan, H. E. Beck, Y. Yang, D. Yamazaki, R. Frasson, C. H. David,

M. Durand, T. M. Pavelsky, G. H. Allen, *et al.*, "Global reconstruction of naturalized river flows at 2.94 million reaches," *Water resources research*, vol. 55, no. 8, pp. 6499–6516, 2019.

[42] S. Shin, Y. Pokhrel, D. Yamazaki, X. Huang, N. Torbick, J. Qi, S. Pattanakiat, T. Ngo-Duc, and T. D. Nguyen, "High resolution modeling of river-floodplain-reservoir inundation dynamics in the mekong river basin," *Water Resources Research*, vol. 56, no. 5, p. e2019WR026449, 2020.

[43] T. K. Peucker and D. H. Douglas, "Detection of surface-specific points by local parallel processing of discrete terrain elevation data," *Computer Graphics and image processing*, vol. 4, no. 4, pp. 375–387, 1975.

[44] A. D. Nobre, L. A. Cuartas, M. Hodnett, C. D. Rennó, G. Rodrigues, A. Silveira, and S. Saleska, "Height above the nearest drainage–a hydrologically relevant new terrain model," *Journal of Hydrology*, vol. 404, no. 1-2, pp. 13–29, 2011.

[45] J. Muñoz-Sabater, E. Dutra, A. Agustí-Panareda, C. Albergel, G. Arduini, G. Balsamo, S. Boussetta, M. Choulga, S. Harrigan, H. Hersbach, *et al.*, "Era5-land: A state-of-the-art global reanalysis dataset for land applications," *Earth system science data*, vol. 13, no. 9, pp. 4349–4383, 2021.

[46] T. G. Farr, P. A. Rosen, E. Caro, R. Crippen, R. Duren, S. Hensley, M. Kobrick, M. Paller, E. Rodriguez, L. Roth, *et al.*, "The shuttle radar topography mission," *Reviews of geophysics*, vol. 45, no. 2, 2007.

[47] G. Falorni, V. Teles, E. R. Vivoni, R. L. Bras, and K. S. Amaratunga, "Analysis and characterization of the vertical accuracy of digital elevation models from the shuttle radar topography mission," *Journal of Geophysical Research: Earth Surface*, vol. 110, no. F2, 2005.

[48] L. Breiman, "Random forests," *Machine learning*, vol. 45, pp. 5–32, 2001.

[49] Z. Akhavan, M. Hasanlou, M. Hosseini, and H. McNairn, "Decomposition-based soil moisture estimation using uavsar fully polarimetric images," *Agronomy*, vol. 11, no. 1, p. 145, 2021.

[50] M. Belgiu and L. Drăguţ, "Random forest in remote sensing: A review of applications and future directions," *ISPRS journal of photogrammetry and remote sensing*, vol. 114, pp. 24–31, 2016.

[51] D. P. Roy, H. B. Kashongwe, and J. Armston, "The impact of geolocation uncertainty on gedi tropical forest canopy height estimation and change monitoring," *Science of Remote Sensing*, vol. 4, p. 100024, 2021.

[52] R. V. Leite, C. A. Silva, E. N. Broadbent, C. H. Do Amaral, V. Liesenberg, D. R. A. De Almeida, M. Mohan, S. Godinho, A. Cardil, C. Hamamura, *et al.*, "Large scale multi-layer fuel load characterization in tropical savanna using gedi spaceborne lidar data," *Remote Sensing of Environment*, vol. 268, p. 112764, 2022.

[53] S. Dhargay, C. S. Lyell, T. P. Brown, A. Inbar, G. J. Sheridan, and P. N. Lane, "Performance of gedi space-borne lidar for quantifying structural variation in the temperate forests of south-eastern australia," *Remote Sensing*, vol. 14, no. 15, p. 3615, 2022.

[54] H. Tamiminia, B. Salehi, M. Mahdianpari, and T. Goulden, "State-wide forest canopy height and aboveground biomass map for new york with 10 m resolution, integrating gedi, sentinel-1, and sentinel-2 data," *Ecological informatics*, vol. 79, p. 102404, 2024.

# Chapter 7

# Summary, Conclusions, and Future Outlook

## 7.1 Summary

In this thesis, the potential of various EO data sources was explored, including optical (Sentinel-2), SAR (Sentinel-1 and RCM), and LiDAR (GEDI), to discriminate and characterize wetland classes — bog, fen, marsh, swamp, and shallow-water — in Canada. The investigation assessed the strengths and limitations of these data types and their derived features, providing an in-depth comparison to evaluate their suitability for distinguishing among closely related wetland classes. Through this comparative analysis, the thesis contributes to the literature on wetland mapping by enhancing the understanding of EO data selection and the impact of feature extraction in land cover classification.

In pursuit of methodological advancements, in this thesis, several new techniques were introduced to address the challenges of land cover, particularly wetland mapping, and characterization. A multi-branch DL framework was developed, which combined both SAR and optical imagery to leverage their complementary strengths. This innovative DL approach underscored the importance of a multi-source data fusion framework, enabling higher classification accuracy and providing insights into spectral and textural variations unique to wetland classes. This framework also addressed limitations in traditional approaches by capturing distinct surface characteristics observable

only through SAR or optical bands.

A key innovation in this thesis was the application of CP-SAR data from the RCM, making this work one of the first in which CP-SAR's potential in wetland characterization has been examined. The study introduced a novel decomposition technique and a CPS descriptor, which represent a paradigm shift in the approach to wetland monitoring by capturing complex backscatter characteristics specific to wetland phenological stages. This advancement not only improves the accuracy of wetland classification but also opens up new possibilities for studying the phenological growth cycles of various wetland types. The integration of CP-SAR data brought a significant improvement in classification outcomes over traditional methods, especially when compared to single-polarization SAR approaches.

Additionally, the effectiveness of time-series CP-SAR data in capturing dynamic changes within wetland ecosystems was demonstrated. By utilizing its temporal aspect, this study provided insights into both seasonal variations and long-term trends within wetland classes, offering a more comprehensive understanding of the resilience and adaptability of these ecosystems. The findings suggest that time-series data enhances the capacity for wetland monitoring, ultimately supporting sustainable land management and conservation initiatives.

Furthermore, in this research, the role of wetland canopy height information, derived from LiDAR data, in refining classification accuracy was highlighted. The canopy height maps contributed valuable structural information, reinforcing class distinctions and enhancing overall land cover analysis. This incorporation of LiDAR demonstrated the advantages of integrating vertical structure data in EO analysis, emphasizing the importance of 3D information for complex landscapes like wetlands.

Overall, in this thesis, significant advancements in wetland mapping and characterization were presented, offering new techniques and insights that pave the way for future EO-based wetland studies. The findings underscore the value of integrating multi-source EO data and innovative analysis methods to overcome the inherent challenges of wetland classification. These contributions provide a foundation for continued research and practical applications in wetland conservation and management, potentially extending to other complex and diverse ecosystems.

## 7.2 Conclusions

In this thesis, multiple facets of wetland monitoring through RS were explored, incorporating various data types, AI techniques, and novel methodologies. A comprehensive review of the global landscape of RS-based wetland studies was conducted, identifying key trends and gaps. Over 344 papers from the past three decades were analyzed, highlighting the role of RS and AI tools in advancing wetland monitoring. This analysis provided insight into various subfields, including the geographical distribution of studies, the evolution of wetland mapping techniques, and the growing reliance on ML algorithms to improve classification accuracies. The findings underscored the importance of these technologies in addressing global environmental challenges, particularly in preserving and restoring wetlands.

In addition to the review, this thesis also contributed to the development of new approaches for wetland classification. It introduced a novel workflow combining GCN and CNN models, which demonstrated superior performance in classifying wetland types with minimal training data. By integrating SAR and optical imagery, the study highlighted the potential of multi-source data for accurate wetland mapping. The results revealed that advanced DL models could overcome challenges such as limited training samples, paving the way for more efficient and scalable wetland classification methods.

The use of CP-SAR data from the RCM to assess wetland scattering behavior was also investigated through the current research. It demonstrated the effectiveness of multi-temporal CP-SAR data in distinguishing wetland classes and revealed new findings regarding the unique scattering mechanisms of bogs, fens, and marshes. The development of a new scattering decomposition technique, $\mu - \chi$, outperformed traditional methods in wetland classification accuracy. This study demonstrated the sensitivity of CP-SAR data to changes in vegetation structure, offering a promising tool for monitoring wetland dynamics over time.

Furthermore, the thesis emphasized the importance of integrating multi-source data for wetland mapping. By incorporating complementary EO data such as GEDI footprints, Merit Hydro, and ERA5 datasets, this research highlighted the potential for enhancing wetland classification accuracy. Introducing a new structural variable, VCH, proved to be a critical feature for wetland classification, offering a promising

approach for more accurate wetland mapping. The results confirmed the utility of VCH across different wetland types, suggesting its potential for large-scale wetland mapping applications.

This thesis has contributed valuable methodologies for the effective monitoring and characterization of wetlands. By employing advanced RS technologies and AI models, it has made significant contributions to the field of wetland monitoring, offering new tools and perspectives for environmental researchers and policymakers. Moving forward, continued development and validation of these methods will be essential for operationalizing large-scale wetland monitoring systems, ensuring that these critical ecosystems are better protected and managed in the face of growing environmental pressures.

## 7.3 Future Outlook

### 7.3.1 Wetland Mapping Benchmark Dataset

Unfortunately, the current LULC datasets and available benchmark (BM) archives are not suitable for effective wetland mapping applications. These datasets often rely on data sources that do not adequately represent the diversity of wetland ecosystems, particularly in regions where wetlands exhibit significant variability. One key challenge is the inconsistency in category labels between computer vision models and RS-based BM archives. The differences in classification schemes often result in discrepancies when attempting to apply these datasets for accurate wetland delineation. Furthermore, the morphological and spectral similarities between wetland classes, such as freshwater and saltwater marshes, often lead to misclassifications in DL models trained on these existing datasets. This underscores the urgent need for a comprehensive and region-specific wetland BM dataset that can support the development of more accurate, automated mapping techniques. A robust wetland BM dataset would provide a foundation for the design and optimization of DL models, facilitating better discrimination of wetland types and improving the accuracy of wetland classification.

### 7.3.2 Wetlands in Tidal Zones

Wetlands in tidal zones, such as salt marshes and mangrove forests, present additional challenges in RS image classification. The dynamic nature of tidal wetlands—affected by shifting water levels, salinity gradients, and varying vegetation—introduces significant variability that is often difficult to capture with traditional satellite data. Moreover, the seasonal and tidal variations further complicate the accurate characterization of these wetlands over time. Current datasets often lack temporal and spatial resolution, failing to account for the fine-scale variations inherent in tidal wetlands. As a result, these wetlands are underrepresented in RS archives, leading to poor model performance when these regions are included in wetland classification tasks. Future efforts should prioritize the creation of high-resolution time-series datasets specifically focused on tidal zones, incorporating both optical and SAR data to capture their complex dynamics. This would allow for better representation and, ultimately, more accurate mapping of tidal wetland ecosystems, which are critical for biodiversity and carbon sequestration.

### 7.3.3 Toward Physics-Informed AI for Wetland Mapping

The application of advanced AI and DL models to wetland characterization faces limitations due to their insufficient incorporation of physical principles underlying RS data. While wetlands are complex and dynamic, current models typically treat RS inputs (e.g., SAR and optical imagery) as statistical data rather than interpreting them through the lens of physics, such as electromagnetic interactions with water and vegetation. This disconnect hampers generalization and reduces accuracy across wetland types and seasons. Many existing AI models neglect core RS physics, such as how electromagnetic waves interact with water, soil, and vegetation. This physics-agnostic approach can lead to reduced model performance, particularly in regions with varied environmental conditions. For instance, conventional DL models may fail to generalize effectively when applied across different geographies or seasons.

To address these limitations, there is a growing interest in physics-informed AI—an approach that incorporates known physical laws and models directly into AI architectures. This could involve embedding radiative transfer equations, hydrological

constraints, or vegetation scattering models into the learning process. One promising direction is the use of physics-informed neural networks, which integrate differential equations governing physical processes into the loss functions of neural networks. Adopting such approaches in wetland RS could enhance model robustness, interpretability, and transferability. A multidisciplinary framework that fuses AI, RS physics, and ecological modeling offers strong potential for advancing operational wetland monitoring systems.

In conclusion, addressing the remaining gaps will require an integrated approach, combining improved datasets, more sophisticated AI algorithms, and a deeper understanding of the physical processes that govern wetland environments. By tackling these challenges, we can significantly advance the capabilities of RS in wetland characterization and support more informed decision-making in environmental management and conservation.